EXPERIMENTAL CHARACTERIZATION AND SYNTHESIS OF NANOTWINNED Ni-Mo-W ALLOYS

by
Gianna M. Valentino

A dissertation submitted to Johns Hopkins University in conformity with the requirements for the degree of Doctor of Philosophy

Baltimore, Maryland
August 2019

© 2019 Gianna M. Valentino
All Rights Reserved

Abstract

Microelectromechanical systems (MEMS) have transformed consumer and industrial products through the integration of mechanical and electrical components within a single package. MEMS are ubiquitous in society, found predominantly in consumer electronics and automotive industries, providing interconnectivity across a wide variety of devices and everyday objects. To date, the materials selection for the structural element of many MEMS devices has been limited to a relatively small subset of materials, with silicon being the dominant choice. Employing MEMS sensors and switches in extreme environments will need advanced materials with a synergistic balance of properties, e.g. high strength, density, electrical conductivity, dimensional stability, and microscale manufacturability, but MEMS materials with this suite of properties are not readily available. Metallic systems are especially attractive for these applications due to their high density, strength and electrical conductivity. For this reason, metal MEMS materials are the motivation and focus for this dissertation.

The synthesis of nanotwinned nickel-molybdenum-tungsten (Ni-Mo-W) alloys resulted in thin films with a very favorable suite of properties. Combinatorial techniques were employed to deposit a compositional spread of $Ni_{85}Mo_xW_{15-x}$, alloys and to investigate their physical and mechanical properties as a function of alloy chemistry. The addition of Mo and W was shown to significantly decrease the coefficient of thermal expansion (CTE) and provide a route for tailoring the CTE and its temperature dependence with compositional control. The measured CTE values for Ni-Mo-W matched that of commercial glass substrates currently employed in MEMS devices, broadening the spectrum of materials with the requisite dimensional stability for use in layered structures. Microscale mechanical testing was used to

measure the in-plane tensile properties; a linear-elastic response with fracture strengths ranging from 2-3 GPa was uncovered. The ultrahigh tensile strengths are attributed to the presence of highly-aligned nanotwins and their effectiveness as obstacles to dislocation motion. In situ micropillar experiments demonstrated compressive strengths of 3-4 GPa and extremely localized plasticity, both of which are strongly orientation dependent. The nanoscale twins underpinning this mechanical behavior do not impede motion of electrons, and nanotwinned Ni-Mo-W thin films were found to posses the electrical conductivity of bulk Ni alloys. Taken as a whole, this study highlights the balance of physical, thermal and mechanical properties for Ni-Mo-W, driven by nanoscale twin formation.

Deposition of Ni-Mo-W films displayed a wide processing window for the formation of the requisite nanotwinned microstructure and attendant properties (CTE, strength, ductility and electrical resistivity). Microcantilever beams were designed and fabricated using traditional integrated circuit processing to translate thin film properties into prototype MEMS device structures. Laser interferometry was used to certify the dimensional stability of the cantilever beams as-fabricated and after thermal exposure at elevated temperatures associated with wafer bonding. Micromachined cantilever beams showed excellent dimensional stability with beam deflection profiles on the order of tens of nanometers, elucidating a path beyond outstanding material properties to actual device structures for next generation metal MEMS devices.

Advisor: Professor Kevin J. Hemker

Readers: Professors Kevin J. Hemker, Jaafar A. El-Awady, Jessica A. Krogstad

Acknowledgments

This dissertation would not have been possible without the assistance and immense support from my colleagues, friends and family. First and foremost, I would like to express the deepest appreciation to my advisor, Professor Kevin Hemker, for giving me the wonderful opportunity to join his research group in 2014. I first came to Johns Hopkins as a young physicist that had never heard of the words stress and strain, but over the past five years, Professor Hemker's guidance and passion for new discovery has shaped me into the interdisciplinary researcher, scientist and engineer that I am today. His unwavering support and commitment to my success provided me with every opportunity during my Ph.D. From the countless conferences, the summer internship, the extended travel to work with experts in our field and the day-to-day discussions, I am extremely grateful. I owe much of my success to the mentorship I have received from Professor Hemker.

I want to acknowledge all of my professors from the Departments of Mechanical Engineering and Materials Science and Engineering for providing me with the fundamental knowledge to tackle a research project that bridges the two disciplines. I am grateful for my thesis committee, Professors Jaafar El-Awady and Jessica Krogstad, and for their valued input into this work. I would like to thank Professor El-Awady for lending his group's experience and equipment during the early stages of my indentation experiments. I specifically want to recognize Dr. Quan Jiao and Steve Lavenstein for training and providing general expertise. I want to express particular gratitude to Professor Krogstad, who hosted me in Illinois for two weeks and continually allowed me to use and abuse her sputtering chamber. Much of the work presented in this thesis would not have been possible if not for her continued enthusiasm and support. I would like to express my gratitude to Professor Tim

Weihs for his expertise in thin film mechanics and use of his sputtering chamber for the initial Ni-Mo-W films.

I was lucky enough to work on a research project that connected me with a wide variety of experts and collaborators throughout the past five years. I would like to thank Dr. Chris Keimel for serving as a mentor on my research project in the early years and as a boss during my summer internship at GE Global Research. During my time at GE I worked with numerous colleagues that taught me manufacturing and characterization techniques that I later implemented into my own research. To Dr. Marco Aimi, Joleyn Brewer and Nick Yost, I am immensely grateful for our discussions and for allowing me to use your lab equipment. Additionally, I had the wonderful opportunity to work with the staff at the Quattrone Nanofabrication facility at the University of Pennsylvania. The thin films and micromachining expertise from Dr. Gyuseok Kim, Dr. Hiromichi Yamamoto, Meredith Metzler and David Jones were instrumental in many of the design protocols outlined in this dissertation.

For the past two years I was fortunate enough to be invited to a nanoindentation summer camp hosted by Professor George Pharr and Dr. Warren Oliver. Their knowledge on indentation mechanics and discovery of “the Donald” deformation facilitated much of the later work presented in this thesis. I want to specifically thank Professor George Pharr and his wife Marilyn for graciously hosting me on several occasions during my visits to Tennessee and Texas. Through my many travels and various collaborations I was lucky enough to work with many talented scientists. I want to especially acknowledge Dr. Pralav Shetty for indulging my every request for sputter deposited films. Many of the investigations presented in this thesis would not be possible without your assistance in film deposition.

Additionally I want to thank Dr. Sisi Xiang for her time and expertise in FIB specimen preparation.

Over the past five years, I had the privilege of working with the awesome members of the Hemker research group, both past and present. To the many postdoctoral fellows I have worked with (Professor Kelvin Xie, Professor Gi-dong Sim, Professor Yong Zhang, Professor Madhav Reddy, Dr. Zafir Alam, Dr. Ankur Chauhan) and the many graduate students (Dr. Binwei Zhang, Dr. Stephen Ryan, Dr. Suman Dasgupta, Dr. Simon Lockyer-Bratton, Dr. Paul Rottmann, Dr. Brady Butler, Dr. David Eastman, Betsy Congdon, Luoning Ma, Matt Vaughn, Jalil Alidoost, Arunima Banerjee, Ojaswi Agarwal, Sam Present) I am indebted to you all for your support and help over the past five years. I want to particularly acknowledge Professor Gi-dong Sim for teaching me about small-scale mechanical testing during my early years as a Ph.D. student. I need to thank Professor Kelvin Xie for his expertise in TEM and his friendship over the past five years; his enthusiasm for scholarship has always been an inspiration to me. I am grateful for Luoning Ma's kindness and willingness to help me with TEM and ASTAR. I also want to recognize my "work brother", David. I would not have survived the day-to-day struggles of Ph.D. life without you.

I had the pleasure of mentoring and working with some extremely talented undergraduate students over the years (Glenn Balbus, Minjae Jo, Felicia Koerner, Kevin Peters, Michael Swiercz, Adrian Au, Avi Gordon, John Cai). I have greatly benefited from interacting and collaborating with other postdoctoral fellows and graduate students. I want to thank the members of the Ramesh, Nguyen, El-Awady, Weihs, Ghosh, Hufnagel and Kang groups for their support and assistance. For all of you that helped proofread this dissertation (Matt, Jalil, Arunima, Ojaswi, Sam, Harsh, Tracy Ling), I am extremely appreciative for your help.

"*Friendship is the hardest thing in the world to explain. It's not something you learn in school. But if you haven't learned the meaning of friendship, you really haven't learned anything*" – Muhammad Ali. I am extremely grateful and appreciative for all of my friends who have cheered me on and supported me over the years, especially the friends I have made during my Ph.D. journey. To all of the people who started their Ph.D. with me, we have struggled through classes together, qualifying exams together and shared many drinks together. I am happy to say we remained great friends since day one (Andrew Robinson, Kimmie Andes, Dan Willen, Michelle Chen, Andrew Spielvogel, Anu Kaushik, Steve Lavenstein). In a very real sense, my friends have become my family in Baltimore. Whether it was the spontaneous trip to Iceland (Harsh, Amy Dagro, Debjoy Mallick, Anu Kaushik, Tracy Ling), the countless movies in Harbor East (Matt Vaughn, Jason Parker, Morgan Kuczler, Harsh, Amy, Debjoy) or just a Friday night playing Cards Against Humanity (Andrew Spielvogel, Jess Keene, Harsh, Anu, Tracy), you all have kept me sane and made the past five years an unforgettable experience. I need to acknowledge the "food fam" for always forcing me to enjoy some much needed time away from the lab and taste-test almost every restaurant within a 20 mile radius of Baltimore City (Harsh, Anu, Tracy). I want to particularly acknowledge Harsh, who very quickly became one of my closest friends and my biggest support system.

I would like to especially thank Professor Paul Angiolillo, who was not only my favorite undergraduate professor but also my biggest supporter and a wonderful friend. He was the most influential person in getting me where I am today, and for that I am eternally grateful. In addition, I need to acknowledge all of the wonderful friends from my time as an undergraduate student, especially Martin Iwanicki. We made it through physics together

(with John Mike Devany) and have spent the past five years keeping each other sane throughout our respective Ph.Ds. I am forever grateful for my best friend, college roommate and personal lawyer (Kristen Capriotti) being a captive audience while I practiced my science talks in our living room. She is my biggest cheerleader and I am lucky to have her and Mike Bucher as lifelong friends. I also want to particularly thank one of my best friends, Katie Abdill, for letting me sleep at her house countless times over the past few years while working in the cleanroom. She has been a huge support system since the day we met and always reminds me to take a break and to have fun. I am grateful for all of my high school friends that have been encouraging my dreams for more than a decade, I am happy to have you all in my life (Sami Kofsky, Cara McCoach, Molly Moskowitz, Pat Schetter, Jeff Chiusano, Pat Leach, Peter Sanchez, Eric McCoach, Jen Garavente, Mike Randall).

Finally, I could not be where I am today without the love and support of my family. To my parents, Carmen and Cindy, I am extremely appreciative for all that you have sacrificed for me. I am thankful that from a very young age you raised me to question everything and dream the impossible. I am lucky to have an extremely supportive family network, which in an Italian family is quite a long list. To keep it short, I want to recognize my older brother Carmine, my sister-in-law Lindsay, their beautiful baby Vincenzo and my younger sister Isabella. I am so fortunate and thankful to have three of my grandparents supporting me every step of the way. Last but certainly not least, I want to dedicate this thesis to my Mommom, Tina Valentino, who died in June 2006. She taught me to be a strong and independent thinker from a very young age; she was my role model and biggest supporter.

Table of Contents

Abstract ..... **ii**

Acknowledgments ..... **iv**

List of Tables ..... **xii**

List of Figures ..... **xiii**

CHAPTER 1: INTRODUCTION AND BACKGROUND **1**

1.1 Motivation **1**

1.2 Background **2**

1.2.1 LIGA Ni 4

1.2.2 Ni alloys 7

1.2.2.1 Electrodeposition 7

1.2.2.2 Vapor-phase-aluminization 8

1.2.2.3 Sputter deposition 9

1.3 Sputter deposited Ni-Mo-W alloys **10**

1.4 Nanotwinned fcc metals **14**

1.5 Thesis overview **17**

1.6 References for Chapter 1 ..... **20**

CHAPTER 2: TAILORING THE COEFFICIENT OF THERMAL EXPANSION OF Ni-Mo-W ALLOYS WITH CHEMISTRY **25**

2.1 Introduction **25**

2.2 Experimental procedure **26**

2.2.1 Methods 26

2.2.2 Materials 28

2.2.2.1 Wavelength-dispersive spectroscopy (WDS) 31

2.2.2.2 Four-point probe electrical resistivity 31

2.2.3 Measuring thermal displacements 33

2.3 Calibration **39**

2.4 The Influence of Alloy Chemistry **44**

2.4.1 Measured physical properties 44

2.4.2 Tailorable CTE 49

2.5 Chapter summary **53**

2.6 References for Chapter 2 ..... **54**

CHAPTER 3: MICROSTRUCTURAL EFFECTS ON THE THERMAL AND MECHANICAL BEHAVIOR OF Ni-Mo-W ALLOYS 57
3.1 Introduction 57
3.2 Experimental methods 58
3.2.1 Specimen fabrication and characterization 58
3.2.1.1 EBSD sample preparation 62
3.2.2 Mechanical testing 63
3.3 Microstructural morphology 65
3.3.1 Cross-sectional microstructure 65
3.3.2 As-sputtered variations 68
3.3.3 XRD texture analysis 72
3.3.3.1 Lattice constant 72
3.3.3.2 Texture gradient 76
3.4 Mechanical response 79
3.4.1 Fracture strength 79
3.4.2 Elastic modulus 84
3.4.3 Nanotwins 86
3.5 MEMS integration 87
3.6 Chapter summary 89
3.7 References for Chapter 3 90
CHAPTER 4: LOCALIZED ANISOTROPIC PLASTICITY IN NANOTWINNED Ni-Mo-W 94
4.1 Introduction 94
4.2 Materials and methods 95
4.2.1 Material fabrication and characterization 95
4.2.2 Mechanical testing 96
4.2.2.1 Nanoindentation 96
4.2.2.2 In situ compression 101
4.2.3 Post-mortem characterization 102
4.2.3.1 TEM-based orientation mapping 102
4.3 Hardness and local instabilities in nanoindentation 104
4.4 Micropillar compression 110
4.4.1 In situ mechanical loading 110
4.4.2 TEM observations of plasticity in deformed micropillars 120
4.4.3 Hardening and strengthening due to nanotwins 126
4.5 Chapter summary 129
4.6 References for Chapter 4 131

CHAPTER 5: THE EFFECT OF DEPOSITION RATE ON NANOTWIN FORMATION IN Ni-Mo-W ... 134
5.1 Introduction ... 134
5.2 Materials and methods ... 135
5.3 Microstructural characterization ... 137
5.3.1 Texture and grain size ... 137
5.3.2 Nanotwin thickness ... 141
5.4 Mechanical strength ... 144
5.5 Microstructural stability ... 147
5.6 Chapter summary ... 150
5.7 References for Chapter 5 ... 152
CHAPTER 6: FABRICATION AND CHARACTERIZATION OF Ni-Mo-W MICROCANTILEVER BEAMS ... 154
6.1 Introduction ... 154
6.2 Fabricating Ni-Mo-W microcantilevers ... 155
6.2.1 Blanket thin films ... 155
6.2.2 Micromachining ... 163
6.3 Characterizing dimensional stability ... 167
6.3.1 Interferometry ... 167
6.3.2 Released beam deflections ... 170
6.3.3 Deflections associated with thermal exposure ... 175
6.4 Mechanistic interpretation of dimensional changes ... 175
6.4.1 Quantifying intrinsic stresses ... 175
6.4.2 Effect of temperature ... 179
6.5 Chapter summary ... 182
6.6 References for Chapter 6 ... 183
CHAPTER 7: SUMMARY AND FINDINGS ... 185
7.1 Review of key findings ... 185
7.2 Future directions ... 190
7.3 References for Chapter 7 ... 194
APPENDIX 1: X-RAY PENETRATION DEPTH ... 196
APPENDIX 2: MICROPILLAR COMPRESSION ... 199
APPENDIX 3: MICROCANTILEVER FABRICATION ... 205
Vita ... 213

List of Tables

Table 2.1: Electrical resistivity measured using four-point probe technique. All compositions have a maximum standard deviation of ± 0.1 atomic percent Ni, Mo and W. 44

Table 2.2: Alloy composition and CTE values from room temperature (RT) and 600°C for the sputter deposited Ni-Mo-W films. 47

Table 2.3: Predicted CTE values at room temperature (RT) and 600°C for $Ni_{85}Mo_{15}$ and $Ni_{85}W_{15}$ using the rule-of mixtures. 50

Table 3.1: Summary of the subset of Ni-Mo-W alloys tested in uniaxial tension with reported fracture strength and elastic modulus for films as-deposited and heat treated for 1 hour at 400°C. Film thickness, the contribution of the nanocrystalline (nc) region and the columnar tilt angles were measured from FIB channeling contrast images (Figure 3.7). 67

Table 4.1: Alloy composition and calculated activation volume from the hardness measurements at different strain rates. For each strain rate, 20 indents were performed. 105

Table 5.1: Summary of the deposition conditions used for the $Ni_{84}Mo_{11}W_5$ (at. %) films, all deposited at room temperature. 136

Table 5.2: A summary of the in-plane grain size, nanotwin thickness, hardness and calculated compressive yield strength as a function of deposition rate. 146

Table 6.1: Average film stress from wafer curvature measurements for various Ni-Mo-W films as-deposited. Deposition rates calculated from ~2.5 µm thick films with dc powers 200-600 W and Ar gas pressures 1-4 mTorr. 163

Table 6.2: Summary of micro-cantilever beam deflections for beams of length 100, 50 and 20 µm averaged over the respective widths for the as-fabricated and heat treated beams at 200°C and 400°C for 1 hour. 174

Table 6.3: Summary of micro-cantilever beam takeoff angles, curvatures and maximum stress gradients averaged over all beam lengths for the as-fabricated and heat treated beams at 200°C and 400°C for 1 hour. 174

List of Figures

Figure 1.1: A schematic representation of the components of MEMS, adapted from [1]....... 3

Figure 1.2: Examples of existing and potential MEMS materials for different temperature applications [13].. 4

Figure 1.3: (a) Illustration of the basic workflow of the LIGA process, where (b) describes all of the steps needed to achieve the high aspect ratio structure [15].................................... 5

Figure 1.4: Example of a microsystem consisting of LIGA Ni components; an escapement mechanism used for damping of a spring-mass-accelerometer structure through a rack-and-pinion coupling [17].. 6

Figure 1.5: Microhardness of LIGA Ni and different alloy content LIGA Ni-W alloys as a function of annealing temperature (2 hour duration) [21]. 7

Figure 1.6: Uniaxial tension stress-strain curves for as-deposited and annealed Ni-W with (a) Ni-5at.%W and (b) Ni-15at.%W [23]... 8

Figure 1.7: Aluminized LIGA Ni-Al, showing two phase Ni-Ni_3Al (γ-γ’) microstructure after homogenizing for 62 hours at 1200°C, adapted from [29].. 9

Figure 1.8: Sputter deposited commercial Ni alloy 718 aged at 720°C for 8 hours and 620°C for 8 hours, adapted from [33]. The high strength of 2 GPa is far superior to the bulk reported value and retains a moderate 3% ductility. 10

Figure 1.9: Coefficient of thermal expansion versus temperature for Ni and Ni-Mo alloys determined from commercial dilatometer methods, adapted from [37]. 11

Figure 1.10: Uniaxial tension stress-strain curve for $Ni_{83.6}Mo_{14}W_{2.4}$ compared to polysilicon, nanocrystaline Ni, Ni-15.at%W and nanotwinned copper (Cu) to demonstrate the ultrahigh 3.5 GPa strength. Adapted from [38].. 12

Figure 1.11: (a) Cross-sectional focused ion beam channeling contrast image of the $Ni_{83.6}Mo_{14}W_{2.4}$ films. (b) Transmission electron microscope (TEM) bright field micrograph with a selected area electron diffraction pattern inset, showing the matrix and twin. (c) High resolution TEM image of the matrix (red), twins (blue) and stacking faults (yellow). Adapted from [38]. 13

Figure 1.12: Plane view bright field transmission electron microscopy image of the $Ni_{83.6}Mo_{14}W_{2.4}$ films (a) as-deposited, heat treated at (b) 600°C, (c) 800°C and (d) 1000°C [41]... 14

Figure 1.13: Uniaxial tension stress-strain response for nanotwinned Cu specimens showing the effect of twin spacing, taken from [59].. 16

Figure 2.1: Design of a CTE furnace for planer specimen testing. (a) Schematic of the furnace base with heating coils, quartz rod specimen holder and thermocouple. (b) Schematic of furnace lid with central viewport (optical quality quartz) and two angled quartz rods for illumination. (c) Full setup with camera imaging through the central viewport, illuminated via LED.. 28

Figure 2.2: (a) Custom-built sputtering chamber in Timothy Weihs' laboratory at JHU and (b) custom alloy target with binary alloys Ni-Mo and Ni-W joined on a bias. 29

Figure 2.3: (a) Schematic of alloy target geometry and (b) Ni-Mo-W film on the brass substrate after sputter deposition. 29

Figure 2.4: Cylindrical bar of SMR 738 sectioned into 2 mm x 2 mm using wire EDM. Individual specimens were sliced from the bar using a diamond wire saw. 30

Figure 2.5: Principle of wavelength dispersive spectroscopy [7]. 31

Figure 2.6: Four-point probe measurement setup, where four probes are equally spaced and current is applied through probes 1 and 4 while the associated voltage change is measured with probes 2 and 3. 32

Figure 2.7: A representative displacement versus position plot from SRM 738 at image 300 (385°C). More than 4700 DIC tracking markers are fit to a linear line (red) and the measured slope provides a one-dimensional strain value with a resolution of $\pm 10^{-5}$. 35

Figure 2.8: The calculated thermal strain as a function of image number for SRM 738 while heating from room temperature, 505°C and cooling down. 36

Figure 2.9: The calculated thermal strain as a function of temperature for SRM 738 while heating from room temperature, 505°C (ramp up) and cooling down (ramp down). 37

Figure 2.10: Third-order polynomial fitting of the mean strain for SRM 738. 38

Figure 2.11: Calculated CTE of SRM 738 from the derivative of the polynomial fit with respect to temperature. 38

Figure 2.12: Strain versus temperature measured thermal displacements (raw) for SRM 738 compared to NIST standard data for comparison [6]. 40

Figure 2.13: Representative image with DIC speckle pattern applied to both the specimen holder (red) and the NIST SRM 738 (yellow). 41

Figure 2.14: Strain versus temperature for SRM 738. The corrected data, obtained by subtracting the measured offset from the raw data, is compared to NIST [6]. 42

Figure 2.15: Calculated values of CTE determined from the measured thermal displacements for SRM 738. The corrected data is compared to NIST standard data [6]. 43

Figure 2.16: Thermal strain measurements as a function of temperature for $Ni_{85.1}Mo_{4.6}W_{10.3}$. 45

Figure 2.17: CTE versus temperature for compositional spread of Ni-Mo-W alloys, with associated at.% composition, compared to pure Ni [18]. 46

Figure 2.18: CTE versus temperature for W-rich alloys, compared to pure Ni [18]. 48

Figure 2.19: CTE versus temperature for Mo-rich alloys, compared to pure Ni [18]. 48

Figure 2.20: Variations of the CTE at room temperature (RT) and 600°C against the concentration of Mo and W for the calculated rule-of mixtures and the sputtered Ni-Mo-W alloys, where $Ni_{85}Mo_xW_{15-x}$ with x ranging 2-13 at. % Mo. 51

Figure 3.1: A schematic of the sputtering chamber (top-down view) with Ni-Mo-W target mounted on the outside wall and brass substrates mounted on the rotatable carousel. 59

Figure 3.2: A representation of the sputtered films, sectioned and labeled 1-8 with their chemical composition (atomic percent) for identification. 60

Figure 3.3: Principle of symmetric X-ray diffraction (XRD), where the incident angle and the diffracted angle are the same throughout the scan [22]. 61

Figure 3.4: (a) Vacuum tube furnace used for heat treatments and (b) magnified image of the Ni-Mo-W films sandwiched between alumina plates inside the evacuated tube................... 62

Figure 3.5: Microtensile load frame, adapted from [24]... 64

Figure 3.6: Microtensile specimen clamped between two flat plates during mechanical testing. 64

Figure 3.7: Cross-sectional FIB channeling contrast images for a subset of the as-deposited Ni-Mo-W films with increasing Mo-content: (a) alloy 1 ($Ni_{84.9}Mo_{2.1}W_{13}$), (b) alloy 2 ($Ni_{85.4}Mo_{3.3}W_{11.3}$), (c) alloy 3 ($Ni_{85.1}Mo_{4.6}W_{10.3}$), (d) alloy 4 ($Ni_{85.4}Mo_{5.9}W_{8.7}$), (e) alloy 6 ($Ni_{84.4}Mo_{10.7}W_{4.9}$), and (f) alloy 7 ($Ni_{84.2}Mo_{11.8}W_{4.0}$). All cross-sections show a 31-37% nanocrystalline layer at the bottom of the films, with the remainder columnar grains oriented along the growth direction. 66

Figure 3.8: Bright-field TEM micrographs of columnar grains filled with nanotwins and an inset of a selected-area electron diffraction pattern indexed for the twin and the matrix. (a) W-rich alloy 2 ($Ni_{85.4}Mo_{3.3}W_{11.3}$) and (b) Mo-rich alloy 6 ($Ni_{84.4}Mo_{10.7}W_{4.9}$). 68

Figure 3.9: IPF plotted for the direction perpendicular to the as-deposited films. (a) Alloy 2 ($Ni_{85.4}Mo_{3.3}W_{11.3}$) with a ~15° columnar tilt with respect to the surface normal, (b) alloy 4 ($Ni_{85.4}Mo_{5.9}W_{8.7}$) with nominally aligned grains with the surface normal and (c) alloy 6 ($Ni_{84.4}Mo_{10.7}W_{4.9}$) with 11° columnar tilt with respect to the surface normal. 71

Figure 3.10: XRD peaks for the as-deposited freestanding Ni-Mo-W alloys with (a) the substrate side upwards showing a more balance of diffraction peaks for and (b) the columnar grain side upward with exclusively (111) diffraction peaks across all eight investigated compositions. XRD peaks for polycrystalline Ni (black) are shown for comparison. 73

Figure 3.11: XRD peaks from a subset of the freestanding Ni-Mo-W alloys after 1 hour 400°C heat treatment with (a) the substrate side upwards and (b) the columnar grain side upwards. XRD peaks for polycrystalline Ni (black) are shown for comparison. 75

Figure 3.12: Fractional intensity of {111} peaks obtained via XRD for the (a) as-deposited and (b) heat treated at 400°C freestanding Ni-Mo-W films. The bottom portion of the film showed some randomized nanocrystalline (nc) grains while the continued growth and top portion of the film has long columnar grains. 78

Figure 3.13: Stress-strain response for a representative subset of the as-deposited Ni-Mo-W films showing brittle linear-elastic behavior. Elastic modulus is measured from the slope of each curve and the fracture strength is taken as the maximum value before fracture. For each alloy, two to three specimens were tested. 80

Figure 3.14: Cross-sectional SEM of the fracture surface of as-deposited Ni-Mo-W alloy 4 ($Ni_{85.4}Mo_{5.9}W_{8.7}$) with brittle failure. Cleavage along the columnar grain boundaries is highlighted in red. The nanocrystalline portion (yellow) shows modest evidence of dimpling. 81

Figure 3.15: Stress-strain response for a representative subset of heat treated films for 1 hour at 400°C in 10^{-6} Torr vacuum showing brittle linear-elastic behavior. Elastic modulus is measured from the slope of each curve and the fracture strength is taken as the maximum value before fracture. For each alloy, two to three specimens were tested. 82

Figure 3.16: Tensile specimen with thickness variation 10.3 ± 0.3 μm failed in the grip section during loading due to sidewall roughness from wire EDM machining........ 83

Figure 3.17: Cross-sectional SEM micrograph of the fracture surface exhibiting dimpling, indicating microplasticity, for a laser machined $Ni_{83.6}Mo_{14}W_{2.4}$ tensile specimen. 84

Figure 3.18: Micrograph of the in-plane surface morphology of alloy 7 ($Ni_{84.2}Mo_{11.8}W_{4.0}$) displaying a random distribution of voids after heat treatment for 1 hour at 400°C. 88

Figure 4.1: (a) A schematic of the load-displacement curve obtained during a typical indentation experiment, labeled with the quantities: P_{max} is the maximum load reached during indentation, h_{max} is the indenter displacement at the maximum load, h_f is the final depth of the contact impression after unloading and S is the initial unloading stiffness. (b) The contact depth h_c is defined as the vertical distance along which contact was made, while h_s is the displacement of the surface at the perimeter of contact. Adapted from [3]........ 98

Figure 4.2: Nanomechanics Inc. iNano system, equipped with a 50 mN load cell and a custom machined puck equipped for mounting SEM stubs........ 99

Figure 4.3: Representative frame stiffness (K_f) calibration for the custom machined puck (Figure 4.2) using the intercept of the linear fit. 100

Figure 4.4: NanoMechanics Inc. in situ compression stages. (a) The NanoFlip has a 50 mN load cell and also allows the user to flip the specimen 90° for easier imaging in the SEM. (b) InSEM has a 1 N load cell, but cannot flip the specimen. 101

Figure 4.5: Representative plot of the measured hardness as a function of depth at strain rate 0.1 s^{-1}. Average hardness is reported from depths 200-250 nm........ 105

Figure 4.6: Instrumented nanoindentation load-depth curves during loading of $Ni_{84.4}Mo_{10.7}W_{4.9}$ films, offset 100 nm for visualization, at strain rates 0.02-1 s^{-1}. Arrows point to examples of local instabilities........ 106

Figure 4.7: SEM micrographs of the Berkovich indent at strain rates 0.02, 0.1, 0.2 and 1 s^{-1} showing evidence of shear banding. 107

Figure 4.8: Natural log of strain rate versus the hardness for $Ni_{84.4}Mo_{10.7}W_{4.9}$ films. Linear line fit through the data has a slope of 2.19×10^{-9} Pa^{-1}, which is used to calculate the activation volume........ 108

Figure 4.9: Symmetric impression made by pressing the flat punch into the Ni-Mo-W film surface at high load ~45 mN, indicating proper alignment between the tip and the specimen surface during in situ compression loading. Plastic deformation and extruded material are observed locally around the indenter impression........ 110

Figure 4.10: The stress-strain response of a micropillar compressed to a depth of 1 μm at a nominal strain rate of 10^{-3} s^{-1} showing extremely high flow strength and discrete strain bursts. 112

Figure 4.11: A deformed micropillar after being compressed to a depth of 1 μm at a constant nominal strain rate of 10^{-3} s^{-1}, with associated mechanical response in Figure 4.10. 112

Figure 4.12: Stress-strain curve of a micropillar that was loaded-unloaded-reloaded for 10 cycles at a nominal strain rate of 10^{-3} s^{-1}. Ultrahigh flow strengths have a repeatable 3.51±0.23 GPa yield point. 114

Figure 4.13: In situ pillar compression associated with incremental load-unload-reload cycles (Figure 4.12) with representative deformed images taken at (a) 0%, (b) 4.5%, (c) 12.2%, (d) 21.1% and (e) 31.8% nominal strain. All of the deformation is highly localized at the top of the pillar and has a directional dependence. 115

Figure 4.14: Four deformed micropillars exhibiting repeatable highly localized anisotropic plasticity. 116

Figure 4.15: (a) FIB channeling contrast image of a cross-section of the Ni-Mo-W film used to machine micropillars and (b) representative SAED pattern, indexed for the matrix and the twin, with streaking that is representative of stacking faults. 117

Figure 4.16: Schematic of the microstructural geometry with respect to the compression loading direction. (a) Columnar grains and nanotwins at a slight 11° tilt with respect to the compression axis and (b) nanotwins aligned perpendicular to the compression axis 118

Figure 4.17: Stress-strain curve of a micropillar with well-aligned columnar grains and perpendicular nanotwins with the compression axis. Five different loaded-unloaded-reloaded cycles were performed at a nominal strain rate of 10^{-4} s^{-1}. Ultrahigh flow strengths with a very repeatable 3.55±0.13 GPa yield point was observed for each of the loading steps. 119

Figure 4.18: In situ pillar compression of the well-aligned microstructure, associated with incremental load-unload-reload cycles (Figure 4.17) with representative deformed image taken at 14% nominal strain. All of the deformation is highly localized at the top of the pillar, but the deformation spread more evenly about the transverse direction. 119

Figure 4.19: Cross-sectional TEM lift-out of a deformed micropillar, before final thinning. Vast amounts of material re-deposition is observed around the micropillar. Platinum re-deposition is visibly lighter in color, outlining the micropillar, whereas the Ni-Mo-W re-deposition is darker in color and fills in the empty cavity surrounding the micropillar. 120

Figure 4.20: (a) Cross-sectional TEM lift-out of a deformed micropillar thinned to electron transparency. The bottom portion of the micropillar displays the tilted columnar gains at an 11° tilt. SAED patterns taken in the starred regions show (b) the nanotwinned (red) and (c) the nanocrystalline (yellow) microstructures. 121

Figure 4.21: Bright field micrograph with IPF mapping from ACOM overlaid in the region of the first shear band. The IPF is shown for the loading direction (z) orientation and the inset is used for location identification. Regions marked (i) indicate columnar grains with nanotwins, whereas regions marked (ii) indicate nanocrystalline fcc shear band, separated by dashed lines. 124

Figure 4.22: (a) Pole figure (PF) for the nanotwinned regions marked (i) in the z-direction and (b) PF for nanotwinned region rotated 25° about the x-direction. (c) Bright field micrograph with the 25° rotated IPF in the z-direction. 125

Figure 5.1: XRD data of the Ni-Mo-W films across the deposition rates, with polycrystalline Ni peaks (black) shown for reference. Intensity is normalized to the (111) peak for comparison and a strong (400) Si peak is evident for the films attached to their substrate.. 137

Figure 5.2: Inverse pole figure (IPF) mapping overlaid with the confidence index (CI), showing strong {111} texture oriented parallel to the growth direction, for films sputtered at (a) 0.5, (b) 0.7, (c) 0.9, and (d) 2.3 nm/s. 138

Figure 5.3: IPF mapping overlaid with the CI showing the in-plane direction for films sputtered at (a) 0.5, (b) 0.7, (c) 0.9, and (d) 2.3 nm/s. 139

Figure 5.4: Average in-plane grain size for the films sputtered at different deposition rates. The error bars represent one standard deviation from the average grain size. 140

Figure 5.5: Bright field TEM micrographs of the films sputtered at (a) 0.5, (b) 0.7, (c) 0.9 and (d) 2.3 nm/s with upward growth direction. Insets of SAED patterns on the [011] zone axis are indexed for twin and matrix orientations. 141

Figure 5.6: (a) Representative gray scale intensity used to measure the twin thickness from (b) along the red line in the bright field micrograph for films sputtered at a deposition rate of 0.9 nm/s. 142

Figure 5.7: Distribution of nanotwin spacing for films sputtered at (a) 0.5, (b) 0.7, (c) 0.9, and (d) 2.3 nm/s. 143

Figure 5.8: The average nanotwin thickness as a function of deposition rate, with error bars representing one standard deviation. 144

Figure 5.9: Scanning electron microscopy (SEM) micrographs of the surface impressions left behind from nanoindentation for films with deposition rates (a) 0.5, (b) 0.7, (c) 0.9, and (d) 2.3 nm/s. 145

Figure 5.10: The hardness measured from instrumented nanindentation as a function deposition rate, with error bars representing one standard deviation. 146

Figure 5.11: PF showing strong texture of the {111} columnar grains for films with deposition rates (a) 0.5, (b) 0.7, (c) 0.9, and (d) 2.3 nm/s. 148

Figure 5.12: Representative low-magnification bright field micrograph from the films deposited at 0.5 nm/s, indicating a high density of nanotwins spanning across several grains. 149

Figure 6.1: (a) AJA International Inc. ATC 1800 UHV located at UIUC in Jessica Krogstad's laboratory and (b) Kurt J. Lesker Pro Line PVD 75 located inside the cleanroom at UPenn Singh Center for Nanotechnology. 156

Figure 6.2: TEM micrograph of (a) entire film thickness on 300 nm of silicon nitride and silicon, (b) magnified bright field image of columnar grain with (c) magnified view of nanotwins and (d) the associated selected area electron diffraction pattern indexed for the matrix and twins. 158

Figure 6.3: (a) The relative contributions from the intrinsic growth stress compared to the CTE thermally induced stress [15]. (b) The tensile to compressive transition Ar pressure for different sputter deposited metals, adapted from [13], highlighted for Ni. 161

Figure 6.4: (a) KLA Tencor P7 2 Profilometer located inside the cleanroom at UPenn Singh Center for Nanotechnology and (b) magnified image of the probe tip scanning a silicon wafer to measure its curvature. 162

Figure 6.5: Wafer curvature measurement for the blank Si/Si_3N_4 substrate, the curvature after Ni-Mo-W film deposition and the difference between the two. The Ni-Mo-W has an average radius of curvature -4.537 m, used to calculate the residual stress. 162

Figure 6.6: Process for fabricating micro-cantilever beams though lithography and etching blanket Ni-Mo-W thin films. 164

Figure 6.7: (a) Front chromium lithographic mask consisting of hundreds of arrays of microcantilevers, donated from GEGR. (b) Repeated arrays of micro-cantilever beams from the front chromium lithographic mask. (c) Empty windows representing the back lithographic mask. 165

Figure 6.8: Cross-sectional view of 20 µm long cantilevers, demonstrating the perpendicular sidewalls achieved using the Nichrome wet etchant. No visible undercut was observed. ... 166

Figure 6.9: Principle of a Michelson interferometer, consisting of a beamsplitter and two mirrors (or reflectors).......................... 168

Figure 6.10: Interferometry measurement of the out-of-plane deflection profile measured along the length of a 50 µm cantilever beam compared with a polynomial fit.......................... 169

Figure 6.11: (a) SEM image of array of freestanding microcantilever beams group by length (500, 200, 100, 50 and 20 µm) with a range of widths (100, 50, 40, 30, 20, 10 µm) for each length. (b) Interferometry fringes for 100 µm long cantilevers with widths of 100, 50, 40, 30 and 20 µm. Spacing between cantilevers is 100 µm, not shown to scale here. 171

Figure 6.12: As-fabricated micro-cantilever beam deflection profiles for 100 µm long beams with different widths ranging from 10-100 µm. 172

Figure 6.13: As-fabricated micro-cantilever beam deflection profiles for 50 µm long beams with different widths ranging from 10-100 µm. 172

Figure 6.14: As-fabricated micro-cantilever beam deflection profiles for 20 µm long beams with different widths ranging from 10-100 µm. 173

Figure 6.15: The average across different beam widths (10-100 µm) for three different beam lengths (20, 50 and 100 µm). 173

Figure 6.16: Schematic of a freestanding microcantilever and stress state prior to release, during hypothetical intermediate stages and after release, adapted from [18]. (a) As-fabricated stress gradient and uniform compressive stress in the thin film prior to release, (b) the effect of relieving the uniform compressive stress (σ_0) but maintaining the gradient (σ_1), (c) the effect relieving the stress gradient (σ_1) but maintaining the uniform compressive stress (σ_0) and (d) the geometric shape of the fully stress-relieved cantilever with zero stresses throughout the beam. 178

Figure 6.17: The structure zone model for sputter deposited films, adapted from [14]. 181

Figure A2.1: Stress-strain curve of a micropillar with an 11° columnar grain tilt that was loaded-unloaded-reloaded for 3 cycles in increments of 1 μm at a nominal strain rate of 10^{-3} s^{-1}. 199

Figure A2.2: Stress-strain curve of a micropillar with an 11° columnar grain tilt that was loaded-unloaded-reloaded for 3 cycles in increments of 1 μm at a nominal strain rate of 10^{-3} s^{-1}. 200

Figure A2.3: Stress-strain curve of a micropillar with an 11° columnar grain tilt that was loaded to a depth of 2 μm at a nominal strain rate of 10^{-3} s^{-1}. 200

Figure A2.4: Stress-strain curve of a micropillar with an 11° columnar grain tilt that was loaded-unloaded-reloaded for 2 cycles in increments of 1 μm at a nominal strain rate of 10^{-3} s^{-1}. 201

Figure A2.5: Stress-strain curve of a micropillar with an 11° columnar grain tilt that was loaded-unloaded-reloaded for 5 cycles in increments of 100 nm at a nominal strain rate of 10^{-3} s^{-1}. 201

Figure A2.6: Stress-strain curve of a micropillar with an 11° columnar grain tilt that was loaded-unloaded-reloaded for 9 cycles in increments of 50 nm at a nominal strain rate of 10^{-4} s^{-1}, where loading step 1 started at 150 nm. 202

Figure A2.7: Stress-strain curve of a micropillar with an 11° columnar grain tilt that was loaded-unloaded-reloaded for 3 cycles in increments of 100 nm at a nominal strain rate of 10^{-4} s^{-1}, where loading step 1 started at 200 nm. 202

Figure A2.8: Stress-strain curve of a micropillar with an 11° columnar grain tilt that was loaded-unloaded-reloaded for 12 cycles in increments of 50-100 nm at a nominal strain rate of 10^{-4} s^{-1}, where loading step 1 started at 200 nm. Pillar diameter was 5 μm instead of 3 μm to examine size effects. 203

Figure A2.9: Stress-strain curve of a micropillar with well-aligned columnar grains and perpendicular nanotwins with the compression axis. Six different loaded-unloaded-reloaded cycles were performed in 50 nm increments at a nominal strain rate of 10^{-4} s^{-1}. 204

Figure A2.10: Stress-strain curve of a micropillar with well-aligned columnar grains and perpendicular nanotwins with the compression axis. Six different loaded-unloaded-reloaded cycles were performed in 50 nm increments at a nominal strain rate of 10^{-4} s^{-1}, where loading step 1 started at 100 nm. 204

Figure A3.1: Frontside lithography processes with: (a) the blank wafer, (b) Ni-Mo-W thin film deposition, (c) spin-coated photoresist, (d) patterned photoresist, (e) wet etch to shape the Ni-Mo-W cantilevers and (f) removal of the photoresist. 211

Figure A3.2: Backside lithography processes with: (a) spin-coated photoresist, (b) patterned photoresist, (c) backside RIE to remove silicon nitride, (d) spin-coated ProTEK B3, (e) KOH wet etch of Si and (f) removal of the ProTEK. 212

CHAPTER 1: INTRODUCTION AND BACKGROUND

1.1 Motivation

Over the past several decades, microelectromechanical systems (MEMS) have revolutionized consumer and industrial products through the integration of mechanical and electrical components onto a single platform. These miniaturized devices have the ability to sense and actuate on the micrometer scale (10^{-6} or one millionth of a meter), while generating an effect on the macroscopic scale [1]. Among the first to conceptualize MEMS devices was world-renown physicist and Nobel laureate Richard Feynman. In December 1959, he delivered his seminal lecture at the annual American Physical Society meeting, titled "There's Plenty of Room at the Bottom", where he proposed the feasibility of manipulating and controlling materials on the nanometer scale (10^{-9} or one billionth of a meter). He concluded his talk by issuing a challenge to the scientific community, offering a $1,000 prize to the first person to construct an electrical motor smaller than 1/64th of an inch (around 400 micrometers).

MEMS have since become an integral part of a multi-billion dollar per year industry with numerous sensors, actuators and resonators [2, 3]. The onset of the computer age in the early 1990's [4] sparked a societal shift towards miniaturization and the advent of the "Internet of Things" (IoT), where MEMS have the potential to provide ubiquitous sensing and connectivity across both consumer and industrial sectors [5]. To date, the materials available for the structural element of MEMS devices has been limited to a relatively small subset, with silicon (Si) being the dominant choice. However, future MEMS devices can and will

benefit from high temperature structural materials with potential applications in aviation, power generation [6, 7], sub-sea drilling and high frequency switches [8].

A broader variety of MEMS materials would offer a wider range of functionality and stimulate an increasingly expanding assortment of applications. The vast majority of commercial MEMS devices are still fabricated out of Si due the availability of integrated circuit (IC) foundries and photolithography techniques, providing the ability to shape structures on the micrometer scale in batch processing. Si also exhibits an extremely repeatable and predictable linear-elastic mechanical response and low coefficient of thermal expansion (CTE). However, poor mechanical properties at elevated temperatures hinder its use at these temperatures [9, 10]. Employing MEMS in extreme environments requires a broader spectrum of materials with a balance of physical, electrical and mechanical properties. Advanced metallic systems are especially attractive for these applications because they offer high density, strength and electrical and thermal conductivity. This dissertation describes the efforts to develop and characterize metallic materials with a superior balance of physical, electrical and mechanical properties for use in high temperature MEMS applications. Particular attention in this dissertation has been given to the careful control and design of the underlying microstructure that facilitates the desired suite of properties.

1.2 Background

Fundamentally, MEMS consist of micrometer scale structures, sensors, actuators and electronics all wrapped into the same package, Figure 1.1. Materials performance criteria vary depending on the application, but structural stability is critical in most applications.

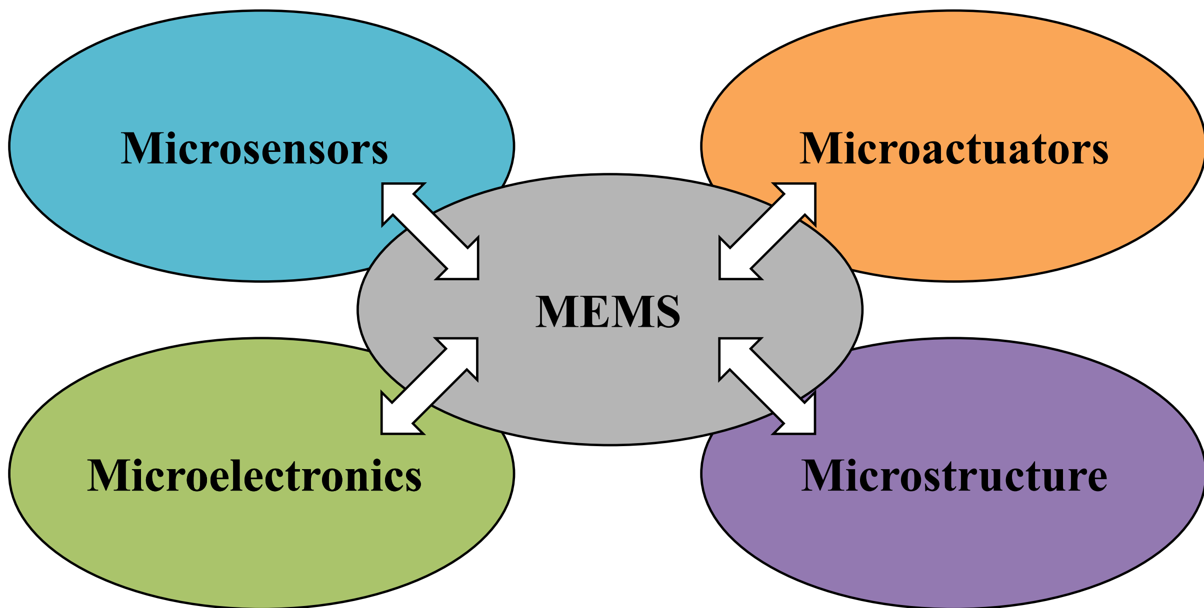

Figure 1.1: A schematic representation of the components of MEMS, adapted from [1].

Dimensional stability is particularly important in capacitive-based sensors and guidance, where shape changes caused by thermal expansion or microstructural evolution must be significantly less than the expected changes induced during operation of the device. For this reason, Si is often chosen for its low CTE, but temperatures above 120°C have significant junction leakage [11] and Si exhibits poor creep strength at elevated temperatures. Although silicon-based devices currently dominate the market, there is increasing interest in developing emerging materials for high temperature MEMS applications [12-14]. Krogstad et al. reviewed the current materials available for high temperature MEMS [13], finding very few materials that possess a balance of thermal and mechanical stability above 200°C, Figure 1.2. The use of ceramics, such as silicon carbide (SiC) and silicon carbon nitride (SiCN), have emerged as suitable materials for high temperature MEMS, but inherent residual stresses and complex fabrication techniques have limited their widespread use [11-13].

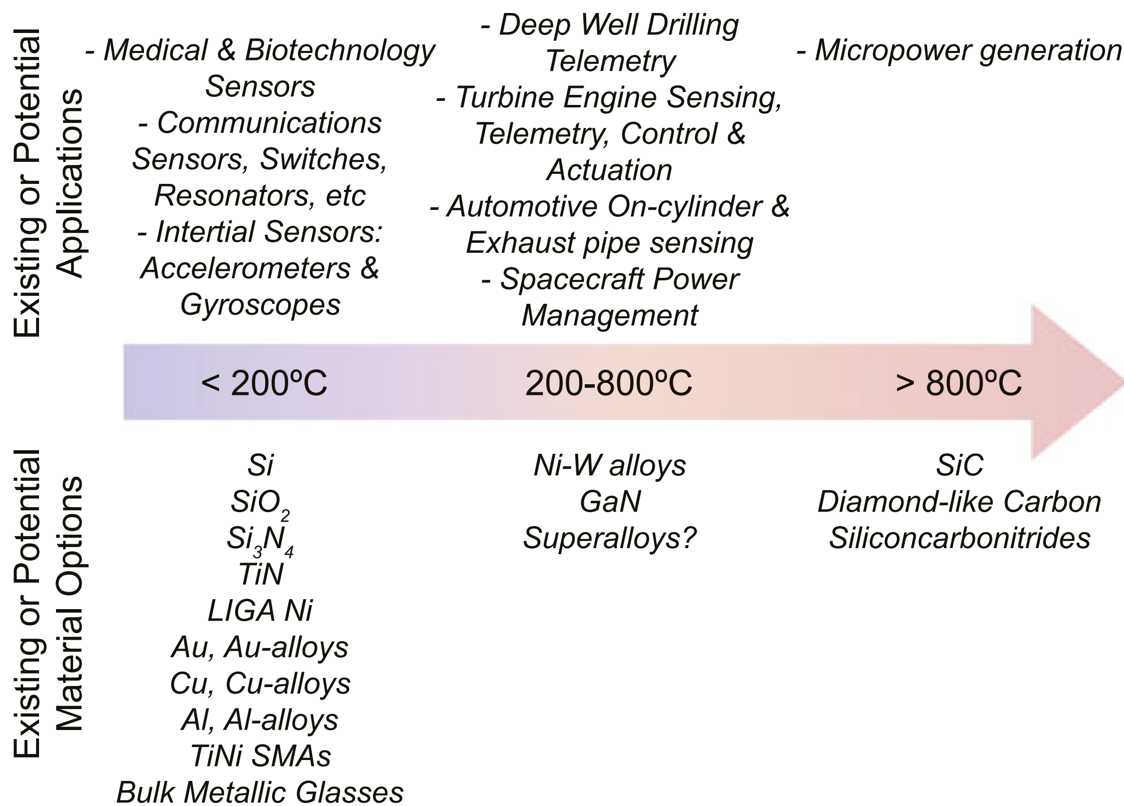

Figure 1.2: Examples of existing and potential MEMS materials for different temperature applications [13].

1.2.1 LIGA Ni

MEMS in extreme environments may also require the structural material to be both mechanically robust and electrically conductive, which points to metals. LIGA, which is a German acronym for lithography, electroplating and molding, was developed as a technique to produce high aspect ratio structural elements with complex shapes. The basic methodology is described in Figure 1.3 [15], where X-ray synchrotron radiation is used to expose thick polymer resist to create a mold in the desired shape, followed by electroplating and separation to release the newly shaped structure.

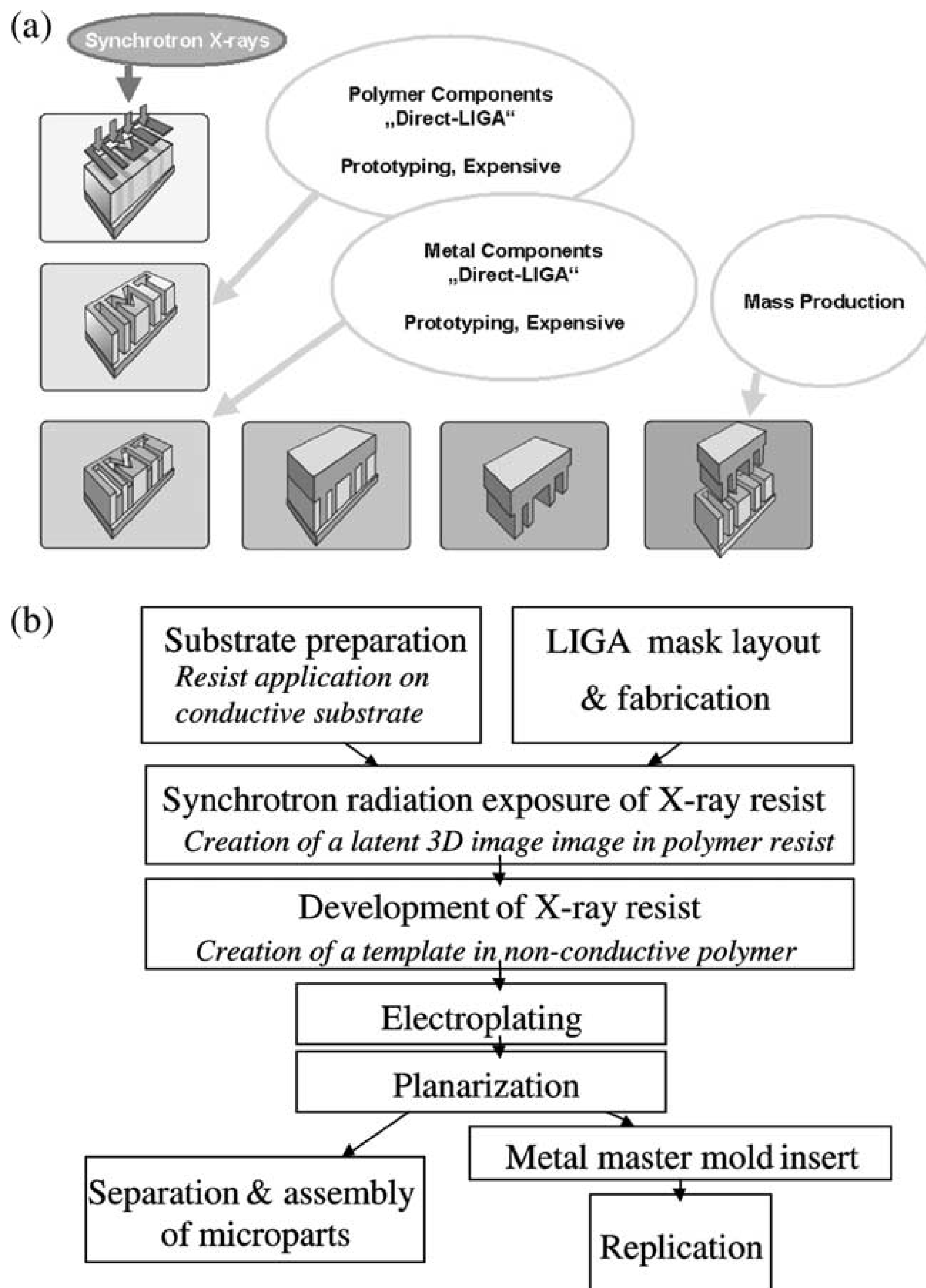

Figure 1.3: (a) Illustration of the basic workflow of the LIGA process, where (b) describes all of the steps needed to achieve the high aspect ratio structure [15].

Nickel (Ni) is very easily electrodeposited and has been well explored using the LIGA technique to offer a balance of electrical conductivity and load bearing capacity in high aspect ratio parts [16], see for example Figure 1.4 [17]. Reduced grain sizes (<100 nm) have been shown to dramatically increase the room temperature strength of LIGA Ni [18], but these small grain sizes exhibited poor thermal stability leading to grain growth and a significant loss in strength at temperatures as low as 200°C [19]. Moreover, the as-deposited microstructure and properties have been shown to vary dramatically with exact deposition conditions [17], and LIGA Ni has shown significant room temperature creep [20]. The use of LIGA Ni for commercial MEMS has been limited by this debilitating loss of microstructural stability and attendant properties at relatively low temperatures.

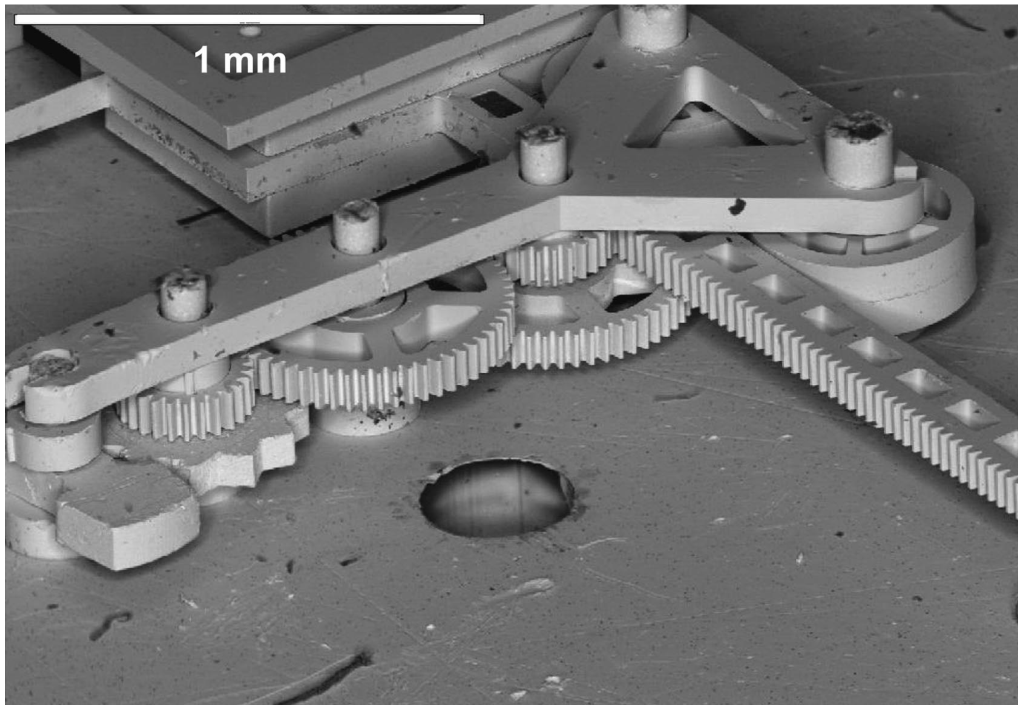

Figure 1.4: Example of a microsystem consisting of LIGA Ni components; an escapement mechanism used for damping of a spring-mass-accelerometer structure through a rack-and-pinion coupling [17].

1.2.2 Ni alloys

1.2.2.1 Electrodeposition

Significant efforts have been made to improve the thermal stability of LIGA Ni through alloying with various solutes, such as tungsten (W) [21-24], cobalt (Co) [25, 26] and manganese (Mn) [25, 27, 28]. The binary Ni alloys showed improved room temperature stability compared to nanocrystalline LIGA Ni. At elevated temperatures Ni-Co alloys exhibited grain coarsening [25, 26] and Ni-Mn alloys retained much of its as-deposited strength, but the magnetic properties and low density limited their implementation into MEMS [25]. Haj-Taieb et al. demonstrated the enhanced thermal and mechanical stability achieved by alloying with 12-15 at.% W, as shown in Figure 1.5 [21]. The increased strength was largely due to the fine nanometer grain size achieved through electrodeposition, which appears to stabilize with small additions of W in solid solution [22, 23].

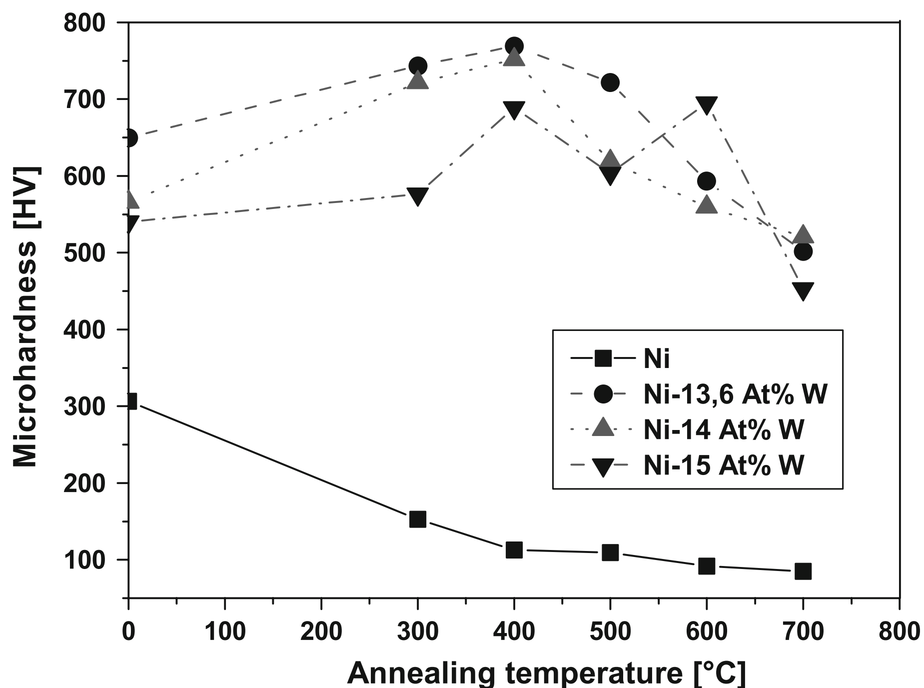

Figure 1.5: Microhardness of LIGA Ni and different alloy content LIGA Ni-W alloys as a function of annealing temperature (2 hour duration) [21].

Although electrodeposition can be integrated with MEMS processing, precise compositional control is challenging when depositing a multi-alloy system. Additionally, the attendant properties are highly sensitive to deposition conditions, requiring optimization for each new composition. For example, in Figure 1.6 LIGA Ni-5at%W and Ni-15at%W alloys were deposited with modest variations in parameters but displayed a 2x change in strength [23]. The authors note that the decrease in strength between the two alloys cannot be explained by the solute content, but instead by the microporosity associated with the processing parameters.

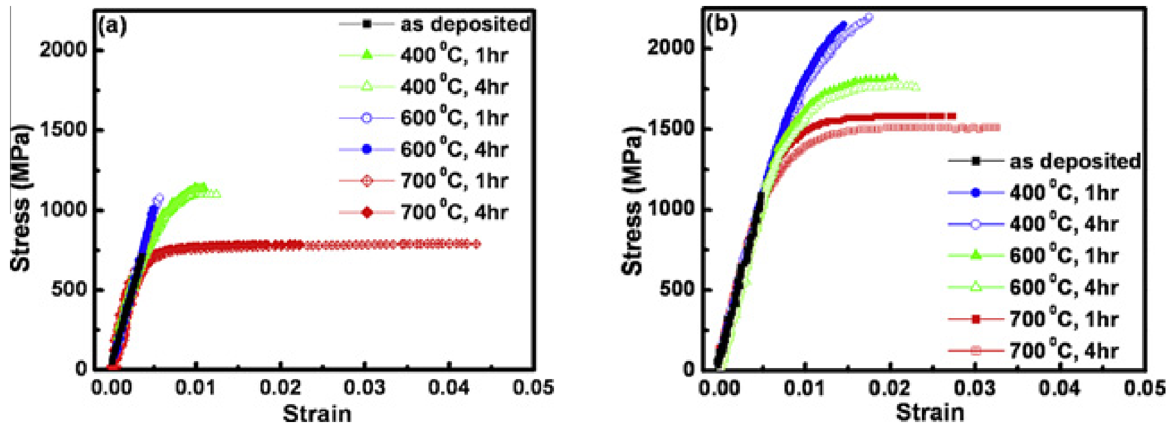

Figure 1.6: Uniaxial tension stress-strain curves for as-deposited and annealed Ni-W with (a) Ni-5at.%W and (b) Ni-15at.%W [23].

1.2.2.2 Vapor-phase-aluminization

Burns et al. proposed the use of pure LIGA Ni enhanced by vapor-phase-aluminization to impart the multiphase strengthening behavior commonly associated with Ni-base superalloys [29]. The resultant dual phase Ni-Ni_3Al (γ-γ’) microstructure shown in Figure 1.7 showed astounding microstructural stability compared to LIGA Ni with a 3-4x increase in strength. However, the multi-step fabrication process and long heat treatments at high temperature (62

hours at 1200°C) required for homogenization would be detrimental for integration with electrical components in MEMS devices.

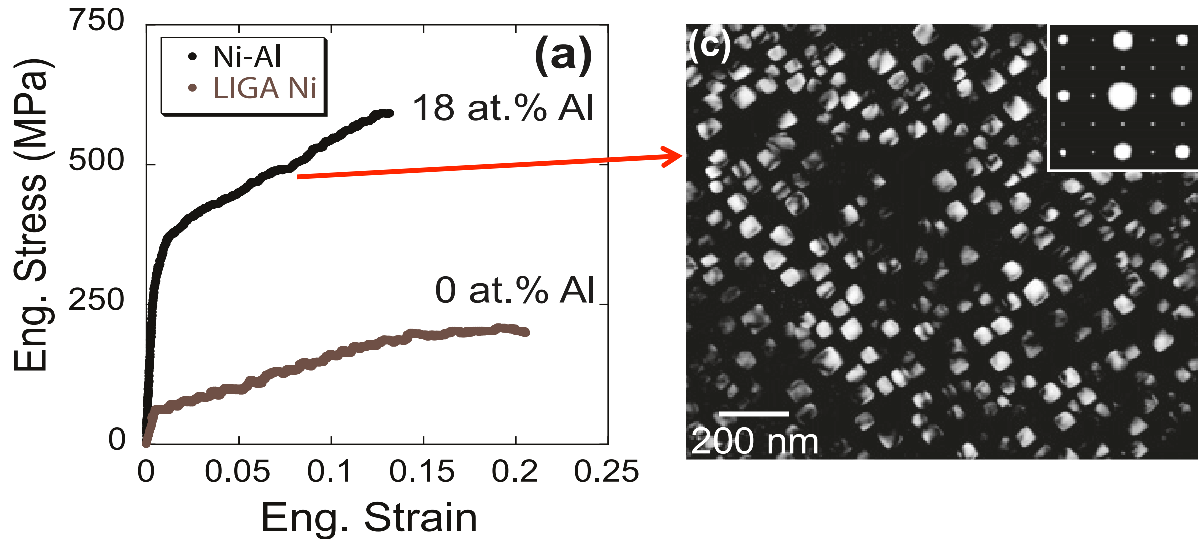

Figure 1.7: Aluminized LIGA Ni-Al, showing two phase Ni-Ni_3Al (γ-γ') microstructure after homogenizing for 62 hours at 1200°C, adapted from [29].

1.2.2.3 Sputter deposition

Sputter deposition methods have the ability to maintain multi-alloy compositions with ease and are commonly used in MEMS fabrication to deposit sacrificial or conductive layers [30]. Binary Ni-W alloys have demonstrated a wide range of compositions, beyond the equilibrium solubility limits, with enhanced microstructural control [31, 32]. Continued efforts from Burns et al, demonstrated the ability to sputter the desired composition of a Ni-base superalloy, Inconel 718, with a balance of thermal and mechanical properties [33]. The as-sputtered microstructure was shown to have small nanocrystalline grains, providing fracture strength slightly higher than the bulk value. After standard aging procedures for

Inconel 718, far superior strength (2 GPa) was observed and attributed to the fine grain structure that did not coarsen during heat treatment (Figure 1.8).

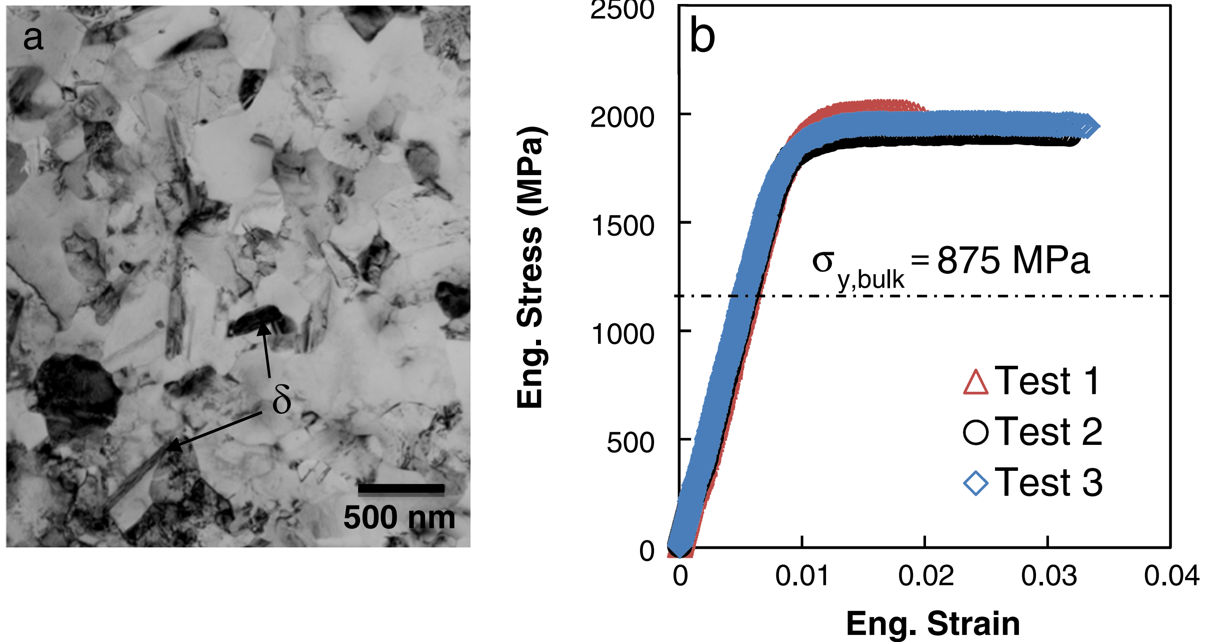

Figure 1.8: Sputter deposited commercial Ni alloy 718 aged at 720°C for 8 hours and 620°C for 8 hours, adapted from [33]. The high strength of 2 GPa is far superior to the bulk reported value and retains a moderate 3% ductility.

The high strength and tailorable microstructure realized in both Inconel 718 and the supersaturated binary Ni-W alloys suggest that sputtering offers unique opportunities for developing novel far-from-equilibrium microstructures and properties of multi-component alloys.

1.3 Sputter deposited Ni-Mo-W alloys

The evolution of metal MEMS materials has demonstrated huge advances from the instabilities associated with LIGA Ni. Sputter deposition offers the most flexibility and compatibility with existing MEMS processes. However, the use of metal alloys in high temperature MEMS will require more than a balance of physical and mechanical properties.

MEMS devices depend on the ability to shape features on the micrometer scale and hold the requisite dimensional stability during device operation. The quest for metal MEMS materials with dimensional stability leads to a discussion of the CTE. Most MEMS are composed of multi-layered structures, where matching the CTE of individual layers to the substrate provides a pathway to reduce thermal distortions. Nickel-molybdenum (Ni-Mo) alloys have been shown to reduce the CTE and improve creep and corrosion resistance when compared to pure Ni [34-37]. Pavlovic et al. has shown Mo to be an effective alloying element for reducing the CTE of Ni [37], as shown in Figure 1.9.

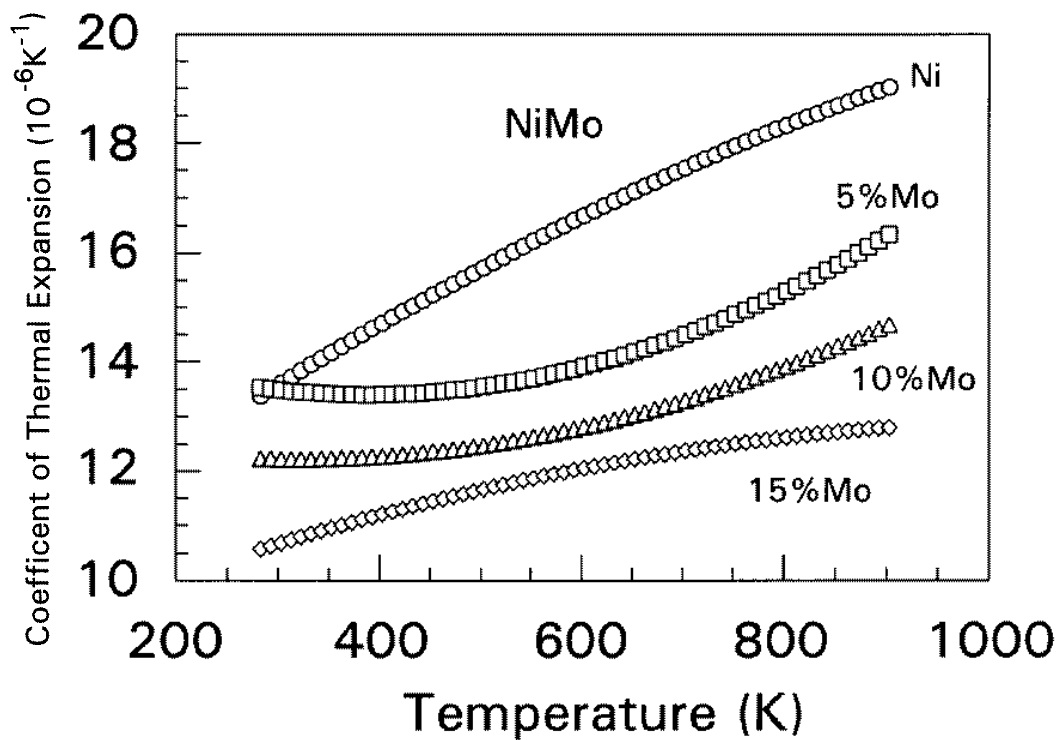

Figure 1.9: Coefficient of thermal expansion versus temperature for Ni and Ni-Mo alloys determined from commercial dilatometer methods, adapted from [37].

The ability to hold geometrical tolerances and mechanical integrity are paramount for the design of MEMS, which motivated the development of sputter deposited nickel-molybdenum-tungsten (Ni-Mo-W) thin films. The improved stability of Ni-W, outlined in section 1.2.2.1, combined with the CTE benefit of Mo was hypothesized to further decrease the CTE of Ni while retaining its stable thermal and mechanical behavior.

Initial studies on sputter deposited solid solution $Ni_{83.6}Mo_{14}W_{2.4}$ have shown exceptional strength and linear-elastic behavior to 3.5 GPa, as shown in Figure 1.10 [38]. The enhanced strength was found to evolve from high density of growth nanotwins and stacking faults that form perpendicular to the <111> face-centered cubic (fcc) growth direction (Figure 1.11) [38].

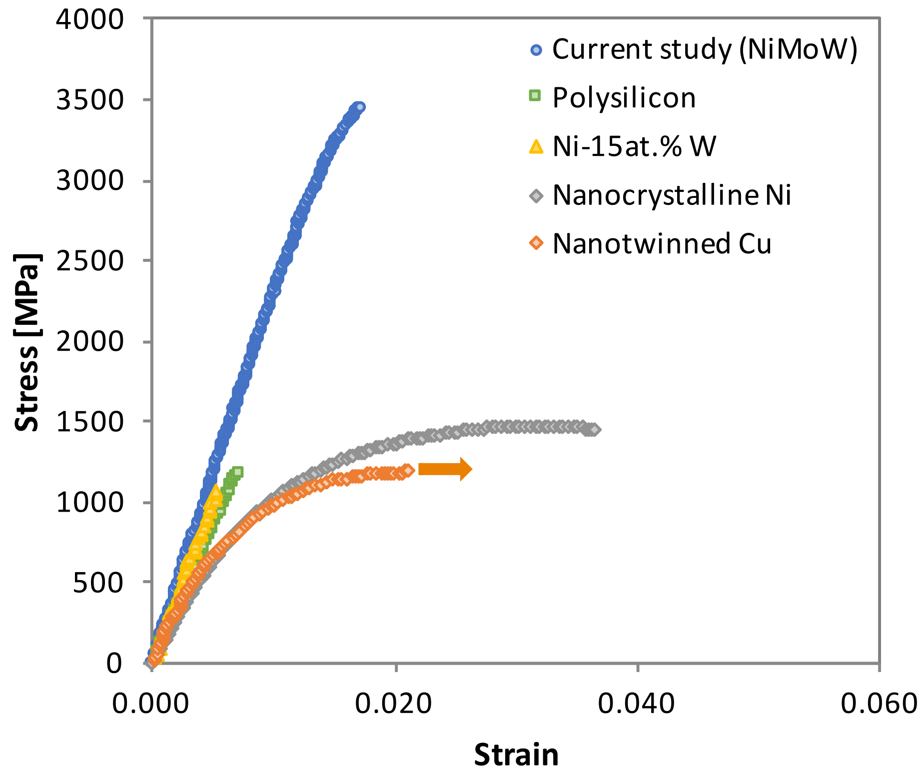

Figure 1.10: Uniaxial tension stress-strain curve for $Ni_{83.6}Mo_{14}W_{2.4}$ compared to polysilicon, nanocrystaline Ni, Ni-15.at%W and nanotwinned copper (Cu) to demonstrate the ultrahigh 3.5 GPa strength. Adapted from [38].

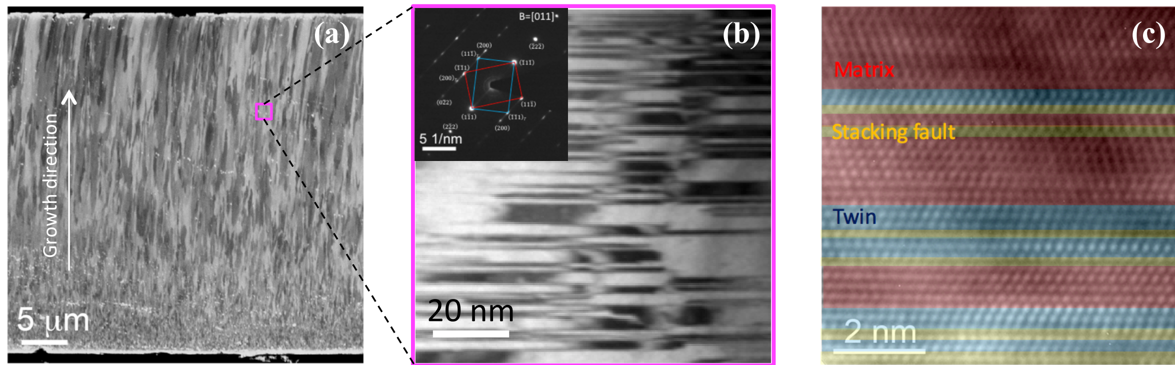

Figure 1.11: (a) Cross-sectional focused ion beam channeling contrast image of the $Ni_{83.6}Mo_{14}W_{2.4}$ films. (b) Transmission electron microscope (TEM) bright field micrograph with a selected area electron diffraction pattern inset, showing the matrix and twin. (c) High resolution TEM image of the matrix (red), twins (blue) and stacking faults (yellow). Adapted from [38].

The mechanical response was attributed to the combined solid solution strengthening, described using the well-known Fleischer model [39] that accounts for dislocation-solute interactions from local changes in elastic modulus and atomic spacing, and twin boundary strengthening using the confined layer slip (CLS) model [40]. The nanotwins do not impede electron motion, offering high electrical conductivity while retaining the small planar defect spacing that underpins the ultrahigh strengths [38]. The underlying microstructure has been shown to have stability through 600°C and undergo significant recrystallization only after 800-1000°C, as shown in Figure 1.12 [41]. The thermal, mechanical and electrical properties of $Ni_{83.6}Mo_{14}W_{2.4}$ are largely attributed to the unexpected nanotwin formation. A review of other nanotwinned fcc metals showing similar strength and stability will be discussed in 1.4.

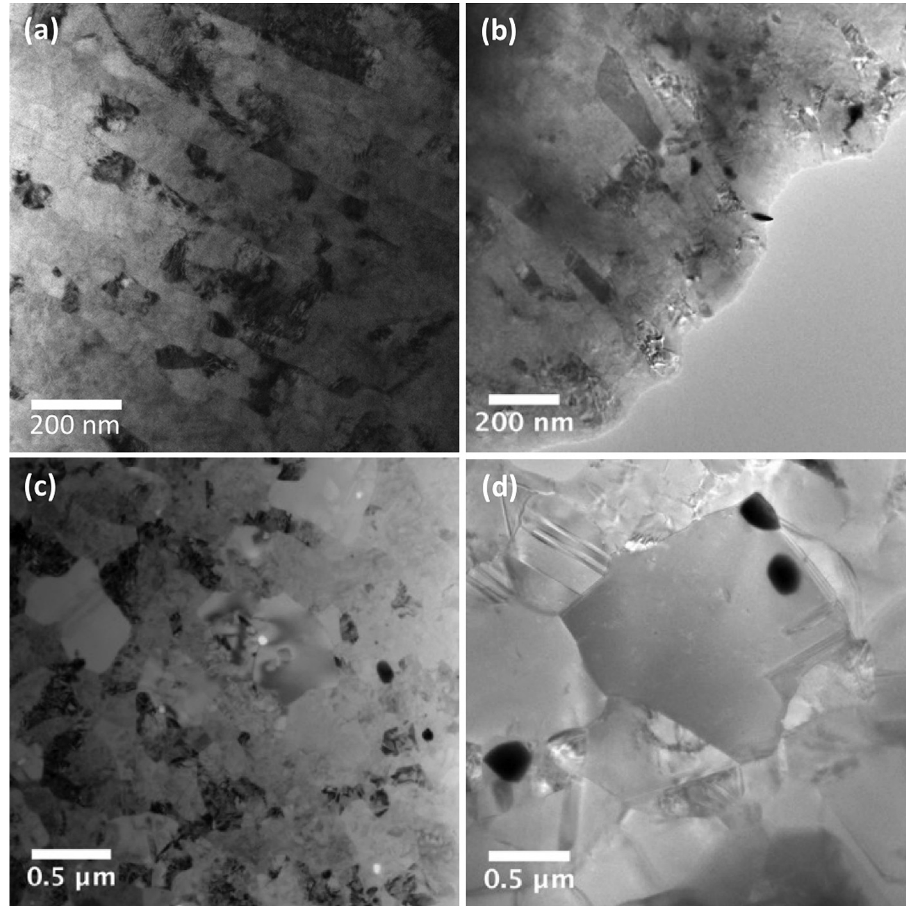

Figure 1.12: Plane view bright field transmission electron microscopy image of the $Ni_{83.6}Mo_{14}W_{2.4}$ films (a) as-deposited, heat treated at (b) 600°C, (c) 800°C and (d) 1000°C [41].

1.4 Nanotwinned fcc metals

Nanostructured materials have received considerable attention in recent years for various engineering applications [42]. The design of these nanoscale materials is grounded in the exploitation of the processing-structure-properties relations to achieve a balance of strength and ductility [43-47]. Nanocrystalline materials typically exhibit higher strength than their more conventional microcrystalline counterparts, but the suppression of the dislocation-based plasticity at such small grain sizes inhibits significant ductility and work hardening [42, 46]. Despite their improved hardness and strength, nanocrystalline metals are often susceptible to

thermal and mechanical microstructural instabilities [48-54] with lower electrical conductivity. In comparison, nanotwinned fcc metals offer strength enhancements similar to those for nanocrystalline materials, while also maintaining a more beneficial suite of properties.

Significant interest in nanostructured materials synthesis was focused on nanotwinned metals after the realization of the ultrahigh strength and electrical conductivity achievable with nanotwinned Cu [55]. The unusually high strength (~1 GPa) and ductility for nanotwinned Cu have been attributed to a high density of coherent twin boundaries (CTBs) spaced a few nanometers apart, within sub-micrometer grains. CTBs are predicted to be more stable against migration than conventional grain boundaries since their excess energies are much lower than that of grain boundaries [56, 57]. The dependence on nanotwin thickness has been shown to be analogous to the well-known Hall-Petch relation [58], where fine twin lamella are pivotal to maximizing both strength and ductility [59, 60]. Figure 1.13 shows the tensile stress-strain response of nanotwinned Cu for various twin thickness [59]. The dependence on twin spacing is clear and post-mortem transmission electron microscopy (TEM) observations of these samples revealed dislocation pile-ups at the twin boundaries, suggesting that the enhanced strength is associated with the effectiveness of twin boundaries as obstacles to dislocation motion. This is consistent with the “smaller is stronger” phenomenon, but below a critical twin thickness partial dislocation nucleation and glide on the twin planes can result in a degradation of strength [60, 61].

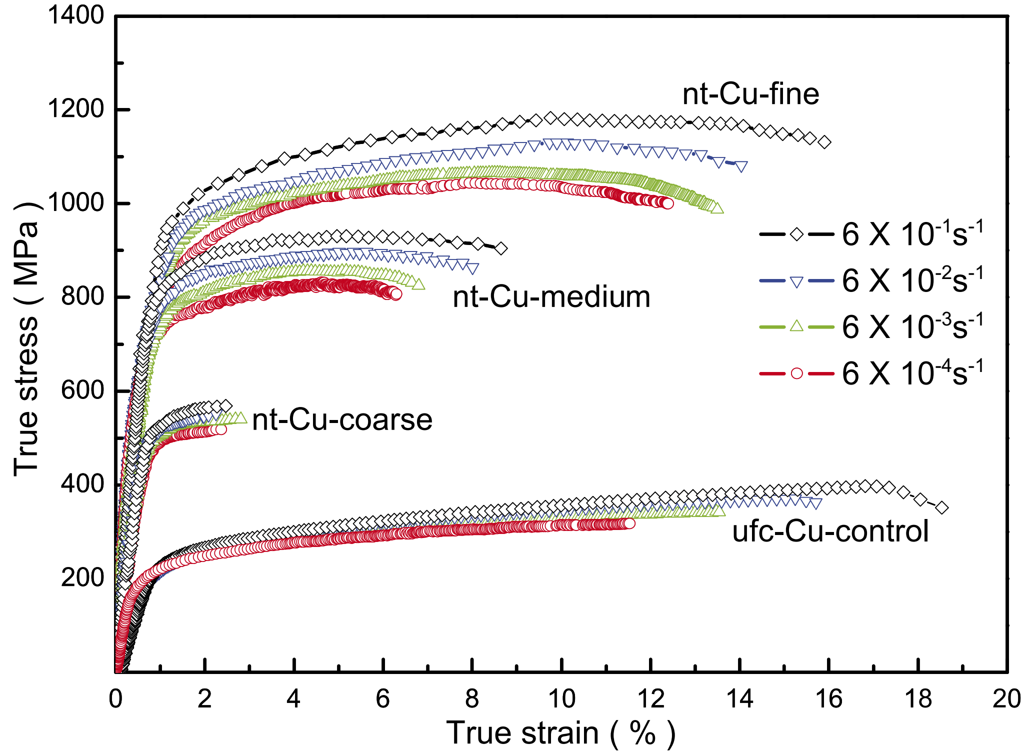

Figure 1.13: Uniaxial tension stress-strain response for nanotwinned Cu specimens showing the effect of twin spacing, taken from [59].

The orientation of the CTBs with respect to the loading direction determines the active deformation mechanism for nanotwinned metals. CTBs can confine dislocation motion within the twin, provide easy dislocation glide along the twin planes or act as barriers to dislocation transmission. You et al. demonstrated anisotropic plasticity in columnar-grained nanotwinned Cu by loading at 0°, 45° and 90° with respect to the CTBs and identifying the dominant active mechanisms for each orientation [62]. Furthermore, nanopillar compression experiments and molecular dynamics simulations have been used to investigate the role of twin thickness in the absence of grain boundaries on the operative deformation mechanisms [63]. Dislocation transmission across the CTB was observed when loading perpendicular to

the CTBs, while those with inclined CTBs experienced detwinning. The various interactions between dislocations and CTBs define the anisotropic nature of the deformation.

To date, most investigations of nanotwinned materials have been focused on Cu and low stacking fault energy (SFE) fcc metals and alloys [64-67], such as austenitic stainless steel [68] and Ag [68-71]. The formation of nanotwins in higher SFE materials, such as Ni, Al or Pd, would be highly desirable but is recognized to be very difficult [65]. Dahlgren et al. reported the formation of irregularly spaced 0.17 μm twins in sputter deposited Ni, which was attributed to the very high deposition rates [72]. Binary Ni-W [23, 73, 74] and Ni-Mo [73] alloys have also been shown to produce sporadic nanotwins. The observation of nanotwins in $Ni_{83.6}Mo_{14}W_{2.4}$ was fortuitous, but might have been predictable since Shang et al. performed a first-principles calculation for 26 different alloying elements in binary $Ni_{71}X_{28}$, finding that Mo and W reduce the SFE of Ni by 20%. This appears to promote the formation of very fine nanotwins.

1.5 Thesis overview

This thesis work originated from an interdisciplinary team of engineers and scientists from General Electric Global Research (GEGR) and Johns Hopkins University (JHU) who undertook a study to develop metal alloys for high temperature MEMS sensors and micro-switches. It was funded by the National Science Foundation – Grant Opportunities for Academic Liaison with Industry (NSF-GOALI). The primary objective of the project was to "expand the MEMS material set beyond silicon to materials that can be deposited and shaped on the micro-scale and offer an attractive balance of properties: electrical and thermal conductivity, high density, low thermal expansion, strength, ductility, and toughness". The overall goal of this work is to characterize and synthesize a broad spectrum of materials with

properties that can be used as the structural component in high temperature MEMS applications (300-500°C). The initial observation of nanotwins in sputter deposited $Ni_{83.6}Mo_{14}W_{2.4}$ (outlined in section 1.3) was unexpected, but subsequent characterization of the material suggests that the nanotwins are responsible for the overall strength and stability. This work motivated an additional study to elucidate the fundamental deformation mechanisms governing nanotwinned Ni-Mo-W alloys, which is funded by the Department of Energy. The overarching aim of this investigation is to "develop the techniques and conduct the experiments that will lead to a deeper fundamental understanding of the underlying mechanisms that govern the enhanced mechanical behavior and microstructural stability of nanotwinned Ni-Mo-W". The chapters ahead will detail advances made in thermal and mechanical characterization for a combinatorial study of nanotwinned Ni-Mo-W alloys and their integration into MEMS.

Chapter 1 outlines the history of metal MEMS and the motivation for Ni-Mo-W alloys. Chapter 2 introduces a non-contact technique developed to measure the CTE in thin films. Results from sputter deposited $Ni_{85}Mo_xW_{15-x}$ alloys are presented and their compatibility with conventional MEMS substrates discussed. Chapter 3 details the microstructural characterization of a combinatorial spread of $Ni_{85}Mo_xW_{15-x}$ alloys and the effect of composition on tensile properties. Heat treatment temperatures of 400°C were investigated to demonstrate their thermal and mechanical stability. Chapter 4 demonstrates the extremely anisotropic plasticity observed when the loading orientation is perpendicular with respect to the twin boundaries. In situ micropillar compression of nanotwinned Ni-Mo-W alloys was coupled with post-mortem TEM analysis to identify the operative deformation mechanisms. Chapter 5 investigates the formation of growth nanotwins in Ni-Mo-W as a function of the

sputter deposition rate. Fixed alloy chemistry was deposited with different direct current powers and bright field TEM micrographs were used to quantify the average nanotwin thickness. Instrumented nanoindentation was used to measure the compressive yield strength and to determine its evolution with deposition rate. Chapter 6 describes the detailed fabrication process and requisite characterization to manufacture and shape Ni-Mo-W alloys into actual devices structures for future integration into MEMS. Finally, Chapter 7 provides a summary of the key findings from this dissertation.

1.6 References for Chapter 1

1. Partnership, P.F., *An introduction to MEMS (micro-Electromechanical systems).* Prime Faraday Partnership, 2002.
2. Lyshevski, S.E., *MEMS and NEMS: systems, devices, and structures*. 2002: CRC press.
3. Xie, H., S. Todd, A. Jain, G. Fedder, and C. Leondes, *MEMS/NEMS: Handbook Techniques and Applications, vol. 5*. 2006, New York: Springer-Verlag.
4. Castells, M., *The information age: Economy, society and culture (3 volumes).* Blackwell, Oxford, 1996. **1997**: p. 1998.
5. Ashton, K., *In the real world, things matter more than ideas.* RFID Journal, 2009.
6. Chou, S., W. Yang, K. Chua, J. Li, and K. Zhang, *Development of micro power generators–a review.* Applied Energy, 2011. **88**(1): p. 1-16.
7. Epstein, A.H., S.D. Senturia, G. Anathasuresh, A. Ayon, K. Breuer, K.-S. Chen, F. Ehrich, G. Gauba, R. Ghodssi, and C. Groshenry. *Power MEMS and microengines*. in *Solid State Sensors and Actuators, 1997. TRANSDUCERS'97 Chicago., 1997 International Conference on*. 1997. IEEE.
8. Keimel, C.F., M.F. Aimi, S. Bansal, R.R. Corderman, K.V.S.R. Kishore, E.S. Reddy, A. Saha, K. Subramanian, P. Thakre, and A.D. Corwin, *Switch structure and method*. 2013, Google Patents.
9. Nakao, S., T. Ando, M. Shikida, and K. Sato, *Mechanical properties of a micron-sized SCS film in a high-temperature environment.* Journal of Micromechanics and Microengineering, 2006. **16**(4): p. 715.
10. Sharpe, W.N. *Tensile testing of MEMS materials at high temperatures*. in *Applied Mechanics and Materials*. 2005. Trans Tech Publ.
11. Neudeck, P.G., R.S. Okojie, and L.-Y. Chen, *High-temperature electronics-a role for wide bandgap semiconductors?* Proceedings of the IEEE, 2002. **90**(6): p. 1065-1076.
12. Jiang, L. and R. Cheung, *A review of silicon carbide development in MEMS applications.* International Journal of Computational Materials Science and Surface Engineering, 2009. **2**(3-4): p. 227-242.
13. Krogstad, J.A., C. Keimel, and K.J. Hemker, *Emerging materials for microelectromechanical systems at elevated temperatures.* Journal of Materials Research, 2014. **29**(15): p. 1597-1608.
14. Liew, L.-A., W. Zhang, A. Linan, T. Cross, A.L. Dann, V. Bright, J.W. Daily, R. Raj, and K. Ansech, *Ceramic MEMS new materials, innovative processing and future applications.* American Ceramic Society Bulletin, 2001. **80**(5): p. 25-30.
15. Malek, C.K. and V. Saile, *Applications of LIGA technology to precision manufacturing of high-aspect-ratio micro-components and-systems: a review.* Microelectronics journal, 2004. **35**(2): p. 131-143.

16. Saile, V., U. Wallrabe, O. Tabata, J.G. Korvink, O. Brand, G.K. Fedder, and C. Hierold, *LIGA and its Applications*. Vol. 7. 2009: John Wiley & Sons.

17. Buchheit, T.E., J.R. Michael, T.R. Christenson, D.A. LaVan, and S.D. Leith, *Microstructural and mechanical properties investigation of electrodeposited and annealed LIGA nickel structures.* Metallurgical and Materials Transactions A, 2002. **33**(3): p. 539-554.

18. Ebrahimi, F., G. Bourne, M.S. Kelly, and T. Matthews, *Mechanical properties of nanocrystalline nickel produced by electrodeposition.* Nanostructured Materials, 1999. **11**(3): p. 343-350.

19. Cho, H., K. Hemker, K. Lian, J. Goettert, and G. Dirras, *Measured mechanical properties of LIGA Ni structures.* Sensors and Actuators A: Physical, 2003. **103**(1): p. 59-63.

20. Collins, J.G., M.C. Wright, and C.L. Muhlstein, *Cyclic stabilization of electrodeposited nickel structural films.* Journal of Microelectromechanical Systems, 2011. **20**(3): p. 753-763.

21. Haj-Taieb, M., A. Haseeb, J. Caulfield, K. Bade, J. Aktaa, and K. Hemker, *Thermal stability of electrodeposited LIGA Ni–W alloys for high temperature MEMS applications.* Microsystem Technologies, 2008. **14**(9-11): p. 1531-1536.

22. Schuh, C., T. Nieh, and H. Iwasaki, *The effect of solid solution W additions on the mechanical properties of nanocrystalline Ni.* Acta Materialia, 2003. **51**(2): p. 431-443.

23. Suresha, S., M. Haj-Taieb, K. Bade, J. Aktaa, and K. Hemker, *The influence of tungsten on the thermal stability and mechanical behavior of electrodeposited nickel MEMS structures.* Scripta Materialia, 2010. **63**(12): p. 1141-1144.

24. Yamasaki, T., *High-strength nanocrystalline Ni-W alloys produced by electrodeposition and their embrittlement behaviors during grain growth.* Scripta Materialia, 2001. **8**(44): p. 1497-1502.

25. Goods, S., J. Kelly, and N. Yang, *Electrodeposited nickel–manganese: an alloy for microsystem applications.* Microsystem technologies, 2004. **10**(6-7): p. 498-505.

26. Hibbard, G., K. Aust, and U. Erb, *Thermal stability of electrodeposited nanocrystalline Ni–Co alloys.* Materials Science and Engineering: A, 2006. **433**(1-2): p. 195-202.

27. Kelly, J., S. Goods, and N. Yang, *High performance nanostructured Ni-Mn alloy for microsystem applications.* Electrochemical and solid-state letters, 2003. **6**(6): p. C88-C91.

28. Talin, A., E. Marquis, S. Goods, J. Kelly, and M.K. Miller, *Thermal stability of Ni–Mn electrodeposits.* Acta materialia, 2006. **54**(7): p. 1935-1947.

29. Burns, D.E., Y. Zhang, M. Teutsch, K. Bade, J. Aktaa, and K.J. Hemker, *Development of Ni-based superalloys for microelectromechanical systems.* Scripta Materialia, 2012. **67**(5): p. 459-462.

30. Chandra, S., V. Bhatt, and R. Singh, *RF sputtering: A viable tool for MEMS fabrication.* Sadhana, 2009. **34**(4): p. 543.

31. Borgia, C., T. Scharowsky, A. Furrer, C. Solenthaler, and R. Spolenak, *A combinatorial study on the influence of elemental composition and heat treatment on the phase composition, microstructure and mechanical properties of Ni–W alloy thin films.* Acta materialia, 2011. **59**(1): p. 386-399.

32. Rupert, T.J., J.C. Trenkle, and C.A. Schuh, *Enhanced solid solution effects on the strength of nanocrystalline alloys.* Acta Materialia, 2011. **59**(4): p. 1619-1631.

33. Burns, D.E., Y. Zhang, T.P. Weihs, and K.J. Hemker, *Properties of sputter deposited Ni-base superalloys for microelectromechanical systems.* Thin Solid Films, 2014. **558**: p. 20-23.

34. Abrosimova, G., A. Aronin, Y.V. Kir'Janov, I. Zver'Kova, V. Molokanov, H. Alves, and U. Köster, *The formation, structure and properties of nanocrystalline Ni-Mo-B alloys.* Journal of materials science, 1999. **34**(7): p. 1611-1618.

35. Donten, M., H. Cesiulis, and Z. Stojek, *Electrodeposition of amorphous/nanocrystalline and polycrystalline Ni–Mo alloys from pyrophosphate baths.* Electrochimica Acta, 2005. **50**(6): p. 1405-1412.

36. Liu, G., G. Zhang, F. Jiang, X. Ding, Y. Sun, J. Sun, and E. Ma, *Nanostructured high-strength molybdenum alloys with unprecedented tensile ductility.* Nature materials, 2013. **12**(4): p. 344.

37. Pavlovic, A., V.S. Babu, and M.S. Seehra, *High-temperature thermal expansion of binary alloys of Ni with Cr, Mo and Re: a comparison with molecular dynamics simulations.* Journal of Physics: Condensed Matter, 1996. **8**(18): p. 3139.

38. Sim, G.-D., J.A. Krogstad, K.M. Reddy, K.Y. Xie, G.M. Valentino, T.P. Weihs, and K.J. Hemker, *Nanotwinned metal MEMS films with unprecedented strength and stability.* Science Advances, 2017. **3**(6): p. e1700685.

39. Fleischer, R.L., *Solid-solution hardening.* The strengthening of metals, 1964: p. 93-140.

40. Misra, A., J. Hirth, and R. Hoagland, *Length-scale-dependent deformation mechanisms in incoherent metallic multilayered composites.* Acta materialia, 2005. **53**(18): p. 4817-4824.

41. Sim, G.-D., J.A. Krogstad, K.Y. Xie, S. Dasgupta, G.M. Valentino, T.P. Weihs, and K.J. Hemker, *Tailoring the mechanical properties of sputter deposited nanotwinned nickel-molybdenum-tungsten films.* Acta Materialia, 2018. **144**: p. 216-225.

42. Koch, C., I. Ovid'ko, S. Seal, and S. Veprek, *Structural nanocrystalline materials: fundamentals and applications*. 2007: Cambridge University Press.

43. Aricò, A.S., P. Bruce, B. Scrosati, J.-M. Tarascon, and W. Van Schalkwijk, *Nanostructured materials for advanced energy conversion and storage devices.* Nature materials, 2005. **4**(5): p. 366-377.

44. Courtney, T.H., *Mechanical behavior of materials*. 2005: Waveland Press.

45. Gleiter, H., *Nanostructured materials: basic concepts and microstructure.* Acta materialia, 2000. **48**(1): p. 1-29.

46. Meyers, M.A., A. Mishra, and D.J. Benson, *Mechanical properties of nanocrystalline materials.* Progress in materials science, 2006. **51**(4): p. 427-556.

47. Moriarty, P., *Nanostructured materials.* Reports on Progress in Physics, 2001. **64**(3): p. 297.

48. Gianola, D., S. Van Petegem, M. Legros, S. Brandstetter, H. Van Swygenhoven, and K. Hemker, *Stress-assisted discontinuous grain growth and its effect on the deformation behavior of nanocrystalline aluminum thin films.* Acta Materialia, 2006. **54**(8): p. 2253-2263.

49. Jin, M., A. Minor, E. Stach, and J. Morris, *Direct observation of deformation-induced grain growth during the nanoindentation of ultrafine-grained Al at room temperature.* Acta Materialia, 2004. **52**(18): p. 5381-5387.

50. Klement, U., U. Erb, A. El-Sherik, and K. Aust, *Thermal stability of nanocrystalline Ni.* Materials Science and Engineering: A, 1995. **203**(1-2): p. 177-186.

51. Legros, M., D.S. Gianola, and K.J. Hemker, *In situ TEM observations of fast grain-boundary motion in stressed nanocrystalline aluminum films.* Acta Materialia, 2008. **56**(14): p. 3380-3393.

52. Lu, L., N. Tao, L. Wang, B. Ding, and K. Lu, *Grain growth and strain release in nanocrystalline copper.* Journal of Applied Physics, 2001. **89**(11): p. 6408-6414.

53. Rupert, T., D. Gianola, Y. Gan, and K. Hemker, *Experimental observations of stress-driven grain boundary migration.* Science, 2009. **326**(5960): p. 1686-1690.

54. Zhang, K., J. Weertman, and J. Eastman, *Rapid stress-driven grain coarsening in nanocrystalline Cu at ambient and cryogenic temperatures.* Applied Physics Letters, 2005. **87**(6): p. 061921.

55. Lu, L., Y. Shen, X. Chen, L. Qian, and K. Lu, *Ultrahigh strength and high electrical conductivity in copper.* Science, 2004. **304**(5669): p. 422-426.

56. Anderoglu, O., A. Misra, H. Wang, and X. Zhang, *Thermal stability of sputtered Cu films with nanoscale growth twins.* Journal of Applied Physics, 2008. **103**(9): p. 094322.

57. Zhang, X., A. Misra, H. Wang, M. Nastasi, J. Embury, T. Mitchell, R. Hoagland, and J. Hirth, *Nanoscale-twinning-induced strengthening in austenitic stainless steel thin films.* Applied physics letters, 2004. **84**(7): p. 1096-1098.

58. Shen, Y., L. Lu, Q. Lu, Z. Jin, and K. Lu, *Tensile properties of copper with nano-scale twins.* Scripta Materialia, 2005. **52**(10): p. 989-994.

59. Dao, M., L. Lu, Y. Shen, and S. Suresh, *Strength, strain-rate sensitivity and ductility of copper with nanoscale twins.* Acta Materialia, 2006. **54**(20): p. 5421-5432.

60. Lu, L., X. Chen, X. Huang, and K. Lu, *Revealing the maximum strength in nanotwinned copper.* Science, 2009. **323**(5914): p. 607-610.

61. Li, X., Y. Wei, L. Lu, K. Lu, and H. Gao, *Dislocation nucleation governed softening and maximum strength in nano-twinned metals.* Nature, 2010. **464**(7290): p. 877-880.

62. You, Z., X. Li, L. Gui, Q. Lu, T. Zhu, H. Gao, and L. Lu, *Plastic anisotropy and associated deformation mechanisms in nanotwinned metals.* Acta Materialia, 2013. **61**(1): p. 217-227.

63. Jang, D., X. Li, H. Gao, and J.R. Greer, *Deformation mechanisms in nanotwinned metal nanopillars.* Nature nanotechnology, 2012. **7**(9): p. 594-601.

64. Beyerlein, I.J., X. Zhang, and A. Misra, *Growth twins and deformation twins in metals.* Annual Review of Materials Research, 2014. **44**: p. 329-363.

65. Liu, Y., N. Li, D. Bufford, J. Lee, J. Wang, H. Wang, and X. Zhang, *In situ nanoindentation studies on detwinning and work hardening in nanotwinned monolithic metals.* JOM, 2016. **68**(1): p. 127-135.

66. Lu, K., L. Lu, and S. Suresh, *Strengthening materials by engineering coherent internal boundaries at the nanoscale.* Science, 2009. **324**(5925): p. 349-352.

67. Ovid'ko, I. and A. Sheinerman, *MECHANICAL PROPERTIES OF NANOTWINNED METALS: A REVIEW.* Reviews on Advanced Materials Science, 2016. **44**(1).

68. Zhang, X., A. Misra, H. Wang, T. Shen, M. Nastasi, T. Mitchell, J. Hirth, R. Hoagland, and J. Embury, *Enhanced hardening in Cu/330 stainless steel multilayers by nanoscale twinning.* Acta Materialia, 2004. **52**(4): p. 995-1002.

69. Bufford, D., H. Wang, and X. Zhang, *Thermal stability of twins and strengthening mechanisms in differently oriented epitaxial nanotwinned Ag films.* Journal of Materials Research, 2013. **28**(13): p. 1729-1739.

70. Furnish, T. and A. Hodge, *On the mechanical performance and deformation of nanotwinned Ag.* APL Materials, 2014. **2**(4): p. 046112.

71. Ott, R., J. Geng, M. Besser, M. Kramer, Y. Wang, E. Park, R. LeSar, and A. King, *Optimization of strength and ductility in nanotwinned ultra-fine grained Ag: Twin density and grain orientations.* Acta Materialia, 2015. **96**: p. 378-389.

72. Dahlgren, S., W. Nicholson, M. Merz, W. Bollmann, J. Devlin, and R. Wang, *Microstructural analysis and tensile properties of thick copper and nickel sputter deposits.* Thin Solid Films, 1977. **40**: p. 345-353.

73. Kurz, S., C. Ensslen, U. Welzel, A. Leineweber, and E. Mittemeijer, *The thermal stability of Ni–Mo and Ni–W thin films: Solute segregation and planar faults.* Scripta Materialia, 2013. **69**(1): p. 65-68.

74. Kurz, S., A. Leineweber, and E.-J. Mittemeijer, *Anomalously high density and thermal stability of nanotwins in Ni (W) thin films: Quantitative analysis by x-ray diffraction.* Journal of Materials Research, 2014. **29**(15): p. 1642-1655.

CHAPTER 2: TAILORING THE COEFFICIENT OF THERMAL EXPANSION OF Ni-Mo-W ALLOYS WITH CHEMISTRY

2.1 Introduction

Everyday household objects produce elongations or contractions when exposed to different temperatures, this is called thermal expansion. The dimensional change is fully reversible, such that upon cooling, the material exhibits thermal contraction. The magnitude of the shape change is different for each material, governed by the atomic bonding, and it can vary directionally depending on the material symmetry. It is worth noting that there are some materials that display the opposite behavior and shrink when exposed to temperature [1], but these materials are beyond the scope and focus of this thesis.

The small thermal expansion of materials commonly goes unnoticed in everyday life, but when considering microelectromechanical systems (MEMS), where feature sizes are smaller than the diameter of a human hair, these thermally induced shape changes are significant and can be detrimental to device function. MEMS devices are inherently grounded by their dimensional stability, a requisite for providing reliable sensing and actuation. Shape changes caused by differences in thermal expansion can be equivalent to or larger than the movements induced by device operation, which precludes use of those materials in sensors. Dimension stability of layered structures requires matching the coefficient of thermal expansion (CTE) of various layers with their substrates. Therefore, a thorough understanding of the CTE and its evolution with temperature is required for MEMS applications.

This chapter focuses on the dimensional stability of sputter deposited nickel-molybdenum-tungsten (Ni-Mo-W) alloy thin films as determined through CTE

measurements. The Ni-Mo-W films were deposited as single-phase solid solution alloys with a high density of nanotwins that give the films ultrahigh strength [2, 3]. Electrical resistivity measurements show good agreement with bulk Ni alloys, suggesting the nanotwins do not impede electron movement. The CTE measurements were performed using a novel, planar method via non-contact optical techniques. Calibrations and distortion corrections associated with high temperature imaging and digital image correlation (DIC) were addressed and implemented, facilitating the CTE measurement of a series of chemical compositions of Ni-Mo-W alloys. The results of this study suggest that the CTE of ternary alloys of Ni-Mo-W is considerably lower than that of pure Ni and can be tailored with composition, offering a balance of physical properties that broadens the design space for future high temperature MEMS applications.

2.2 Experimental procedure

2.2.1 Methods

A non-contact method of measuring CTE was developed to avoid the buckling of freestanding thin films under compressive loading. Thin film buckling would be a problem in commercial dilatometers. A non-contact method for measuring CTE was developed and implemented at JHU in 2007 [4], but the very large thermal mass of the furnace and lengthy cool-down cycles made it impractical for thin film use. In this chapter, a furnace based off of a similar device implemented in Christoph Eberl's research group [5] was customized with a smaller thermal mass and optical windows for improved measurements of thermal displacements. This custom-built clamshell furnace has multiple optical ports for lighting and imaging. Figure 2.1a shows a schematic of the bottom of the furnace, with a coiled Kanthal Al resistance-heating wire around the inner diameter of the furnace base. The heating

element is connected to an external power supply and has a maximum operational temperature of 1100°C. The center cylindrical post serves as the specimen holder and is made of quartz, chosen for its low CTE and high melting temperature. Thin film specimens sit on the surface of the holder with a thermocouple positioned in the same plane as the specimen, but without touching it, to ensure accurate temperature readings. The furnace lid (Figure 2.1b) was designed with two angled ports at 35° with respect to the horizontal and fit with quartz rods for illuminating the inside of the furnace with a LED source. The central port on the furnace lid is used to image the specimen in the furnace through use of a long 10 cm, double-side polished optical-quality quartz rod.

Images are captured over a prescribed temperature range with a 6.6 megapixel camera (Pixelink Model B782) and a fixed magnification 4x telecentric lens (Edmund Optics Model No. 59838). The high-resolution camera was specifically chosen to resolve the small thermally induced displacements, whereas the telecentric lens was selected to increase the depth of field and reduce small out-of-plane perspective errors that contribute to a decrease in dimensional accuracy. The optics provide a 2 mm x 2.6 mm field of view. Figure 2.1c shows the full CTE setup with all the components interfaced through a National Instruments DAQ in LabVIEW, automating the entire test procedure. Typical furnace temperatures ramp from room temperature to the maximum prescribed temperature at a rate of 1°C/minute, and once the maximum temperature is achieved, the same rate of 1°C/minute is used to cool to room temperature. The slow heating and cooling cycles were chosen to ensure thermal stability and equilibrium. However, it could be increased to a maximum of 3°C/minute, with the limiting factor the ability to control the ramp down temperature accurately given the thermal mass of the furnace.

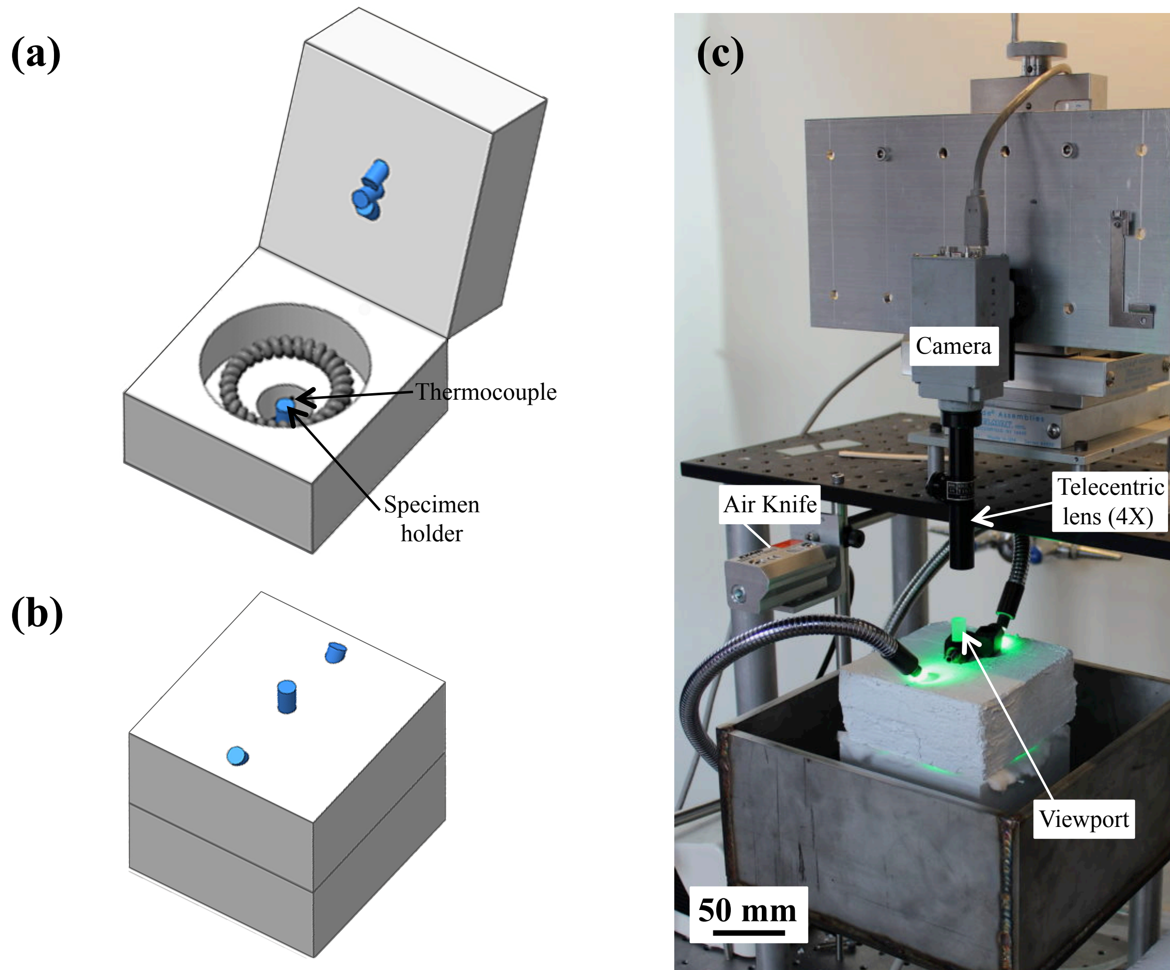

Figure 2.1: Design of a CTE furnace for planer specimen testing. (a) Schematic of the furnace base with heating coils, quartz rod specimen holder and thermocouple. (b) Schematic of furnace lid with central viewport (optical quality quartz) and two angled quartz rods for illumination. (c) Full setup with camera imaging through the central viewport, illuminated via LED.

2.2.2 Materials

Ternary alloys of nickel-molybdenum-tungsten (Ni-Mo-W) thin films were fabricated by Jessica Krogstad using direct current (dc) magnetron sputter deposition in a custom-built chamber designed for high deposition rates, located in Timothy Weihs' laboratory (Figure 2.2a). A large custom alloy target 12 inch x 5 inch was designed with binary Ni-Mo and Ni-W alloys joined on a bias, illustrated in Figures 2.2b and 2.3a.

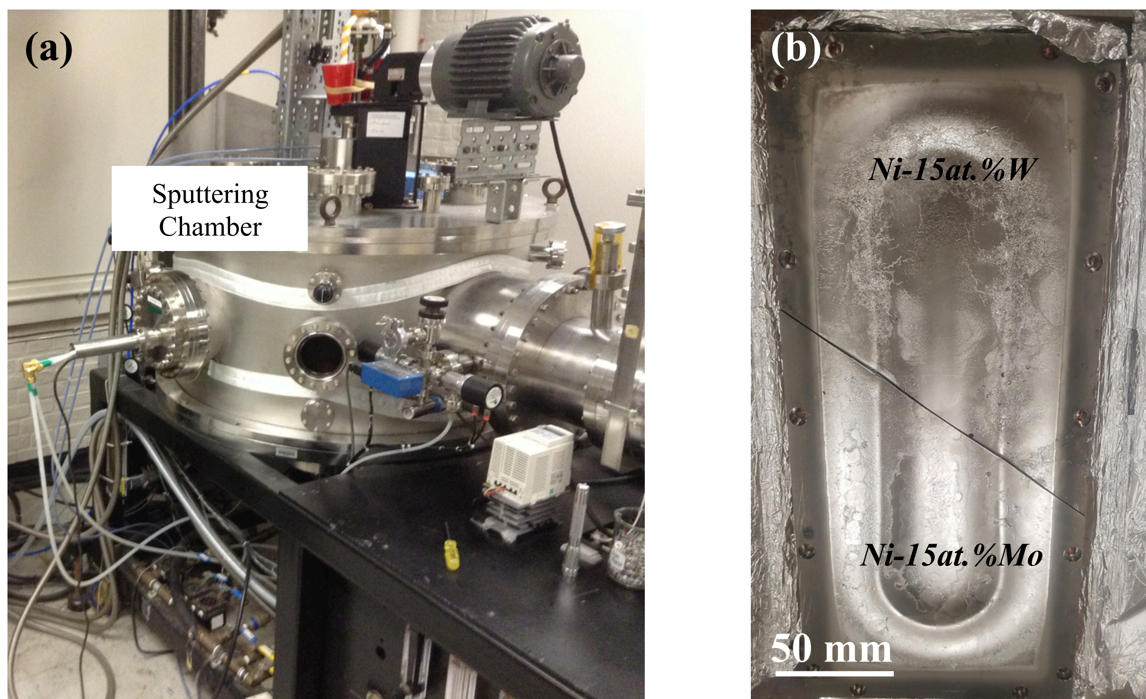

Figure 2.2: (a) Custom-built sputtering chamber in Timothy Weihs' laboratory at JHU and (b) custom alloy target with binary alloys Ni-Mo and Ni-W joined on a bias.

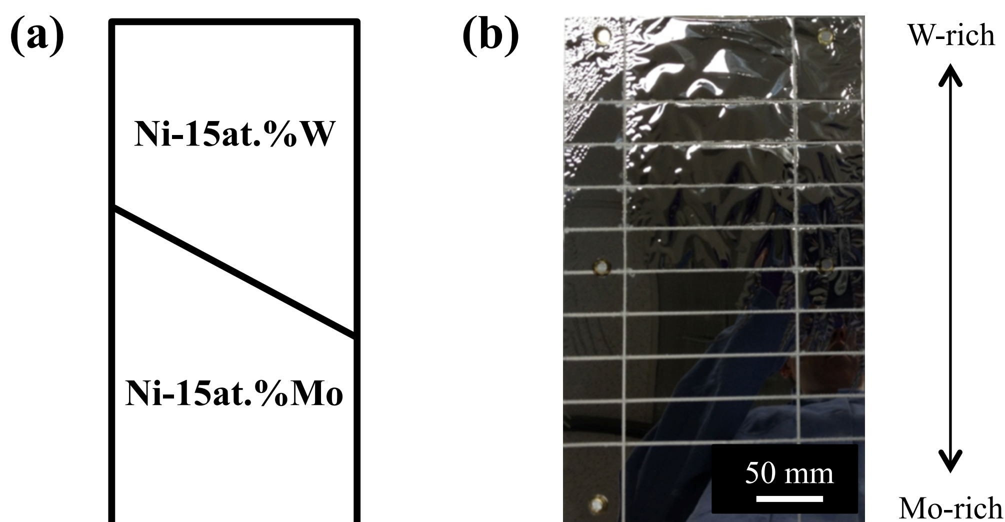

Figure 2.3: (a) Schematic of alloy target geometry and (b) Ni-Mo-W film on the brass substrate after sputter deposition.

Ni-Mo-W alloys were deposited using 2500 W power and 1 mTorr argon gas pressure onto a 12 inch x 7 inch brass substrate with stationary deposition to create a gradient in chemical composition (Figure 2.3). Single-phase solid solution face centered cubic (fcc) films with <111> out-of-plane texture [2] were achieved from alloy targets with nominally 85 atomic percent (at.%) Ni and Mo and W contents ranging from $Mo_{13}W_2$ to Mo_2W_{13}. Films were grown to a thickness of 20-30 μm to achieve robust freestanding films. Calibrated wavelength-dispersive spectroscopy (WDS) with Ni, Mo, and W crystals was used to determine the atomic composition of each alloy and the associated electrical resistivity was measured using four-point probe methods. CTE specimens were sectioned into 2 mm x 2 mm square and required no additional polishing or thinning. Calibration testing was performed using a National Institute of Standards and Technology (NIST) stainless steel standard reference material (SMR 738) for thermal expansion [6]. The cylindrical bar of SMR 738 is typically used for calibrating dilatometers, but in the current study a rod was sectioned, with wire electrical discharge machining (EDM) and a diamond wire, saw to create planar thin film specimens, Figure 2.4. The bulk SMR 738 was cut to a cross-sectional area of 2 mm x 2 mm and mechanically polished to a thickness of 100 μm.

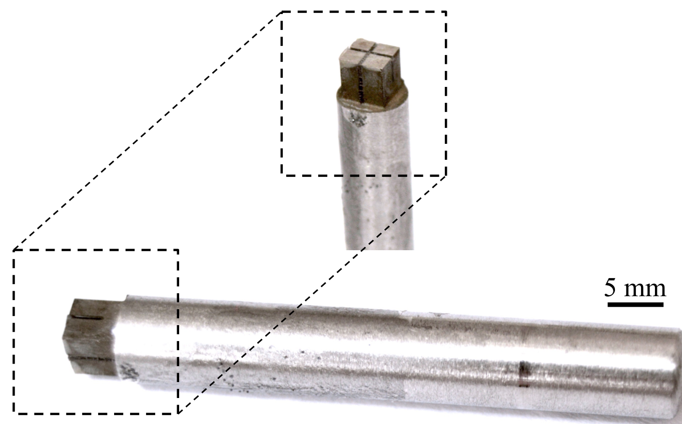

Figure 2.4: Cylindrical bar of SMR 738 sectioned into 2 mm x 2 mm using wire EDM. Individual specimens were sliced from the bar using a diamond wire saw.

2.2.2.1 Wavelength-dispersive spectroscopy (WDS)

The principle of WDS comes from Bragg's law ($\lambda = 2d \sin\theta$), where λ is the X-ray wavelength, d is the interplanar spacing of the crystal and 2theta (2θ) is the scattering angle. When electrons interact with a specimen, characteristic X-rays are emitted and used to quantify the element from which they were emitted. A single crystal of a calibration material is placed equally between the X-ray detector and the specimen of interest on a Rowland circle (Figure 2.5), which implements spherical gratings that combine diffraction and focusing of X-rays [7]. Measuring the angle of diffraction (θ) from the crystals allows for precise measurements of the wavelength (λ).

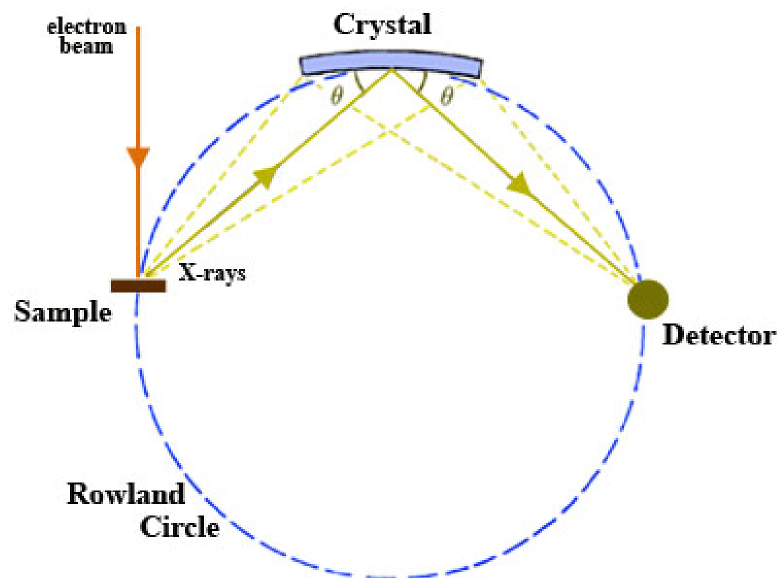

Figure 2.5: Principle of wavelength dispersive spectroscopy [7].

2.2.2.2 Four-point probe electrical resistivity

The electrical resistivity was measured using four-point probe geometry shown in Figure 2.6. The four probes are evenly spaced and the outer probes (1 and 4) apply a current (I) to the specimen, while the inner probes (2 and 3) measure the voltage (V) change in the

material. The sheet resistance (ρ_s) was measured using Equation 2.1 and the bulk resistance (ρ) was calculated using the film thickness (t) in Equation 2.2.

$$\rho_s = \frac{\pi}{\ln(2)} \frac{V}{I} \quad \textbf{(2.1)}$$

$$\rho = \rho_s t \quad \textbf{(2.2)}$$

The units of bulk resistance are typically reported Ω-m, which more specifically comes from the specimen's resistance, the cross-sectional area and length, such Ω-m^2/m. However, for sheet resistance the bulk resistance is scaled by the thickness, providing units conventionally noted "ohms per square" (Ω/□) that is dimensionally equivalent to units of Ω.

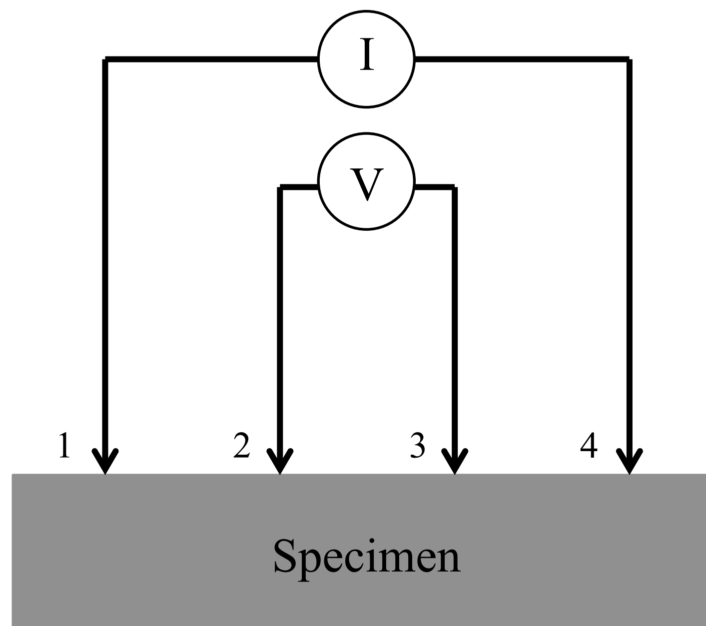

Figure 2.6: Four-point probe measurement setup, where four probes are equally spaced and current is applied through probes 1 and 4 while the associated voltage change is measured with probes 2 and 3.

2.2.3 Measuring thermal displacements

The detailed experimental setup in Figure 2.1 is designed to capture images of the specimen surface during the entirety of the experiment and post-process them with the popular non-contact method of DIC. Sutton and his colleagues at the University of South Carolina developed DIC [8-11] in the 1980's and it has since been widely accepted and implemented in the scientific community. This technique uses the digital images captured during the experiment and tracks pixel intensities between subsequent images. A randomized pattern of markers (speckle pattern) is applied to the specimen surface before imaging to create good contrast between the markers and the specimen surface. Images are captured at room temperature (reference image) and consecutively every 2 minutes while heating the furnace. Post-processing DIC algorithms sub-divide each image into smaller subsets that are tracked throughout the deformation. The black and white pixel intensity distribution inside each of the subsets is tracked from the reference image and matched to the next image (current image). The quality of matching is evaluated by maximizing the 2D cross correlation coefficient (C_{ij}), defined in Equation 2.3. The gray scale value of the individual pixel intensities in the reference image are represented by $F(x_i, y_j)$, where x_i and y_j are the pixel locations in the reference image. Similarly, the gray scale value of the individual pixel intensities in the current image are represented by $G(x_i^*, y_j^*)$, where x_i^* and y_j^* are the pixel locations in the current image. The values $\bar{F}$ and $\bar{G}$ are the mean values of the gray scale pixel intensity matrices F and G, respectively.

$$C_{ij} = \frac{\sum_i \sum_j \left[\left(F(x_i, y_j) - \bar{F} \right) \times \left(G(x_i^*, y_j^*) - \bar{G} \right) \right]}{\sqrt{\left[\sum_i \sum_j \left(F(x_i, y_j) - \bar{F} \right)^2 \right] \times \left[\sum_i \sum_j \left(G(x_i^*, y_j^*) - \bar{G} \right)^2 \right]}} \tag{2.3}$$

Pixel displacements of the center of the subset (u, v) are outputs of the DIC used for further analysis, which is determined through deformation mapping from the reference coordinates (x_i, y_j) to the current coordinates (x_i^*, y_j^*). The mapping for in-plane deformation is approximated by a 2D affine transform, where Δx and Δy are the distances between the center of the subset and the point (x, y) and $\frac{\partial u}{\partial x}, \frac{\partial u}{\partial y}, \frac{\partial v}{\partial x}, \frac{\partial v}{\partial y}$ are the displacement gradients, shown in Equation 2.4.

$$\begin{aligned} x^* &= x + \quad + \frac{\partial u}{\partial x}\Delta x + \frac{\partial u}{\partial y}\Delta y \\ y^* &= y + v + \frac{\partial v}{\partial x}\Delta x + \frac{\partial v}{\partial y}\Delta y \end{aligned} \tag{2.4}$$

Therefore, to assure good correlation between subsequent images, it is critical to obtain distinct black and white contrast with the surface speckle pattern. Traditionally this is achieved using black and white paint, where the specimen surface is coated in white and then speckled with random black markers. However, most paints cannot withstand high temperatures, precluding the use of paint for CTE measurements. Instead, specimens were speckled using fused silica powders (Aremco Ceramacast™ 645N) dispersed in acetone to create a suspension that evenly distributed particles onto the surface. This speckling method provided an average speckle size of 10 µm, which could be imaged with the optics outlined in the section 2.2.1.

The pixel displacements were obtained using a MATLAB based DIC code [12] written and developed by previous students and postdocs at JHU. In-plane thermal displacements were used to calculate the thermally induced strains (ε^{th}). Since CTE is isotropic for all cubic materials, measurements of individual x and y thermal strains are redundant. For simplicity, the thermal strains in the x-direction will be denoted going forward. In-plane thermal strains were calculated using Equation 2.3, where u is the measured pixel displacement and x^* is the current pixel position both in the in the x-direction, obtained from DIC. Figure 2.7 shows a representative plot of the pixel displacement (u) versus current pixel position (x^*) for SRM 738 at image number 300 (385°C).

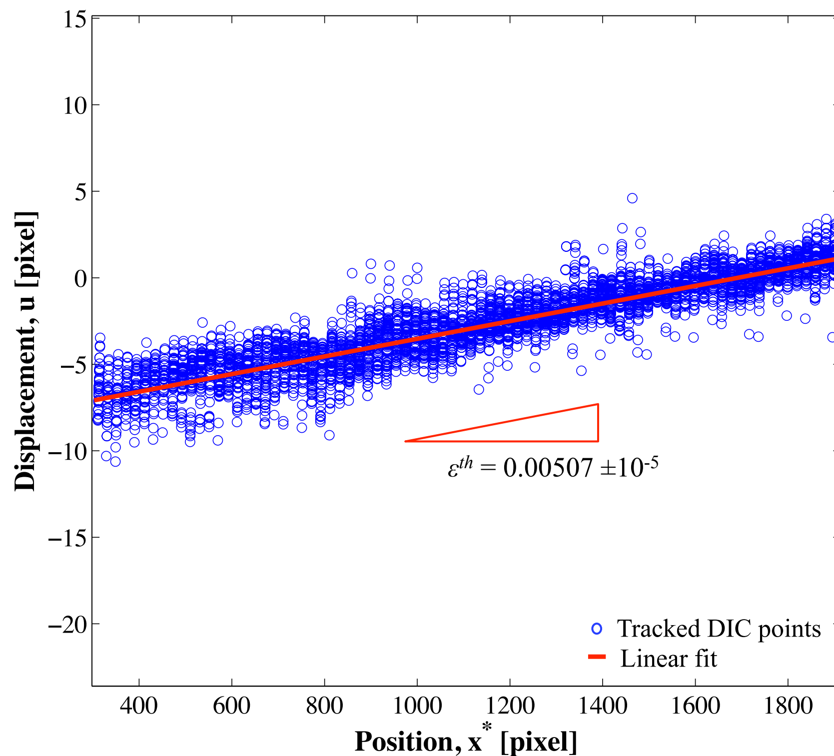

Figure 2.7: A representative displacement versus position plot from SRM 738 at image 300 (385°C). More than 4700 DIC tracking markers are fit to a linear line (red) and the measured slope provides a one-dimensional strain value with a resolution of $\pm 10^{-5}$.

A linear line is fit through the tracked DIC points and the slope is recorded as the one-dimensional average thermal strain, similar to Equation 2.5.

$$\varepsilon^{th} = \frac{\partial u}{\partial x^*} \tag{2.5}$$

$$\alpha = \frac{d\varepsilon^{th}}{dT} = \frac{d}{dT}\left(\frac{\partial u}{\partial x^*}\right) \tag{2.6}$$

This procedure was carried out for each image acquired and the resultant thermal strain as a function of image number was generated for SRM 738, Figure 2.8.

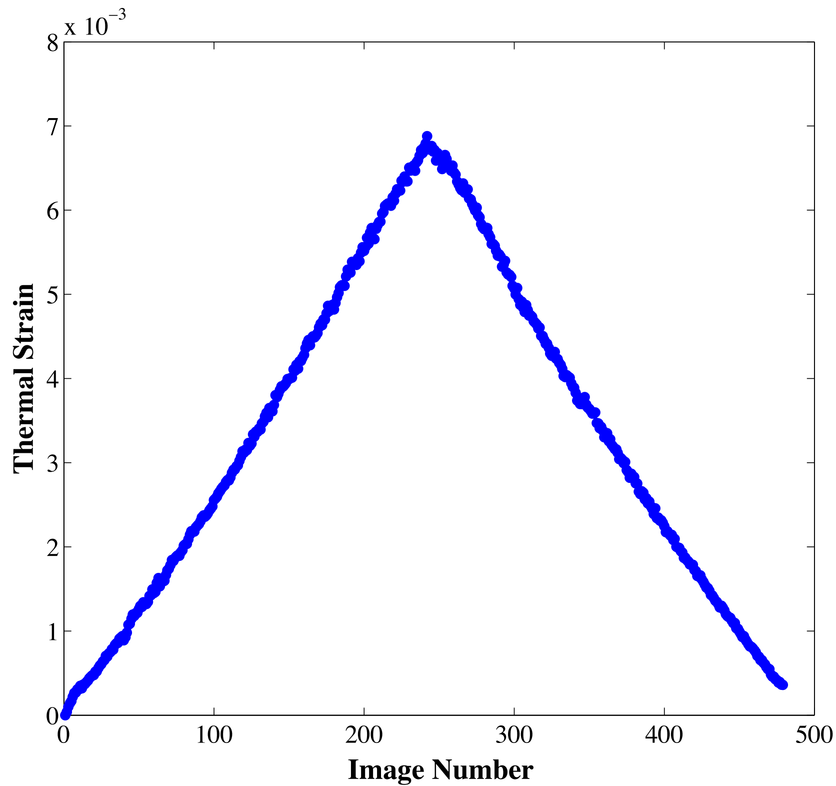

Figure 2.8: The calculated thermal strain as a function of image number for SRM 738 while heating from room temperature, 505°C and cooling down.

The timestamp of each image was matched to the associated temperature output recorded during data acquisition to achieve the thermal strain as a function of temperature, illustrated in Figure 2.9. Thermally induced strains are inherently reversible, providing fully recoverable expansion from the ramp up and ramp down temperature cycles.

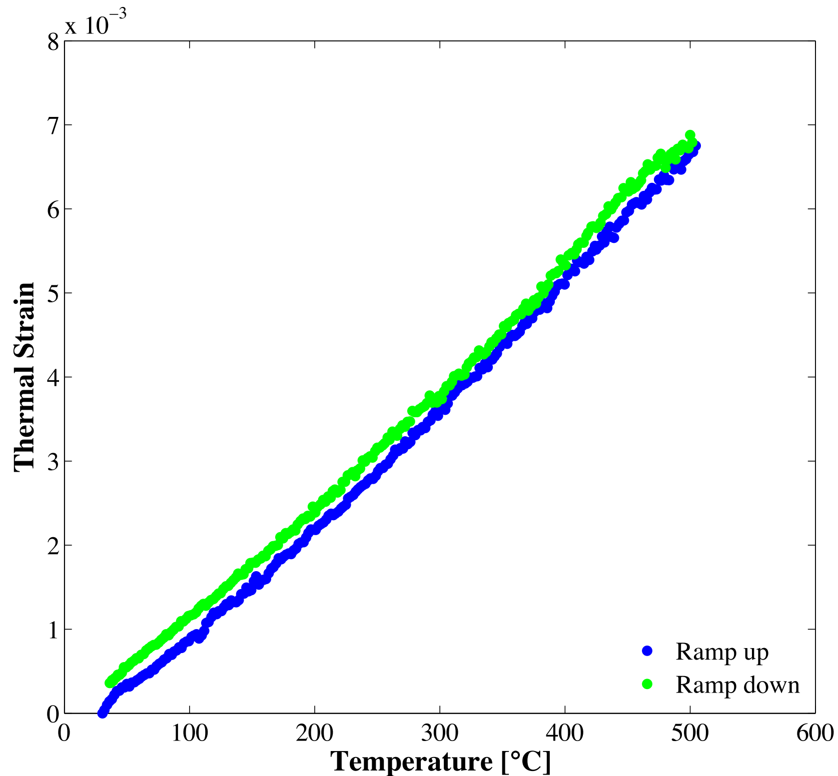

Figure 2.9: The calculated thermal strain as a function of temperature for SRM 738 while heating from room temperature, 505°C (ramp up) and cooling down (ramp down).

The two strain curves can be averaged to provide a mean strain, Figure 2.10. CTE (α) was calculated as a function of temperature using Equation 2.6 by taking the derivative of a third-order polynomial fit [13] to the mean strain dataset. The resultant CTE for SRM 738 is plotted as a function of temperature in Figure 2.11.

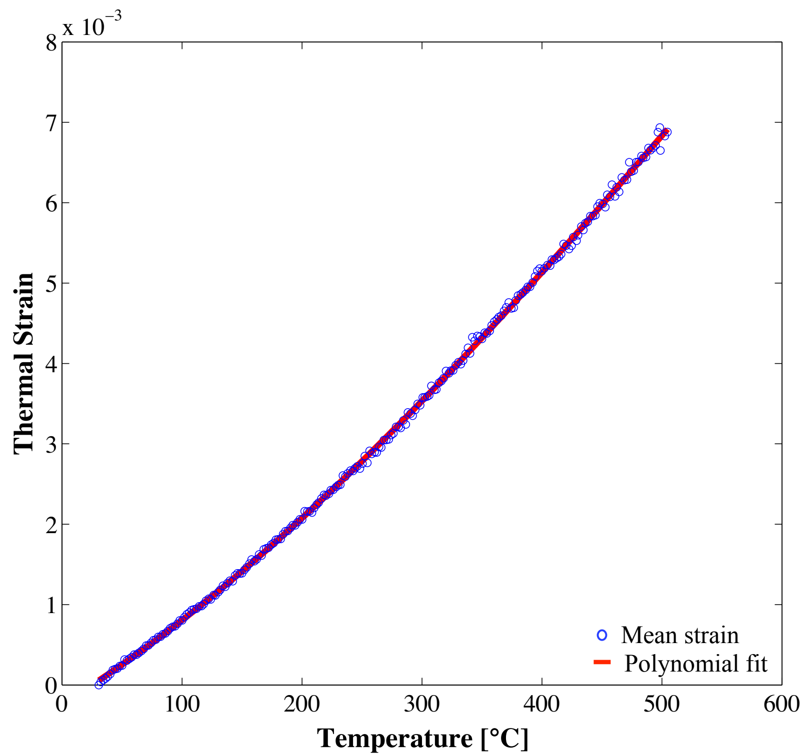

Figure 2.10: Third-order polynomial fitting of the mean strain for SRM 738.

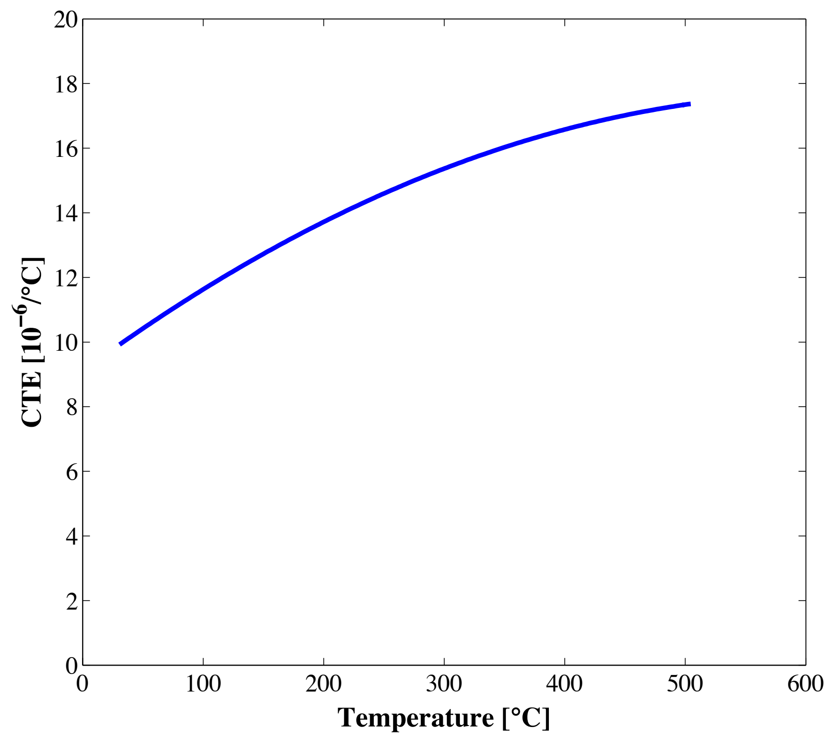

Figure 2.11: Calculated CTE of SRM 738 from the derivative of the polynomial fit with respect to temperature.

2.3 Calibration

Monitoring thermal displacements of SRM 738 involved the use of DIC, and well-focused images at a constant magnification were needed to obtain the requisite DIC resolution for the entire duration of image collection. Therefore, correcting for the optical distortions in the experimental setup was vital to obtaining adequate images for correlation. Out-of-plane displacements during image acquisition degrade image quality and DIC tracking and resolution. These effects were minimized by use of a low-expansion quartz holder and a fixed magnification telecentric lens, but additional distortions can arise. Convection currents in the furnace will lead to a circular flow of air and cause the blurring of images during acquisition. Commercial clamshell furnaces typically employ optically transparent plates or viewing windows that allow one to peer into the furnace. We found that reducing the air gap between the specimen and the viewing window greatly reduces the effect of convection on the image quality. Positioning a long cylindrical optical-quality quartz rod above the specimen, as close as possible, such that it extends through the furnace wall and has one polished face outside the furnace, greatly reduces the air gap and the shimmer associated with convection. Moreover, the fact that the image on the bottom face is transferred to the top face allows the camera to be focused on the top face, greatly simplifying the image acquisition.

Even with the quartz cylinder, imaging distortions related to temperature gradients in the air on the top of the cylinder can also affect the fidelity of the DIC measurements. These distortions are caused by changes in the refractive index of air with temperature [14] and heat that escapes from the furnace viewport. It has been suggested that using a fan or air knife to mix and cool the air above the furnace will mitigate this problem and greatly improve the

imaging quality [15]. For the CTE setup built and employed for this study, an Exair Air Knife was integrated to blow compressed air between the quartz cylinder and the camera lens to cool the air for enhanced accuracy of the DIC measurements.

An additional unforeseen problem was uncovered in the calibration, for example the measured values for the thermal strain of a SRM 738 specimen is plotted as a function of temperature in Figure 2.12. The raw data measurements made with our setup had the same general trend as the NIST certified data [6], but the absolute values of the data are offset by 10% at temperatures below 250°C and as much as 20-28% at higher temperatures. The reason for this apparent increase in thermal strain eluded explanation until it was realized that the refractive index of the quartz cylinder varies as a function of temperature.

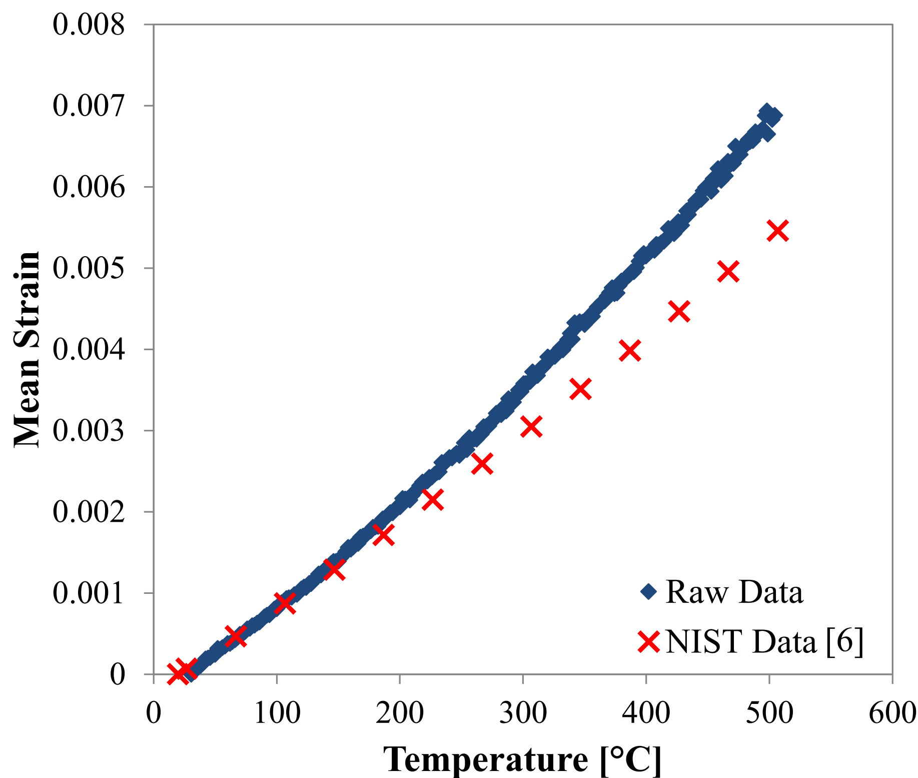

Figure 2.12: Strain versus temperature measured thermal displacements (raw) for SRM 738 compared to NIST standard data for comparison [6].

In the current setup, the vertical quartz rod has a temperature gradient, from highest inside the furnace to lowest outside the furnace. This gradient in temperature causes a gradient in refractive index along the length of the cylinder, distorting the images and producing fictitious displacements. Lyons et al. made note of the quality of the viewport and its effect on image quality [15], but they did not discuss the consequences of temperature and refractive index gradients along the optical path of the viewport. In practice, these temperature gradients are highly variable and difficult to accurately measure and predict.

To address this challenge, a speckle pattern was applied to the top surface of the quartz specimen holder such that DIC could be used to compare direct measurements of the thermal displacement of the quartz holder with the SRM 738 specimen. The prescribed field of view contained both the SRM 738 specimen and a portion of the quartz holder, allowing for simultaneous imaging (Figure 2.13).

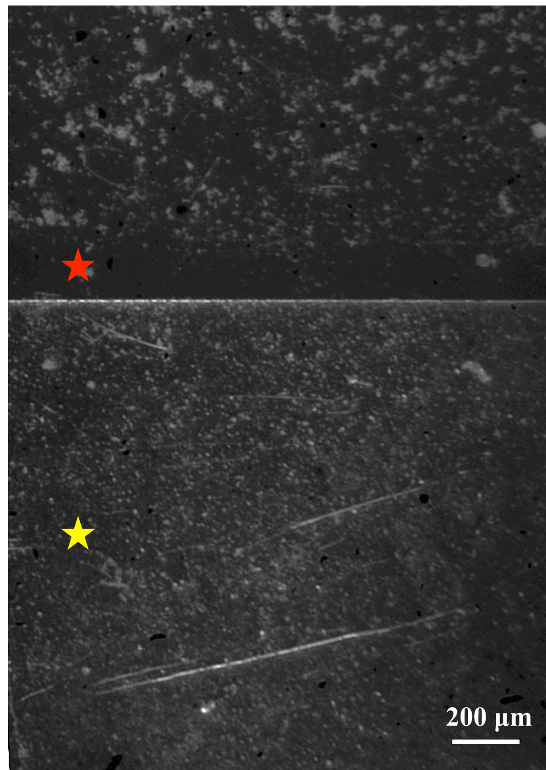

Figure 2.13: Representative image with DIC speckle pattern applied to both the specimen holder (red) and the NIST SRM 738 (yellow).

The quartz holder displacements were tracked and used to determine an offset correction that could then be applied to the raw SRM 738 data. Subtracting this measured offset correction from the raw stainless steel strain data, where the investigated temperature ranged from room temperature to the maximum calibrated temperature (505°C), resulted in the corrected dataset (Figure 2.14). The corrected strain dataset is in very good agreement with the NIST calibration values [6].

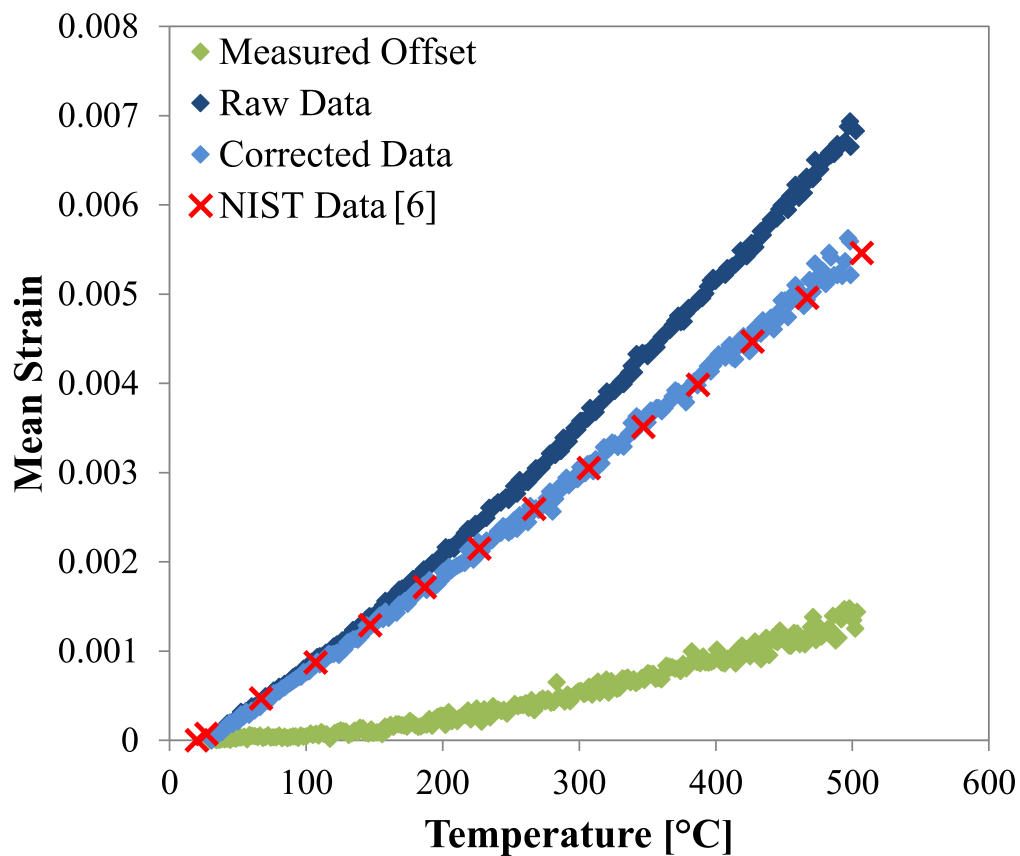

Figure 2.14: Strain versus temperature for SRM 738. The corrected data, obtained by subtracting the measured offset from the raw data, is compared to NIST [6].

Differentiating the thermal strain data with the method outlined in section 2.2.3 provides the associated CTE as a function of temperature, and curves made by differentiating the raw and corrected datasets are plotted in Figure 2.15. The measured and corrected dataset for thin fiml specimens yielded a CTE that matches bulk dilatometer measurements [6] with an accuracy of $\pm 0.4 \times 10^{-6}$ /°C, ensuring a well calibrated setup.

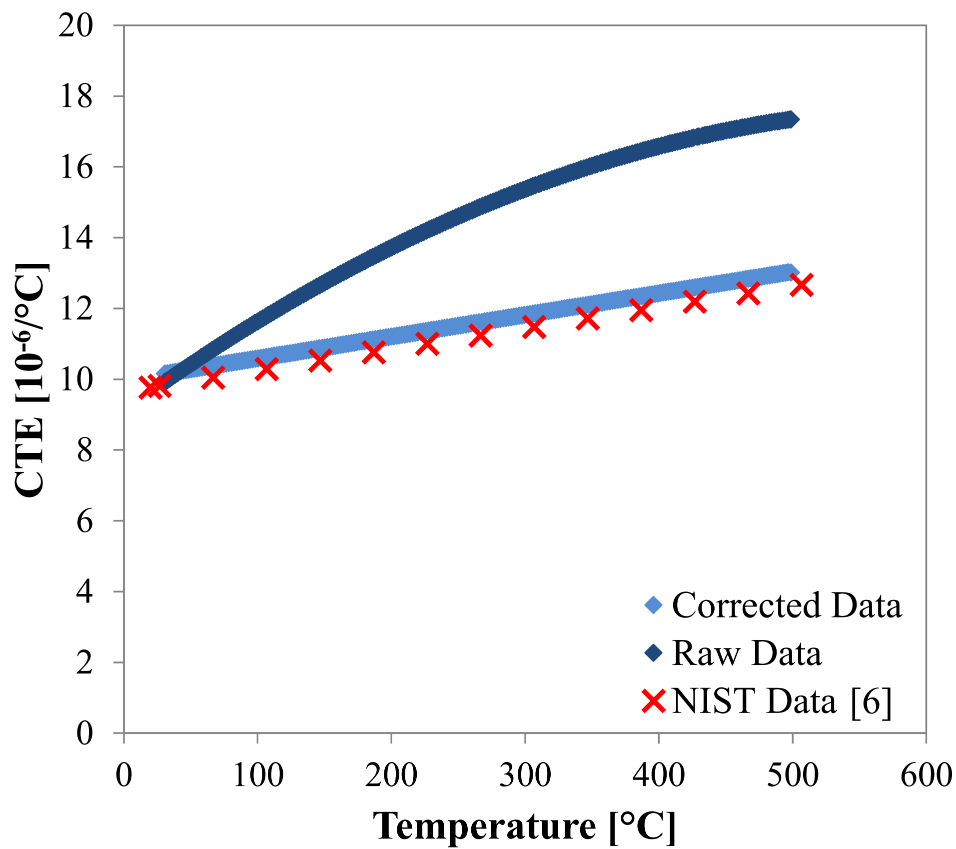

Figure 2.15: Calculated values of CTE determined from the measured thermal displacements for SRM 738. The corrected data is compared to NIST standard data [6].

2.4 The Influence of Alloy Chemistry

2.4.1 Measured physical properties

Combinatorial subsets of the Ni-Mo-W films were cut from the gradient film and analyzed for their physical properties. The chemical composition measured via WDS and the bulk electrical resistivity obtained with four-point probe measurements are reported in Table 2.1. The electrical resistivity showed minimal fluctuations with composition and are comparable to the values reported for bulk nickel-base superalloys (120-133 μΩ-cm), nickel-molybdenum alloys (118-135 μΩ-cm) and nickel-chromium alloys (103-129 μΩ-cm) [16]. The fact that the thin film electrical resistivity is on par with that of bulk Ni alloys suggests that the underlying microstructure does not impede electron motion [17].

Table 2.1: Electrical resistivity measured using four-point probe technique. All compositions have a maximum standard deviation of ± 0.1 atomic percent Ni, Mo and W.

Composition [at.%]	Film thickness [μm]	Sheet resistance [Ω/□]	Bulk resistance [μΩ-cm]
$Ni_{85.4}Mo_{3.3}W_{11.3}$	19.7 ± 0.1	0.0591	116.4 ± 1.9
$Ni_{85.1}Mo_{4.6}W_{10.3}$	20.6 ± 0.2	0.0505	104.1 ± 0.6
$Ni_{85.4}Mo_{5.9}W_{8.7}$	23.2 ± 0.1	0.0472	109.4 ± 2.1
$Ni_{84.3}Mo_{8.9}W_{6.8}$	22.0 ± 0.3	0.0491	108.1 ± 0.9
$Ni_{84.4}Mo_{10.7}W_{4.9}$	21.4 ± 0.1	0.0503	107.6 ± 0.6
$Ni_{84.2}Mo_{11.8}W_{4.0}$	20.6 ± 0.1	0.0554	114.1 ± 1.3
$Ni_{85.2}Mo_{12.7}W_{2.1}$	20.2 ± 0.1	0.0519	104.9 ± 2.1

The CTE of Ni-Mo-W alloy films with compositions ranging from nearly $Ni_{85}Mo_{15}$ to $Ni_{85}W_{15}$ were investigated from room temperature up to 625°C. Figure 2.16 displays a representative dataset of the measured thermal strains as a function of temperature for the alloy $Ni_{85.1}Mo_{4.6}W_{10.3}$. Individual data points are magnified and shown in the inset, demonstrating the smooth thermal loading achievable with minimal scatter. The thermal strains were used to calculate CTE by measuring the slope of the strain dataset, as outlined in section 2.2.3, resulting in a CTE that ranged from 8.87-13.0×10^{-6} /°C between room temperature and 600°C.

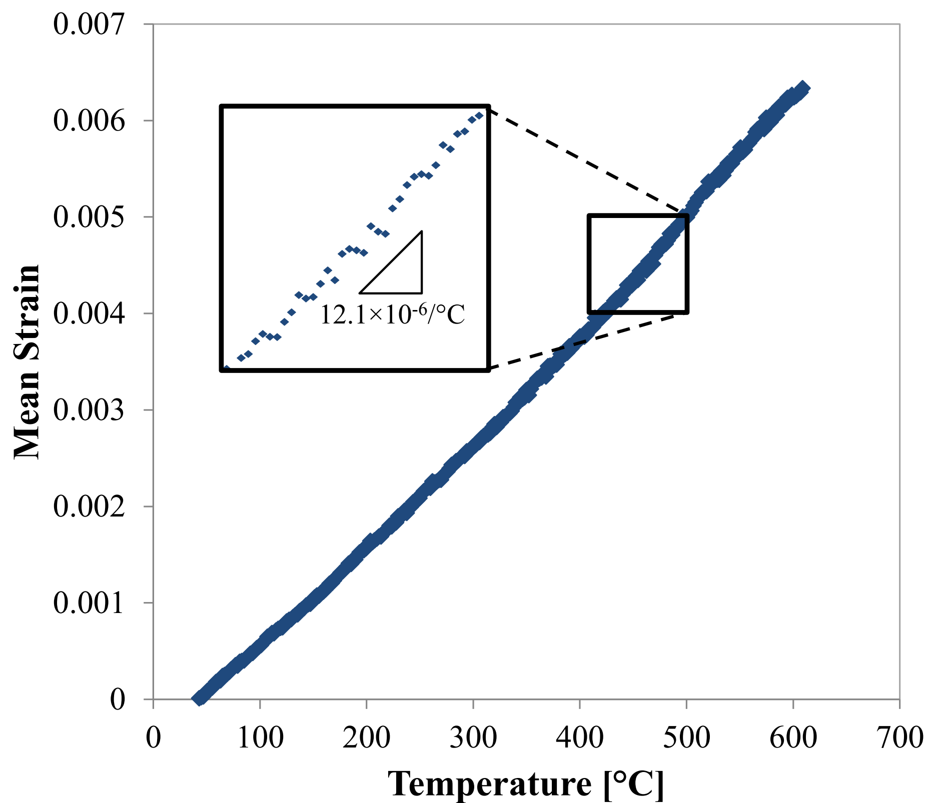

Figure 2.16: Thermal strain measurements as a function of temperature for $Ni_{85.1}Mo_{4.6}W_{10.3}$.

The CTE for different alloy compositions is plotted as a function of temperature and compared to the CTE for pure Ni [18], in Figure 2.17. The chemistry of each alloy and CTE values measured at room temperature (RT) and at 600°C are given in Table 2.2.

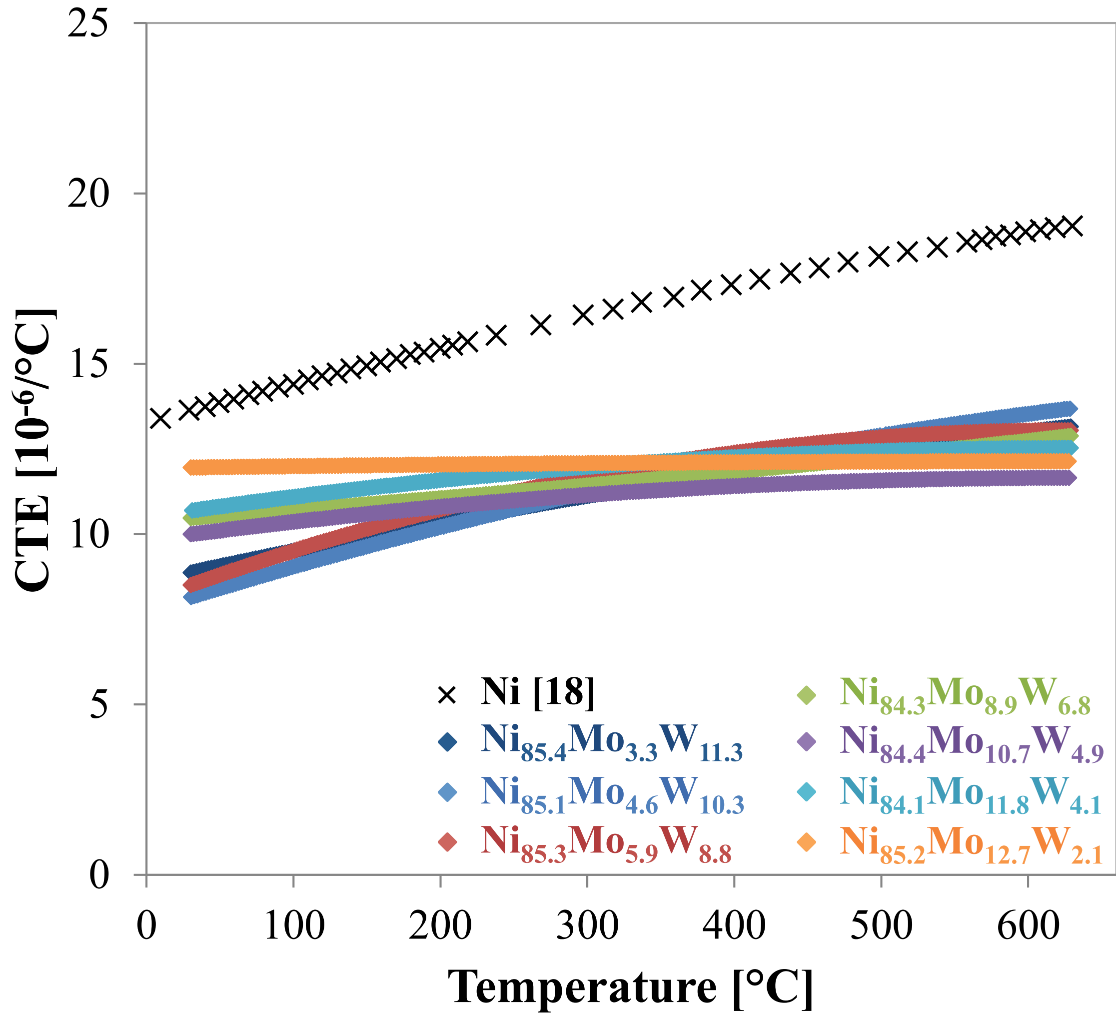

Figure 2.17: CTE versus temperature for compositional spread of Ni-Mo-W alloys, with associated at.% composition, compared to pure Ni [18].

It is clear from the results presented in this figure and table that alloying with Mo and W are both effective ways of decreasing the overall CTE as compared to pure Ni and that the effect on CTE differs with alloying content. For illustration, W-rich alloys and Mo-rich alloys are plotted as a function of temperature in Figures 2.18 and 2.19, respectively.

Table 2.2: Alloy composition and CTE values from room temperature (RT) and 600°C for the sputter deposited Ni-Mo-W films.

Alloy Composition [at.%]	**RT CTE [10^{-6}/°C]**	**600°C CTE [10^{-6}/°C]**
$Ni_{85.4}Mo_{3.3}W_{11.3}$	8.87	13.0
$Ni_{85.1}Mo_{4.6}W_{10.3}$	8.16	13.5
$Ni_{85.3}Mo_{5.9}W_{8.8}$	8.51	13.0
$Ni_{84.3}Mo_{8.9}W_{6.8}$	10.5	12.7
$Ni_{84.4}Mo_{10.7}W_{4.9}$	10.0	11.7
$Ni_{84.1}Mo_{11.8}W_{4.1}$	10.7	12.5
$Ni_{85.2}Mo_{12.7}W_{2.1}$	11.9	12.1

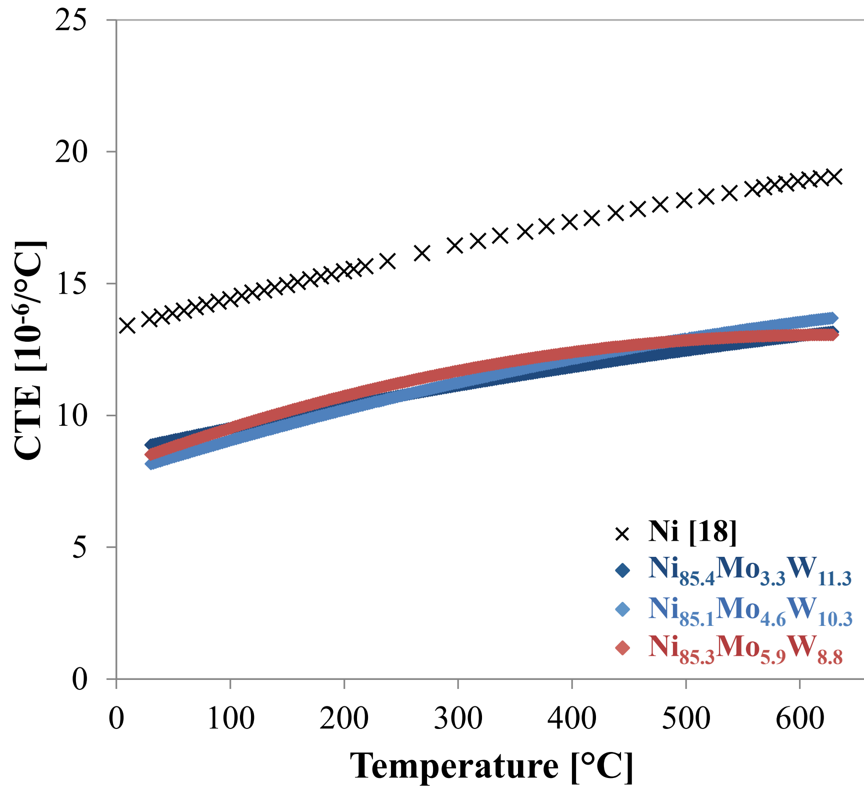

Figure 2.18: CTE versus temperature for W-rich alloys, compared to pure Ni [18].

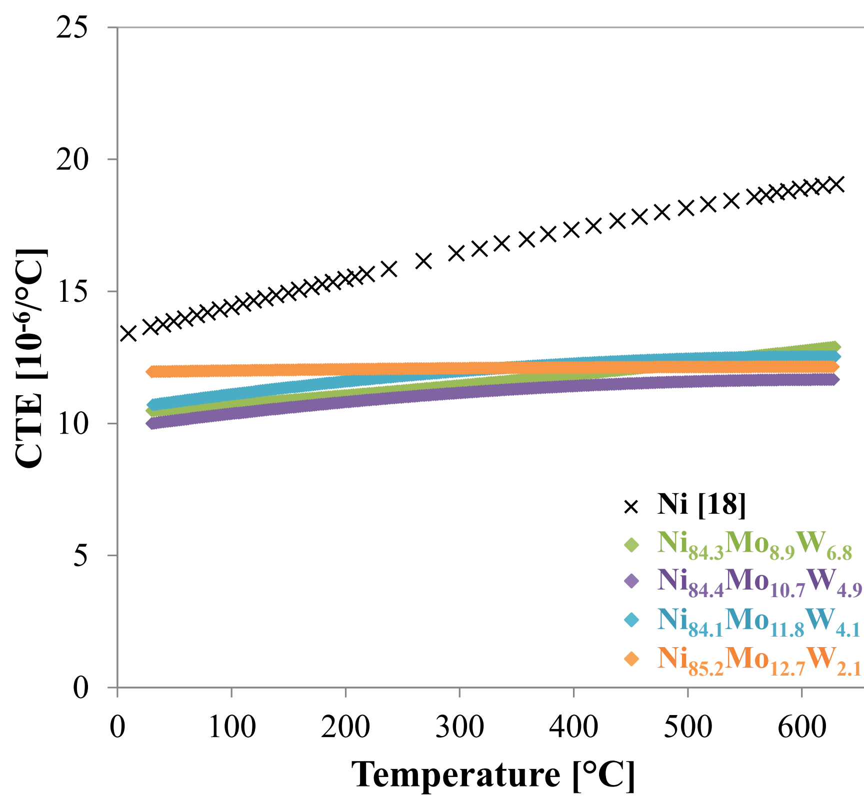

Figure 2.19: CTE versus temperature for Mo-rich alloys, compared to pure Ni [18].

Most MEMS devices are composed of layered structures, and matching the CTE of individual layers to the substrate is a highly desirable way of mitigating thermal distortions. In recent years, glass substrates have replaced silicon as the substrate of choice for many applications, in part because of its tailorable properties. Unlike silicon, commercial glass substrates display a wide range of CTE values, which depend on the glass composition. Substantial advantages for the packaging industry came when the CTE of glass substrates could be reduced to that of silicon, eliminating warping during multi-stack processes [19]. It has been shown that changing the chemical composition of glass substrates can vary the CTE from 3.0-12.0×10^{-6} /°C [20-22]. All the RT CTE values reported for Ni-Mo-W in Table 2.2 fall within the range of achievable values for glass substrates. Therefore, Ni-Mo-W alloys can be paired with a glass substrate that matches its CTE, reducing the geometric changes that would otherwise arise during heating.

2.4.2 Tailorable CTE

A simple rule-of mixtures, Equation 2.7, can be used to predict the CTE as a function of alloy concentration, where each element (n) has a respective CTE (α_n) and volume fraction (V_n). The CTE for Ni has been reported to range from 12.4-13.4×10^{-6} /°C at room temperature and 15.3-17.5×10^{-6} /°C at 600°C [18, 23, 24]. For the rule-of mixtures calculation, the average values of 13×10^{-6} /°C and 16.4×10^{-6} /°C will be used for the CTE of Ni at room temperature and 600°C, respectively. Suh et al. measured and reported the thermal expansion coefficients for pure Mo and W using standard dilatometer methods [23]. These pure metal values can be used in Equation 2.7 to predict CTE values for various alloy compositions as a function of temperature. The volume of Ni, Mo and W atoms are calculated by the method outlined by King [25], where the atomic volume of a solute atom is

measured while dissolved into a particular solvent. Since CTE inherently is based upon volumetric changes in a crystal rather than an atomic volume average, the effective volumes of Mo and W in the Ni lattice were chosen rather than their own atomic volumes. It can be assumed that the solute atoms in single-phased solid solution Ni-Mo-W [3] are substitutional in the Ni lattice, due to similar or larger atomic radii of Mo and W compared that of Ni [26].

$$\alpha = \sum_{n} \alpha_n V_n \quad \textbf{(2.7)}$$

$$V_{sf} = \frac{(V^* - V_{Ni})}{V_{Ni}} \quad \textbf{(2.8)}$$

The effective volume of a substitutional atom (V^*) in the Ni lattice is defined by the volume size factor (V_{SF}) in Equation 2.8, where V_{Ni} is the atomic volume of Ni [27] and V_{SF} for Mo and W solutes are reported by King [25]. Binary $Ni_{85}Mo_{15}$ and $Ni_{85}W_{15}$ were investigated as the upper bounds for the ternary Ni-Mo-W alloy system and their predicted CTE values are 11.6 and 11.4 $\times 10^{-6}$ /°C, as given in Table 2.3.

Table 2.3: Predicted CTE values at room temperature (RT) and 600°C for $Ni_{85}Mo_{15}$ and $Ni_{85}W_{15}$ using the rule-of mixtures.

	Ni [18, 23, 34]	**Mo** [23]	**W** [23]	**$Ni_{85}Mo_{15}$**	**$Ni_{85}W_{15}$**
RT CTE [10^{-6} /°C]	13.0	5.08	4.97	11.6	11.4
600°C CTE [10^{-6} /°C]	16.4	6.59	8.63	14.7	14.9
Volume size factor, V_{SF} [25]	---	+22.27%	+36.93%	---	---
Atomic Volume in Ni lattice [25] [Å^3]	10.94	13.37	14.98	---	---

This prediction suggests that the addition of Mo and W should have an almost identical effect, reducing the CTE by 10% compared to that of Ni, independent of composition. However, experimental investigations on binary Ni-Mo and Ni-W alloys showed a compositionally dependent behavior. For example, Pavlovic et al. showed that $Ni_{85}Mo_{15}$ reduced the CTE of Ni by 23%[18], whereas Dosovitskiy et al. shows that $Ni_{95}W_5$ reduced the CTE of Ni by 17% [28]. Similarly, the measurements of the sputter deposited combinatorial $Ni_{85}Mo_xW_{15-x}$ thin films indicate that the composition of the ternary alloying elements does play an important role in determining the CTE. The measured CTE values are plotted as a function of solute concentration Mo_xW_{15-x} and compared with the rule-of-mixtures predictions in Figure 2.20.

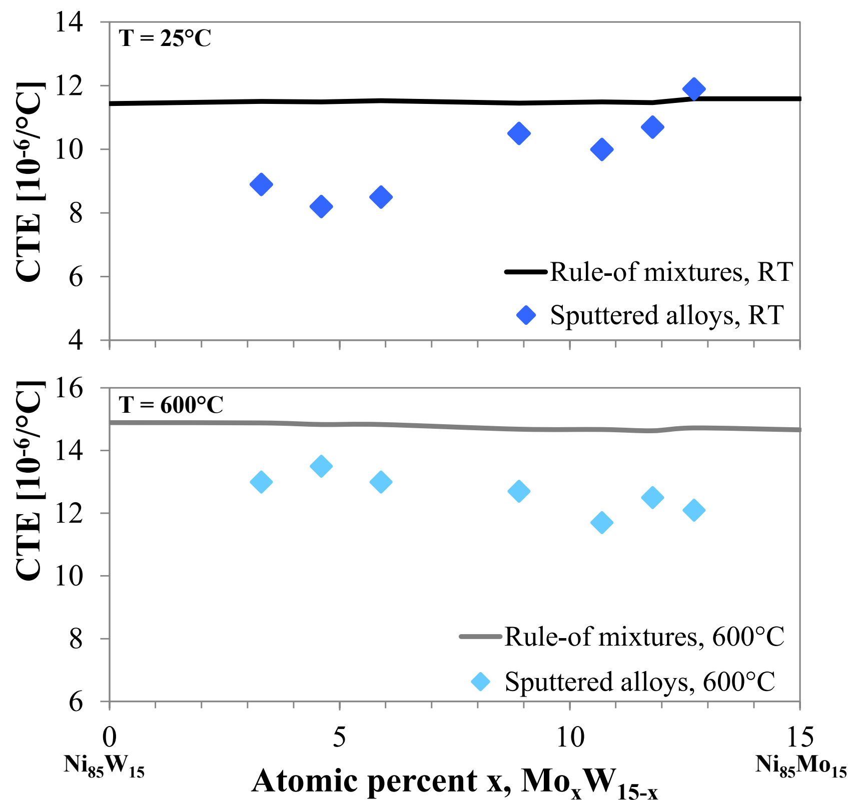

Figure 2.20: Variations of the CTE at room temperature (RT) and 600°C against the concentration of Mo and W for the calculated rule-of mixtures and the sputtered Ni-Mo-W alloys, where $Ni_{85}Mo_xW_{15-x}$ with x ranging 2-13 at. % Mo.

All of the experimental data falls at or below the predicted values of CTE given by the rule-of-mixtures. The experimental values also show greater variation with composition. At room temperature the Mo-rich films have a CTE similar to what was predicted, but the CTE of the W-rich films was measured to be considerably lower. The inverse was observed at 600°C where the Mo-rich films were lower.

The fact that the reduction of the CTE for all of the $Ni_{85}Mo_xW_{15-x}$ films was measured to be greater than what was predicted and the finding that the temperature dependence of the CTE is compositionally dependent both have significant technological ramifications. The observed overlap of the CTE of Ni-Mo-W metallic thin films and glass substrates provides an opportunity to dramatically reduce the residual stresses. The ability to tailor the temperature dependence of the film CTE with alloy composition provides an additional design element for engineering dimensional stability into MEMS devices.

The scientific mechanisms and physics that underpin these enhanced and tailorable properties are not yet fully understood. The microstructure of the Ni-Mo-W films have been shown to possess strong {111} texture with numerous nanotwins and stacking faults aligned parallel to the plane of the thin film [2, 3]. This results in local non-cubic symmetry that could lead to an anisotropic CTE, which is not incorporated in the rule-of mixtures calculation. Localized and preferential solute atom segregation could also play a role in modifying local bonding and CTE values. We note that Kurz et al. reported that for binary Ni alloys with twins and stacking faults, Mo solute atoms segregate to the grain boundaries at elevated temperatures whereas W segregation was kinetically hindered [29]. The temperature invariant CTE shown for Mo-rich Ni-Mo-W films could be the result of local bonding variations from Mo segregation, which may provide the requisite local anisotropic CTE for a

temperature independent behavior that is not observed in W-rich films. The compositional control of sputter deposited Ni-Mo-W alloys provided the combined benefits of overall reduction in CTE as compared to pure Ni and tailorable CTE at elevated temperatures, supporting a more expansive materials selection for high temperature MEMS applications.

2.5 Chapter summary

A non-contact optical method based on digital image correlation was developed to measure the coefficient of thermal expansion of thin film specimens as a function of temperature. NIST stainless steel (SRM 738) was used to correct for imaging aberrations that led to erroneous displacement measurements and to calibrate the system with an accuracy of $\pm 0.4\times10^{-6}$ /°C. This non-contact DIC-based technique can be applied to materials where conventional dilatometry is impractical. Metal MEMS Ni-Mo-W films were sputter deposited with a combinatorial range of compositions ($Ni_{85}Mo_xW_{15-x}$) and demonstrated to have a CTE that is well matched to commercial glass substrates for MEMS-based micro-sensors and switches. The non-contact measurements showed the CTE of all $Ni_{85}Mo_xW_{15-x}$ films to be significantly lower than that of pure Ni. The room temperature CTE was found to be lowest for W-rich alloys, while the Mo-rich alloys were found to have a temperature invariant CTE. The dual benefits of reduced and compositionally tailorable CTE suggest that Ni-Mo-W alloys are promising candidates for metal MEMS applications.

2.6 References for Chapter 2

1. Fisher, D. *Negative thermal expansion materials*. 2018. Materials Research Forum LLC.

2. Sim, G.-D., J.A. Krogstad, K.M. Reddy, K.Y. Xie, G.M. Valentino, T.P. Weihs, and K.J. Hemker, *Nanotwinned metal MEMS films with unprecedented strength and stability.* Science Advances, 2017. **3**(6): p. e1700685.

3. Sim, G.-D., J.A. Krogstad, K.Y. Xie, S. Dasgupta, G.M. Valentino, T.P. Weihs, and K.J. Hemker, *Tailoring the mechanical properties of sputter deposited nanotwinned nickel-molybdenum-tungsten films.* Acta Materialia, 2018. **144**: p. 216-225.

4. Thompson, R. and K. Hemker. *Thermal expansion measurements on coating materials by digital image correlation*. in *Proceedings of the 2007 SEM Annual Conference and Exposition on Experimental and Applied Mechanics, Springfield, Massachusetts*. 2007.

5. Leisen, D., R. Rusanov, F. Rohlfing, T. Fuchs, C. Eberl, H. Riesch-Oppermann, and O. Kraft, *Mechanical characterization between room temperature and 1000 °C of SiC free-standing thin films by a novel high-temperature micro-tensile setup.* Review of Scientific Instruments, 2015. **86**(5): p. 055104.

6. Hahn, T.A. and T.E. Gills, *Standard Reference Material 738*, M.M. Laboratory, Editor. 1993, National Institute of Standards and Technology: Gaithersburg, MD 20899.

7. Henry, D. and J. Goodge, *Wavelength-dispersive X-ray spectroscopy (WDS).* Science Education Resource Center at Carleton College, 2016. **10**.

8. Bruck, H., S. McNeill, M.A. Sutton, and W. Peters, *Digital image correlation using Newton-Raphson method of partial differential correction.* Experimental mechanics, 1989. **29**(3): p. 261-267.

9. Chu, T., W. Ranson, and M.A. Sutton, *Applications of digital-image-correlation techniques to experimental mechanics.* Experimental mechanics, 1985. **25**(3): p. 232-244.

10. Sutton, M., W. Wolters, W. Peters, W. Ranson, and S. McNeill, *Determination of displacements using an improved digital correlation method.* Image and vision computing, 1983. **1**(3): p. 133-139.

11. Sutton, M.A., J.J. Orteu, and H. Schreier, *Image correlation for shape, motion and deformation measurements: basic concepts, theory and applications*. 2009: Springer Science & Business Media.

12. Eberl, C., D.S. Gianola, R. Thompson, and K.J. Hemker, *Digital Image Correlation and Tracking*. 2010, MathWorks: MATLABCentral.

13. D'Errico, J., *SLM - Shape Language Modeling*. 2016, MathWorks: MATLABCentral.

14. Edlén, B., *The refractive index of air.* Metrologia, 1966. **2**(2): p. 71.

15. Lyons, J., J. Liu, and M. Sutton, *High-temperature deformation measurements using digital-image correlation.* Experimental mechanics, 1996. **36**(1): p. 64-70.

16. Everhart, J.L., in *Engineering Properties of Nickel and Nickel Alloys*. 1971, Springer: US. p. 229.

17. Lu, L., Y. Shen, X. Chen, L. Qian, and K. Lu, *Ultrahigh strength and high electrical conductivity in copper.* Science, 2004. **304**(5669): p. 422-426.

18. Pavlovic, A., V.S. Babu, and M.S. Seehra, *High-temperature thermal expansion of binary alloys of Ni with Cr, Mo and Re: a comparison with molecular dynamics simulations.* Journal of Physics: Condensed Matter, 1996. **8**(18): p. 3139.

19. Trott, G.R. and A. Shorey. *Glass wafer mechanical properties: A comparison to silicon*. in *Microsystems, Packaging, Assembly and Circuits Technology Conference (IMPACT), 2011 6th International*. 2011. IEEE.

20. Hayashi, K., S. Sawamura, S. Nomura, N. Suzuki, and M. Takekoshi. *Development and Evaluation of Carrier Glass Substrate for Fan-Out WLP/PLP Process*. in *Electronic Components and Technology Conference (ECTC), 2017 IEEE 67th*. 2017. IEEE.

21. Qin, X., N. Kumbhat, V. Sundaram, and R. Tummala. *Highly-reliable silicon and glass interposers-to-printed wiring board SMT interconnections: Modeling, design, fabrication and reliability*. in *Electronic Components and Technology Conference (ECTC), 2012 IEEE 62nd*. 2012. IEEE.

22. Shorey, A., S. Pollard, A. Streltsov, G. Piech, and R. Wagner. *Development of substrates for through glass vias (TGV) for 3DS-IC integration*. in *Electronic Components and Technology Conference (ECTC), 2012 IEEE 62nd*. 2012. IEEE.

23. Suh, I.-K., H. Ohta, and Y. Waseda, *High-temperature thermal expansion of six metallic elements measured by dilatation method and X-ray diffraction.* Journal of Materials Science, 1988. **23**(2): p. 757-760.

24. Sung, P. and D.R. Poirier, *Estimation of densities and coefficients of thermal expansion of solid Ni-base superalloys.* Materials Science and Engineering: A, 1998. **245**(1): p. 135-141.

25. King, H., *Quantitative size-factors for metallic solid solutions.* Journal of Materials Science, 1966. **1**(1): p. 79-90.

26. Slater, J.C., *Atomic radii in crystals.* The Journal of Chemical Physics, 1964. **41**(10): p. 3199-3204.

27. Cai, W. and W.D. Nix, *Imperfections in crystalline solids*. 2016, Cambridge University Press. p. 82, 493.

28. Dosovitskiy, G., S. Samoilenkov, A. Kaul, and D. Rodionov, *Thermal expansion of Ni–W, Ni–Cr, and Ni–Cr–W alloys between room temperature and 800 C.* International Journal of Thermophysics, 2009. **30**(6): p. 1931-1937.

29. Kurz, S., C. Ensslen, U. Welzel, A. Leineweber, and E. Mittemeijer, *The thermal stability of Ni–Mo and Ni–W thin films: Solute segregation and planar faults.* Scripta Materialia, 2013. **69**(1): p. 65-68.

CHAPTER 3: MICROSTRUCTURAL EFFECTS ON THE THERMAL AND MECHANICAL BEHAVIOR OF Ni-Mo-W ALLOYS

3.1 Introduction

The most universal mechanical testing technique is the tensile test, where a specimen with known dimensions is loaded in uniaxial tension while monitoring the associated elongation (or vice versa). A wide variety of mechanical properties can easily be measured from a single test, such as Young's modulus, yield strength, ultimate tensile strength and elongation to failure. However, as materials approach the micrometer or nanometer length scales, their properties have been shown to deviate from those measured at the bulk size scale [1-3]. The grain structure as well as internal defects, voids and porosity [4] can dominate the mechanical response. This is especially important at the small length scales associated with thin films.

The underlying microstructure associated with the physical vapor deposition (PVD) of thin films has been shown to depend heavily on the material and the conditions in which they were deposited [4-7]. A number of nanocrystalline metals have shown higher hardness and strength [8, 9], but lower ductility and microstructural instability [10-17] compared to their more coarse-grained counterparts. In contrast, nanotwinned Cu has shown strength enhancements similar to those for nanocrystalline materials while also maintaining a more beneficial balance of properties. The seminal paper by Lu et al. highlighting the ultrahigh strength and high electrical conductivity of nanotwinned Cu [18] has created a wave of research to understand the thermal and mechanical stability of nanotwinned metals, as outlined in section 1.4.

In a quest to find materials suitable for high temperature microelectromechanical systems (MEMS), Sim et al. showed remarkable tensile strength for nanotwinned $Ni_{83.6}Mo_{14}W_{2.4}$, exceeding 3 GPa, with a balance of properties and microstructural stability [19, 20]. The presence of the nanotwins was fortuitous and provided the attendant properties. However, MEMS devices will require a larger design space than one specific alloy, necessitating the development of an expansive set of materials.

This chapter presents a compositional spread of single-phased $Ni_{85}Mo_xW_{15-x}$ alloys to investigate their mechanical properties as a function of chemistry and underlying microstructure. Uniaxial tension specimens, representing a range of compositions, were evaluated in the as-deposited state and after a 1 hour heat treatment at 400°C. Ultrahigh tensile strengths (2-3 GPa) were observed for both sets of specimens. As-sputtered microstructures were investigated using focused ion beam (FIB) channeling contrast techniques and the crystallographic texture was quantified using X-ray diffraction (XRD) before and after the thermal exposure at 400°C. Modest variations in mechanical properties were found to depend on alloy microstructure rather than alloy chemistry. This study suggests that careful control and design of the underlying microstructure can be used to tailor the strength of Ni-Mo-W alloys. The wide compositional spread of mechanically robust and thermally stable Ni-Mo-W films greatly expands the breadth of structural materials available for MEMS applications at elevated temperatures.

3.2 Experimental methods

3.2.1 Specimen fabrication and characterization

Ni-Mo-W thin films were fabricated using a custom magnetron sputter deposition chamber to achieve dense films at high deposition rates. Thin films were deposited using

direct current (dc) power of 2500 W and 1.0 mTorr high purity argon sputtering gas in a custom-built chamber in Timothy Weihs' laboratory at JHU. A compositional spread of $Ni_{85}Mo_xW_{15-x}$ alloys, with x ranging from 2-13 atomic percent, were grown on brass substrates using a custom alloy target, as described in section 2.2.2. Figure 3.1 shows the sputtering chamber schematic from an overhead view. The combinatorial $Ni_{85}Mo_{15}$ and $Ni_{85}W_{15}$ target is mounted on the inside wall of the chamber and the substrates are fixed to the central rotatable carousel. The desired compositional gradient across the substrate was achieved though stationary deposition. Post deposition films were peeled from the substrate and sectioned vertically for further analysis.

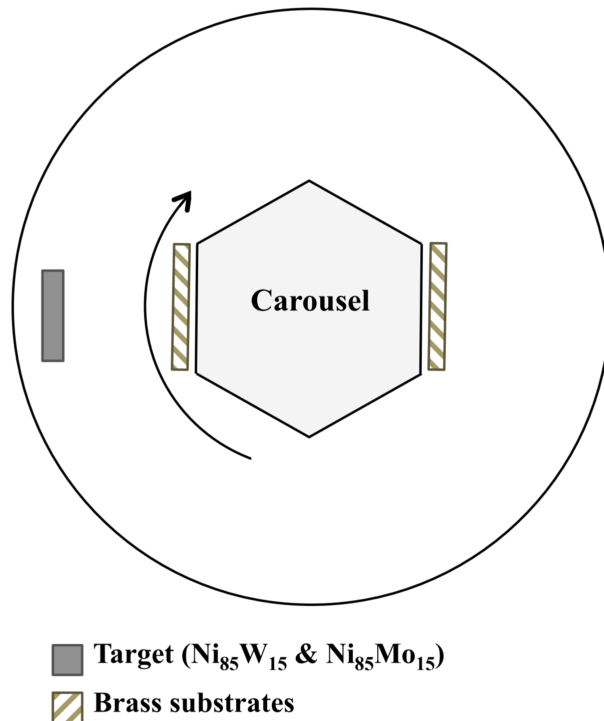

Figure 3.1: A schematic of the sputtering chamber (top-down view) with Ni-Mo-W target mounted on the outside wall and brass substrates mounted on the rotatable carousel.

The chemical composition was identified using wavelength dispersive spectroscopy (WDS) in a JEOL 8600 Superprobe instrument, calibrated with standard crystals of Ni, Mo and W, as outlined in section 2.2.2.1. All values are reported in atomic percent (Figure 3.2) and the films are enumerated 1-8, representing the most W-rich to the most Mo-rich alloys.

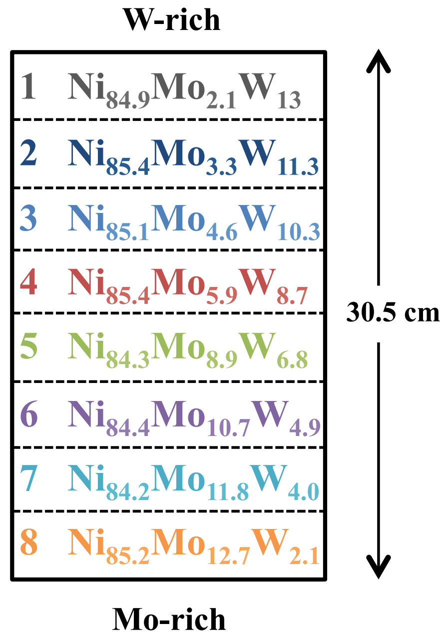

Figure 3.2: A representation of the sputtered films, sectioned and labeled 1-8 with their chemical composition (atomic percent) for identification.

Ion beam channeling contrast images [21] were investigated to determine the cross-sectional grain morphology in a FEI Strata DB235 Dual-Beam scanning electron microscope (SEM) and focused ion beam (FIB). The phase and crystallographic texture were obtained through the use of XRD (Figure 3.3) using Bragg's law ($\lambda = 2d\sin\theta$), where λ is the X-ray wavelength generated from a Cu K-α source (1.5406 Å), d is the interplanar spacing of the crystal and 2θ is the scattering angle [22].

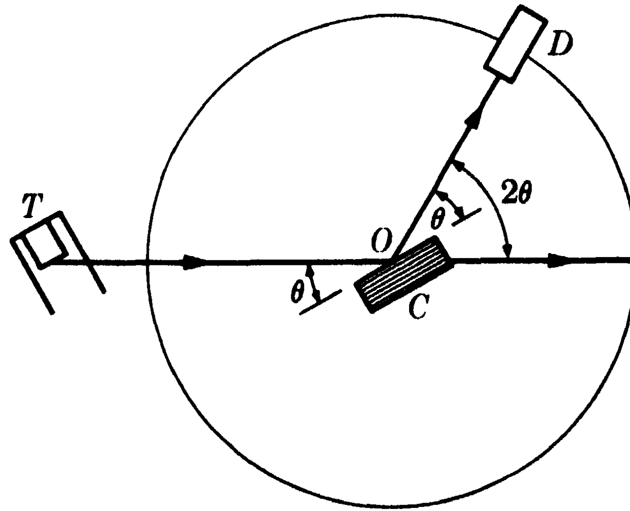

Figure 3.3: Principle of symmetric X-ray diffraction (XRD), where the incident angle and the diffracted angle are the same throughout the scan [22].

Transmission electron microscopy (TEM) specimens were prepared using conventional FIB lift-out techniques and the microstructure was characterized using selected area electron diffraction (SAED) patterns and bright field imagining in a Thermo Scientific TF30 TEM. The phase and crystallographic texture were obtained through XRD and confirmed with electron backscattered diffraction (EBSD) in a Tescan Mira field emission SEM. One-hour vacuum heat treatments at 400°C were carried out inside a custom-built vacuum tube furnace evacuated to 10^{-6} Torr, shown in Figure 3.4. The Ni-Mo-W films were sandwiched between two 0.635 mm thick alumina plates, with dimensions 114 mm x 35 mm, to prevent the films from curling during the heating cycle.

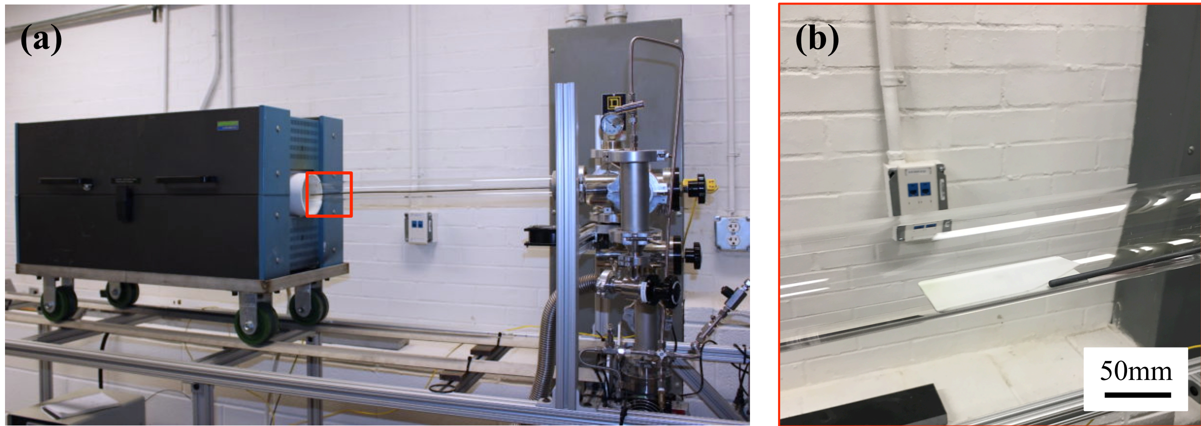

Figure 3.4: (a) Vacuum tube furnace used for heat treatments and (b) magnified image of the Ni-Mo-W films sandwiched between alumina plates inside the evacuated tube.

3.2.1.1 EBSD sample preparation

EBSD is a surface-sensitive technique that uses Kikuchi diffraction patterns generated by coherent backscattered electrons to determine the orientation of crystalline materials. The specimen surface quality is paramount to obtaining suitable diffraction signals for post-processing. Analysis of the Kikuchi patterns is typically performed using commercial software, where the user identifies the crystallographic phase(s) in the material and Hough transforms are used to index the experimental pattern with a bank of idealized crystal orientations [23]. All EBSD characterization was performed using the OIM Analysis™ (EDAX-TSL) software. Preparing the Ni-Mo-W freestanding films for EBSD began with sandwiching the films between two Ni bars using Quick-Cure™ 5-minute epoxy (Bob Smith Industries Inc.) mixed with graphite powder for electrical conductivity. After the epoxy cured, the cross-sectional films were mechanically polished to a mirror-like surface finish. First, the surface was made flat by grinding with 200 grit silicon carbide paper. The remaining polishing recipe was carried out with 150 rotations per minute for 45 minutes at each step: 400, 600, 800 and 1200 grit. Immediately before performing EBSD, final

polishing with 5 nm colloidal silica was performed for 30 minutes and the specimens were rinsed with tap water and ethanol.

3.2.2 Mechanical testing

A representative subset of Ni-Mo-W alloys was extracted from the range of chemical compositions that span from W-rich to Mo-rich, as illustrated in Figure 3.2. Tensile specimens were designed for room temperature testing in a custom built microsample frame [24] with a 25 pound (111 N) load cell, linear actuator and air bearing. A high-resolution camera was used to capture images every 1 s for digital image correlation (DIC) post-processing [25], as outlined in section 2.2.1. The specimen was illuminated with a ring light attached to the lens (Edmund Optics R-200 rear assembly and OBJ-9 front objective) with a 5.25 mm x 3.86 mm field of view. The full mechanical and optical setup is shown in Figure 3.5. Tensile geometries were machined using wire electrical discharge machining (EDM) to achieve gage widths and lengths of 460 μm and 1.6 mm, respectively. During machining Ni-Mo-W films were secured between two Ni plates with silver paint adhesive to insure conductivity and good surface finish. The tensile geometry was modified to have an elongated grip section that could be clamped between flat plats during loading (Figure 3.6). Specimen gage sections were speckled with 10 μm silica powders suspected in acetone and loaded at a nominal strain rate of 10^{-5} s^{-1}. In total, 24 room temperature tensile tests were conducted on Ni-Mo-W films in either the as-deposited state or heat treated conditions.

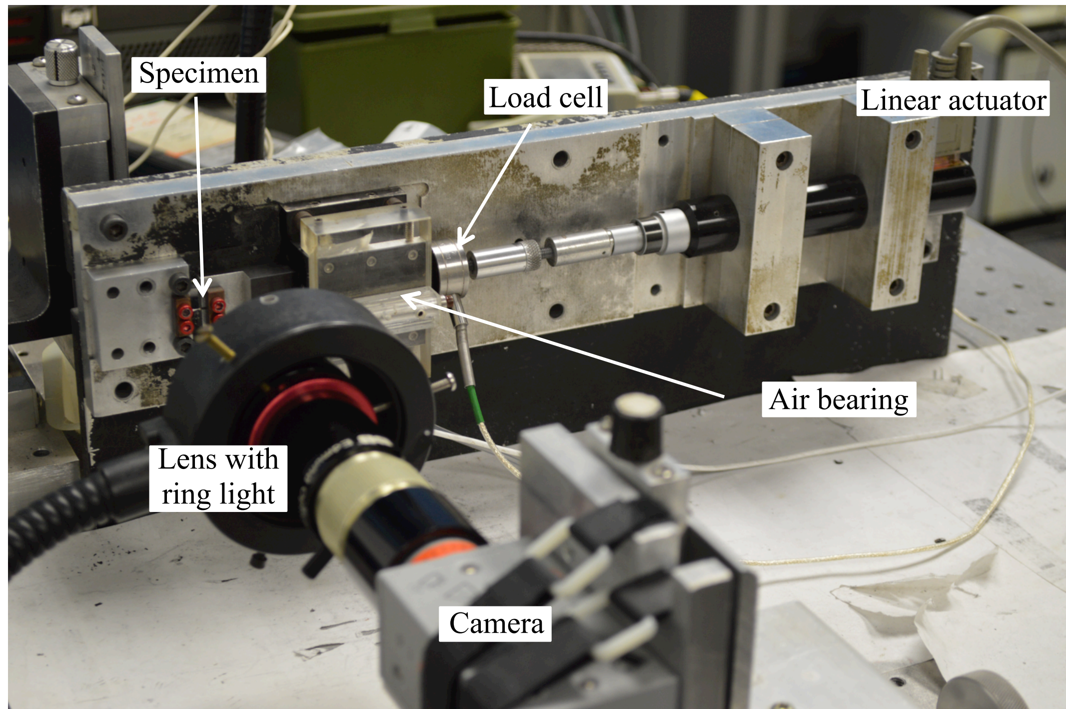

Figure 3.5: Microtensile load frame, adapted from [24].

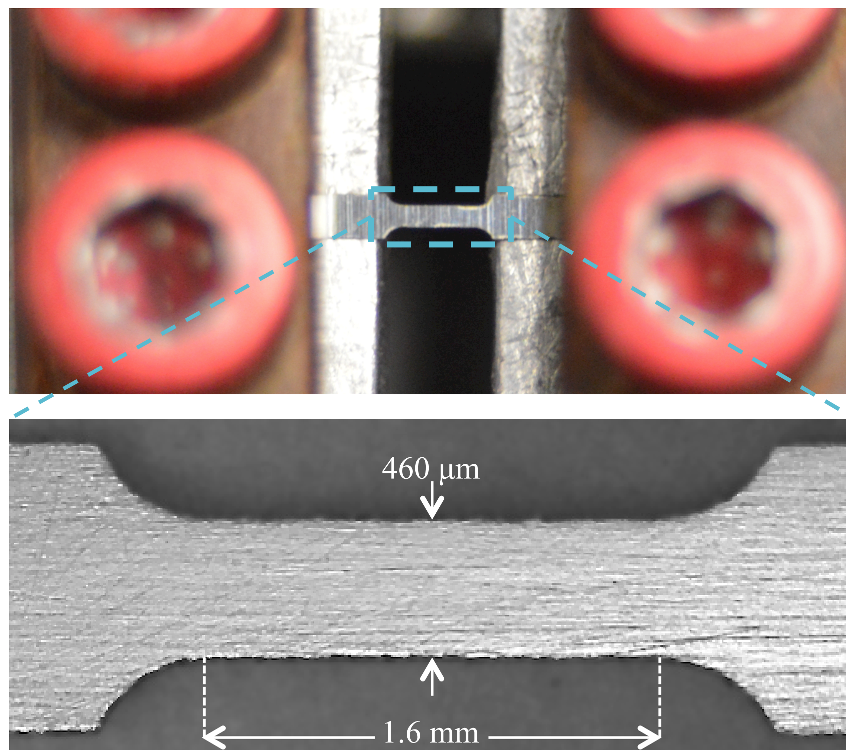

Figure 3.6: Microtensile specimen clamped between two flat plates during mechanical testing.

3.3 Microstructural morphology

3.3.1 Cross-sectional microstructure

Cross-sectional FIB channeling contrast images shown in Figure 3.7 are representative of the Ni-Mo-W films that were prepared for mechanical testing. Figures 3.7a-d are the most W-rich alloys and Figures 3.7e-f are the most Mo-rich alloys. The bottom of all films show evidence of equiaxed nanocrystalline grains from initial growth on the brass substrate, which is entirely consistent with observations of room temperature PVD films [4, 26]. The nanocrystalline regions accounted for 31-37% of the overall Ni-Mo-W film thickness, largely due to the high deposition rate and low sputtering temperature. When the substrate temperature is significantly less than the material melt temperature, the adatom mobility is considered low and the incoming deposition atoms are essentially frozen where they land. Upon thickening the heat generated by the deposition process increases the substrate temperature and surface diffusion, which leads to the columnar grain structure [26]. The bulk of the films display long columnar grains oriented towards the vertical growth direction, but they are not always perpendicular to the film. For example, alloy 6 ($Ni_{84.4}Mo_{10.7}W_{4.9}$) in Figure 3.7e has columnar grains that are tilted 11° with respect to the normal, while alloy 4 ($Ni_{85.4}Mo_{5.9}W_{8.7}$) in Figure 3.7d seems well aligned and perpendicular to the film. Other films, such as alloy 2 ($Ni_{85.4}Mo_{3.3}W_{11.3}$), show discrete interfaces through the thickness (Figure 3.7b). The observed interfaces are attributed to an out-of-plane tilt of the columnar grains that is not observable in this cross-sectional view. The projected dimensions of the columnar grains in Figure 3.7b have an aspect ratio about 4:1, which can be used to approximate the out-of-plane viewing tilt to 15° or more. A summary of the film thickness and columnar tilt alignment with respect to the films perpendicular is summarized in Table

3.1. The implications of the columnar tilt on the mechanical properties will be discussed in section 3.4.

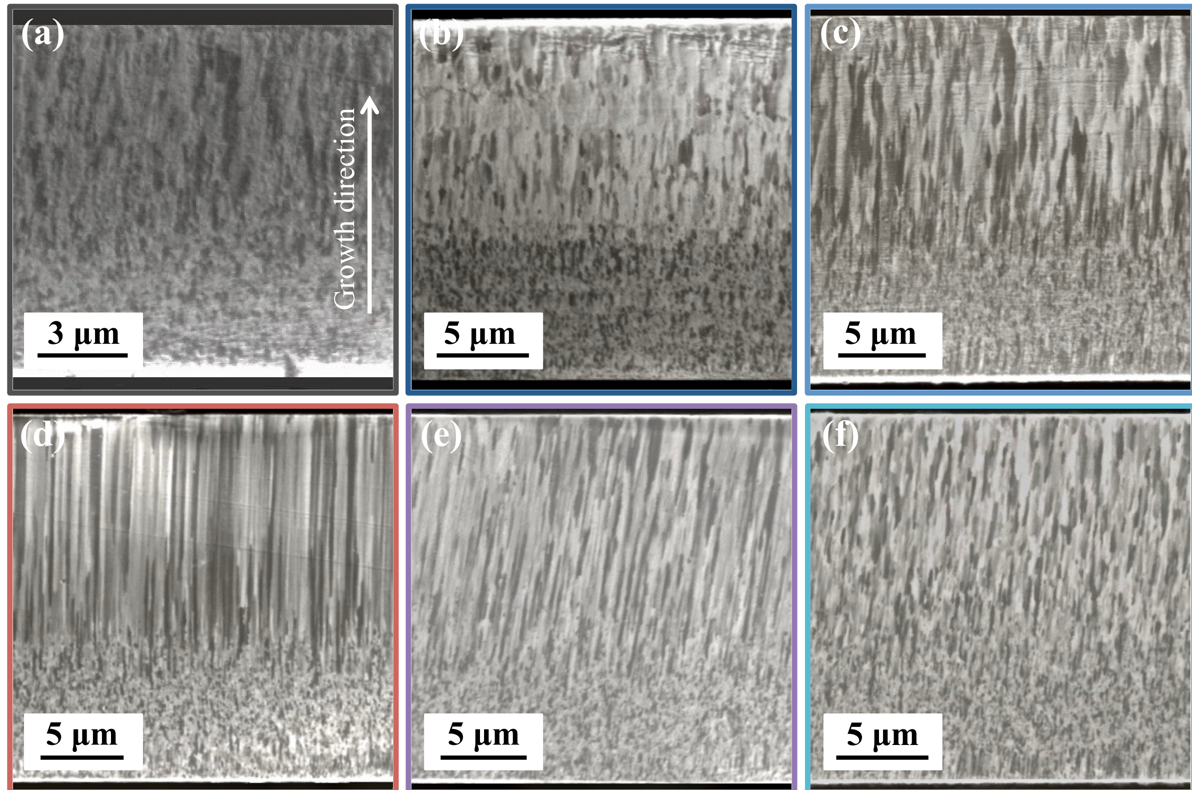

Figure 3.7: Cross-sectional FIB channeling contrast images for a subset of the as-deposited Ni-Mo-W films with increasing Mo-content: (a) alloy 1 ($Ni_{84.9}Mo_{2.1}W_{13}$), (b) alloy 2 ($Ni_{85.4}Mo_{3.3}W_{11.3}$), (c) alloy 3 ($Ni_{85.1}Mo_{4.6}W_{10.3}$), (d) alloy 4 ($Ni_{85.4}Mo_{5.9}W_{8.7}$), (e) alloy 6 ($Ni_{84.4}Mo_{10.7}W_{4.9}$), and (f) alloy 7 ($Ni_{84.2}Mo_{11.8}W_{4.0}$). All cross-sections show a 31-37% nanocrystalline layer at the bottom of the films, with the remainder columnar grains oriented along the growth direction.

Table 3.1: Summary of the subset of Ni-Mo-W alloys tested in uniaxial tension with reported fracture strength and elastic modulus for films as-deposited and heat treated for 1 hour at 400°C. Film thickness, the contribution of the nanocrystalline (nc) region and the columnar tilt angles were measured from FIB channeling contrast images (Figure 3.7).

Alloy number	Composition [at.%]	Film thickness [μm]	Contribution from nc region [% thickness]	Columnar tilt with respect to normal [°]	Elastic modulus [GPa]	As-deposited fracture strength [GPa]	After 400°C fracture strength [GPa]
1	$Ni_{84.9}Mo_{2.1}W_{13}$	10.3 ± 0.3	34.7	7	201 ± 9	2.0 ± 0.5	-----------
2	$Ni_{85.4}Mo_{3.3}W_{11.3}$	19.7 ± 0.1	36.8	>15	180 ± 7	1.9 ± 0.2	1.4 ± 0.1
3	$Ni_{85.1}Mo_{4.6}W_{10.3}$	20.6 ± 0.2	33.3	4	206 ± 4	2.2 ± 0.4	1.6 ± 0.1
4	$Ni_{85.4}Mo_{5.9}W_{8.7}$	23.2 ± 0.3	34.4	0	220 ± 3	2.7 ± 0.2	2.0 ± 0.6
6	$Ni_{84.4}Mo_{10.7}W_{4.9}$	21.4 ± 0.1	31.7	11	199 ± 4	2.6 ± 0.1	2.2 ± 0.1
7	$Ni_{84.2}Mo_{11.8}W_{4.0}$	20.6 ± 0.1	34.5	7	194 ± 4	2.7 ± 0.1	2.3 ± 0.4

Bright field TEM micrographs in Figure 3.8 display the columnar grain structure filled with a high density of perpendicular nanotwins for W-rich alloy 2 ($Ni_{85.4}Mo_{3.3}W_{11.3}$) and Mo-rich alloy 6 ($Ni_{84.4}Mo_{10.7}W_{4.9}$). SAED patterns were indexed on a [011] zone axis and found to have diffraction spots with mirror symmetry parallel to (1-11), indicating a twin plane. Throughout the columnar grains, SAED pattern analysis demonstrated growth nanotwins for both Mo-rich and W-rich compositions, as shown in the inset of Figures 3.8a and 3.8b. Similar nanotwinned micrographs were observed in all films prepared in this study.

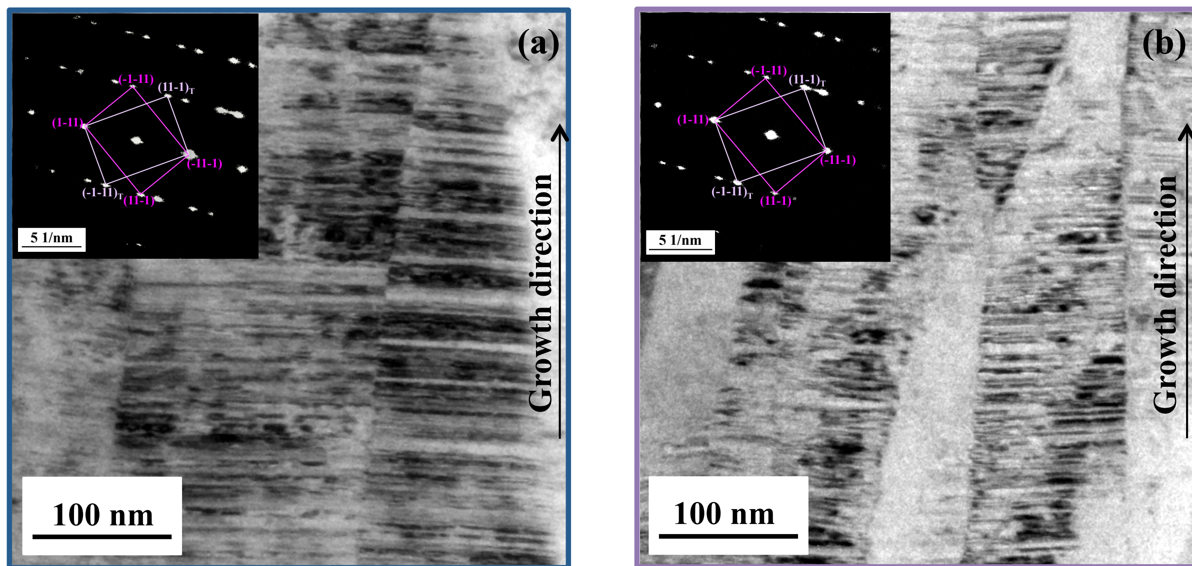

Figure 3.8: Bright-field TEM micrographs of columnar grains filled with nanotwins and an inset of a selected-area electron diffraction pattern indexed for the twin and the matrix. (a) W-rich alloy 2 ($Ni_{85.4}Mo_{3.3}W_{11.3}$) and (b) Mo-rich alloy 6 ($Ni_{84.4}Mo_{10.7}W_{4.9}$).

3.3.2 As-sputtered variations

The variations in microstructure observed across the combinatorial study of Ni-Mo-W alloys can be attributed to artifacts that arose during the sputtering process. Therefore, a re-evaluation of the deposition process is needed. The grain growth direction is intimately related to the density and direction of the plasma generated during sputtering. In magnetron

sputtering, typically the magnetic field creates a circular erosion racetrack in the disk-shaped target and a uniform plasma is generated. The densest part of the plasma is produced perpendicular to the surface of the target and hence, the substrate is typically positioned parallel to the target during deposition. The resulting microstructure grows perpendicular to the film surface. However, the combinatorial $Ni_{85}Mo_{15}$ and $Ni_{85}W_{15}$ rectangular target shown in Figure 2.2b creates an asymmetric Ni-Mo-W plasma due to the elliptical erosion racetrack and sputter yield differences between Mo and W. The most dense and most uniform Ni-Mo-W plasma is generated at the center of the target, where Mo and W contents are relatively equal. In comparison, the top and bottom of the target generates a less dense and less uniform Ni-Mo-W plasma due to the transverse location of Mo and W in the target and the differences in their sputter yields. As a result, the top and bottom of the rectangular substrate (Figure 3.2) are no longer positioned perpendicular to the dense and uniform plasma, but are at some angular tilt. The thin film growth direction would then match the angle of the impinging atoms on the substrate rather than the substrate normal, creating a variation in the growth direction across the length of the substrate. Additionally, the vertical mounting of the substrate and target for the custom sputtering chamber shown in Figure 3.1 involves a rotating carousel, which allows multiple substrates to be loaded at once without having to vent and pump down the chamber between subsequent depositions. However, any misalignments between the target and the substrate from imprecise rotations of the carousel can also cause variations in the microstructure. Similar reports of this phenomenon for PVD techniques have been explored in the literature. The commonly referred “tangent rule” describes the effect of angular alignment between the substrate normal and the vapor flux concentration with respect to grain morphology [27]. The resulting microstructure has an

inclination of columnar grains with respect to the substrate normal. This is often referenced as shadowing, where the geometric constraint influences the microstructure formation [4, 28].

It is clear from the film cross-sections in Figure 3.7 that the columnar grains exhibit a variety of tilt angles as a result of the unique alloy target geometry and small misalignments between the brass substrate and the Ni-Mo-W target during deposition. The transverse location of the sectioned film shown in Figure 3.2 will govern the columnar tilt angle. For example, alloy 4 thin film with well aligned microstructure to the film normal was sectioned from the center portion of the substrate that was aligned with the uniform and dense plasma, whereas alloy 2 thin film with a large out-of-plane tilt was sectioned from the top of the substrate, significantly further and more tilted from the impinging atoms in the dense plasma. Had a symmetric target geometry and its associated plasma been utilized, the microstructural variations in Figure 3.7 would likely not be present.

The effect of the tilted microstructure on crystallographic texture deserves a closer look. Materials with high melting temperatures such as Ni, Mo and W, have low adatom mobility during the sputtering process and surface quenching during deposition allows texture to develop along columnar grains, even when tilted [29]. EBSD analysis of thin film cross-sections determined {111} texture across all Ni-Mo-W compositions, however a subtle but important distinction has been noted. The inverse pole figures (IPFs) indicate that the intensity of {111} texture is not at the same strength for all of the as-deposited films. For example, Figure 3.9 gives the IPF's for three films of alloys 2, 4 and 6.

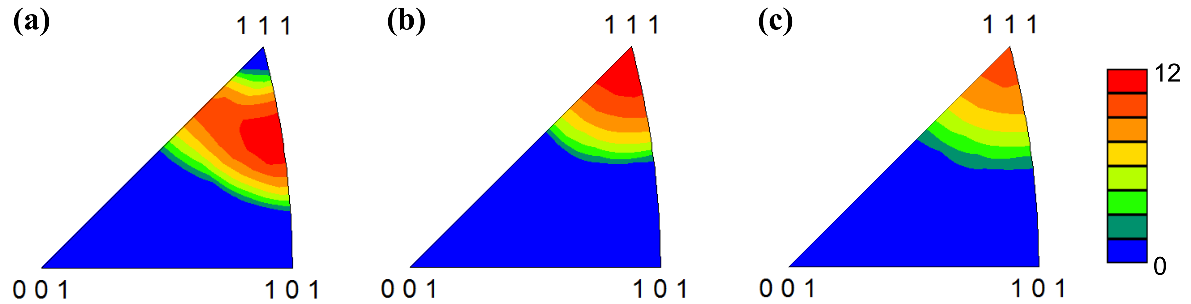

Figure 3.9: IPF plotted for the direction perpendicular to the as-deposited films. (a) Alloy 2 ($Ni_{85.4}Mo_{3.3}W_{11.3}$) with a ~15° columnar tilt with respect to the surface normal, (b) alloy 4 ($Ni_{85.4}Mo_{5.9}W_{8.7}$) with nominally aligned grains with the surface normal and (c) alloy 6 ($Ni_{84.4}Mo_{10.7}W_{4.9}$) with 11° columnar tilt with respect to the surface normal.

The IPF for alloy 4 ($Ni_{85.4}Mo_{5.9}W_{8.7}$) shown in Figure 3.9b shows the strongest {111} texture, which matches the observations that its columnar grains are closely aligned perpendicular to the film surface (Figure 3.7d). The IPF for alloy 6 ($Ni_{84.4}Mo_{10.7}W_{4.9}$) shown in Figure 3.9c has slightly weaker {111} texture, which is consistent with the 11° measured rotation of the columnar grains relative to the surface normal (Figure 3.7e). Most notably, the IPF for alloy 2 ($Ni_{85.4}Mo_{3.3}W_{11.3}$) shown in Figure 3.9a displays the weakest {111} texture and this specimen was found to have its columnar grains oriented ~15° out-of-plane tilt (Figure 3.7b). These microstructural variations do not appear to have any fundamental correlation with alloy composition and are instead taken to be a direct result of the combinatorial alloy target geometry and its plasma disparities during sputtering. These variations in texture and columnar alignments can be expected to affect the mechanical behavior of the thin films and is explored further in section 3.4

3.3.3 XRD texture analysis

3.3.3.1 Lattice constant

XRD data from the both sides of the planar freestanding as-deposited Ni-Mo-W films are compared with standard polycrystalline Ni diffraction peak positions in Figure 3.10. The pronounced (111) and (222) diffraction peaks are consistent with the crystallographic texture associated with high quench rates and energies during sputter deposition [4]. The {111} peaks agree with single-phase face-centered cubic (fcc) Ni, but very few other peaks were observed. The Bragg angle associated with the full width at half maximum value was used to calculate the lattice constant across each of the alloys. Minimal changes in the lattice constant were measured across the eight alloys, with an averaged value of 3.61±0.01 Å. The larger atomic sizes of Mo and W dissolved in the Ni lattice cause a lattice expansion and an associated peak shift with respect to Ni reflections. Since the atomic size of Mo and W are similar, there is little variation in the lattice parameter with respect to composition. Given the larger atomic size of Mo and W compared to that of Ni, the solute atoms are substitutional in the Ni lattice, and therefore, the effective volume of Mo and W atoms can be calculated through the formulation proposed by King [30, 31]. Extending this binary alloy formulation to the ternary alloy regime, the average atomic volume can be written as Equation 3.1; Ω_{Ni} is the atomic volume of pure Ni and χ is the atomic fraction of Ni, Mo and W atoms in the alloy. The effective volume of the solute atoms in the Ni solvent is represented by Ω^*_{Mo} and Ω^*_{W} [30].

$$\Omega(\chi) = \chi_{Ni}\Omega_{\mathrm{Ni}} + \chi_{Mo}\Omega^*_{\mathrm{Mo}} + \chi_{W}\Omega^*_{\mathrm{W}} \quad \mathbf{(3.1)}$$

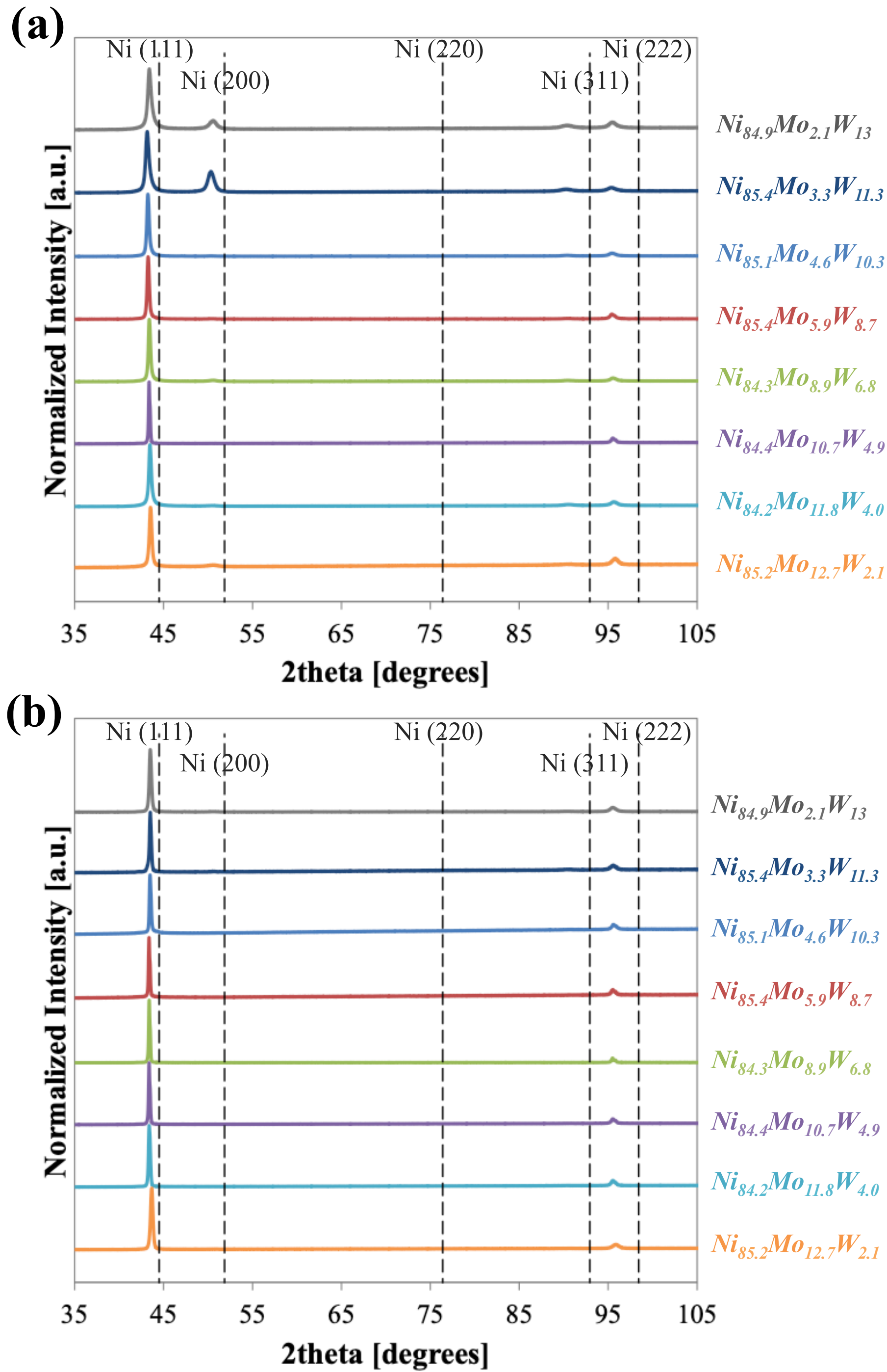

Figure 3.10: XRD peaks for the as-deposited freestanding Ni-Mo-W alloys with (a) the substrate side upwards showing a more balance of diffraction peaks for and (b) the columnar grain side upward with exclusively (111) diffraction peaks across all eight investigated compositions. XRD peaks for polycrystalline Ni (black) are shown for comparison.

The fractional change in volume, or volume size factor, is defined using the effective volume of substitutional atom A in the Ni solute lattice (Equation 3.2), where the measured values of the size factor Ω_{sf} are obtained experimentally from King [31].

$$\Omega_{sf} = \frac{(\Omega_{A}^{*} - \Omega_{Ni})}{\Omega_{Ni}} \quad \textbf{(3.2)}$$

For a Ni solvent, King reported Ω_{sf} of +22.37% and +36.93% for Mo and W solutes, respectively [31]. The average atomic volume for fcc Ni is $\Omega = \frac{a^3}{4}$, combined with Equations 3.1 and 3.2 enables calculations for the average crystal volume for the various Ni-Mo-W alloys reported in Figure 3.2. The predicted lattice constant calculated from the King method is 3.58±0.01 Å across all eight chemical compositions of Ni-Mo-W alloys, showing invariance with composition. This closely matches the experimental value 3.61 Å and literature reported values for solid solution Ni-W alloys [32-34] and Ni-Mo alloys [33, 35]. Even after heat treating for 1 hour at 400°C (Figure 3.11), there was no significant change in lattice parameter.

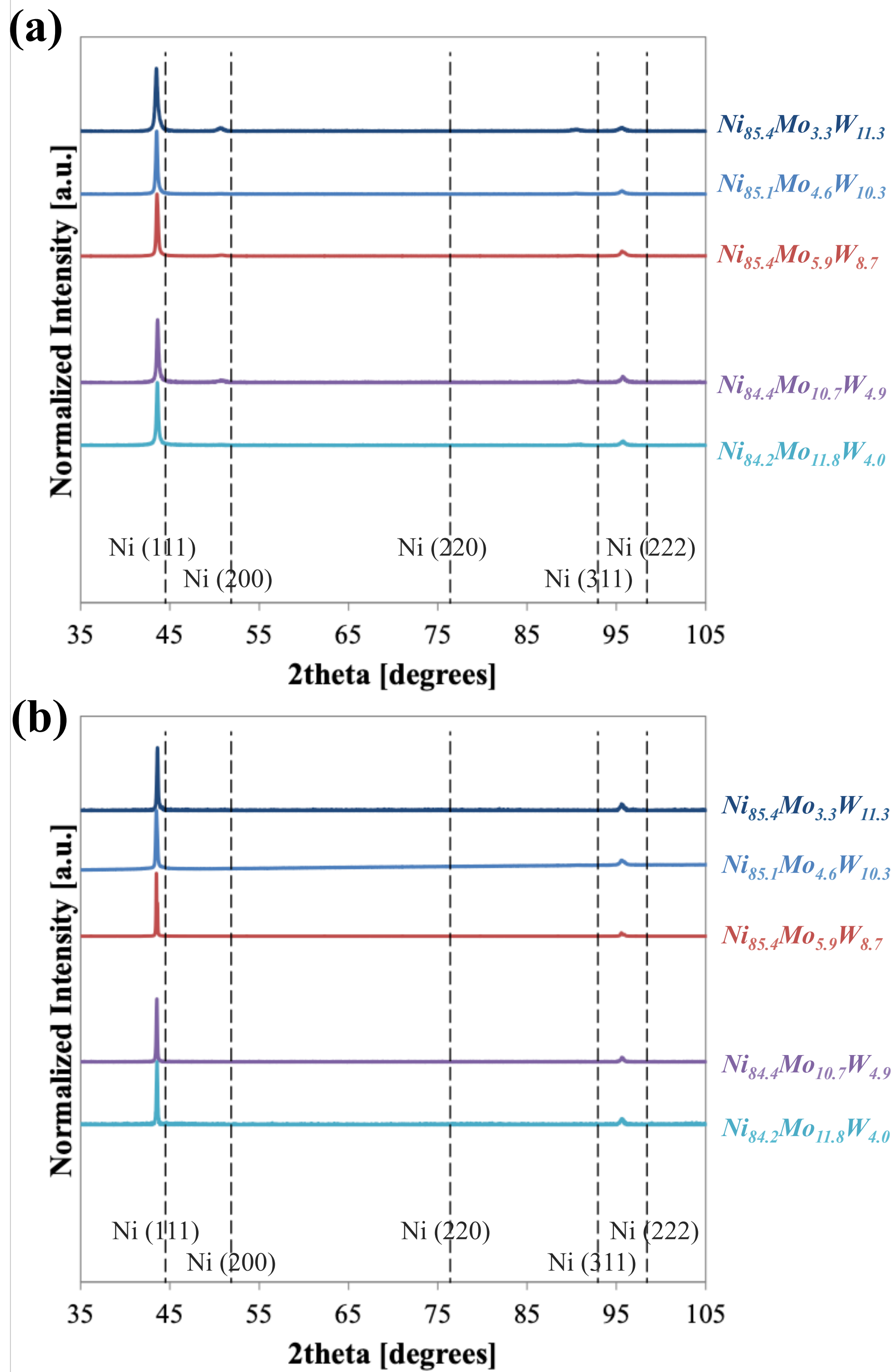

Figure 3.11: XRD peaks from a subset of the freestanding Ni-Mo-W alloys after 1 hour 400°C heat treatment with (a) the substrate side upwards and (b) the columnar grain side upwards. XRD peaks for polycrystalline Ni (black) are shown for comparison.

3.3.3.2 Texture gradient

The effect of the initial nanocrystalline grains is realized from Figure 3.10a, where the diffraction peaks are more evenly distributed than the columnar grain side. W-rich alloys show {200} and {311} crystallographic peaks, indicating that the initial growth stage has more randomized crystallographic texture compared to the columnar grain side of the film (Figure 3.10b) with exclusively {111} peaks. Although the X-ray penetration depth cannot be exactly determined, methods for estimating the depth of penetration were given by Cullity [22] and derived in Appendix 1. For pure Ni and 1.5406 Å Cu K-α X-rays, 50% of the XRD information comes from the first 3-6 μm of the specimen and 95% of the information is gathered from the first 13-25 μm. The distinction between the two sides of the 21 μm thick films is significant, but some overlap can be expected. Quantification of the observable texture gradient is demonstrated by defining the fractional intensity of the {111} peaks from the XRD datasets in Figure 3.10. Equation 3.3 defines the fraction of the {111} peak intensities (I_{111}) as a ratio to the sum of all measured peak intensities.

$$Fractional\ Intensity\ \{111\} = \frac{I_{111}}{(I_{111} + I_{200} + ..)} \quad \textbf{(3.3)}$$

The results are summarized for both sides of the freestanding as-deposited films in Figure 3.12a. As expected, the bottom portion of the Ni-Mo-W films showed modest decrease in the fractional intensity of {111} due to the more randomly oriented nanocrystalline grains. The symmetric XRD geometry illustrated in Figure 3.3 only allows the measurements of crystallographic planes that are parallel to the film surface. For the films with large off-axis <111> tilts, symmetric XRD will naturally reveal more randomized crystallographic peaks

from the planes parallel to the film surface. For the data presented in Figure 3.12a, alloy 2 ($Ni_{85.4}Mo_{3.3}W_{11.3}$) again appeared to be an outlier, showing the largest difference in fractional intensity of {111}. Figure 3.7b displayed this particular film to have the largest nanocrystalline region (37%) through the thickness, which is consistent with the findings from XRD. The combined effect of the ~15° columnar tilt and the more randomly oriented nanocrystalline region is expected to affect the mechanical behavior for this particular film. By comparison, most films showed minimal difference in the fractional intensity of {111} orientation through the thickness.

The XRD profiles for Ni-Mo-W films heat treated for 1 hour at 400°C are shown in Figure 3.11. Interestingly the substrate side of the films that previously showed (200) and (311) peaks for W-rich alloys are no longer are apparent. For ease of comparison, the fractional intensity of the {111} peaks is plotted as a function of solute concentration in Figure 3.12b. For the bottom portion of the films with nanocrystalline grains, the fractional intensity of {111} displayed a modest increase from the as-deposited films. Specifically, alloy 2 ($Ni_{85.4}Mo_{3.3}W_{11.3}$) with the largest contribution of nanocrystalline grains across all of the alloys showed a dramatic 25% increase in {111} texture after the 1 hour heat treatment at 400°C. Multiple studies have reported on the poor thermal stability of nanocrystalline Ni, finding grain growth, recrystallization and reorientation in temperatures as low as 80-300°C [12, 36, 37]. Curiously, the nanocrystalline region in alloy 6 ($Ni_{84.4}Mo_{10.7}W_{4.9}$) displayed a decrease in the fractional intensity of the {111} after heat treatment. The reason behind this behavior is not well understood and might be attributed to measurement error.

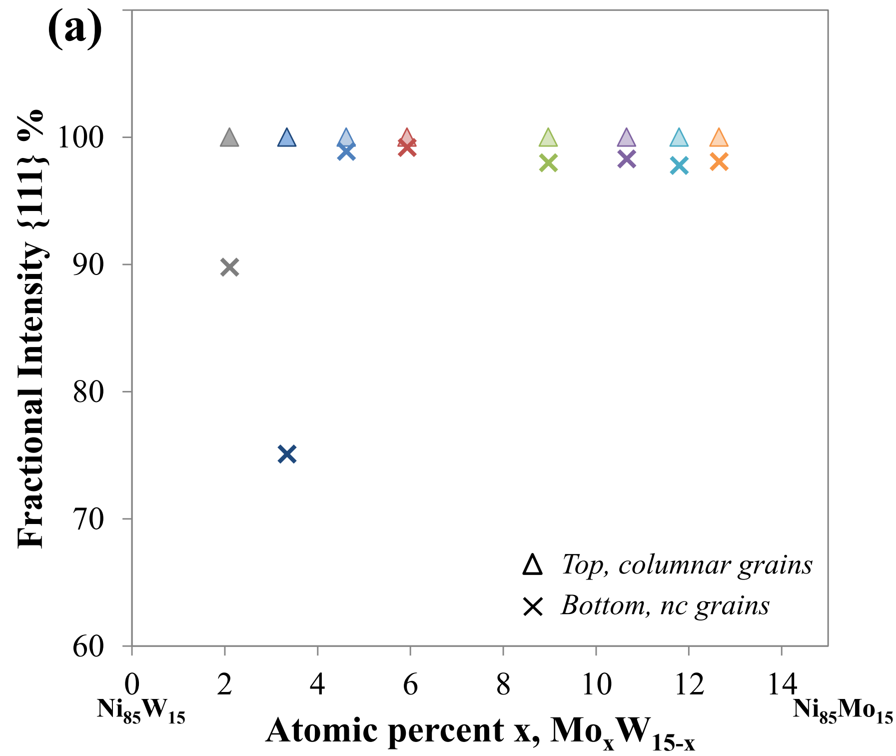

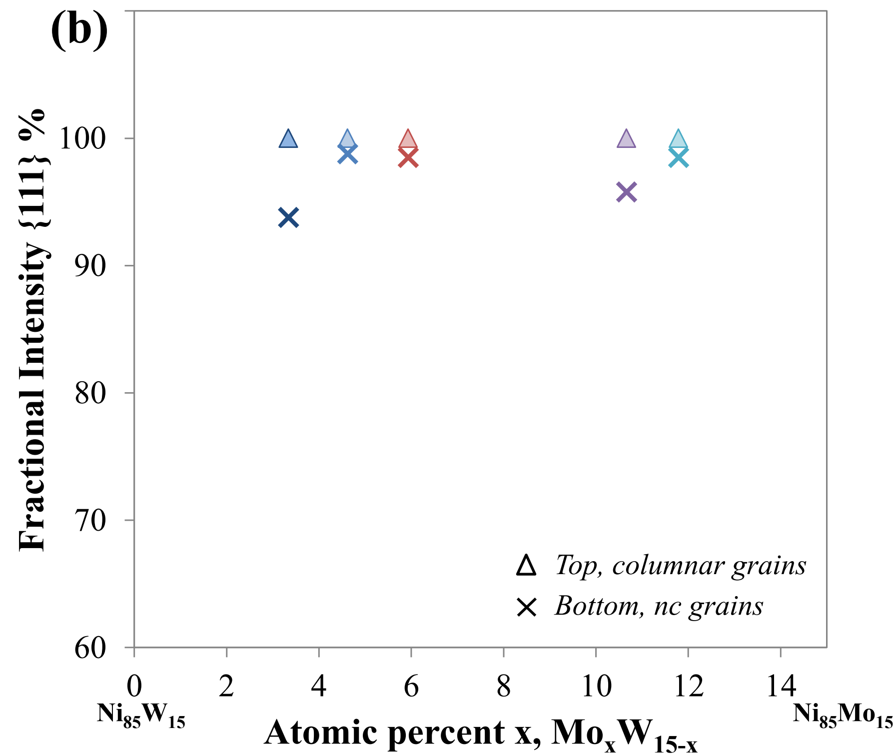

Figure 3.12: Fractional intensity of {111} peaks obtained via XRD for the (a) as-deposited and (b) heat treated at 400°C freestanding Ni-Mo-W films. The bottom portion of the film showed some randomized nanocrystalline (nc) grains while the continued growth and top portion of the film has long columnar grains.

More cross-sectional analysis would be needed to understand the apparent texture change. However, the bulk of the films are governed by the columnar grains, which showed no change in texture with thermal exposure. A recent investigation on $Ni_{83.6}Mo_{14}W_{2.4}$ demonstrated the stability of the nanotwinned columnar microstructure with temperatures as high as 800°C [20]. Thus, engineering Ni-Mo-W alloys without the nanocrystalline region would provide long and continuous columnar grains that are more microstructurally stable through the thickness.

3.4 Mechanical response

3.4.1 Fracture strength

The stress-strain response of a representative set of Ni-Mo-W alloys demonstrates extraordinarily high strengths, as shown in Figure 3.13. The tensile strengths are even higher than what has been reported for nanocrystalline Ni and binary Ni-W [38, 39]. The as-deposited films have a nearly linear-elastic behavior with no macroscopic plasticity, which is a highly desirable behavior for MEMS. For each alloy composition investigated, at least two specimens were tested and showed repeatable behavior. The limited microplasticity at very high stresses may impart some toughness through crack tip blunting.

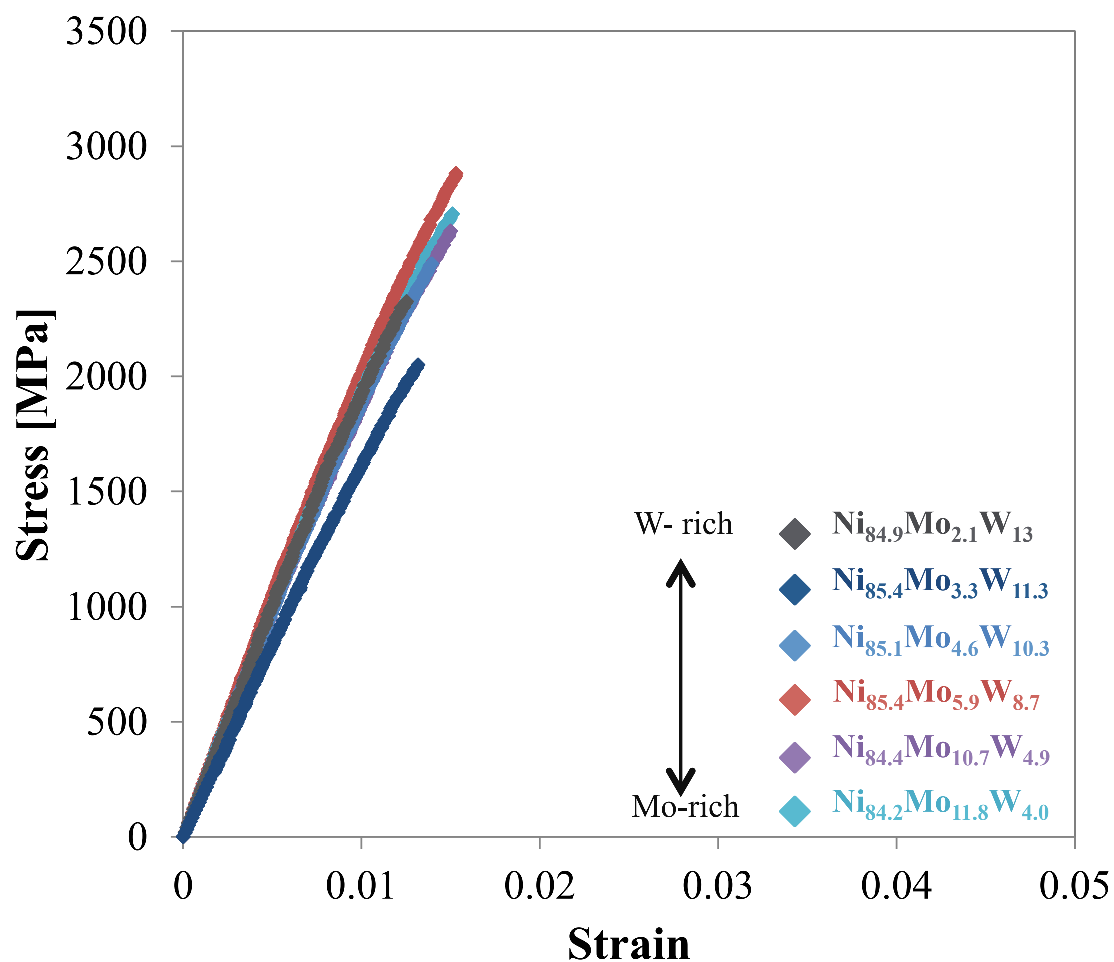

Figure 3.13: Stress-strain response for a representative subset of the as-deposited Ni-Mo-W films showing brittle linear-elastic behavior. Elastic modulus is measured from the slope of each curve and the fracture strength is taken as the maximum value before fracture. For each alloy, two to three specimens were tested.

The cross-sectional failure morphology in Figure 3.14 demonstrates the brittle nature of the columnar grains with cleavage along the grain boundaries, similar to what has been observed for electrodeposited Ni-W alloys [40]. Many sputter deposited Ni alloys show brittle fracture in the as-deposited state, without significant ductility until annealed at temperatures greater than 600°C [19, 20, 39, 41]. However, the bottom portion of the film in Figure 3.14 displays brittle equiaxed grain fracture with some evidence of dimpling, indicating moderate microplasticity in the deformed specimen. This region of the film consists of nanocrystalline grains, where dimpling is commonly associated with grain boundary mediated plasticity mechanisms [42, 43].

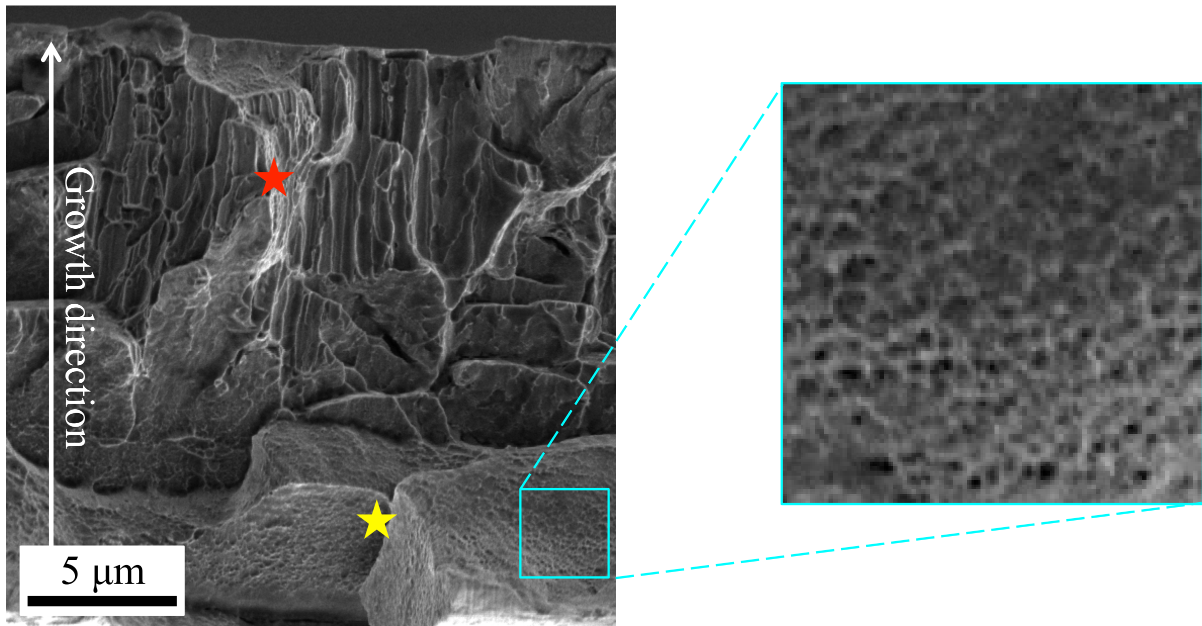

Figure 3.14: Cross-sectional SEM of the fracture surface of as-deposited Ni-Mo-W alloy 4 ($Ni_{85.4}Mo_{5.9}W_{8.7}$) with brittle failure. Cleavage along the columnar grain boundaries is highlighted in red. The nanocrystalline portion (yellow) shows modest evidence of dimpling.

In the absence of significant plasticity, the maximum tensile stress at fracture is reported as the fracture strength for the Ni-Mo-W alloys, summarized in Table 3.1. The W-rich films have a fracture strength ranging 1.9-2.2 GPa with variability as high as 0.5 GPa. By comparison, the Mo-rich films display a higher fracture strength ranging 2.6-2.7 GPa with variability less than 0.2 GPa. Films annealed for 1 hour at 400°C in 10^{-6} Torr vacuum (Figure 3.15) were completely linear-elastic, but the fracture strength decreased compared to the as-deposited films.

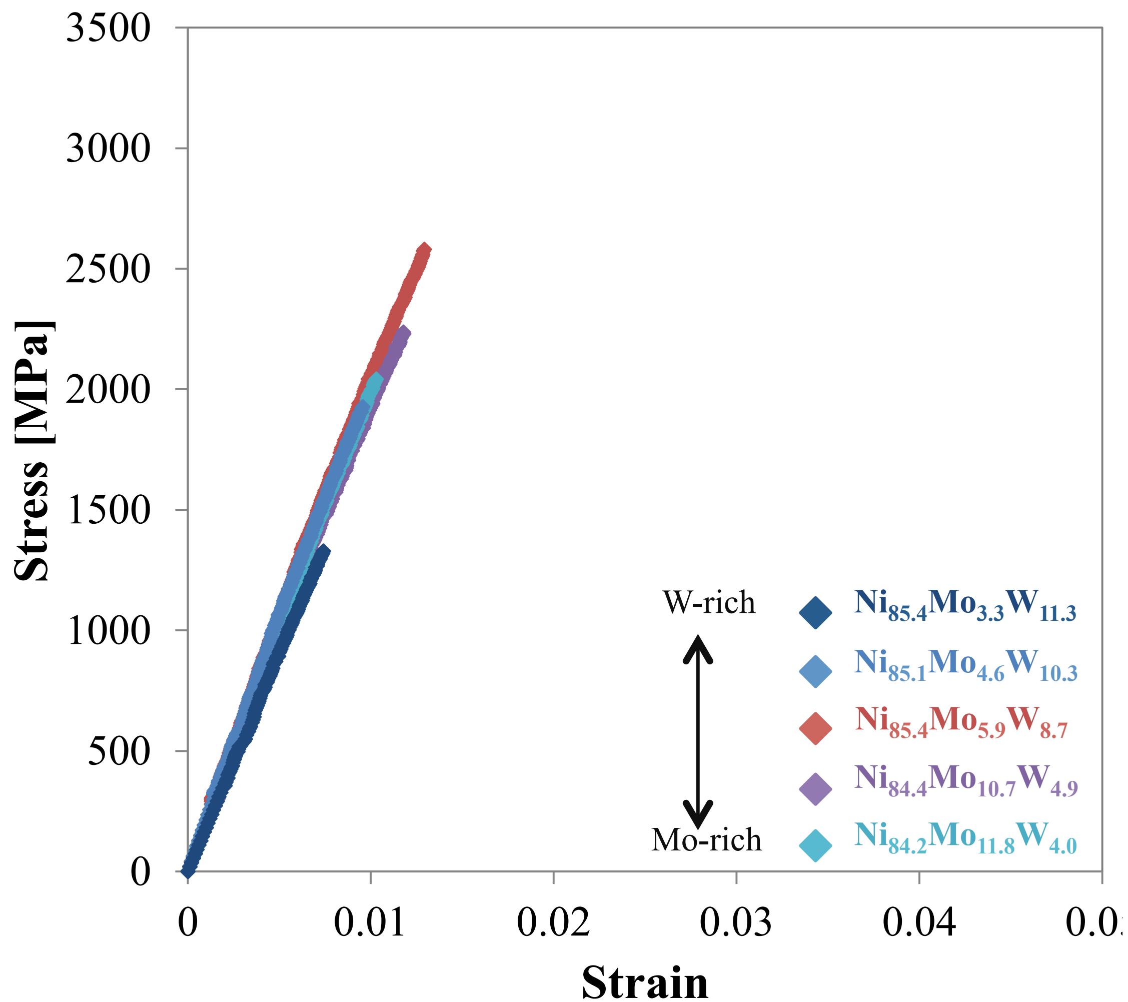

Figure 3.15: Stress-strain response for a representative subset of heat treated films for 1 hour at 400°C in 10^{-6} Torr vacuum showing brittle linear-elastic behavior. Elastic modulus is measured from the slope of each curve and the fracture strength is taken as the maximum value before fracture. For each alloy, two to three specimens were tested.

Specimen fabrication and preparation can contribute to the overall strength of a material at micrometer length scales. Sputtering is inherently a line-of-sight deposition technique, which creates a directional dependence of the film growth and causes non-uniform thicknesses. For example, Ni-Mo-W alloy 1 was sectioned from the top edge of the sputtered film (Figure 3.2) and measured only 10.3 μm in thickness compared to the other 21 μm Ni-Mo-W films investigated.

Wire EDM is widely known to create a recast damage layer onto the cut part. Sidewall roughness can create stress concentrations, causing premature failure. For alloy 1 ($Ni_{84.9}Mo_{2.1}W_{13}$) with 10.3 μm, high variability in the fracture strength was observed with frequent premature failure in the grip section of the tensile specimen due to machining flaws, see for example Figure 3.16. As a result, more variability was observed in these films.

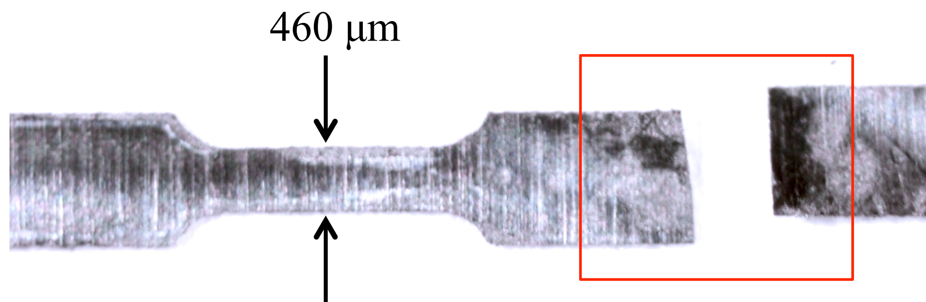

Figure 3.16: Tensile specimen with thickness variation 10.3 ± 0.3 μm failed in the grip section during loading due to sidewall roughness from wire EDM machining.

Improved micro-machining techniques exist to provide pristine surfaces, such as femtosecond laser machining. This machining technique was found to increase the fracture strength of $Ni_{83.6}Mo_{14}W_{2.4}$ from 3.27 GPa to 3.44 GPa (5.2%) with the addition of microplasticity, illustrated by the failure morphology in Figure 3.17 [44]. Employing this

technique for future mechanical characterization could give greater insight into the brittle behavior currently observed and potentially increases the already high strength.

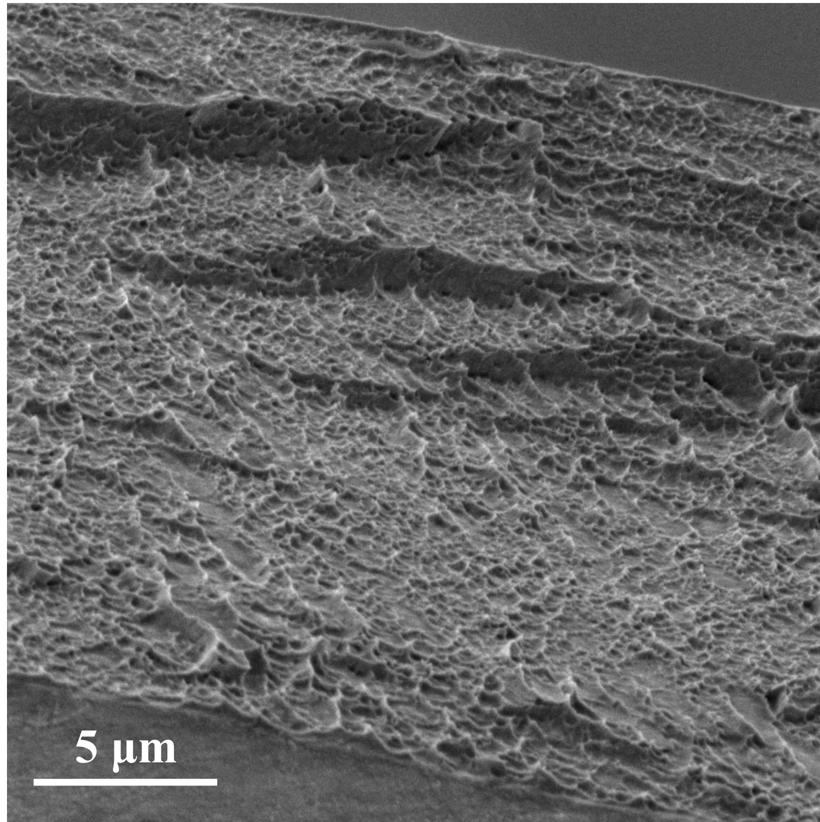

Figure 3.17: Cross-sectional SEM micrograph of the fracture surface exhibiting dimpling, indicating microplasticity, for a laser machined $Ni_{83.6}Mo_{14}W_{2.4}$ tensile specimen.

3.4.2 Elastic modulus

The elastic modulus was determined by measuring the slope of the linear-elastic portion of the tensile stress-strain curve. The value remained unchanged between the films as-deposited and after the 400°C heat treatment, therefore, the measured values were averaged for each film and reported in Table 3.1 The in-plane elastic modulus for <111> Ni is calculated to be 232 GPa from reference values of the stiffness matrix (C_{ij}'s) [45]. In comparison, the Ni-Mo-W films with well-aligned vertical columnar grains from alloy 4

($Ni_{85.4}Mo_{5.9}W_{8.7}$) have a measured elastic modulus of 220 GPa. The slight 5% decrease in expected modulus could emanate from non-uniform thickness in the sputtered films. However, other Ni-Mo-W films with columnar tilt angles 4-11° resulted in a significant reduction of the elastic modulus, with measured values ranging from 194-206 GPa. An even more dramatic reduction in modulus was observed for Ni-Mo-W alloy 2 ($Ni_{85.4}Mo_{3.3}W_{11.3}$), where the large columnar tilt corresponded to the lowest modulus, 180 GPa. The measured elastic moduli have a wide variability from 180-220 GPa that does not scale with the alloy composition. Instead, the tilted microstructure with inclined columnar grains and off-axis <111> orientation facilitates the measured differences in the moduli. Lintymer et al. systematically changed the substrate angle with respect to the vapor flux during sputter deposition to create a variety of microstructural tilt angles, finding that large columnar tilt angles above 20° caused more than 30% decrease in modulus due to the formation of void structures from self-shadowing [46]. This method of void formation has been observed in oblique angle deposition [47], particularly in thicker films [28]. However, for columnar tilts less than 20°, Lintymer et al. reported modulus variations within 12% of the well-aligned columnar value [46]. This is consistent with the spread of Ni-Mo-W columnar tilts 4-11° with an elastic modulus 13% lower than the calculated 232 GPa value. It is likely that the columnar tilt angle of alloy 2 is approaching the critical angular tilt where shadowing dominates the growth process, creating open void boundaries [28]. Thus, the wide distribution of elastic moduli is driven directly by the underlying microstructure, namely the tilted <111> columnar grains.

3.4.3 Nanotwins

Ultrahigh tensile strengths of 1.9-2.7 GPa were observed across the different Ni-Mo-W compositions. Variations in the fracture strength were found to depend on the columnar tilt angle, but the overall strengthening mechanism relies on the nanotwinned microstructure, Figure 3.8. Representative W-rich and Mo-rich films were shown to have a high density of finely spaced growth twins. Similar findings for nanotwinned Cu have demonstrated increases in strength [18, 48, 49] and orientation dependent mechanisms. By changing the loading orientation with respect to the twin boundaries, different dislocation interactions facilitate the mechanical response. You et al. reported that loading 0° and 90° with respect to the twin boundary orientation provided hard deformation modes due to the confinement and blockage of dislocations, whereas loading at 45° activated easy dislocation glide along the twin boundary, which facilitated soft deformation [50]. Sim et al. reported the hard deformation mode when loading parallel to twin boundaries in $Ni_{83.6}Mo_{14}W_{2.4}$, exhibiting nearly 3 GPa of tensile strength [19, 20]. For the Ni-Mo-W films in this study with off-axis columnar tilts, the associated twin boundaries also have a tilt angle with respect to the loading direction. As a result, there is a small resolved shear stress on the tilted twin plane. Using the measured columnar tilts (0-15°) and assuming the associated twin boundaries are at the same tilt, the Schmid factors range from 0-0.25. This crude calculation indicates a low spread in Schmid factor, which would inhibit easy glide as the dominant mechanism. The hard deformation mode, where dislocations are confined between the twin boundaries, is suspected to govern the high tensile strengths.

3.5 MEMS integration

Incorporating Ni-Mo-W alloys into existing MEMS platforms requires the requisite dimensional stability, electrical conductivity and mechanical strength. Ni-Mo-W alloys displayed linear-elastic deformation with exceptionally high tensile strengths due to the presence of nanotwins. Thermal and dimensional stability was demonstrated through control of the coefficient of thermal expansion (CTE) in Chapter 2, finding that Ni-Mo-W alloys have reduced CTE and compatibility with conventional MEMS substrates. Here, specimens heat treated at 400°C were investigated to illustrate the mechanical behavior and microstructural stability of the Ni-Mo-W films. Measured tensile strengths after heat treatments of 400°C showed an overall 24% decrease as compared to the as-sputtered films. A high concentration of quenched vacancies is common with films deposited at high rates. At 400°C it is likely that the vacancies are mobile, while lattice diffusion is not yet thermally active. Figure 3.18 displays a representative film surface after a 1 hour heat treatment at 400°C, illustrating a random distribution of surface voids. This state of unbalanced diffusion can facilitate micro-void formation at the surface or at grain boundaries, attributing to a reduction in the overall mechanical strength, as shown in Figure 3.15. Similar mechanisms were described by Sim et al. for $Ni_{83.6}Mo_{14}W_{2.4}$ heat treated to 600°C, where a much more severe drop in tensile strength was observed, ~78% [20]. The dramatic loss in strength was restored at higher temperatures (800-1000°C) and the stress-strain response displayed up to 10% ductility, where lattice diffusion is active to promote recrystallization and grain growth, mitigating void formation [20]. Thus, this study suggests that 400°C marks the beginning of this small thermal window for which unstable diffusion occurs in the bulk film over the short heating time. Identifying the onset of this thermal window provides a complete picture of the

upper and lower bounds for the unbalanced diffusion in Ni-Mo-W, where the mechanical behavior can be tailored from ultrahigh strength with linear-elasticity to moderate strength with enhanced plasticity [20]. This design consideration is pivotal for engineering MEMS devices with the intended suite of properties.

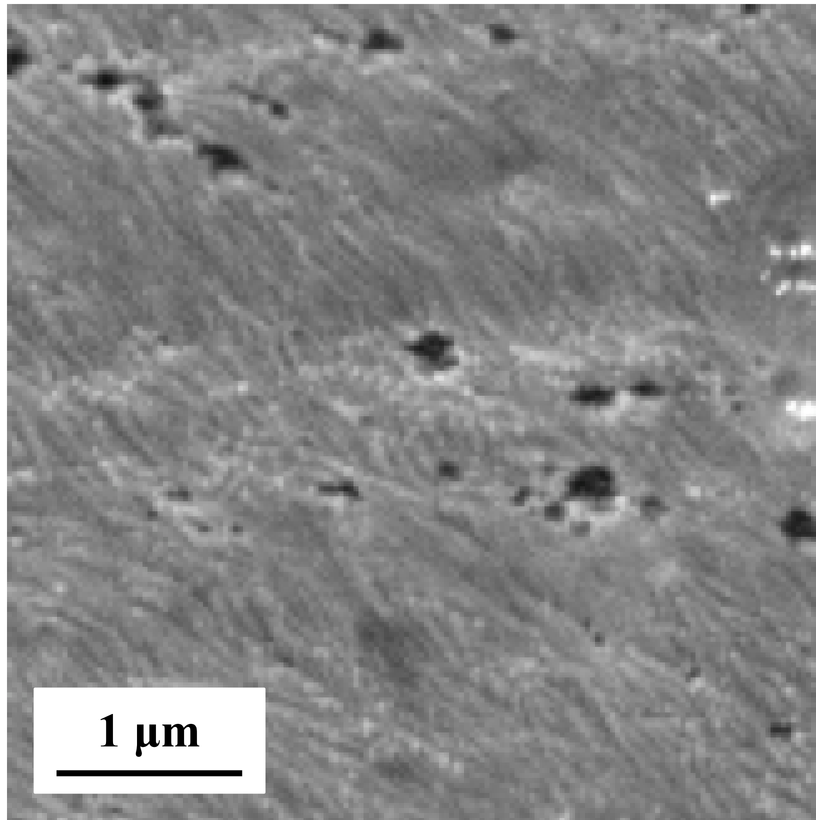

Figure 3.18: Micrograph of the in-plane surface morphology of alloy 7 ($Ni_{84.2}Mo_{11.8}W_{4.0}$) displaying a random distribution of voids after heat treatment for 1 hour at 400°C.

3.6 Chapter summary

A combinatorial study of $Ni_{85}Mo_xW_{5-x}$ alloys, where x ranges 2-13 atomic percent, elucidated extraordinary strength and a balance of physical properties with promise to broaden the available materials for high temperature MEMS applications. Characterization revealed a slightly tilted <111> columnar structure as an artifact of the sputtering process. The stress-strain response displayed an attractive linear-elastic behavior for MEMS, while maintaining high tensile strengths of 2-3 GPa owing to a high density of nanotwins. Variations in the fracture strength and the elastic moduli were driven by the microstructure morphology rather than alloy chemistry. The wide compositional stability and mechanical integrity at temperatures up to 400°C exemplifies the potential of Ni-Mo-W alloys for metal MEMS applications.

3.7 References for Chapter 3

1. Hemker, K.J., *Understanding how nanocrystalline metals deform.* Science, 2004. **304**(5668): p. 221-223.

2. Sanders, P., J. Eastman, and J. Weertman, *Elastic and tensile behavior of nanocrystalline copper and palladium.* Acta materialia, 1997. **45**(10): p. 4019-4025.

3. Sharpe, W.N., B. Yuan, R. Vaidyanathan, and R.L. Edwards. *Measurements of Young's modulus, Poisson's ratio, and tensile strength of polysilicon*. in *Proceedings IEEE the tenth annual international workshop on micro electro mechanical systems. An investigation of micro structures, sensors, actuators, machines and robots*. 1997. IEEE.

4. Ohring, M., *Materials science of thin films*. 2001, Elsevier.

5. Thornton, J.A., *Influence of apparatus geometry and deposition conditions on the structure and topography of thick sputtered coatings.* Journal of Vacuum Science and Technology, 1974. **11**(4): p. 666-670.

6. Thornton, J.A., *Influence of substrate temperature and deposition rate on structure of thick sputtered Cu coatings.* Journal of Vacuum Science and Technology, 1975. **12**(4): p. 830-835.

7. Thornton, J.A. and D. Hoffman, *Stress-related effects in thin films.* Thin solid films, 1989. **171**(1): p. 5-31.

8. Legros, M., B. Elliott, M. Rittner, J. Weertman, and K. Hemker, *Microsample tensile testing of nanocrystalline metals.* Philosophical magazine A, 2000. **80**(4): p. 1017-1026.

9. Wang, Y., M. Chen, F. Zhou, and E. Ma, *High tensile ductility in a nanostructured metal.* Nature, 2002. **419**(6910): p. 912-915.

10. Gianola, D. and W. Sharpe, *Techniques for testing thin films in tension.* Experimental techniques, 2004. **28**(5): p. 23-27.

11. Jin, M., A. Minor, E. Stach, and J. Morris, *Direct observation of deformation-induced grain growth during the nanoindentation of ultrafine-grained Al at room temperature.* Acta Materialia, 2004. **52**(18): p. 5381-5387.

12. Klement, U., U. Erb, A. El-Sherik, and K. Aust, *Thermal stability of nanocrystalline Ni.* Materials Science and Engineering: A, 1995. **203**(1-2): p. 177-186.

13. Legros, M., D.S. Gianola, and K.J. Hemker, *In situ TEM observations of fast grain-boundary motion in stressed nanocrystalline aluminum films.* Acta Materialia, 2008. **56**(14): p. 3380-3393.

14. Lu, L., N. Tao, L. Wang, B. Ding, and K. Lu, *Grain growth and strain release in nanocrystalline copper.* Journal of Applied Physics, 2001. **89**(11): p. 6408-6414.

15. Rupert, T., D. Gianola, Y. Gan, and K. Hemker, *Experimental observations of stress-driven grain boundary migration.* Science, 2009. **326**(5960): p. 1686-1690.

16. Sharon, J.A., H.A. Padilla, and B.L. Boyce, *Interpreting the ductility of nanocrystalline metals.* Journal of Materials Research, 2013. **28**(12): p. 1539-1552.

17. Zhang, K., J. Weertman, and J. Eastman, *Rapid stress-driven grain coarsening in nanocrystalline Cu at ambient and cryogenic temperatures.* Applied Physics Letters, 2005. **87**(6): p. 061921.

18. Lu, L., Y. Shen, X. Chen, L. Qian, and K. Lu, *Ultrahigh strength and high electrical conductivity in copper.* Science, 2004. **304**(5669): p. 422-426.

19. Sim, G.-D., J.A. Krogstad, K.M. Reddy, K.Y. Xie, G.M. Valentino, T.P. Weihs, and K.J. Hemker, *Nanotwinned metal MEMS films with unprecedented strength and stability.* Science Advances, 2017. **3**(6): p. e1700685.

20. Sim, G.-D., J.A. Krogstad, K.Y. Xie, S. Dasgupta, G.M. Valentino, T.P. Weihs, and K.J. Hemker, *Tailoring the mechanical properties of sputter deposited nanotwinned nickel-molybdenum-tungsten films.* Acta Materialia, 2018. **144**: p. 216-225.

21. Canovic, S., T. Jonsson, and M. Halvarsson. *Grain contrast imaging in FIB and SEM*. in *Journal of Physics: Conference Series*. 2008. IOP Publishing.

22. Cullity, B.D., *Elements of X-ray diffraction*. 1956, Addison-Wesley Pub. Co.: Reading, Mass. p. 269-272.

23. Randle, V. and O. Engler, *Introduction to texture analysis: macrotexture, microtexture and orientation mapping*. 2014: CRC press.

24. Zupan, M., M.J. Hayden, C. Boehlert, and K. Hemker, *Development of high-temperature microsample testing.* Experimental Mechanics, 2001. **41**(3): p. 242-247.

25. Eberl, C., D.S. Gianola, R. Thompson, and K.J. Hemker, *Digital Image Correlation and Tracking*. 2010, MathWorks: MATLABCentral.

26. Grovenor, C., H. Hentzell, and D. Smith, *The development of grain structure during growth of metallic films.* Acta Metallurgica, 1984. **32**(5): p. 773-781.

27. Nieuwenhuizen, J. and H. Haanstra, *Microfractography of thin films.* Philips Tech Rev, 1966. **27**(3): p. 87-91.

28. Thornton, J.A., *High rate thick film growth.* Annual review of materials science, 1977. **7**(1): p. 239-260.

29. Dellas, N. and J. Harper, *Effect of deposition angle on fiber axis tilt in sputtered aluminum nitride and pure metal films.* Thin Solid Films, 2006. **515**(4): p. 1647-1650.

30. Cai, W. and W.D. Nix, *Imperfections in crystalline solids*. 2016, Cambridge University Press. p. 82, 493.

31. King, H., *Quantitative size-factors for metallic solid solutions.* Journal of Materials Science, 1966. **1**(1): p. 79-90.

32. Kong, L., J. Liu, W. Lal, and B. Liu, *Correlation of lattice constant versus tungsten concentration of the Ni-based solid solution examined by molecular dynamics simulation.* Journal of alloys and compounds, 2002. **337**(1-2): p. 143-147.

33. Kurz, S., C. Ensslen, U. Welzel, A. Leineweber, and E. Mittemeijer, *The thermal stability of Ni–Mo and Ni–W thin films: Solute segregation and planar faults.* Scripta Materialia, 2013. **69**(1): p. 65-68.

34. Shim, J.-H., S.I. Park, Y.W. Cho, and B.-J. Lee, *Modified embedded-atom method calculation for the Ni–W system.* Journal of materials research, 2003. **18**(8): p. 1863-1867.

35. Kayser, G., *The lattice parameters and microstructures of annealed, nickel-rich nickel-molybdenum alloys.* Journal of materials science, 1989. **24**(8): p. 2677-2680.

36. Cziraki, A., Z. Tonkovics, I. Geröcs, B. Fogarassy, I. Groma, E. Tóth-Kádár, T. Tarnoczi, and I. Bakonyi, *Thermal stability of nanocrystalline nickel electrodeposits: differential scanning calorimetry, transmission electron microscopy and magnetic studies.* Materials Science and Engineering: A, 1994. **179**: p. 531-535.

37. Natter, H., M. Schmelzer, and R. Hempelmann, *Nanocrystalline nickel and nickel-copper alloys: Synthesis, characterization, and thermal stability.* Journal of Materials research, 1998. **13**(5): p. 1186-1197.

38. Schwaiger, R., B. Moser, M. Dao, N. Chollacoop, and S. Suresh, *Some critical experiments on the strain-rate sensitivity of nanocrystalline nickel.* Acta materialia, 2003. **51**(17): p. 5159-5172.

39. Suresha, S., M. Haj-Taieb, K. Bade, J. Aktaa, and K. Hemker, *The influence of tungsten on the thermal stability and mechanical behavior of electrodeposited nickel MEMS structures.* Scripta Materialia, 2010. **63**(12): p. 1141-1144.

40. Haj-Taieb, M., A. Haseeb, J. Caulfield, K. Bade, J. Aktaa, and K. Hemker, *Thermal stability of electrodeposited LIGA Ni–W alloys for high temperature MEMS applications.* Microsystem Technologies, 2008. **14**(9-11): p. 1531-1536.

41. Burns, D.E., Y. Zhang, T.P. Weihs, and K.J. Hemker, *Properties of sputter deposited Ni-base superalloys for microelectromechanical systems.* Thin Solid Films, 2014. **558**: p. 20-23.

42. Kumar, K., S. Suresh, M. Chisholm, J. Horton, and P. Wang, *Deformation of electrodeposited nanocrystalline nickel.* Acta Materialia, 2003. **51**(2): p. 387-405.

43. Shan, Z., E. Stach, J. Wiezorek, J. Knapp, D. Follstaedt, and S. Mao, *Grain boundary-mediated plasticity in nanocrystalline nickel.* Science, 2004. **305**(5684): p. 654-657.

44. Eastman, D., *Microscale Testing and Characterization Techniques for Benchmarking Crystal Plasticity Models*, in *Mechanical Engineering*. 2018, Johns Hopkins University.

45. Ledbetter, H.M. and R.P. Reed, *Elastic Properties of Metals and Alloys, I. Iron, Nickel, and Iron-Nickel Alloys.* Journal of Physical and Chemical Reference Data, 1973. **2**(3): p. 531-618.

46. Lintymer, J., J. Gavoille, N. Martin, and J. Takadoum, *Glancing angle deposition to modify microstructure and properties of sputter deposited chromium thin films.* Surface and Coatings Technology, 2003. **174**: p. 316-323.

47. Tait, R., T. Smy, and M. Brett, *Structural anisotropy in oblique incidence thin metal films.* Journal of Vacuum Science & Technology A: Vacuum, Surfaces, and Films, 1992. **10**(4): p. 1518-1521.

48. Lu, K., L. Lu, and S. Suresh, *Strengthening materials by engineering coherent internal boundaries at the nanoscale.* Science, 2009. **324**(5925): p. 349-352.

49. Lu, L., X. Chen, X. Huang, and K. Lu, *Revealing the maximum strength in nanotwinned copper.* Science, 2009. **323**(5914): p. 607-610.

50. You, Z., X. Li, L. Gui, Q. Lu, T. Zhu, H. Gao, and L. Lu, *Plastic anisotropy and associated deformation mechanisms in nanotwinned metals.* Acta Materialia, 2013. **61**(1): p. 217-227.

CHAPTER 4: LOCALIZED ANISOTROPIC PLASTICITY IN NANOTWINNED Ni-Mo-W

4.1 Introduction

The tensile testing described in Chapter 3 highlighted the microstructural effects on the in-plane mechanical properties of nanotwinned Ni-Mo-W alloys. The improper alignment during sputter deposition resulted in a variety of off-axis <111> columnar grains (0-15°) that exhibited linear-elastic behavior when loaded in uniaxial tension. Although this behavior is desirable for MEMS applications, an important scientific question arises from these results. Given the complex microstructure consisting of nanotwins and highly textured grains, would the same brittle behavior be apparent if loaded in a different orientation?

The extensive research on nanotwinned copper (Cu) has focused on understanding the deformation mechanisms associated with concurrent high strength and ductility, as outlined in section 1.4. Jang et al. performed in situ nanopillar compression on nanotwinned Cu and showed that pillars with twin boundaries aligned perpendicular to the loading axis involve dislocation transmission across twin boundaries, while those with inclined twin boundaries are dominated by easy glide [1]. An additional study by You et al. proposed that the dominant deformation mechanism for nanotwinned Cu can be switched among dislocation modes by changing the loading orientation with respect to the twin planes [2]. They studied three load orientations (0°, 45°, 90°) and reported that the yield strength and strain hardening have a marked dependence on these orientations. The various interactions between dislocations and twin boundaries define the anisotropic nature of the deformation. Nanotwin formation is typically associated with low stacking fault energy (SFE) materials, such as Cu, Ag or Au, but the synthesis of Ni-Mo-W alloys has demonstrated similar microstructures.

Thus, an understanding of their deformation would elucidate the mechanisms operative in higher SFE nanotwinned metals, where dislocation cores are likely to be more compact and their interactions with twin boundaries are more profound.

This chapter outlines an experimental investigation of the active deformation mechanisms for nanotwinned Ni-Mo-W and how they are affected by twin boundary orientation. Micropillar compression experiments were carried out inside of the scanning electron microscope (SEM) to observe the deformation when loading near perpendicular to the twin boundaries. The results from post-mortem transmission electron microscopy (TEM) and automated crystal orientation mapping (ACOM) are presented and discussed in detail in section 4.4. The initial experiments conducted in this chapter were carried out at the University of Tennessee during a nanoindentation training session hosted by George Pharr and Warren Oliver. Their knowledge of indentation mechanics provided a foundation for much of the methods described below.

4.2 Materials and methods

4.2.1 Material fabrication and characterization

Ni-Mo-W films were sputter deposited onto a brass substrate by Jessica Krogstad using a direct current power of 2500 W and argon sputtering gas pressure of 1 mTorr, with details outlined in sections 2.2.2 and 3.2.1. Unlike the study presented in the previous chapters, a single alloy of $Ni_{84.4}Mo_{10.7}W_{4.9}$ was chosen for investigation. During the sputtering process, small regions of nanocrystalline grains developed at the bottom of the film due to the high energy quench rates, but after that columnar grains grew through the thickness of the films (section 3.3.1). The freestanding $Ni_{84.4}Mo_{10.7}W_{4.9}$ films were investigated using X-ray diffraction (XRD) to determine which side of the film was nanocrystalline versus the

columnar microstructure, as shown in section 3.3.3. The $Ni_{84.4}Mo_{10.7}W_{4.9}$ films were mounted on SEM stubs using epoxy mixed with graphite powder for conductivity and oriented with the columnar side upward. All mechanical testing presented in this chapter was conducted on the columnar grain side of the films.

4.2.2 Mechanical testing

4.2.2.1 Nanoindentation

Instrumented nanoindentation was employed using the Oliver-Pharr method [3] to measure the hardness of the thin film at nominal indentation strain rate ($\dot{\varepsilon}$), defined by Equation 4.1 [4], where h is indentation depth, t is time and P is applied load.

$$\dot{\varepsilon} = \frac{1}{h}\frac{\partial h}{\partial t} = \frac{1}{2}\left(\frac{1}{P}\frac{\partial P}{\partial t}\right) \tag{4.1}$$

A typical indentation experiment is shown in Figure 4.1a, where the contact stiffness (S) is measured with the initial unloading slope at the maximum load (P_{max}) [3]. The indentation curve is most often associated with measures of the elastic modulus (E) and the hardness (H) of a material, defined in Equations 4.2 and 4.3.

$$E_r = \frac{\sqrt{\pi}}{2}\frac{S}{\sqrt{A}}$$
$$\frac{1}{E_r} = \frac{1-\nu^2}{E} + \frac{1-\nu_i^2}{E_i} \tag{4.2}$$

$$H = \frac{P_{max}}{A} \quad \textbf{(4.3)}$$

Measuring the contact stiffness (S) and the projected area of the elastic contact (A) provides a direct measure of the reduced modulus (E_r). The reduced modulus represents the total elastic deformation occurring from both the specimen and the indenter tip, which is related to the elastic modulus and Poisson's ratio of the specimen (E and ν) and of indenter (E_i and ν_i). The hardness in Equation 4.3 is calculated from the maximum load (P_{max}) and the projected area (A). Figure 4.1b illustrates a schematic of an indent cross-section with the various quantities used for analysis [3]. The projected area (A) is a function of contact depth (h_c), defined as the vertical distance along which contact is made between the specimen and the indenter tip. This is one of the most important quantities as it is used in all of the analysis calculations. Quality measurements of the elastic modulus and the hardness require an accurate measurement of the projected area, known as the tip area function, which is a representation of the tip geometry. Calibration is typically performed on a specimen with known elastic modulus and the data is fit to a polynomial function [3]. However, using all of these quantities from the indentation curve in Figure 4.1a only provides one measurement of modulus and hardness at the maximum load (P_{max}). By comparison, the continuous stiffness measurement (CSM) provides a nanometer amplitude oscillation during loading, such that the indenter is continually unloading to calculate the contact stiffness as a function of depth. Thus, use of the CSM enables property measurement as a function of depth.

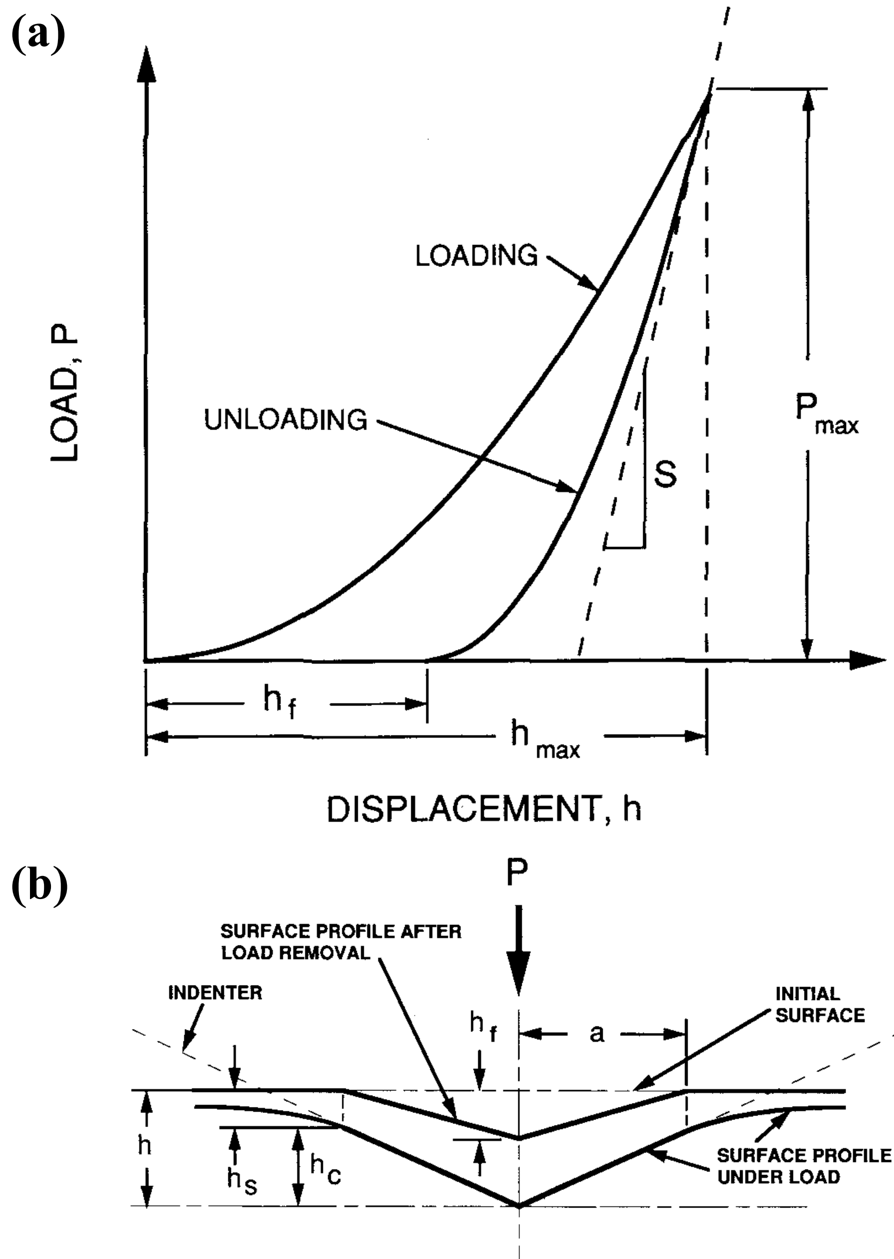

Figure 4.1: (a) A schematic of the load-displacement curve obtained during a typical indentation experiment, labeled with the quantities: P_{max} is the maximum load reached during indentation, h_{max} is the indenter displacement at the maximum load, h_f is the final depth of the contact impression after unloading and S is the initial unloading stiffness. (b) The contact depth h_c is defined as the vertical distance along which contact was made, while h_s is the displacement of the surface at the perimeter of contact. Adapted from [3].

In this study, the NanoMechanics Inc. iNano instrument with a 50 mN load cell and a diamond Berkovich tip was used with CSM methods. Tip calibrations were performed using fused silica before each set of indentation experiments to assure an accurate measure of the tip area function. A custom machined puck that is compatible with the iNano holder was designed with a central hole and side screw to secure a SEM stub, Figure 4.2. Although the specimen is secure, this method of mounting changes the frame stiffness and needs to be accounted for. The total stiffness (K^*) during indentation is comprised of the contact stiffness (S) and the frame stiffness (K_f), defined in Equation 4.4.

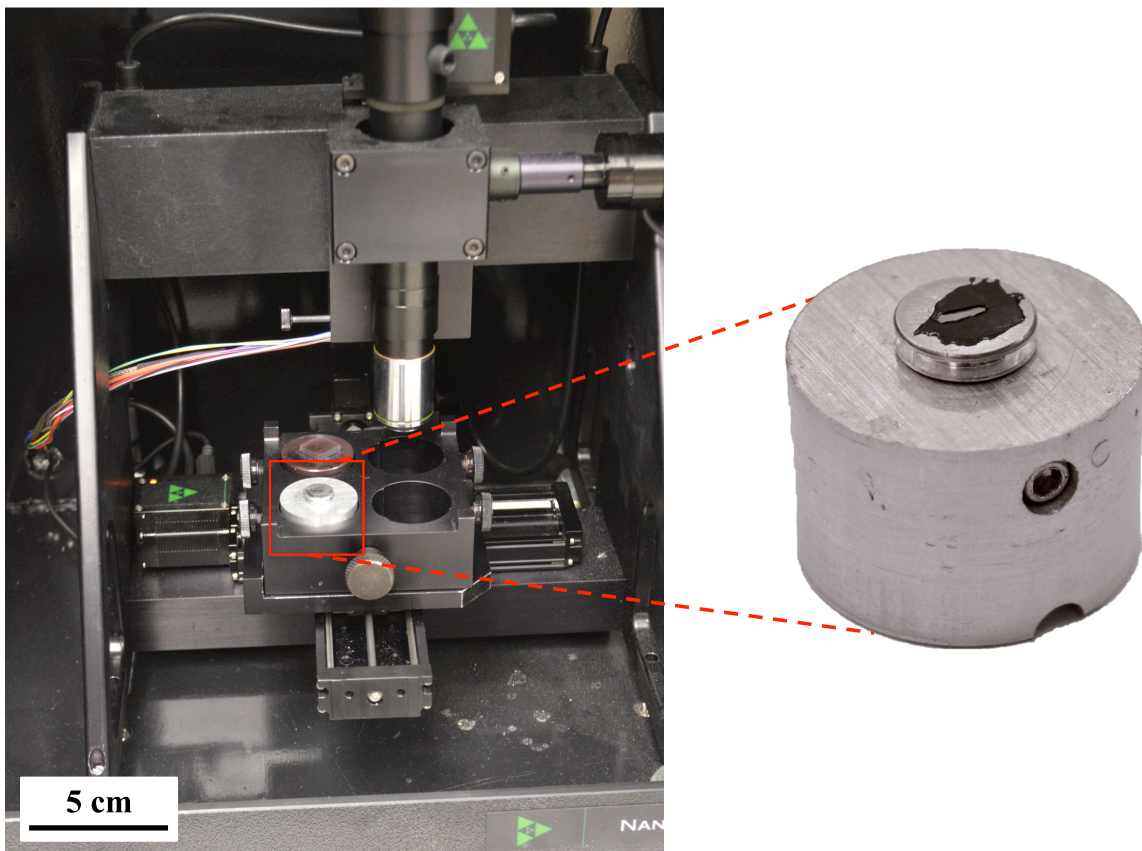

Figure 4.2: Nanomechanics Inc. iNano system, equipped with a 50 mN load cell and a custom machined puck equipped for mounting SEM stubs.

Substituting the relations for contact stiffness (S) and hardness (H) in Equations 4.2 and 4.3 provides the expression in Equation 4.5 for the total stiffness (K^*) as a function of the applied load (P).

$$\frac{1}{K^*} = \frac{1}{S} + \frac{1}{K_f} \qquad \textbf{(4.4)}$$

$$\frac{1}{K^*} = \frac{\sqrt{\pi H}}{2E_r}\left(\frac{1}{\sqrt{P}}\right) + 1/K_f \qquad \textbf{(4.5)}$$

For Equation 4.5, if the reduced modulus (E_r) and hardness (H) are constant values, then a plot of the total compliance ($1/K^*$) versus ($1/\sqrt{P}$) is a linear line with an intercept of the frame compliance ($1/K_f$). An example frame stiffness calculation from the custom machined puck is shown in Figure 4.3 and used to recalculate all measured values.

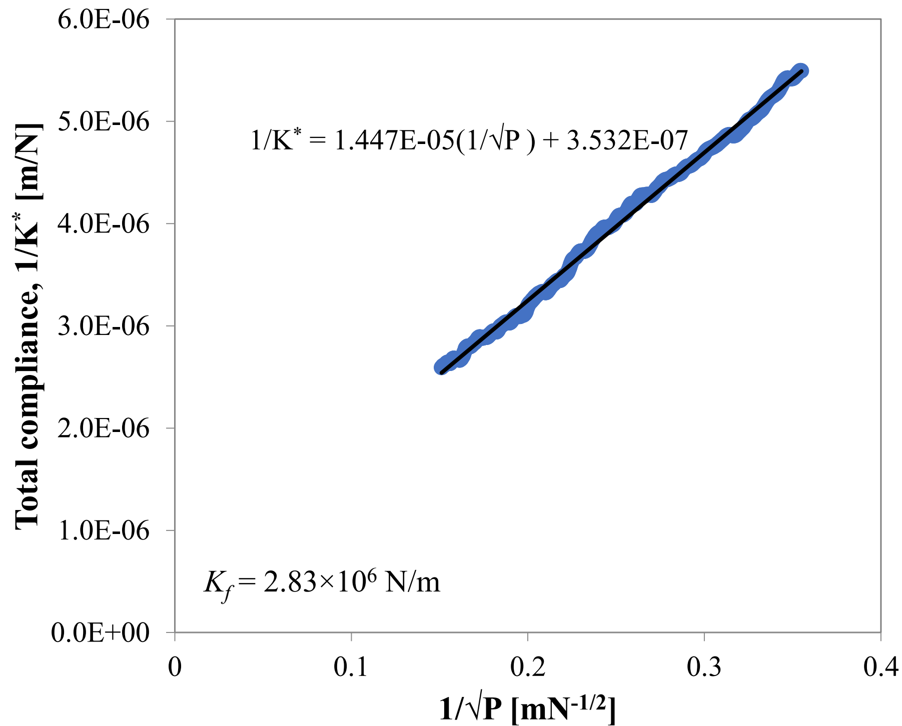

Figure 4.3: Representative frame stiffness (K_f) calibration for the custom machined puck (Figure 4.2) using the intercept of the linear fit.

4.2.2.2 In situ compression

Micrometer-sized pillars were fabricated using annular milling with a FEI Strata DB235 Dual-Beam SEM and FIB. Large 100 μm outer trench diameters were milled using 20 nA current to provide fiducial markers for easy identification. Micropillars with a mid-point diameter of 3.0±0.1 μm, overall length of 6.9±0.1 μm and 1-2° taper angle were fabricated in the center of the large 100 μm plateaus using a final milling current of 300 pA.

In situ micropillar compression was performed with 50 mN and 1 N load cells in the NanoMechanics Inc. NanoFlip (at University of Tennessee) and inSEM (at JHU) shown in Figures 4.4a and b, respectively.

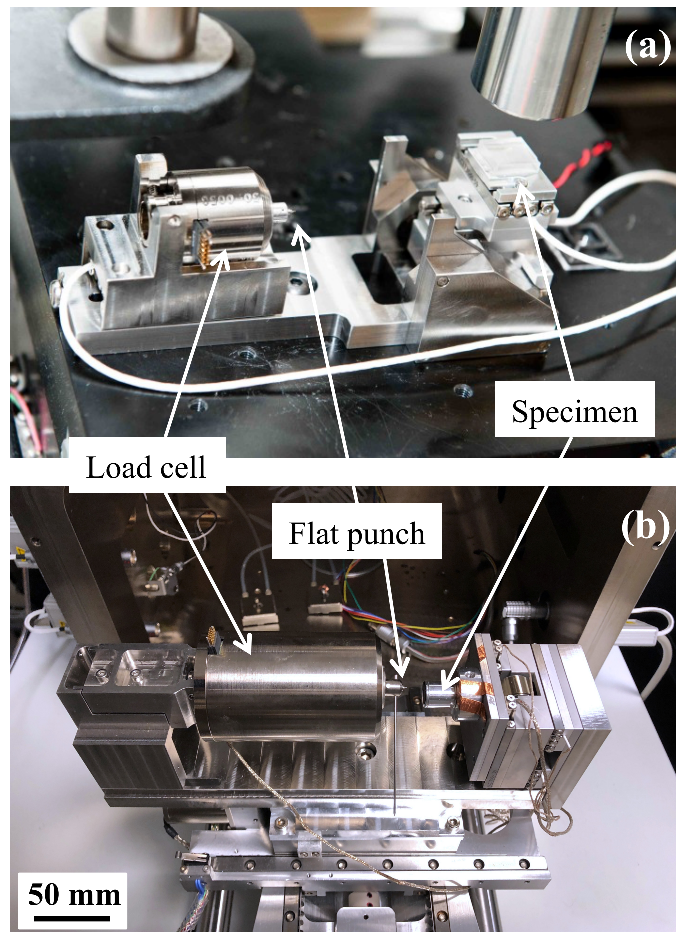

Figure 4.4: NanoMechanics Inc. in situ compression stages. (a) The NanoFlip has a 50 mN load cell and also allows the user to flip the specimen 90° for easier imaging in the SEM. (b) InSEM has a 1 N load cell, but cannot flip the specimen.

The load frames in Figure 4.4 were placed inside the SEM with the mounted specimen. A 10 μm x 10 μm diamond flat punch was used to compress the pillars to a user prescribed depth, held for 1 s at the maximum load and then unloaded. Loading was performed at a nominal indentation strain rate of 10^{-3} and 10^{-4} s^{-1} with a data acquisition rate of 500 Hz. A series of load-unload-reload tests were performed by increasing the maximum depth in subsequent trials and the incremental deformation was examined.

4.2.3 Post-mortem characterization

Berkovich tip shaped nanoindents were imaged using a Tescan Mira field emission SEM to examine the surface impressions for each of the investigated strain rates. Conventional FIB lift-out techniques were used to extract cross-sections of the deformed micropillars in the loading direction, thinning the specimens to electron transparency. The thin films extracted post-mortem from pillars were analyzed using a FEI Tecnai G2 F20 Super-Twin FE-TEM at 200 kV to obtain bright field images and selected area electron diffraction (SAED) patterns. TEM-based ACOM was used in a Thermo Scientific TF30 to determine the crystal orientation after deformation and investigate any changes in the overall microstructure.

4.2.3.1 TEM-based orientation mapping

Microstructural characterization using TEM provides incredible spatial resolution, near the atomic scale. Orientation mapping using the TEM requires scanning a small, converged electron beam across the specimen and the collection of SAED patterns at each point. The SAED patterns are imaged from the phosphor screen in the TEM, using an external camera. After collecting all the SAED patterns over the specified area, the user identifies the expected phase(s) in the specimen and the software cross-references each pattern to a library of thousands of simulated SAED patterns. Equation 4.6 defines the reliability (R) as a measure

of how well the experimentally captured SAED pattern matched to the simulated SAED pattern, where Q_1 is the correlation index of the assigned orientation (best guess) and Q_2 is the correlation index of the second-best guess.

$$R = 100\left(1 - \frac{Q_2}{Q_1}\right) \tag{4.6}$$

A reliability value close to 0 indicates that multiple orientations fit the experimental SAED equally well, indicating poor confidence that the proper orientation was chosen, whereas a reliability value of 100 indicates a completely unique solution. In general, a reliability value of 15 is sufficient to assure the validity of the match [5], but a value greater than 30 is preferred. This process is repeated for each SAED pattern to generate a full orientation dataset across the acquired region of interest. The ACOM system at JHU was purchased and developed by NanoMEGAS and sold as a system known as ASTAR.

The resultant data can be interfaced with OIM Analysis™ software (EDAX-TSL) to perform graphical analysis, such as grain size. Each pixel of data collected is assigned to a crystallographic orientation, determined by the SAED pattern collected. The OIM software defines a grain as a group of points with similar orientation; each point is checked with its neighbors to determine if they are within a specified grain tolerance angle, and if so, it is considered part of the grain. The user can set a minimum grain size value, such that each grain is required to have a particular number of points to be considered a grain, which is useful for eliminating noise in the dataset. For the data reported in this chapter, a grain tolerance angle of 4° and a minimum grain size of 10 nm were used. The average grain size ($\bar{d}$) can be determined by a number fraction, where grain size is numerically averaged, or by

an area fraction, where the grain size area is a weighted average. These calculations are shown in Equations 4.7 and 4.8, respectively, where *N* is the total number of grains, d_i is the diameter and A_i is the area for grain i. Since the Ni-Mo-W grains have a high aspect ratio because of their columnar shape, all grain sizes are reported as the area fraction rather than the number fraction.

$$\bar{d} = \frac{1}{N}\sum_{i=1}^{N} d_i \quad \textbf{(4.7)}$$

$$\bar{d} = \frac{\sum_{i=1}^{N} A_i d_i}{\sum_{i=1}^{N} A_i} \quad \textbf{(4.8)}$$

4.3 Hardness and local instabilities in nanoindentation

To measure the hardness of the Ni-Mo-W films, load-depth data at four strain rates (0.02, 0.1, 0.2 and 1 s^{-1}) were analyzed and calibrated for the frame stiffness according to the methods described in section 4.2.2.1. For each strain rate, 20 indents were performed and the hardness values were extracted from a depth of 200-250 nm to reduce the substrate effects and surface roughness, as illustrated in Figure 4.5. Table 4.1 summarizes the Ni-Mo-W alloy composition and the average measured hardness values, ranging from 8.17-9.67 GPa with increasing strain rate.

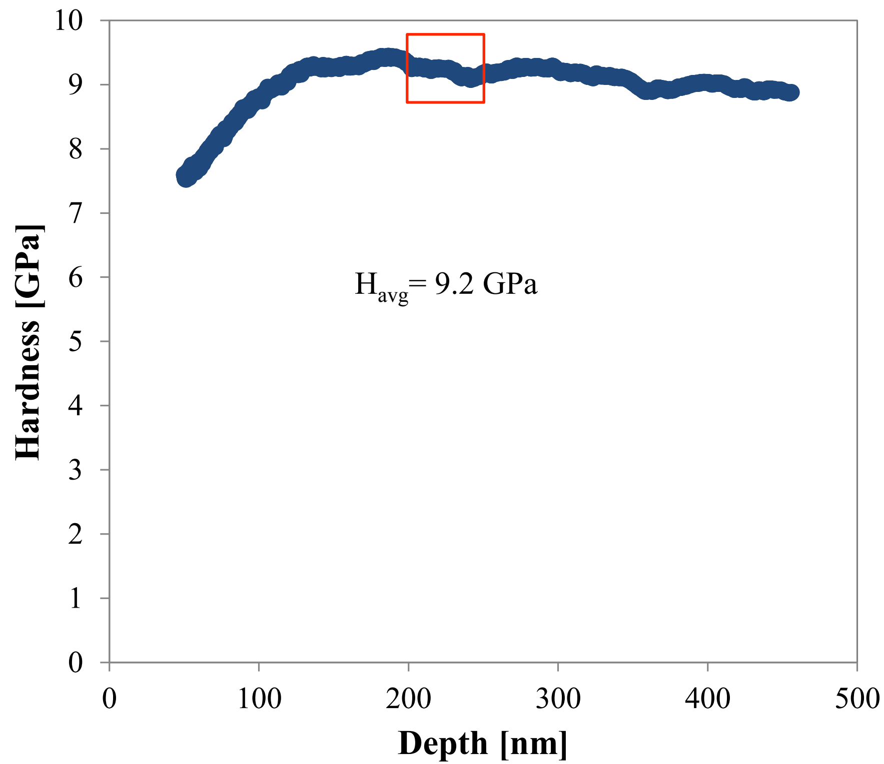

Figure 4.5: Representative plot of the measured hardness as a function of depth at strain rate 0.1 s^{-1}. Average hardness is reported from depths 200-250 nm.

Table 4.1: Alloy composition and calculated activation volume from the hardness measurements at different strain rates. For each strain rate, 20 indents were performed.

Alloy composition [at.%]	Hardness [GPa]				Activation volume [b^3]
	$\dot{\varepsilon}$ = 0.02 s^{-1}	0.1 s^{-1}	0.2 s^{-1}	1 s^{-1}	
$Ni_{84.4\pm0.2}Mo_{10.7\pm0.1}W_{4.9\pm0.2}$	8.17±0.59	8.75±0.53	9.51±0.71	9.67±0.61	2.82

The loading portion of the load-depth curves used to calculate the hardness is shown in Figure 4.6. Small perturbations are observed during loading and appear to have similar frequency and size across the different strain rates investigated, displaying no significant strain rate dependence. Local perturbations in the loading curves of nanoindentation are commonly associated with dislocation activity and shear localizations [6]. Examples of these instabilities are indicated in Figure 4.6 with arrows.

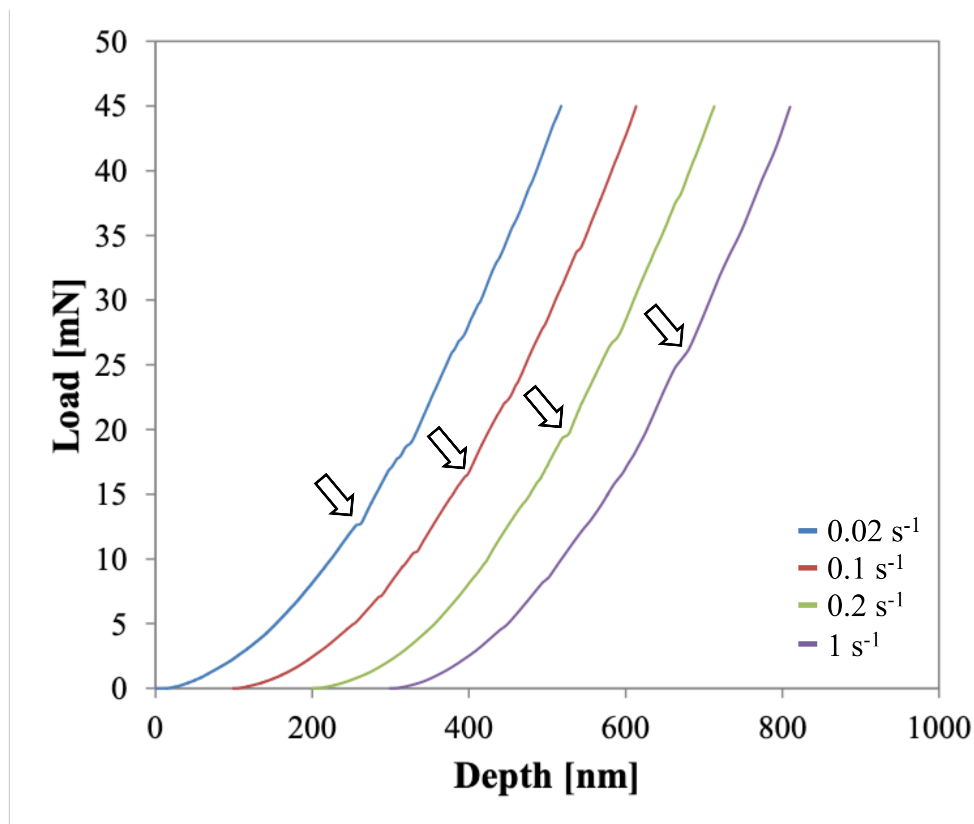

Figure 4.6: Instrumented nanoindentation load-depth curves during loading of $Ni_{84.4}Mo_{10.7}W_{4.9}$ films, offset 100 nm for visualization, at strain rates 0.02-1 s^{-1}. Arrows point to examples of local instabilities.

SEM micrographs of the residual surface impressions are displayed in Figure 4.7. The micrographs show small ridges in the pile-up region next to the indent and in the interior regions of the impression, consistent across all strain rates. These local features are commonly associated with shear band formation and indicative of unstable plastic flow [6, 7]. Extensive shear banding during nanoindentation is commonly observed in metallic glasses, but has also been reported for very fine nanocrystalline grain sizes [7-9]. Although the Ni-Mo-W films are fully crystalline with grain sizes upward of 100 nm, the formation of shear bands is not completely unexpected due to the finely spaced nanotwins. Numerous observations of shear banding have been reported for nanotwined Cu [1, 10-12] and finely spaced nanoscale multilayers [13].

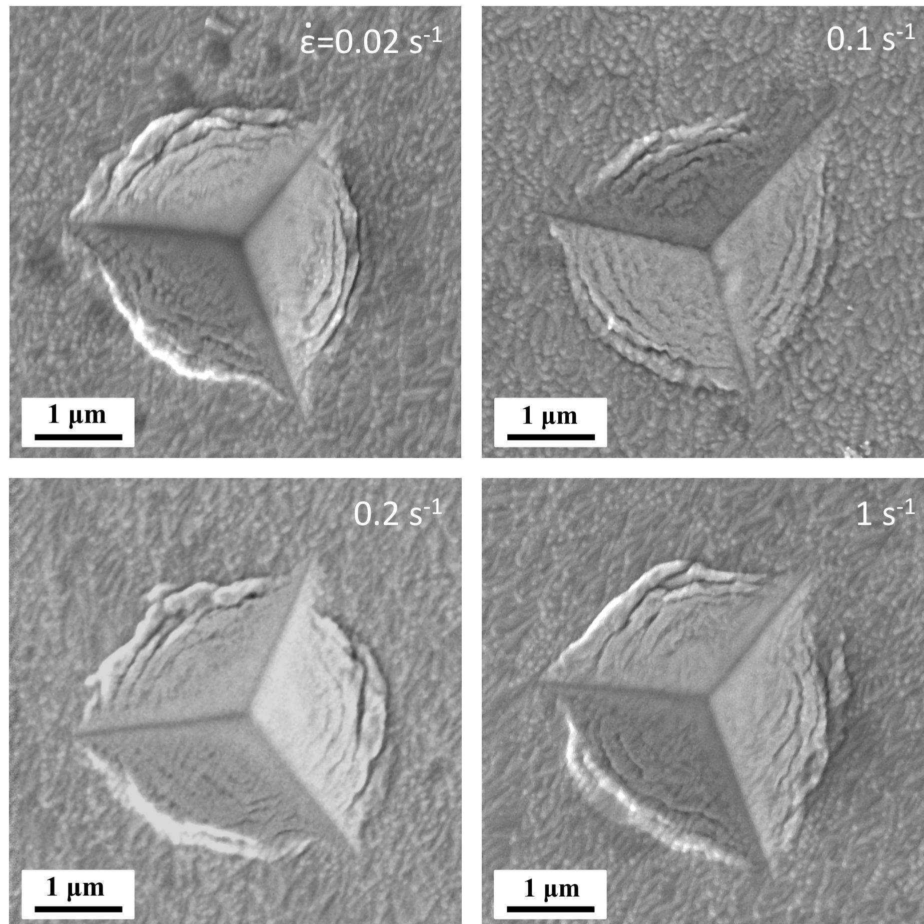

Figure 4.7: SEM micrographs of the Berkovich indent at strain rates 0.02, 0.1, 0.2 and 1 s^{-1} showing evidence of shear banding.

The apparent activation volume (V^*) was calculated to determine the thermally activated deformation processes, using the strain rate sensitivity of the hardness and Equation 4.9, where k_B is the Boltzmann constant, T is temperature, $\dot{\varepsilon}$ is strain rate and σ is the flow stress (assuming the flow stress is 1/3 of the hardness, H).

$$V^* = \sqrt{3} k_B T \frac{\partial \ln \dot{\varepsilon}}{\partial \sigma} = 3\sqrt{3} k_B T \frac{\partial \ln \dot{\varepsilon}}{\partial H} \tag{4.9}$$

Figure 4.8 was used to find the slope of the natural log of the strain rate ($\ln \dot{\varepsilon}$) versus the hardness (H), with a measured value of 2.19×10^{-9} Pa^{-1}.

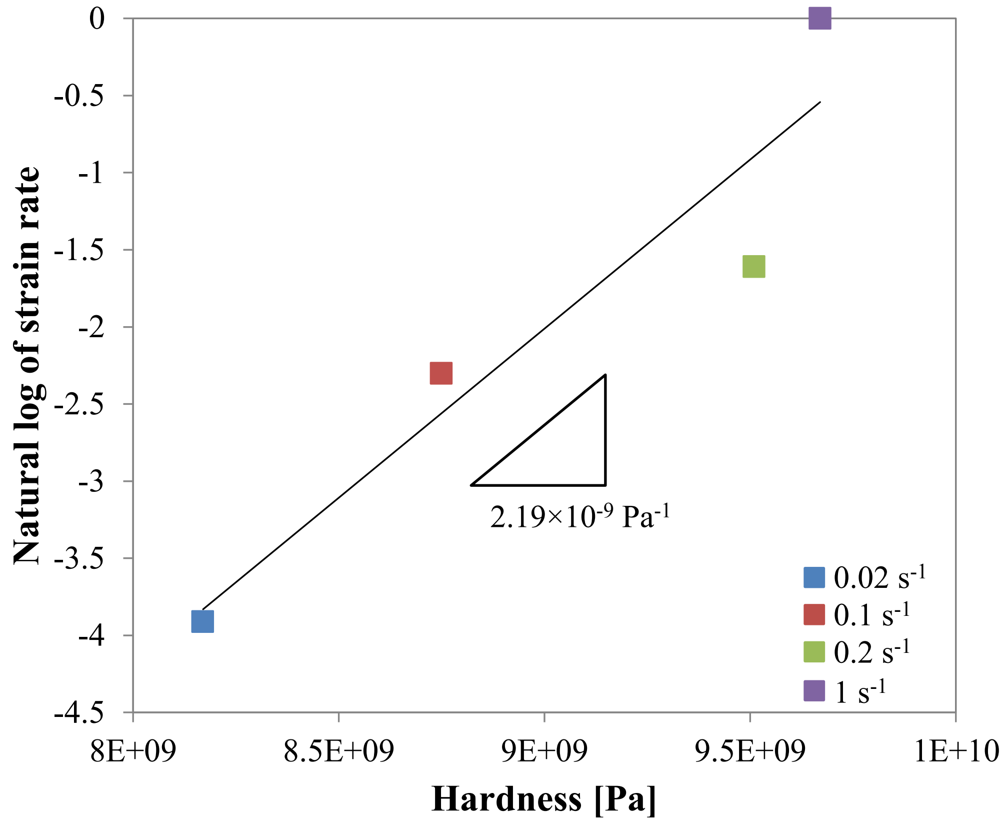

Figure 4.8: Natural log of strain rate versus the hardness for $Ni_{84.4}Mo_{10.7}W_{4.9}$ films. Linear line fit through the data has a slope of 2.19×10^{-9} Pa^{-1}, which is used to calculate the activation volume.

The activation volume was calculated using Equation 4.9 and reported in Table 4.1, using values k_B=1.38×10^{-23} J/K and T=298 K. The activation volume has conventional units of b^3, where b is the magnitude of the Burgers vector. For $Ni_{84.4}Mo_{10.7}W_{4.9}$ films in section 3.3.3.1, the lattice parameter was measured 3.61 Å and can be used to calculate the magnitude of the Burgers vector, 0.255 nm. The calculated activation volume of 2.82b^3 is very small and differs by two or three orders of magnitude from traditional fcc dislocation glide mechanisms.

Other nanotwinned metals such as Cu, have a reported activation volume range of 3-20b^3, where dislocation nucleation mechanisms are believed to govern the deformation [14, 15]. Experimental evidence and MD simulations by You et al. showed that when loading perpendicular to the twin boundaries in nanotwinned Cu, dislocation pile-up and slip transmission at the twin boundaries were observed, indicating that the twin boundary obstruction of dislocation glide facilitated the strengthening mechanisms [2]. Similarly, in nanoscale multilayers the interface boundary has been shown to suppress dislocation glide mechanisms. Zhang et al. investigated gold-copper multilayers and found that as the layer size decreased, the hardness increased but dislocation plasticity is hindered and inhomogenous plastic deformation develops through shear banding [13]. The hard glide mechanism described by You et al. and the refined multilayer spacing described by Zhang et al. are consistent with the ultrahigh hardness values and small activation volume of $Ni_{84.4}Mo_{10.7}W_{4.9}$, suggesting that the suppression of dislocation glide by twin boundaries may be responsible for the observed strengthening and shear banding.

4.4 Micropillar compression

4.4.1 In situ mechanical loading

The FIB machined micropillars were loaded onto the compression stage and the alignment was checked between the flat punch and the specimen surface. Figure 4.9 displays a symmetric imprint that was found by pressing the flat punch into the surface adjacent to the pillars, indicating proper alignment.

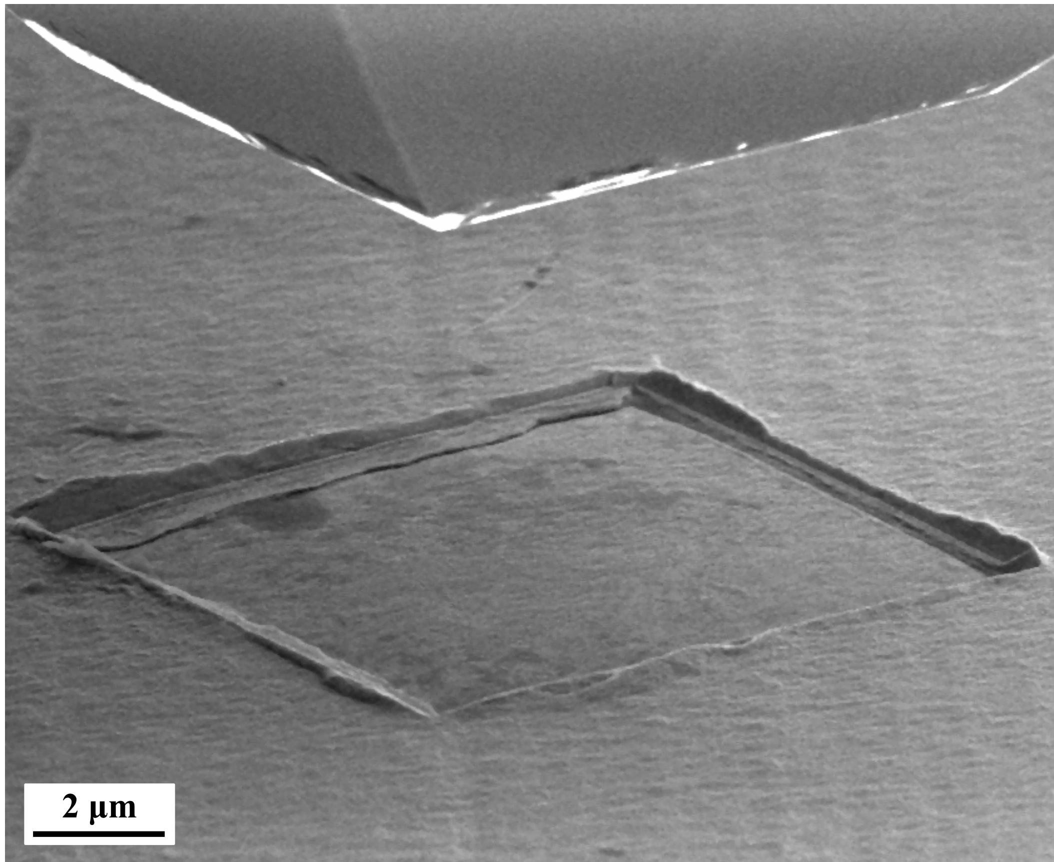

Figure 4.9: Symmetric impression made by pressing the flat punch into the Ni-Mo-W film surface at high load ~45 mN, indicating proper alignment between the tip and the specimen surface during in situ compression loading. Plastic deformation and extruded material are observed locally around the indenter impression.

Compression experiments were then carried out by loading the micropillars to a depth of 1 μm at a nominal strain rate of 10^{-3} s^{-1}. A representative stress-strain response is shown in Figure 4.10, exhibiting high flow strengths exceeding 3.5 GPa. The mechanical response showed elastic loading until 3.5 GPa, where a discrete strain bust was first observed. The yield point of the micropillars is defined by the onset of plastic flow, which is the stress associated with the first strain burst. After the burst event, the pillar exhibits "hardening" to accommodate additional deformation. It is important to note that the term hardening is being used in the most general sense and does not necessarily refer to classical strain hardening, governed by strain-driven dislocation storage [16]. Since the first report of a size-scale dependency on crystal plasticity [17], various computational studies [18-20], in situ TEM [21] and post-mortem TEM [22] investigations have shown the breakdown of classical strain-hardening mechanisms at small length scales. A more detailed discussion on the hardening mechanisms in Ni-Mo-W will be discussed in section 4.4.3. Visual examination of the deformed micropillar (Figure 4.11) revealed plasticity localized at the top of the pillar with no visible deformation in the lower portion. A similar behavior was observed in four different micropillars, with their mechanical behavior detailed in Appendix 2.

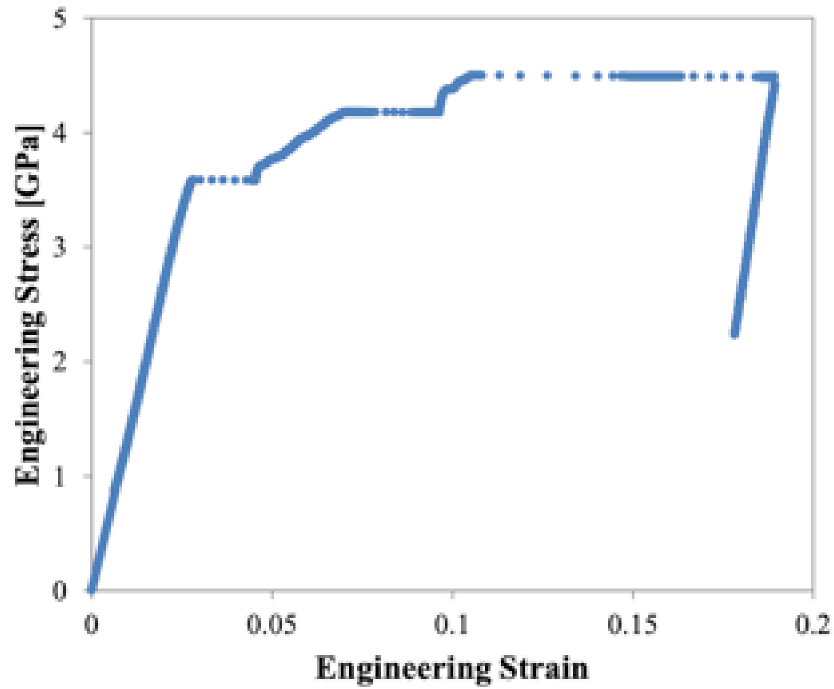

Figure 4.10: The stress-strain response of a micropillar compressed to a depth of 1 μm at a nominal strain rate of 10^{-3} s^{-1} showing extremely high flow strength and discrete strain bursts.

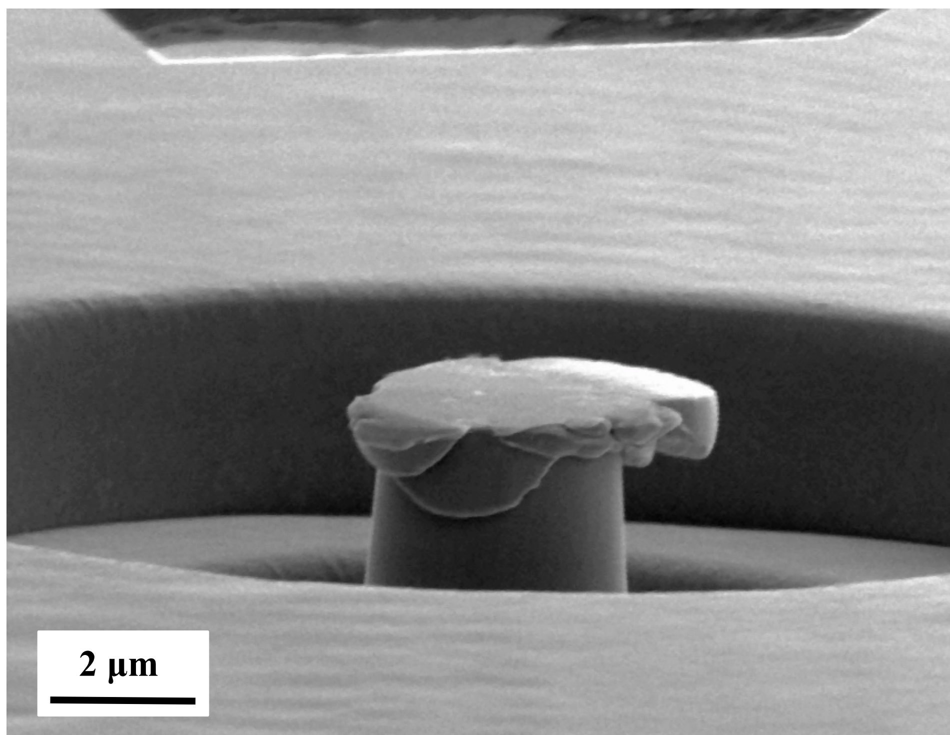

Figure 4.11: A deformed micropillar after being compressed to a depth of 1 μm at a constant nominal strain rate of 10^{-3} s^{-1}, with associated mechanical response in Figure 4.10.

In order to investigate and understand the anisotropic deformation further, additional in situ compression experiments were conducted by loading in smaller steps. Micropillars were incrementally loaded to depths of 50 nm, unloaded and reloaded an additional 50 nm and this process was repeated multiple times. For example, Figure 4.12 has 10 different load-unload-reload curves that form the engineering stress-strain response for a single micropillar. The pillar displayed high flow stress, strain bursts and high hardening, similar to that observed in Figure 4.10. The first two loading steps in Figure 4.12 showed nominally elastic deformation, but by the third loading step the onset of plastic flow was accompanied by a strain burst, followed by hardening. Each of the loading steps showed a repeatable 3.51±0.23 GPa yield point, followed by either another strain burst or hardening. The stress required for subsequent deformation after reloading was found to be below the maximum stress in the previous unloading, indicating that either some relaxation occurred in the pillar or that a new nucleation step formed between loading steps.

The deformed micropillar is displayed in Figure 4.13, where SEM images were taken at the end of the different loading cycles. The first band of localized deformation (or shear band) was imaged after loading to 4.5% strain (Figure 4.13b), which corresponds to the first strain burst in the mechanical response. When reloaded further, deformation occurred in a different portion of the pillar and another burst occurred with an associated shear band and subsequent hardening. The continued incremental loading and the increase in deformation resulted in the extrusion of material at the top of the pillar, with no apparent plasticity in the rest of the pillar, Figure 4.13. The combined effects of modest taper and friction might explain why the deformation initiated at the top of the pillar. Inherently from the annular milling process, small amounts of taper were introduced to the geometry. Using the average

pillar dimensions of 3.0 μm diameter, 6.9 μm length and 1-2° taper angle, the difference in stress at the top versus the bottom of the pillar is calculated 15-27%. Additionally, the contribution from the friction between the diamond flat punch and the pillar surface could lead to a multi-axial stress state at the top of the pillar and the evolution of geometrically necessary dislocations [17, 23, 24]. However, with subsequent deformation these effects should become less significant. Given the extremely localized and highly deformed top portion of the micropillar, it is not likely that the 15-27% difference in stress or the friction are enough to cause the severity of anisotropic plasticity with no deformation transferred to the remainder of the pillar.

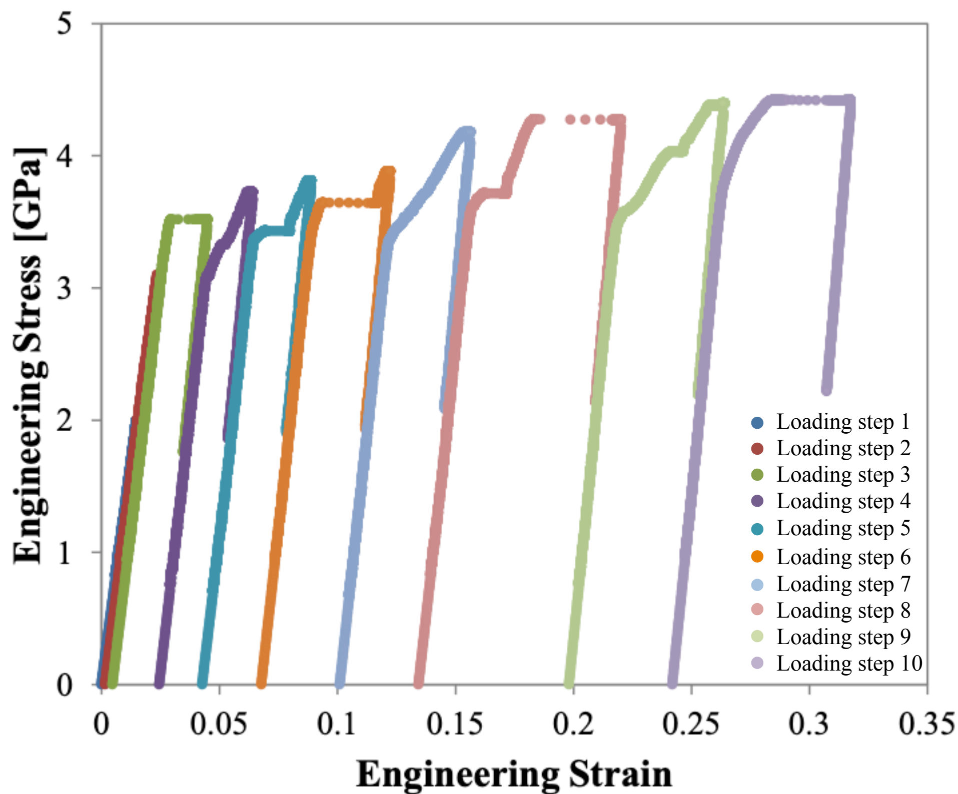

Figure 4.12: Stress-strain curve of a micropillar that was loaded-unloaded-reloaded for 10 cycles at a nominal strain rate of 10^{-3} s^{-1}. Ultrahigh flow strengths have a repeatable 3.51±0.23 GPa yield point.

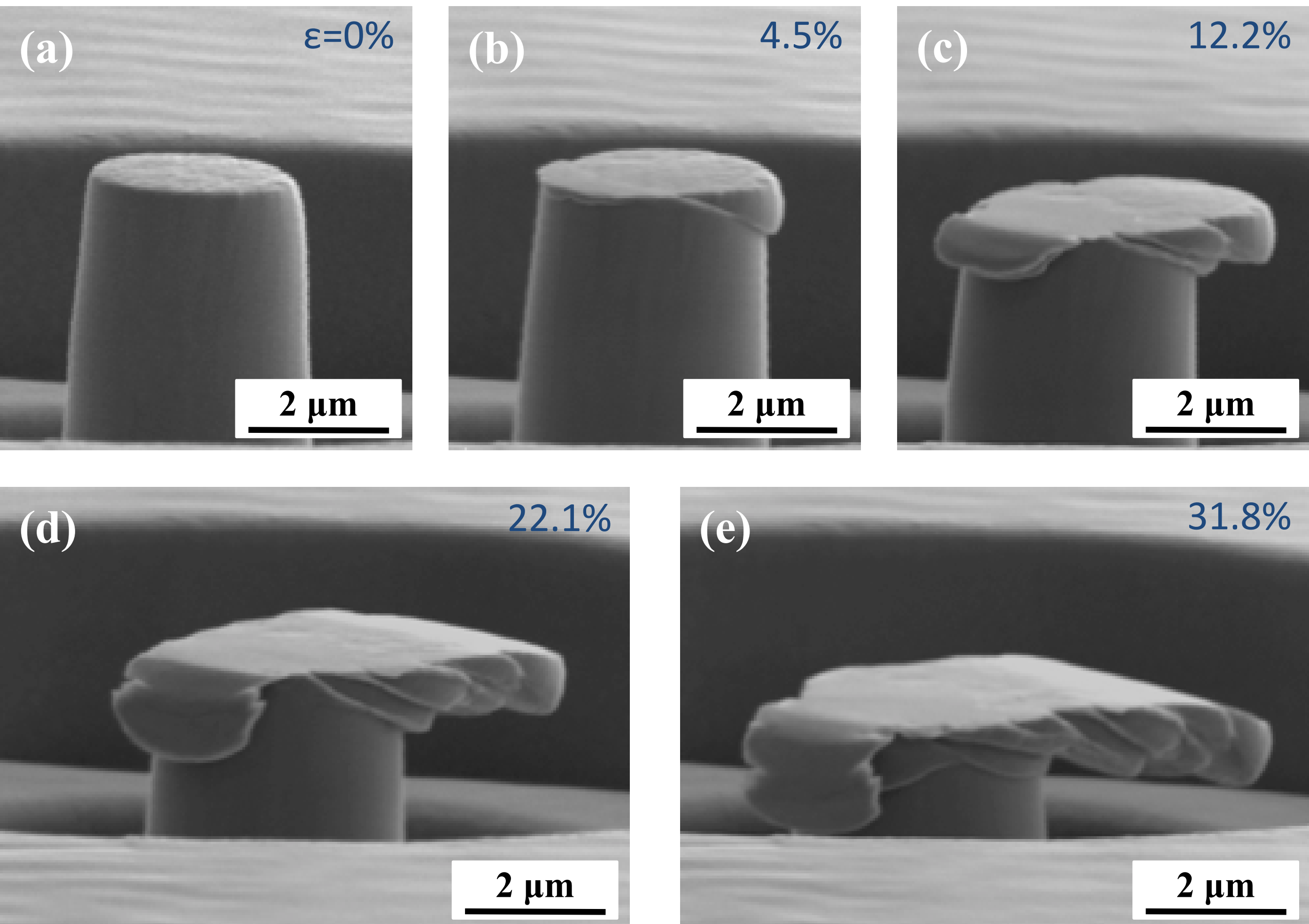

Figure 4.13: In situ pillar compression associated with incremental load-unload-reload cycles (Figure 4.12) with representative deformed images taken at (a) 0%, (b) 4.5%, (c) 12.2%, (d) 21.1% and (e) 31.8% nominal strain. All of the deformation is highly localized at the top of the pillar and has a directional dependence.

All micropillars that were loaded in compression showed a high concentration of plastic deformation at the top of the pillar and extruded material predominately off to one side. This behavior was highly repeatable for a total of 12 deformed micropillars, with examples illustrated in Figure 4.14 and Appendix 2. The symmetric surface impression in Figure 4.9 indicates that the deformed directionality of the extruded material is not an artifact of the tip alignment. Instead, it appears to be related to the underlying microstructure, which requires a re-evaluation of the Ni-Mo-W films.

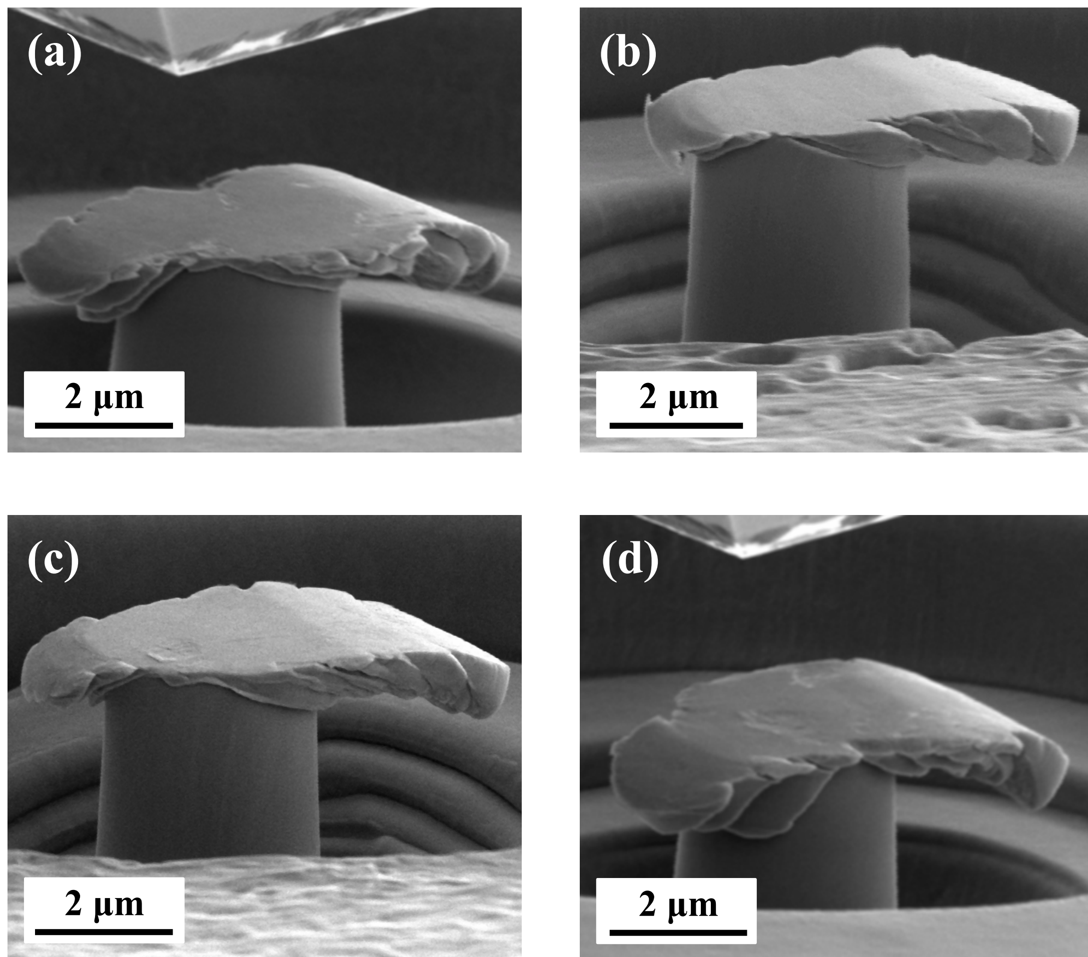

Figure 4.14: Four deformed micropillars exhibiting repeatable highly localized anisotropic plasticity.

The as-deposited microstructures were previously characterized in section 3.3.1 and found to have long columnar <111> grains that were aligned in the growth direction and filled with a high density of very fine nanotwins. For the $Ni_{84.4}Mo_{10.7}W_{4.9}$ films used to machine micropillars in this study, a cross-sectional FIB channeling contrast image in Figure 4.15a indicates that the roughly 100 nm wide columnar grains that were formed grew on an 11° tilt with respect to the film perpendicular. Nanotwins and stacking faults were confirmed with SAED patterns indexed for the matrix and the twin, shown in Figure 4.15b. A more detailed analysis of the twin spacing will be presented in section 5.3.3, but for this discussion they will be quoted as ~3.5 nm thick. The realization of the tilted microstructure provided a loading orientation that was at an 11° angle with respect to the columnar grains and their perpendicular twin boundaries, shown in Figure 4.16a. This suggests that the directionality of the extensive plastic deformation observed in the top of the micropillars may be attributed to the underlying tilted microstructure. Cross-sectional TEM micrographs confirming this observation will be presented and discussed in section 4.4.2.

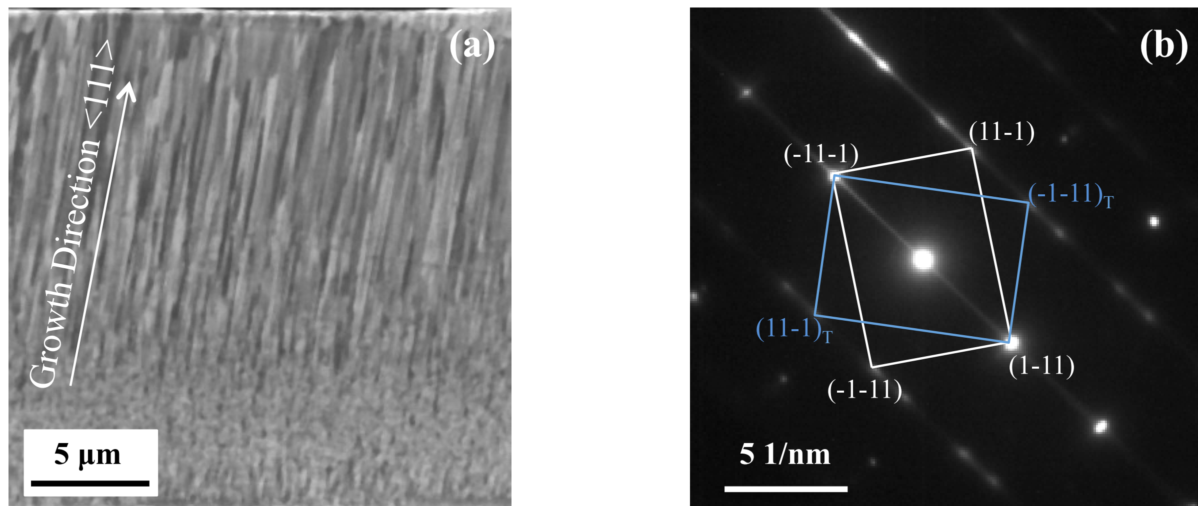

Figure 4.15: (a) FIB channeling contrast image of a cross-section of the Ni-Mo-W film used to machine micropillars and (b) representative SAED pattern, indexed for the matrix and the twin, with streaking that is representative of stacking faults.

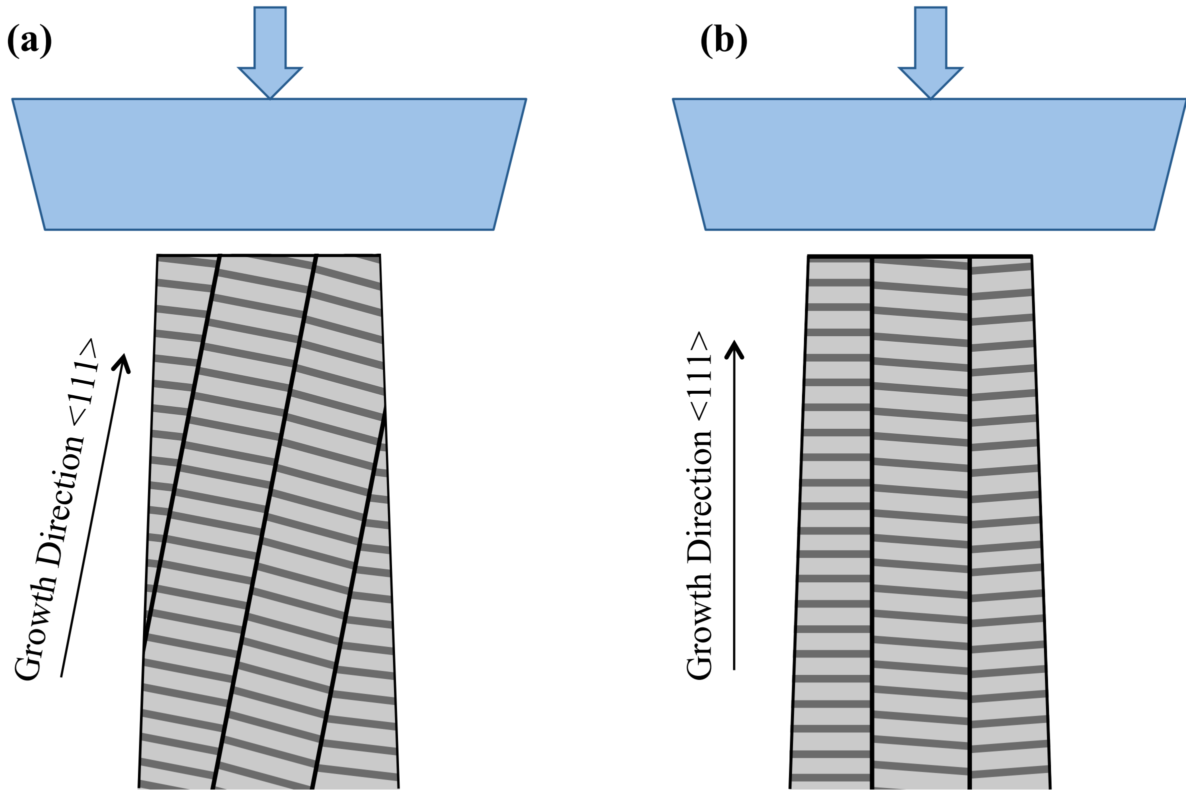

Figure 4.16: Schematic of the microstructural geometry with respect to the compression loading direction. (a) Columnar grains and nanotwins at a slight 11° tilt with respect to the compression axis and (b) nanotwins aligned perpendicular to the compression axis.

The intended loading orientation was perpendicular to the twin boundaries (Figure 4.16b) to investigate the hard glide mechanisms. Additional micropillars were fabricated from well-aligned columnar grains and twins to compare with the unintentional 11° micropillars. Figure 4.17 details five different load-unload-reload curves displaying the initial two loading steps with nominally elastic deformation, while the remaining three loading steps showed a repeatable 3.55±0.13 GPa yield point followed by discrete strain bursts and hardening. The flow strengths for the well-aligned pillar are comparable to what was observed for the micropillars at 11°, but the amount of hardening seems more variable in the well-aligned pillar. The resultant deformed well-aligned micropillar displayed highly localized deformation with material extrusion at the top of the pillar, shown in Figure 4.18.

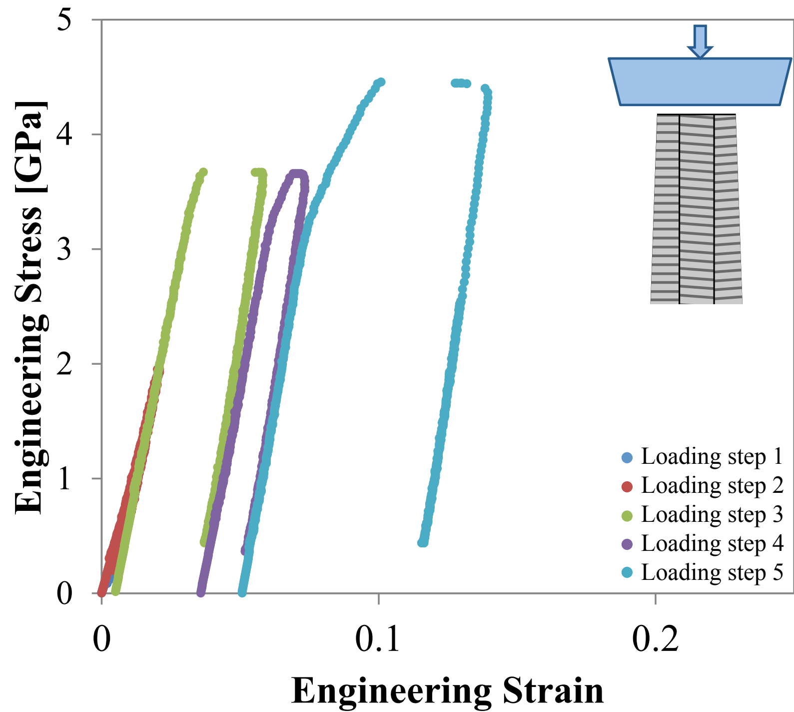

Figure 4.17: Stress-strain curve of a micropillar with well-aligned columnar grains and perpendicular nanotwins with the compression axis. Five different loaded-unloaded-reloaded cycles were performed at a nominal strain rate of 10^{-4} s^{-1}. Ultrahigh flow strengths with a very repeatable 3.55±0.13 GPa yield point was observed for each of the loading steps.

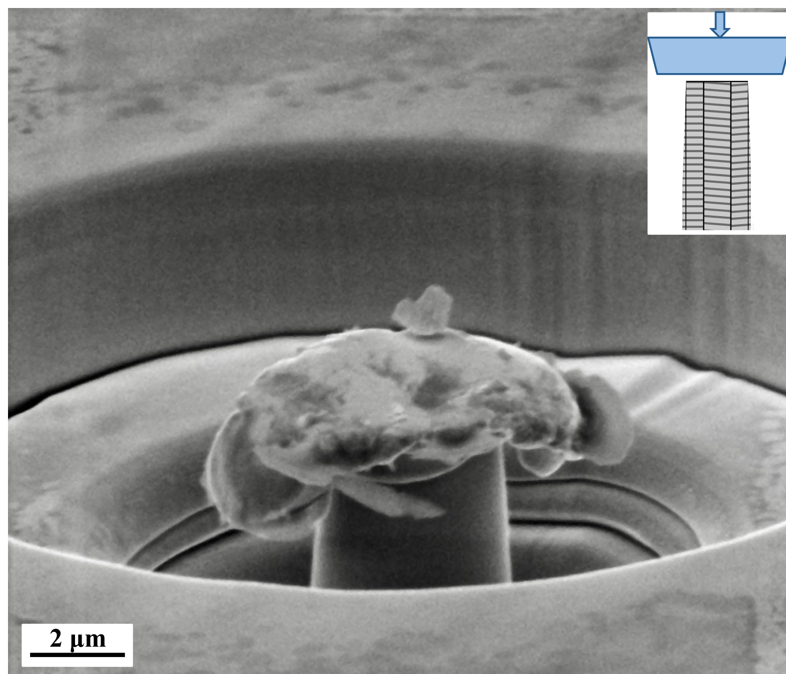

Figure 4.18: In situ pillar compression of the well-aligned microstructure, associated with incremental load-unload-reload cycles (Figure 4.17) with representative deformed image taken at 14% nominal strain. All of the deformation is highly localized at the top of the pillar, but the deformation spread more evenly about the transverse direction.

The directionality of the extruded portion appears to spread more evenly about the transverse direction, compared to those observed in Figures 4.11, 4.13, 4.14, which have a clear directional dependence predominantly to one side. A similar behavior was observed for a total of 3 well-aligned pillars, shown in Appendix 2.

4.4.2 TEM observations of plasticity in deformed micropillars

Further characterization focused on the micropillar with a columnar tilt of 11°, where a cross-sectional thin foil of a deformed $Ni_{84.4}Mo_{10.7}W_{4.9}$ pillar compressed to 30% strain was formed using convention FIB lift-out techniques. Due to the large extruded region at the top of the pillar, the entire trenched area surrounding the pillar required lift-out and thinning. Consequently, a large amount of material (platinum (Pt) and Ni-Mo-W) was re-deposited into the trench of the pillar during this process. Figure 4.19 exhibits the vast re-deposition in the originally empty cavity, which now has Ni-Mo-W and Pt surrounding the micropillar.

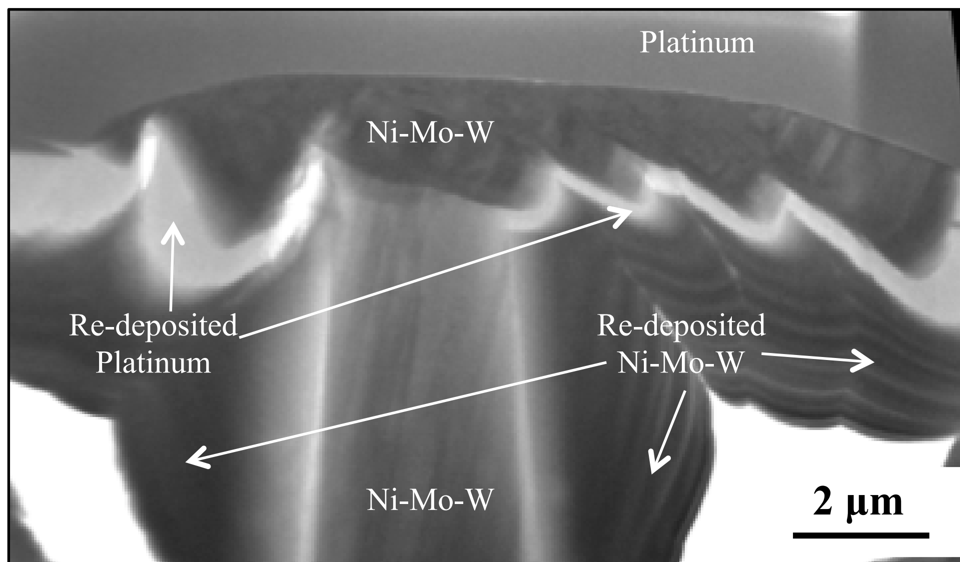

Figure 4.19: Cross-sectional TEM lift-out of a deformed micropillar, before final thinning. Vast amounts of material re-deposition is observed around the micropillar. Platinum re-deposition is visibly lighter in color, outlining the micropillar, whereas the Ni-Mo-W re-deposition is darker in color and fills in the empty cavity surrounding the micropillar.

The TEM micrographs are quite complex because of localized deformation at the top portion of the pillar and required non-uniform thinning to achieve the requisite spatial resolution. Tilt angles less than one degree were needed to adequately thin the top portion of the pillar. Once the pillar was sufficiently thinned, the re-deposition was edited out of the TEM micrograph in Figure 4.20a to isolate and focus on the micropillar and its deformation characteristics. The pillar taper angle appears more extreme in the bright field micrograph compared to the 1-2° previously measured, but this is simply an artifact of the thinning protocol.

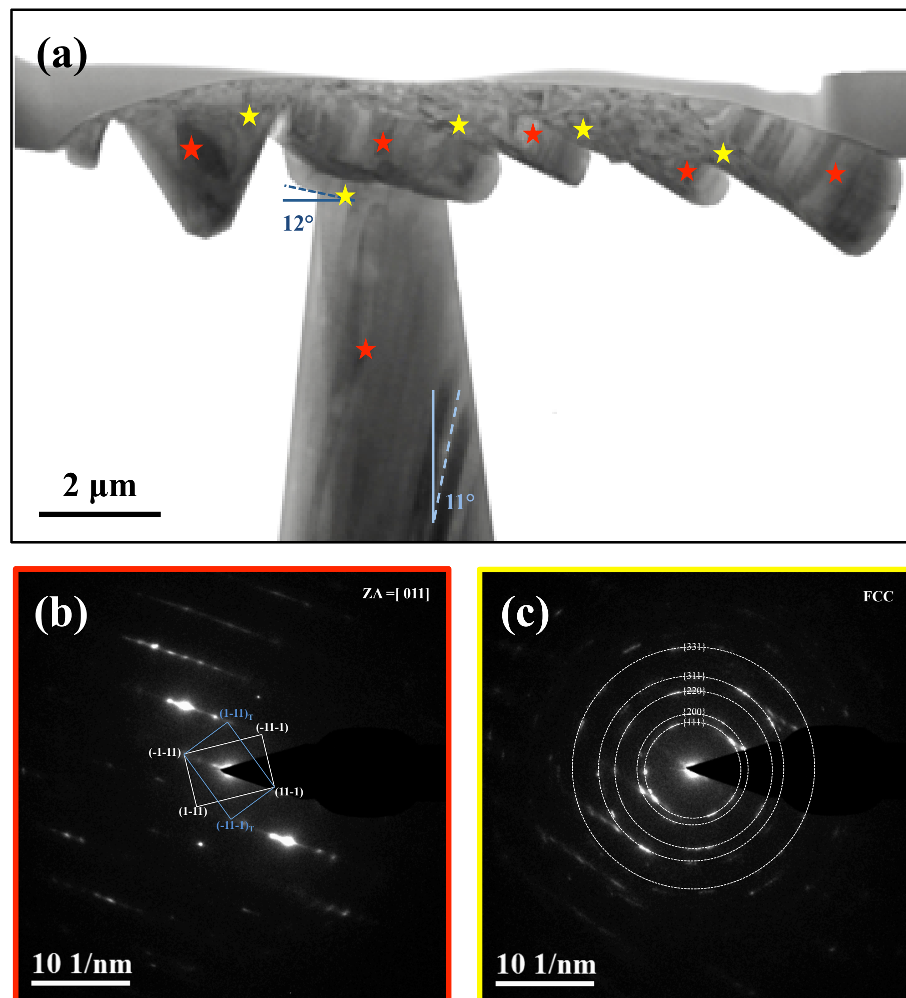

Figure 4.20: (a) Cross-sectional TEM lift-out of a deformed micropillar thinned to electron transparency. The bottom portion of the micropillar displays the tilted columnar gains at an 11° tilt. SAED patterns taken in the starred regions show (b) the nanotwinned (red) and (c) the nanocrystalline (yellow) microstructures.

The tilted columnar grains are visible in the base of the pillar in Figure 4.20a. The large extruded area at the top of the pillar displays discrete regions that sheared off during deformation. The interiors of these sheared regions also appear to maintain the nanotwinned grains, but the boundaries between the sheared regions look different. SAED patterns were collected throughout the micropillar to better characterize the deformed microstructure. Careful analysis of the SAED patterns revealed that the regions that sheared off during deformation did in fact retain their nanotwinned structure. Red stars in Figure 4.20a represent these areas with the associated SAED pattern in Figure 4.20b. Regions of highly concentrated shear deformation, or shear bands, were observed along the boundary between adjacent regions of nanotwinned grains. Investigation of the SAED patterns obtained in these highly sheared regions, indicated by yellow stars in Figure 4.20a, shows that the microstructure recrystallized and no longer contains nanotwins. The representative SAED pattern in Figure 4.20c demonstrates randomly oriented nanocrystalline grains with rings that index to the fcc structure.

Geometric shear bands are commonly described as bands of localized plastic flow that arise from strain softening, without necessarily requiring the material to macroscopically soften [25]. Shear band formation arises from plastic instabilities that develop at high strains and are noted by bands that traverse multiple grain boundaries without deviating on different crystallographic orientations [26]. This description is similar to the phenomenon found for the deformed Ni-Mo-W micropillars. After deforming the micropillars to the first strain burst, an associated shear band extends the entire diameter of the pillar, independent of individual grain orientations (Figure 4.13b). Subsequent deformation causes high hardening rates until an additional shear band is formed, with an associated strain burst (Figure 4.13c).

The incremental deformation behaves in this pattern and the extruded material grows laterally, while the remainder of the pillar shows no signs of plasticity (Figures 4.11, 4.13, 4.14).

ACOM was used to investigate microstructural changes locally at the boundary between the nanocrystalline shear band and neighboring nanotwinned columnar structure. Figure 4.21 shows an inverse pole figure (IPF) map of the first shear band region, overlaid on a bright field micrograph. The crystallographic orientations are rotated to the loading direction, labeled "z". Regions marked (i) indicate the bulk nanotwinned columnar structure that sheared off the pillar during deformation, whereas the region marked (ii) represents the recrystallized shear band microstructure. A reorientation of the initial <111> textured columnar grains occurred without signs of detwinning in region (i). In the portions of the IPF map marked (i), only a few twins were recognized by ACOM due to the resolution of the microscope and spot size. The small average twin spacing of 3.5 nm is just below the detectable limit for ACOM, however, SAED patterns identified nanotwins everywhere in these regions. The columnar grain size measured from ACOM is 91±47 nm, which is in agreement with the as-sputtered grain size of 100 nm.

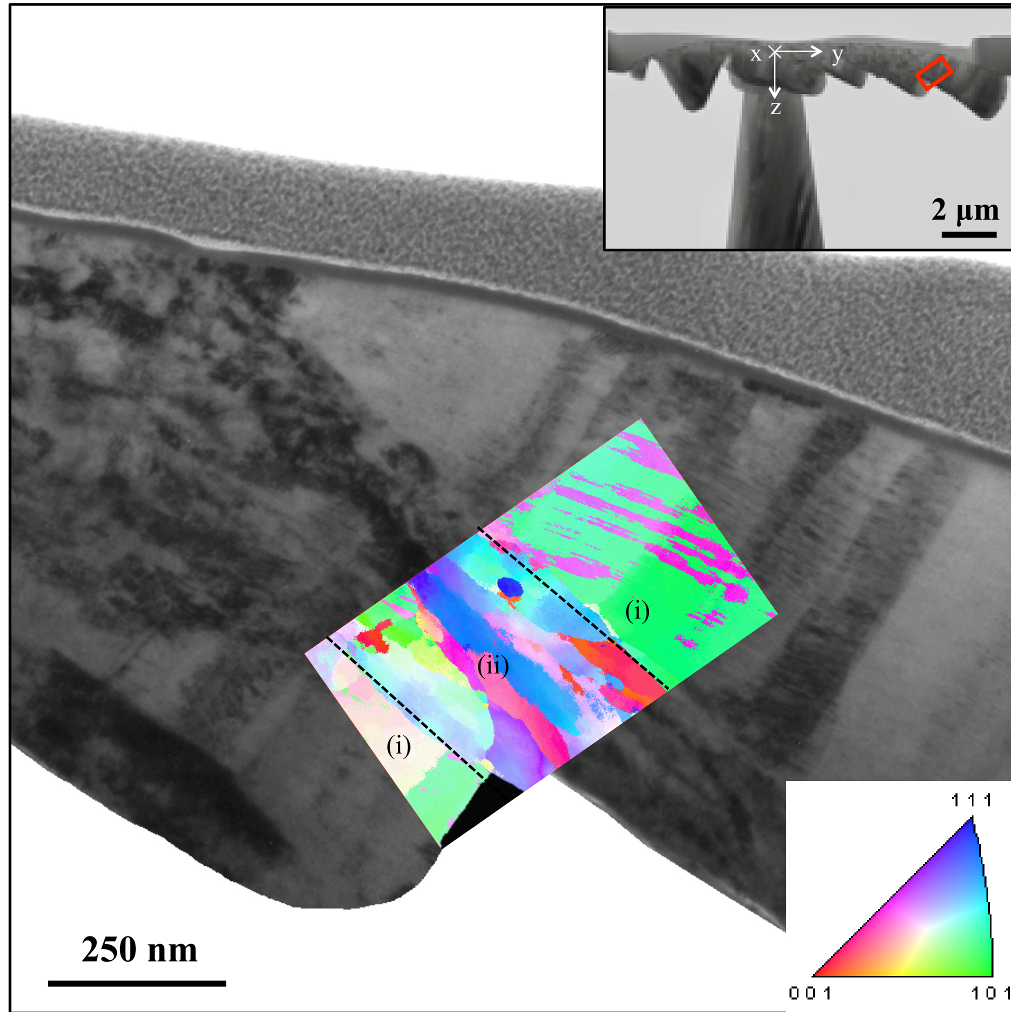

Figure 4.21: Bright field micrograph with IPF mapping from ACOM overlaid in the region of the first shear band. The IPF is shown for the loading direction (z) orientation and the inset is used for location identification. Regions marked (i) indicate columnar grains with nanotwins, whereas regions marked (ii) indicate nanocrystalline fcc shear band, separated by dashed lines.

Region (i) did not indicate any changes in grain size or shape but did rotate 14° as a result of deformation. Combining the deformed columnar grain rotation with the 11° grain tilt of the undeformed pillar, the deformed columnar grains are rotated a total of 25° to achieve perfectly aligned <111> with the loading direction, illustrated in Figure 4.22.

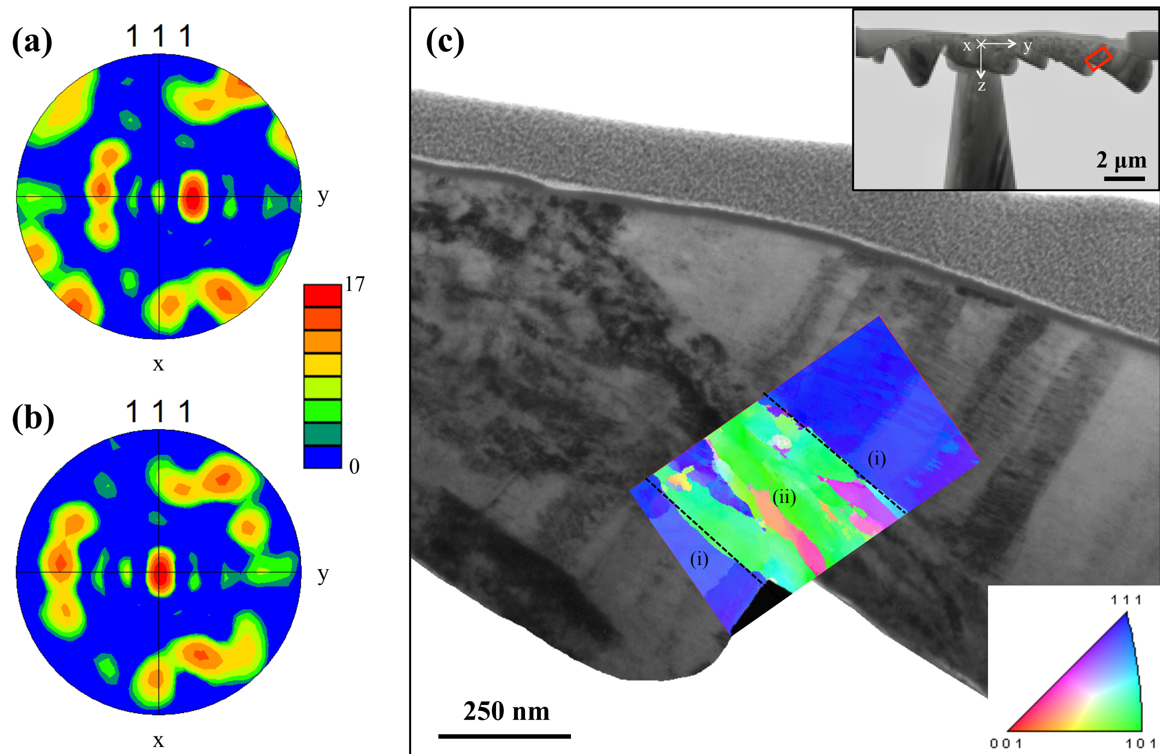

Figure 4.22: (a) Pole figure (PF) for the nanotwinned regions marked (i) in the z-direction and (b) PF for nanotwinned region rotated 25° about the x-direction. (c) Bright field micrograph with the 25° rotated IPF in the z-direction.

The shear band region (ii) displayed a remarkably different microstructure. Within the highly deformed shear band region (ii), the deformation was so intense that the original columnar nanotwinned grains recrystallized to form nanocrystalline grains without any indication of twins. The grains are elongated in the direction of the shear with an aspect ratio nearly 4:1 and average grain size 68.3±38.8 nm. Similar findings have been reported for cold-rolled 70:30 brass, where grains inside a shear band with aspect ratios 2:1-3:1 are elongated in the direction of shear [26, 27]. The directionality of the shear bands with respect to the loading direction is complicated by the incremental deformation caused by the most recent shear band compared to those that were initially formed and subsequently rotated towards the loading direction. Examining the first shear band that formed in Figures 4.21 and

4.22, the 300 nm wide shear band is oriented 45° from the loading. However, examining the final shear band that formed above the base of the micropillar in Figure 4.20a, the shear band is oriented at 78° from the loading direction. The twin boundaries in the pillar are perpendicular to the columnar grains and thus 79° from the loading orientation. Therefore, the final shear band in Figure 4.20a occurred in the direction that is parallel to the twin boundaries.

4.4.3 Hardening and strengthening due to nanotwins

Understanding the high hardening rates of the Ni-Mo-W micropillars requires the consideration of both the very small microstructural features (e.g. 3.5 nm twin spacing) and the moderate micropillar dimensions (e.g. 3 μm diameter). Uchic et al. found that size effects play a considerable role even at large sample sizes, indicating that both the external geometry and the internal structure are pivotal length scale parameters that can be used to characterize the strength of a material [17]. Significant hardening rates have been reported for single crystals with small sample sizes, where a transition from classical Taylor hardening to exhaustion hardening is observed due to a reduction of dislocation sources [19]. Greer et al. suggest that if the conditions for dislocation interaction and multiplication (e.g. Taylor hardening) are not met, the dislocations would leave the small crystals before multiplying, creating a dislocation-starved criteria [28, 29]. From this point of view, each of the strain bursts would correspond to a sudden motion of dislocations moving to the free surface without accumulating inside of the pillar, where the end of the burst event would correspond to the exhaustion of mobile dislocations [30]. Consequently, very high stresses would be necessary to activate a new source and eventually an associated strain burst. Although the observed stress-strain response in Figures 4.10 and 4.12 appear consistent with the

exhaustion hardening mechanism, more than 30 <111> oriented grains span the 3 μm diameter pillars, meaning that the deformation is a true polycrystalline response. It is unlikely that the high density of planar defects would allow dislocations to easily move to the free surface because numerous grain boundaries are present, although it is possible that these grain boundaries could provide such a dislocation source-limited effect.

Because Ni-Mo-W has such a fine 3.5 nm twin spacing, single dislocation-based mechanisms are thought to govern the deformation rather than dislocation pile-up. The transition from classical dislocation pile-up to single dislocation-based mechanisms has been observed in nanoscale multilayers with layer thicknesses on the order of tens of nanometers [31, 32]. Twin boundaries are effective barriers to the transmission of single glide dislocations due to the large geometric misorientation angle between the {111}<110> slip systems on either side of the twin boundary [33]. Zhang et al. investigated the transmission of a single dislocation across a coherent twin boundary in Ni using molecular dynamics (MD) simulations loaded in uniaxial and biaxial tension parallel to the twin boundary [34, 35]. They reported that when loaded under uniaxial tension, a resolved shear stress of 1.77 GPa is required to move a dislocation on a {111} glide plane across the twin boundary interface and onto a complementary {111} glide plane on the other side of the twin boundary [35]. In contrast, loading under biaxial tension provided no net force to move the dislocation from a {111} glide plane across the twin boundary interface to a complementary {111} glide plane [33, 34]. Instead, the dislocation transmits onto an atypical {200} plane and required a very large resolved shear stress (3 GPa) [34]. This resolved shear stress is similar to the yield point of the Ni-Mo-W pillars, except the loading orientations are different. You et al. reported that loading perpendicular to the twin boundaries provides a 10-30% increase in

strength compared to loading parallel to the twin boundaries in Cu [2]. This suggests that the resolved shear stress to transmit a single dislocation across a coherent twin boundary obtained from MD simulations would be even higher when loaded perpendicular to the twin boundaries, closely matching the 3.5 GPa onset of plastic flow observed in the Ni-Mo-W micropillars.

Overall, micropillar compression of nanotwinned Ni-Mo-W revealed the inhomogeneous and highly localized nature of the plasticity. For fcc materials, dislocation plasticity is driven by the {111}<110> slip systems with four possible {111} close packed slip planes. Assuming perfect {111} out-of-plane texture with perpendicular twin boundaries throughout the microstructure, three {111} slip planes are highly inclined to the twin boundaries and one lies parallel to it. As a result, dislocations on the inclined slip planes must cut across the twin boundaries in hard slip mode. Conversely, the {111} slip plane oriented parallel to the twin boundaries allows for easy glide and provides a soft slip mode for dislocation slip. In nanotwinned Cu the hard deformation modes are associated with higher strengths, whereas the soft mode displays enhanced plasticity due to the motion of twin boundaries [2, 36]. The ultrahigh strength observed in the nanotwinned Ni-Mo-W micropillars may be associated with activation of hard slip modes because the loading orientation is nearly perpendicular to the twin boundaries. However, the hard deformation modes require almost no resolved shear stress on the soft mode. It is evident from the deformed micropillars with an 11° tilt (Figures 4.11, 4.13, 4.14) and the well-aligned microstructure (Figure 4.18) that a significant amount of shear is active.

Post-mortem observations of the micropillars with an 11° tilt revealed highly localized and intense shear bands that resulted in recrystallized grains, initiating along the slight twin

boundary misorientation. Hatherly and Malin noted that for metallic materials with twinned microstructures, small crystallites form when aligned twin structures are swept into the shear band, and the bands themselves act as favored sites for nucleation of recrystallized grains [26, 27]. From the TEM investigations in Figures 4.20-4.22, it is likely that the shear band in Ni-Mo-W started along the twin boundary orientation, but after subsequent deformation and recrystallization, it rotated to the plane of maximum shear (45° from the loading direction). However, additional in situ TEM pillar compression experiments are needed to confirm this behavior, the dislocation activity and the role of twin boundary motion with the observed shear banding.

4.5 Chapter summary

In summary, we report the ultrahigh strength of nanotwinned $Ni_{84.4}Mo_{10.7}W_{4.9}$ in compression and the unusual highly localized plasticity governing the deformation. High hardness value 8-9.7 GPa and a small activation volume of $2.82b^3$ were measured via nanoindentation while loading perpendicular to the twin boundaries, underpinned by the finely spaced twin boundaries hypothesized to suppress dislocation glide mechanisms. Local instabilities consistent with shear banding were observed, suggesting concurrent active mechanisms for this loading orientation. Similarly, micropillar compression provided yield strengths of 3.5 GPa, suggesting single dislocation-based mechanisms associated with 3.5 nm twin spacing. However, an extraordinary amount of localized shear and plasticity points to easy dislocation glide mechanisms. The anisotropic nature of the deformation is intimately related to the anisotropic microstructure. Pillar compression perpendicular to the twin boundaries showed highly localized deformation that was symmetric in its lateral shear, while the micropillars with a modest twin inclination displayed highly localized deformation

that was directionally dependent. The resolve shear stress on the twin planes is higher for the inclined orientation, suggesting soft mode dislocation glide. However, no direct evidence of detwinning was observed. Instead, bulk regions of the nanotwinned microstructure sheared laterally, in the direction of the inclined twin boundaries, and a geometric shear band formed. Substantial shear banding was observed to facilitate local softening mechanisms and lateral shear. The physics enabling the formation of shear bands in crystalline Ni-Mo-W films is not fully understood, but the role of the twin orientation is shown to be an important factor.

4.6 References for Chapter 4

1. Jang, D., X. Li, H. Gao, and J.R. Greer, *Deformation mechanisms in nanotwinned metal nanopillars.* Nature nanotechnology, 2012. **7**(9): p. 594-601.
2. You, Z., X. Li, L. Gui, Q. Lu, T. Zhu, H. Gao, and L. Lu, *Plastic anisotropy and associated deformation mechanisms in nanotwinned metals.* Acta Materialia, 2013. **61**(1): p. 217-227.
3. Oliver, W.C. and G.M. Pharr, *An improved technique for determining hardness and elastic modulus using load and displacement sensing indentation experiments.* Journal of materials research, 1992. **7**(6): p. 1564-1583.
4. Lucas, B. and W. Oliver, *Indentation power-law creep of high-purity indium.* Metallurgical and Materials Transactions A, 1999. **30**(3): p. 601-610.
5. Rauch, E. and M. Véron, *Automated crystal orientation and phase mapping in TEM.* Materials Characterization, 2014. **98**: p. 1-9.
6. Schuh, C.A., *Nanoindentation studies of materials.* Materials today, 2006. **9**(5): p. 32-40.
7. Trelewicz, J.R. and C.A. Schuh, *The Hall–Petch breakdown in nanocrystalline metals: a crossover to glass-like deformation.* Acta Materialia, 2007. **55**(17): p. 5948-5958.
8. Carsley, J., A. Fisher, W. Milligan, and E. Aifantis, *Mechanical behavior of a bulk nanostructured iron alloy.* Metallurgical and Materials Transactions A, 1998. **29**(9): p. 2261-2271.
9. Meyers, M.A., A. Mishra, and D.J. Benson, *Mechanical properties of nanocrystalline materials.* Progress in materials science, 2006. **51**(4): p. 427-556.
10. Heckman, N.M., L. Velasco, and A.M. Hodge, *Tensile behavior of fully nanotwinned alloys with varying stacking fault energies.* MRS Communications, 2017. **7**(2): p. 253-258.
11. Hodge, A., T. Furnish, A. Navid, and T. Barbee Jr, *Shear band formation and ductility in nanotwinned Cu.* Scripta Materialia, 2011. **65**(11): p. 1006-1009.
12. Hodge, A., T. Furnish, C. Shute, Y. Liao, X. Huang, C. Hong, Y. Zhu, T. Barbee Jr, and J. Weertman, *Twin stability in highly nanotwinned Cu under compression, torsion and tension.* Scripta Materialia, 2012. **66**(11): p. 872-877.
13. Zhang, G., Y. Liu, W. Wang, and J. Tan, *Experimental evidence of plastic deformation instability in nanoscale Au/ Cu multilayers.* Applied physics letters, 2006. **88**(1): p. 013105.
14. Asaro, R.J. and S. Suresh, *Mechanistic models for the activation volume and rate sensitivity in metals with nanocrystalline grains and nano-scale twins.* Acta Materialia, 2005. **53**(12): p. 3369-3382.

15. Lu, L., R. Schwaiger, Z. Shan, M. Dao, K. Lu, and S. Suresh, *Nano-sized twins induce high rate sensitivity of flow stress in pure copper.* Acta materialia, 2005. **53**(7): p. 2169-2179.

16. Kocks, U. and H. Mecking, *Physics and phenomenology of strain hardening: the FCC case.* Progress in materials science, 2003. **48**(3): p. 171-273.

17. Uchic, M.D., D.M. Dimiduk, J.N. Florando, and W.D. Nix, *Sample dimensions influence strength and crystal plasticity.* Science, 2004. **305**(5686): p. 986-989.

18. Benzerga, A., *An analysis of exhaustion hardening in micron-scale plasticity.* International Journal of Plasticity, 2008. **24**(7): p. 1128-1157.

19. Benzerga, A.A., *Micro-pillar plasticity: 2.5 D mesoscopic simulations.* Journal of the Mechanics and Physics of Solids, 2009. **57**(9): p. 1459-1469.

20. Rao, S.I., D. Dimiduk, T.A. Parthasarathy, M. Uchic, M. Tang, and C. Woodward, *Athermal mechanisms of size-dependent crystal flow gleaned from three-dimensional discrete dislocation simulations.* Acta Materialia, 2008. **56**(13): p. 3245-3259.

21. Kiener, D. and A. Minor, *Source-controlled yield and hardening of Cu (1 0 0) studied by in situ transmission electron microscopy.* Acta Materialia, 2011. **59**(4): p. 1328-1337.

22. Norfleet, D., D. Dimiduk, S. Polasik, M. Uchic, and M. Mills, *Dislocation structures and their relationship to strength in deformed nickel microcrystals.* Acta Materialia, 2008. **56**(13): p. 2988-3001.

23. Ashby, M., *The deformation of plastically non-homogeneous materials.* The Philosophical Magazine: A Journal of Theoretical Experimental and Applied Physics, 1970. **21**(170): p. 399-424.

24. Kiener, D., C. Motz, and G. Dehm, *Micro-compression testing: A critical discussion of experimental constraints.* Materials Science and Engineering: A, 2009. **505**(1-2): p. 79-87.

25. Asaro, R.J., *Geometrical effects in the inhomogeneous deformation of ductile single crystals.* Acta Metallurgica, 1979. **27**(3): p. 445-453.

26. Hatherly, M. and A. Malin, *Shear bands in deformed metals.* Scripta metallurgica, 1984. **18**(5): p. 449-454.

27. Duggan, B., M. Hatherly, W. Hutchinson, and P. Wakefield, *Deformation structures and textures in cold-rolled 70: 30 brass.* Metal Science, 1978. **12**(8): p. 343-351.

28. Greer, J.R. and W.D. Nix, *Nanoscale gold pillars strengthened through dislocation starvation.* Physical Review B, 2006. **73**(24): p. 245410.

29. Greer, J.R., W.C. Oliver, and W.D. Nix, *Size dependence of mechanical properties of gold at the micron scale in the absence of strain gradients.* Acta Materialia, 2005. **53**(6): p. 1821-1830.

30. Ng, K. and A. Ngan, *Stochastic nature of plasticity of aluminum micro-pillars.* Acta Materialia, 2008. **56**(8): p. 1712-1720.

31. Hoagland, R., T. Mitchell, J. Hirth, and H. Kung, *On the strengthening effects of interfaces in multilayer fee metallic composites.* Philosophical magazine A, 2002. **82**(4): p. 643-664.

32. Misra, A., J. Hirth, and H. Kung, *Single-dislocation-based strengthening mechanisms in nanoscale metallic multilayers.* Philosophical Magazine A, 2002. **82**(16): p. 2935-2951.

33. Beyerlein, I.J., X. Zhang, and A. Misra, *Growth twins and deformation twins in metals.* Annual Review of Materials Research, 2014. **44**: p. 329-363.

34. Zhang, X., A. Misra, H. Wang, A. Lima, M. Hundley, and R. Hoagland, *Effects of deposition parameters on residual stresses, hardness and electrical resistivity of nanoscale twinned 330 stainless steel thin films.* Journal of applied physics, 2005. **97**(9): p. 094302.

35. Zhang, X., A. Misra, H. Wang, M. Nastasi, J. Embury, T. Mitchell, R. Hoagland, and J. Hirth, *Nanoscale-twinning-induced strengthening in austenitic stainless steel thin films.* Applied physics letters, 2004. **84**(7): p. 1096-1098.

36. Jang, D., C. Cai, and J.R. Greer, *Influence of homogeneous interfaces on the strength of 500 nm diameter Cu nanopillars.* Nano letters, 2011. **11**(4): p. 1743-1746.

CHAPTER 5: THE EFFECT OF DEPOSITION RATE ON NANOTWIN FORMATION IN Ni-Mo-W

5.1 Introduction

The electrical, thermal and mechanical properties of Ni-Mo-W alloys presented in this thesis rely heavily on the underlying nanotwinned microstructure. This chapter aims to investigate the role of sputter deposition rate on the stability of growth twin formation in Ni-Mo-W alloys. Growth nanotwins have historically been observed in low stacking fault energy (SFE) fcc metals and alloys, with most studies focused on nanotwinned Cu [1-8]. Zhang et al. developed a model to predict the nanotwin formation during sputter deposition, finding that nanotwins will form in either low SFE materials or during very high deposition rates [9]. In addition to forming nanotwins, Lu et al. showed that it was possible to decrease the twin thickness in electrodeposited Cu by either increasing the deposition rate or by decreasing the SFE through alloying with Al or Zn [5].

Pure Ni has a high SFE that inhibits the formation of nanotwins, but there has been some report of nanotwin formation in Ni films deposited at very high rates of 11-30 nm/s [10]. By contrast, the work outlined in this thesis has shown that alloying with Mo and W appears to promote the formation of very fine nanotwins in our Ni-Mo-W system, with deposition rates in the range of 2.2-2.6 nm/s. However, the role of sputter deposition rate on the nanotwin formation in Ni-Mo-W alloys was unknown.

This chapter aims to investigate processing-nanostructure-properties relations for nanotwinned Ni-Mo-W alloys. A fixed alloy chemistry of $Ni_{84}Mo_{11}W_5$ was sputter deposited at different deposition rates between 0.5-2.3 nm/s to determine how the variation of rate affects the nanotwin formation, the defect density and the mechanical behavior of a single

alloy $Ni_{84}Mo_{11}W_5$. X-ray diffraction (XRD) was used to verify the phase and texture of the films, while transmission electron microscope (TEM) was implemented to measure in-plane grain sizes and nanotwin thicknesses. In addition to the governing nanostructure, the compressive yield strength was measured via nanoindentation for films deposited at different deposition rates.

5.2 Materials and methods

Ni-Mo-W thin films were fabricated using two different magnetron sputtering chambers to enhance the spread of direct current (dc) power. The custom sputtering system described in section 2.2.2 was used to deposit $Ni_{84.4}Mo_{10.7}W_{4.9}$ films at a rate of 2.3 nm/s with a dc power of 2500 W, argon (Ar) sputtering gas pressure of 1.0 mTorr and base pressure of 1×10^{-7} Torr. Additional films were deposited using a 3-inch single alloy target of $Ni_{84}Mo_{11}W_5$ and a commercial sputtering chamber AJA International Inc. ATC 1800 UHV located in Jessica Krogstad's laboratory at The University of Illinois Urbana-Champaign. The $Ni_{84}Mo_{11}W_5$ films were deposited onto 4-inch (100) Si wafers at room temperature with deposition rates of 0.5, 0.7 and 0.9 nm/s with a base pressure of 1×10^{-8} Torr. The dc power was varied from 200 to 600 W while the Ar pressure remained a constant 1.0 mTorr. Table 5.1 summarizes the deposition conditions that were investigated.

Table 5.1: Summary of the deposition conditions used for the $Ni_{84}Mo_{11}W_5$ (at. %) films, all deposited at room temperature.

Power [W]	Ar pressure [mTorr]	Film thickness [µm]	Duration [min]	Deposition rate [nm/s]
200	1.0	2.7 ± 0.1	85	0.5
400	1.0	2.6 ± 0.3	60	0.7
600	1.0	2.3 ± 0.2	40	0.9
2500	1.0	21.1 ± 0.2	150	2.3

The phase and crystallographic texture were characterized through XRD and confirmed with TEM-based automated crystal orientation mapping (ACOM) techniques, outlined in section 4.2.3.1. In-plane grain size was measured from TEM specimens prepared using Ar ion milling, with liquid nitrogen to prevent heat-induced damage caused by the ion bombardment. Twin thickness distributions were measured via cross-sectional TEM foils prepared by focused ion beam (FIB) lift-out using FEI Strata DV235 Dual-Beam and FEI Helios G4 UC. Instrumented nanoindentation was used with the Oliver-Pharr method [11] to measure the hardness for the sputtered thin films. A diamond Berkovich indenter tip was used with a 50 mN load cell on the iNano instrument (NanoMechanics Inc.), as discussed in section 4.2.2.1. A constant indentation strain rate of 0.2 s^{-1} was used across 20 indents per thin film. Hardness values were averaged between depths of 200-250 nm from the surface of the film to minimize the substrate effects and surface roughness.

5.3 Microstructural characterization

5.3.1 Texture and grain size

XRD scans of all four as-deposited Ni-Mo-W films showed a dominant peak at 43.4° and a much smaller peak at 95.6°, which corresponds to a single-phase fcc crystal structure with a lattice parameter of 3.61 Å and very strong {111} texture. Figure 5.1 displays the XRD profiles normalized to the (111) peak for ease of comparison. The measured (111) and (222) peaks display a shift from the polycrystalline Ni diffraction peaks, indicating a lattice expansion in the Ni-Mo-W due to the Mo and W atoms dissolved into the Ni lattice.

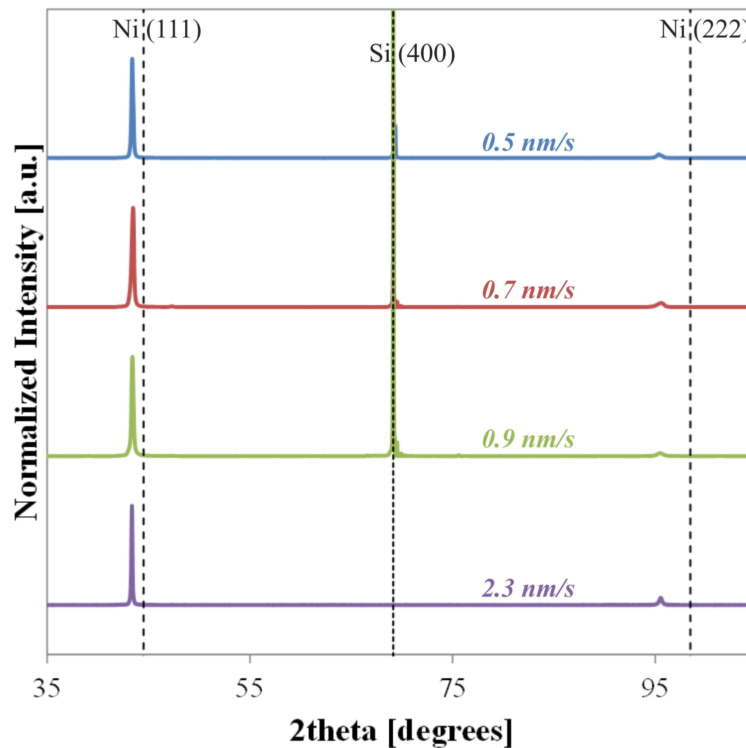

Figure 5.1: XRD data of the Ni-Mo-W films across the deposition rates, with polycrystalline Ni peaks (black) shown for reference. Intensity is normalized to the (111) peak for comparison and a strong (400) Si peak is evident for the films attached to their substrate.

The films sputtered at 2500 W were significantly thicker than those sputtered at lower powers, due to their high deposition rate and longer duration while sputtering (Table 5.1). After deposition, the thicker films deposited at 2500 W were removed from their substrate and investigated as freestanding films. All other films were characterized on their Si substrate, which is evident from the strong (400) Si peak observed in Figure 5.1.

TEM-based ACOM maps confirmed the strong {111} out-of-plane texture across all deposition conditions, illustrated in Figure 5.2, and provided a direct measure of in-plane columnar grain diameters.

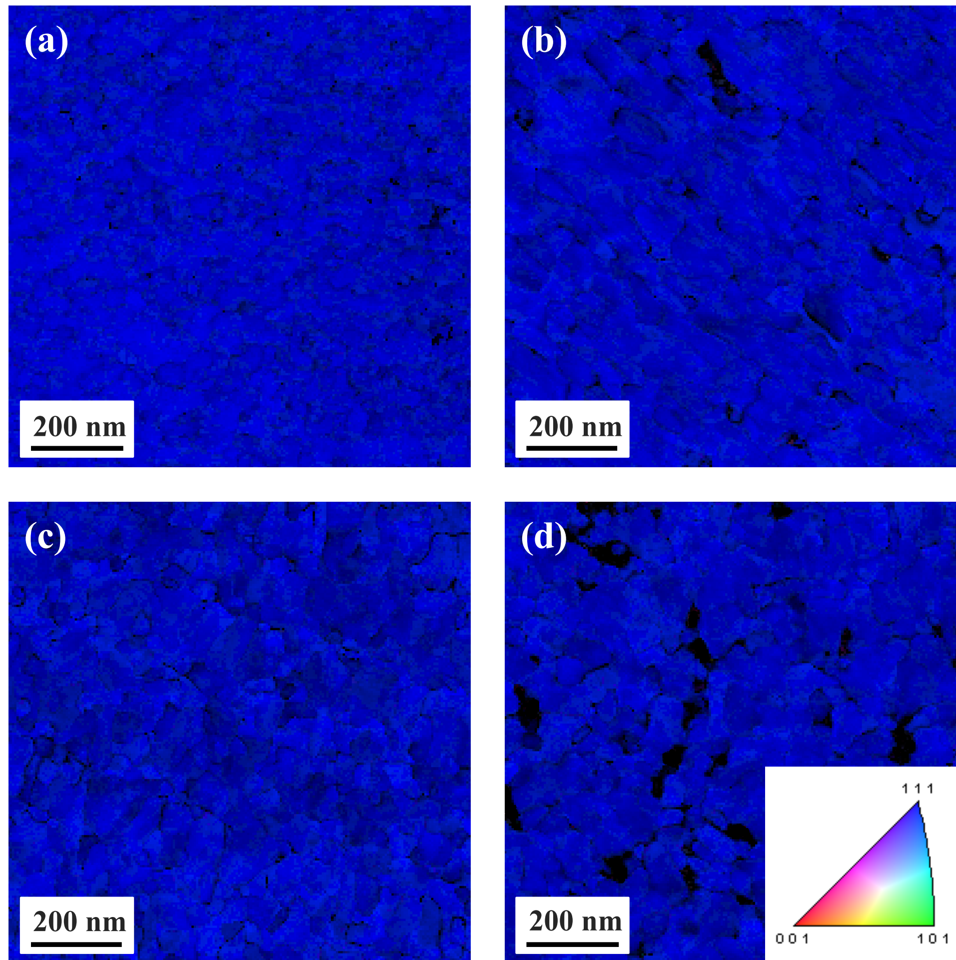

Figure 5.2: Inverse pole figure (IPF) mapping overlaid with the confidence index (CI), showing strong {111} texture oriented parallel to the growth direction, for films sputtered at (a) 0.5, (b) 0.7, (c) 0.9, and (d) 2.3 nm/s.

To better visualize the grain diameter, the in-plane inverse pole figure (IPF) maps are shown in Figure 5.3. The average in-plane grain size is measured using the OIM Analysis^{TM} software, with the method outlined in section 4.2.3.1.

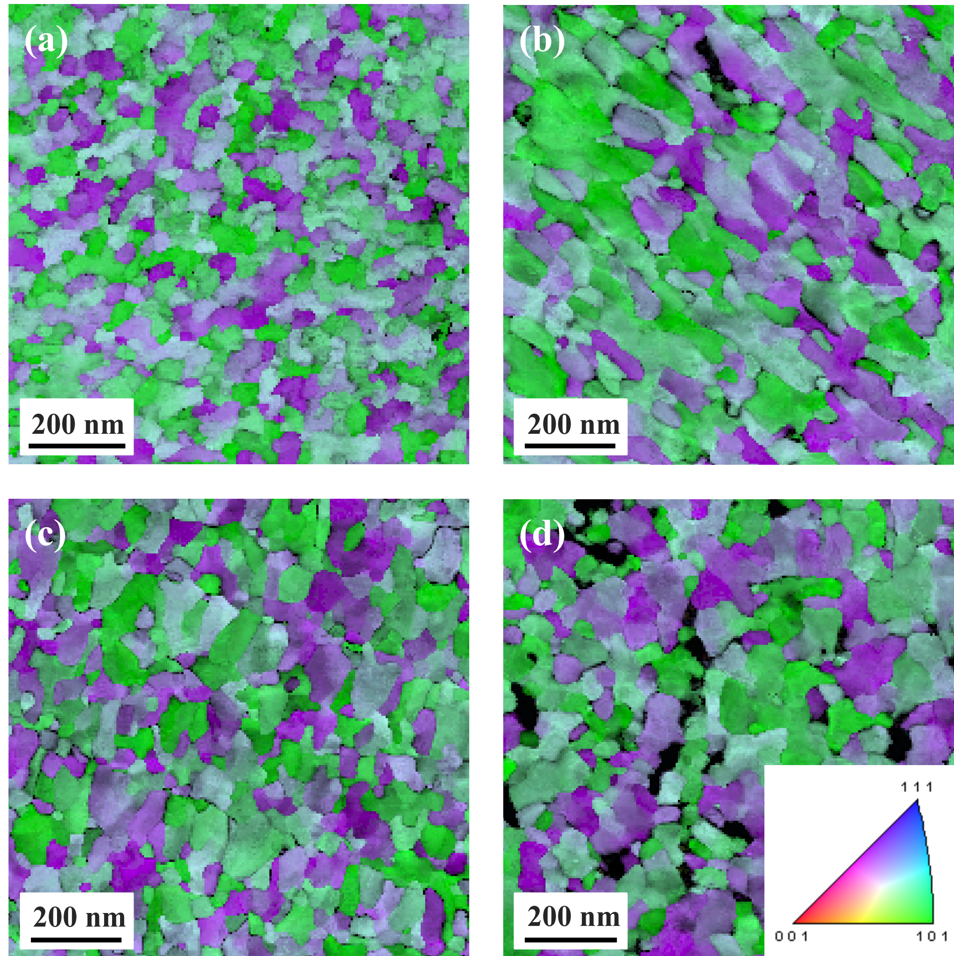

Figure 5.3: IPF mapping overlaid with the CI showing the in-plane direction for films sputtered at (a) 0.5, (b) 0.7, (c) 0.9, and (d) 2.3 nm/s.

The measurements displayed in Figure 5.4 are averaged from two separate scans for each deposition rate in 1.3 μm x 1.3 μm areas. An increase in average grain diameter is observed with increasing deposition rate; the increases do fall within one standard deviation of each other but a constant trend towards larger diameters was observed. During film deposition, atoms are quenched onto the substrate surface with high energy and low surface mobility. As

sputtering continues, modest amounts of heat build up, increasing the overall substrate temperature. Increasing the deposition rate provides higher energy for the atoms impinging on the surface, causing more substrate heating when compared to the lower rates. Thornton has shown that films sputtered with a low homologous temperature (T/T_m) have an increase in columnar width as the temperature increases [12, 13], similar to the observed grain sizes in Figure 5.4. Higher temperatures lead to grain growth and it is worth noting that the average diameter of the grains in the films sputtered at 2500 W were 50% larger than those sputtered at 200 W.

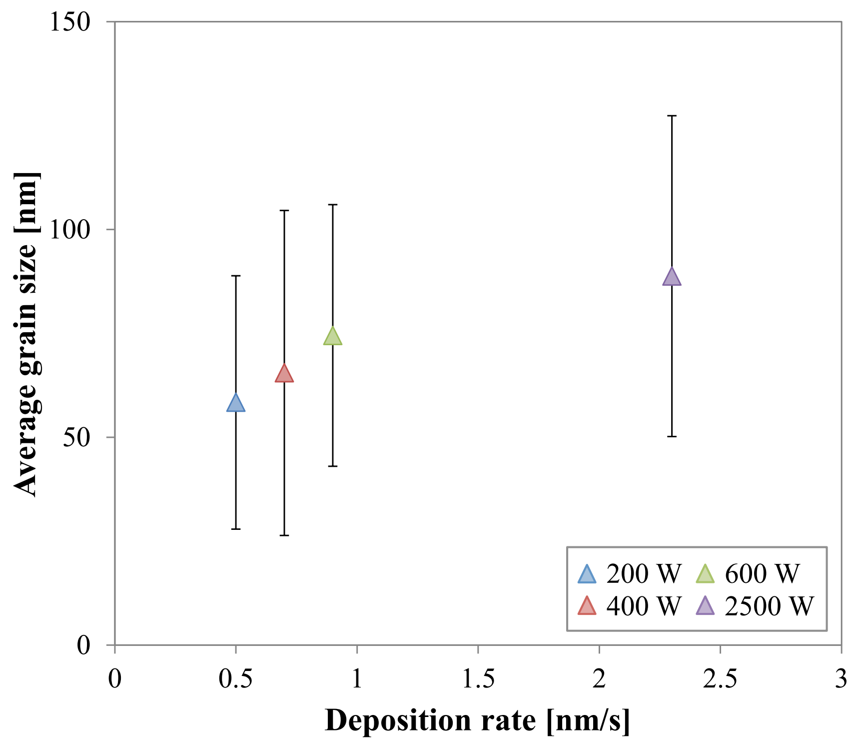

Figure 5.4: Average in-plane grain size for the films sputtered at different deposition rates. The error bars represent one standard deviation from the average grain size.

5.3.2 Nanotwin thickness

Bright field TEM images and selected area electron diffraction (SAED) patterns in Figure 5.5 were used to investigate the nanotwinned microstructure in the as-deposited films. Long columnar grains were observed parallel to the growth direction and a very high density of planar features was found to be oriented perpendicular to the growth direction and along a (111) plane.

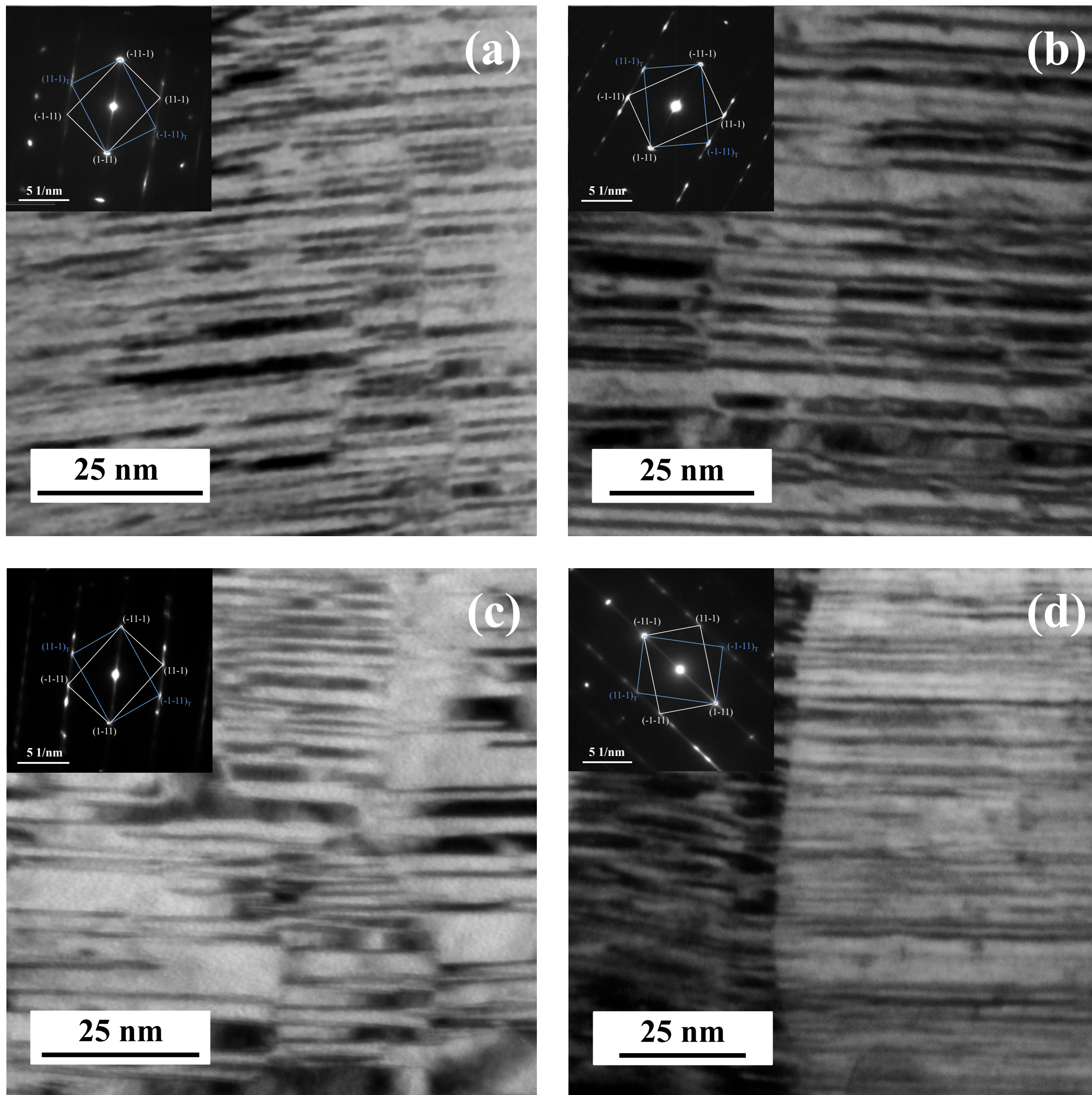

Figure 5.5: Bright field TEM micrographs of the films sputtered at (a) 0.5, (b) 0.7, (c) 0.9 and (d) 2.3 nm/s with upward growth direction. Insets of SAED patterns on the [011] zone axis are indexed for twin and matrix orientations.

SAED patterns confirmed the presence of nanotwins, see for example the insets in Figure 5.5, which were all indexed for both the matrix and the twin orientations. Notable streaking of the diffraction spots, indicative of the presence of stacking faults, are also observed. The bright field micrographs were used to measure the twin thickness by mapping the gray scale intensity across twin boundaries, as shown in Figure 5.6. A region was selected with a linear line (Figure 5.6b) and the gray scale intensity from black (0) to white (255) was plotted as a function of the distance along the prescribed line (Figure 5.6a). The edge-to-edge distance between adjacent peaks was measured and recorded as the twin thickness. This procedure was repeated for more than 100 twins in multiple grains for each deposition condition and the distributions are illustrated in Figure 5.7. All deposition rates displayed fine nanotwin thicknesses, below 11 nm, and their average values are shown in Figure 5.8. The average twin thickness was found to be less than 4 nm across the deposition conditions with minimal variations as a function of deposition rate.

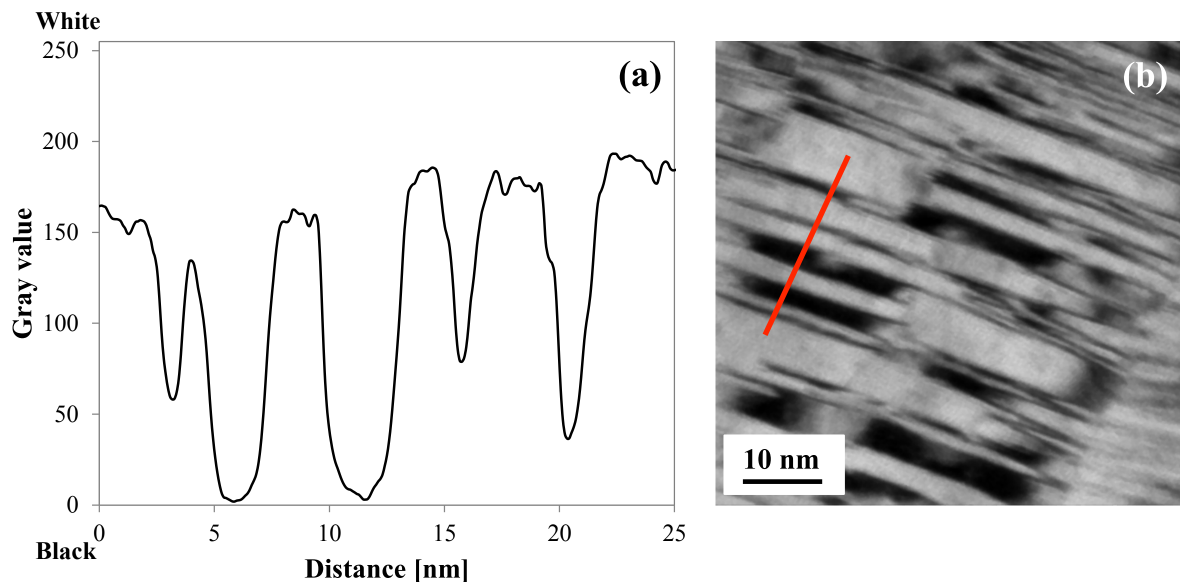

Figure 5.6: (a) Representative gray scale intensity used to measure the twin thickness from (b) along the red line in the bright field micrograph for films sputtered at a deposition rate of 0.9 nm/s.

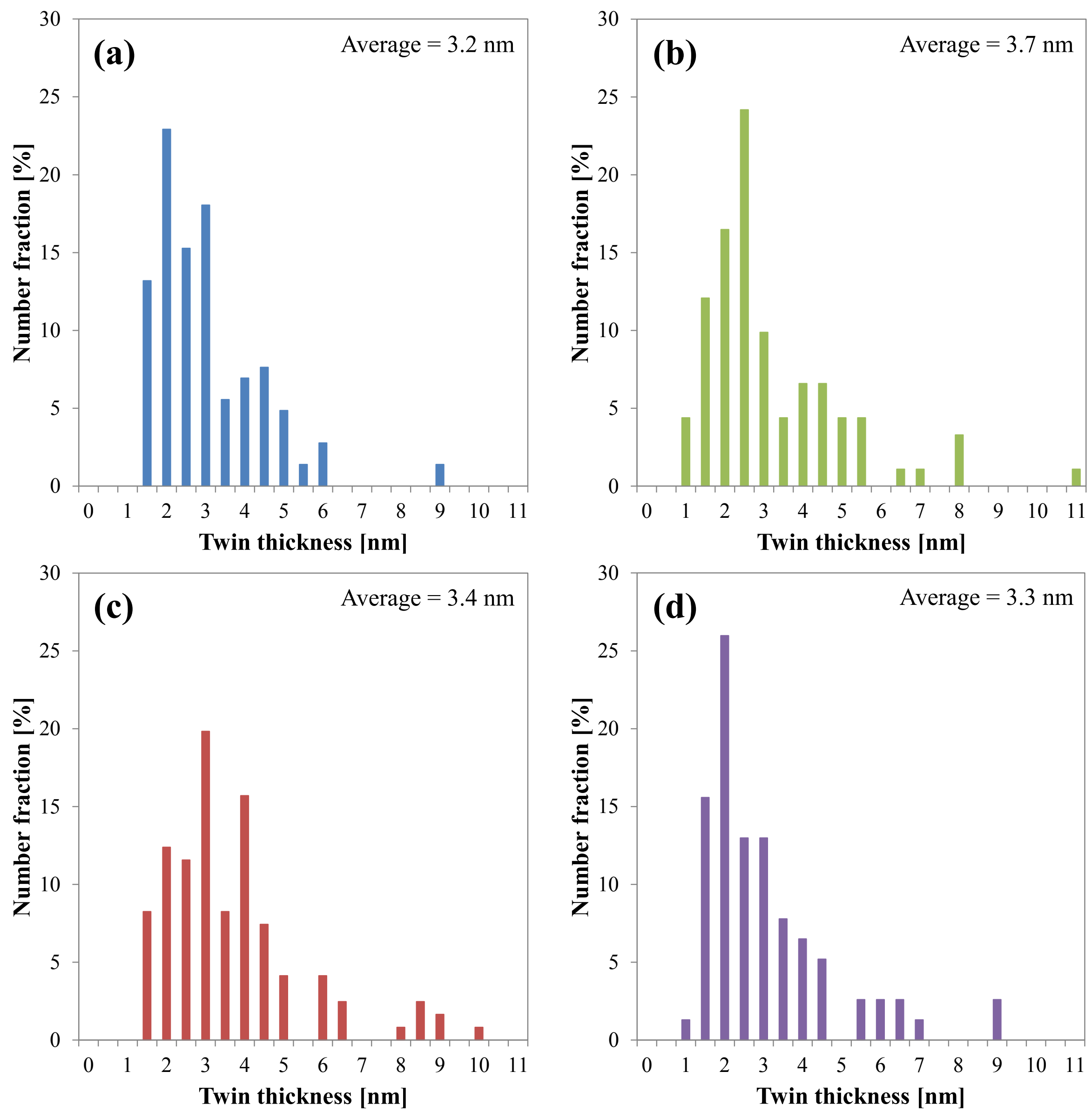

Figure 5.7: Distribution of nanotwin spacing for films sputtered at (a) 0.5, (b) 0.7, (c) 0.9, and (d) 2.3 nm/s.

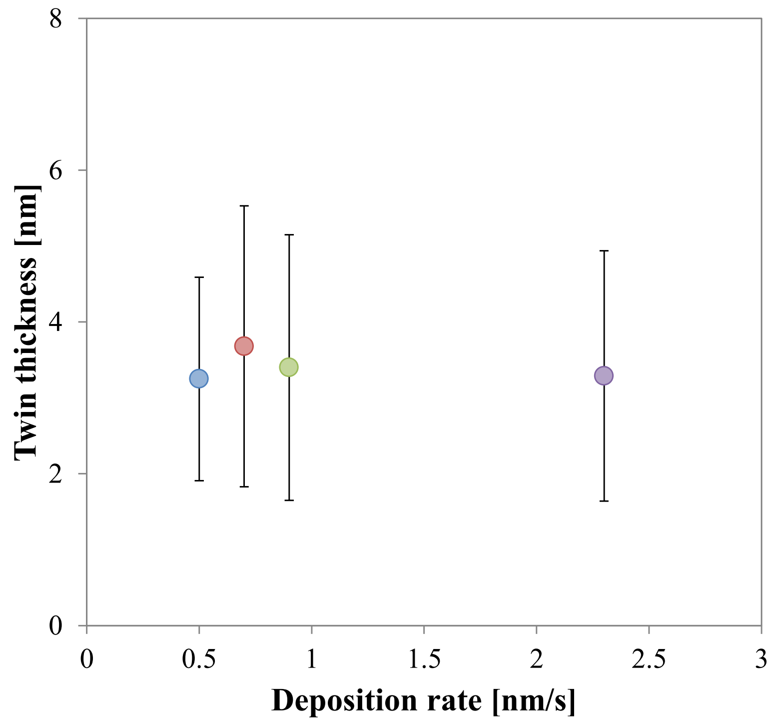

Figure 5.8: The average nanotwin thickness as a function of deposition rate, with error bars representing one standard deviation.

5.4 Mechanical strength

The hardness was measured to assess the effect of the nanotwinned microstructure on the overall mechanical response of the Ni-Mo-W films. Figure 5.9 displays the surface impressions from the indentation experiments, showing ridges consistent with shear banding [14, 15], as discussed in section 4.3. Figure 5.10 gives the average hardness across all deposition rates. The relation between hardness (H) and yield strength (σ_y), $H = 3\sigma_y$, was used to estimate the compressive yield strengths of the films, reported in Table 5.2.

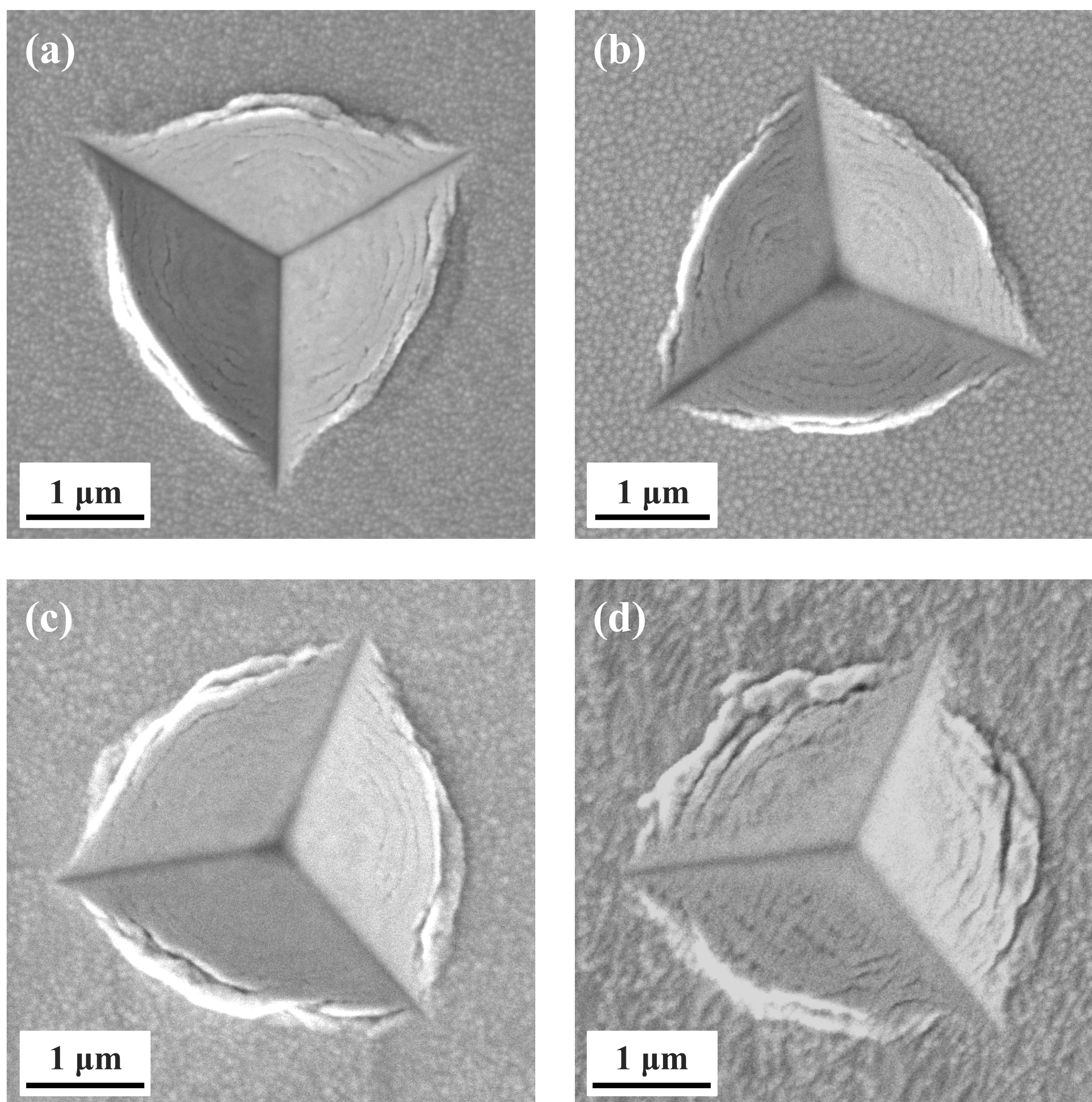

Figure 5.9: Scanning electron microscopy (SEM) micrographs of the surface impressions left behind from nanoindentation for films with deposition rates (a) 0.5, (b) 0.7, (c) 0.9, and (d) 2.3 nm/s.

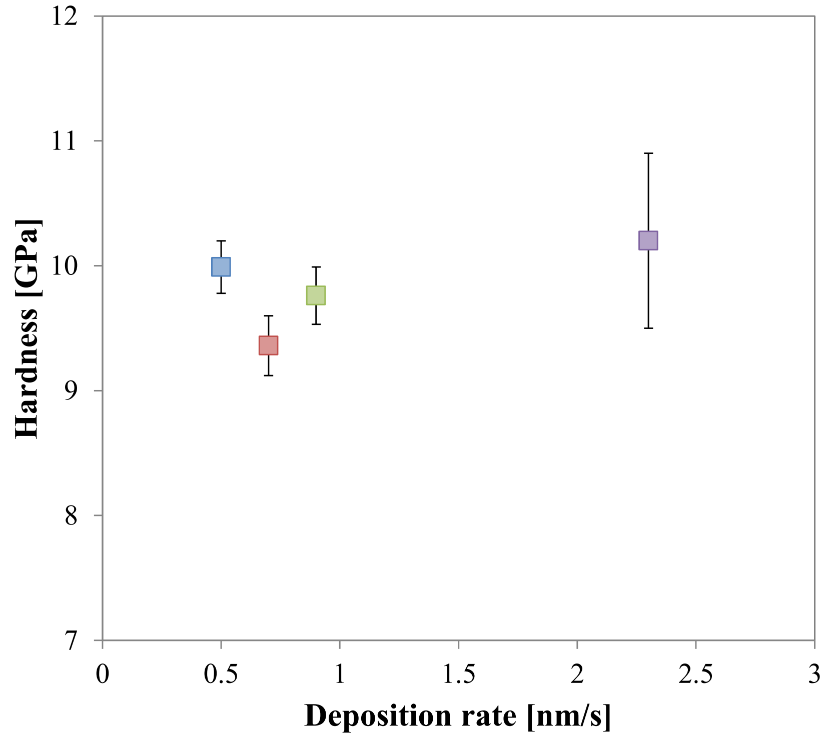

Figure 5.10: The hardness measured from instrumented nanindentation as a function deposition rate, with error bars representing one standard deviation.

Table 5.2: A summary of the in-plane grain size, nanotwin thickness, hardness and calculated compressive yield strength as a function of deposition rate.

Deposition rate [nm/s]	In-plane grain size [nm]	Twin thickness [nm]	Hardness [GPa]	Compressive yield strength [GPa]
0.5	58.4 ± 30.5	3.2 ± 1.3	9.9 ± 0.2	3.3 ± 0.1
0.7	65.5 ± 39.1	3.7 ± 1.9	9.4 ± 0.2	3.1 ± 0.1
0.9	74.5 ± 31.5	3.4 ± 1.8	9.8 ± 0.2	3.3 ± 0.1
2.3	88.8 ± 38.6	3.3 ± 1.7	10.2 ± 0.7	3.4 ± 0.2

The average compressive yield strength for the $Ni_{84}Mo_{11}W_5$ alloy was measured to be greater than 3.1 GPa for all deposition rates, which is similar to what was reported for more Mo-rich $Ni_{83.6}Mo_{14}W_{2.4}$ [16, 17] and similar to the micropillar compressive strength observed in Chapter 4. The measured compressive yield strength is more than 3x higher than that of sputter deposited Ni [10] and even 1.5x higher than sputter deposited Ni-base superalloy 718 [18]. The compressive yield strength of Ni-Mo-W is also 2-3x higher than what has been reported for nanostructured materials, such as nanocrystalline Ni [19] and nanotwinned Cu [2, 6, 20].

The ultrahigh strength of nanotwinned metals has been closely associated with dislocation interactions with the twin boundaries (TBs) and the orientation of the TBs relative to the applied load [4, 8]. Of the four possible {111} slip planes, only one is oriented parallel to the highly-aligned TBs and capable of easy glide. The other three are inclined to the TBs and dislocation glide on them requires cutting of TBs; they are commonly referred to as hard modes of deformation. For the nanoindentation performed in this study, the loading direction is perpendicular to the TBs, but the stress state under the indenter tip is complicated and contains multiple components of stress that likely activates multiple deformation modes. Thus, the yield strength estimated from nanoindentation would contain and be representative of the hard deformation modes.

5.5 Microstructural stability

The Ni-Mo-W films deposited with a range of deposition rates between 0.5-2.3 nm/s showed consistent nanotwin thickness and high compressive yield strengths, independent of the deposition rate. Table 5.2 illustrates that the measurable variations in twin thickness and hardness cannot be attributed to changes in the deposition rate. Instead, the twin thickness

appears inversely proportional to the hardness, such that smaller twin thicknesses produce slightly higher hardness values. Ott et al. investigated the effect of deposition rates 1.5-5.4 nm/s on sputter deposited Ag, finding that there were no changes in twin thickness across these different rates, but there was a change in twin density and texture that attributed to a variation in strength [21]. At the lower deposition rates, they found more randomly textured grains with less twin density across the films, contributing to a decrease in strength [21]. This phenomenon was not observed in the Ni-Mo-W alloy deposited in this study at even lower rates of 0.5-0.9 nm/s. The XRD results in Figure 5.1 show consistent strong {111} texture, without any other diffraction peaks present. Similar texture was observed in the IPF maps in Figure 5.2 and quantified using the pole figure (PF) for each ACOM scan in Figure 5.11, suggesting that the Ni-Mo-W films have good texture stability over a large range of deposition conditions 0.5-2.3 nm/s.

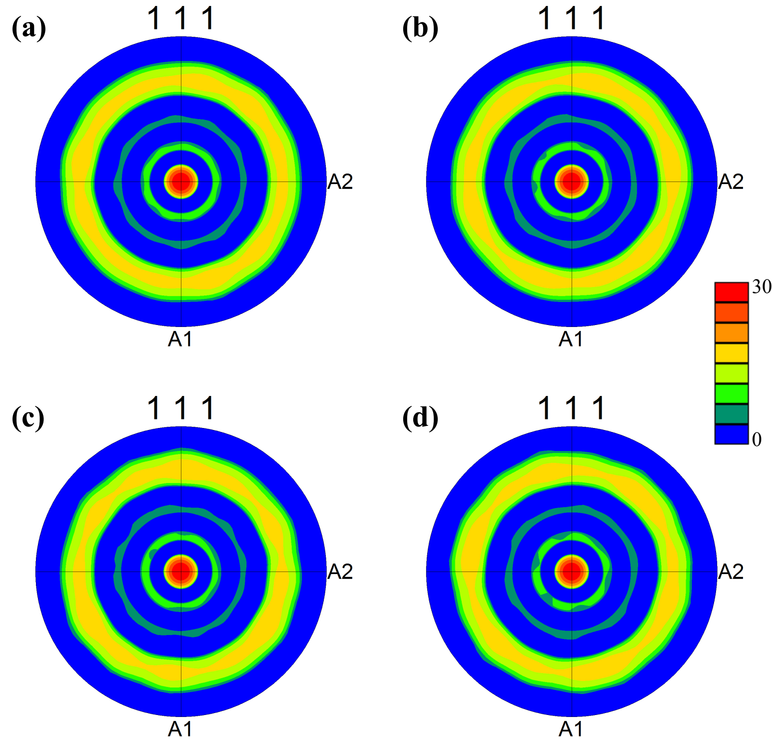

Figure 5.11: PF showing strong texture of the {111} columnar grains for films with deposition rates (a) 0.5, (b) 0.7, (c) 0.9, and (d) 2.3 nm/s.

Similarly, nanotwin formation was demonstrated to be extremely stable over these deposition rates. A representative low magnification bright field micrograph in Figure 5.12 displays a high density of nanotwins throughout the many columnar grained structures for the lowest deposition rate, 0.5 nm/s. The high density of finely spaced nanotwins and the high hardness values suggest that the underlying nanostructure is distributed throughout the columnar grains for all deposition conditions. Thus, this $Ni_{84}Mo_{11}W_5$ alloy has a broad stability range (0.5-2.3 nm/s) for nanotwin formation, where the grains remained strongly {111} textured with a high twin density and strength.

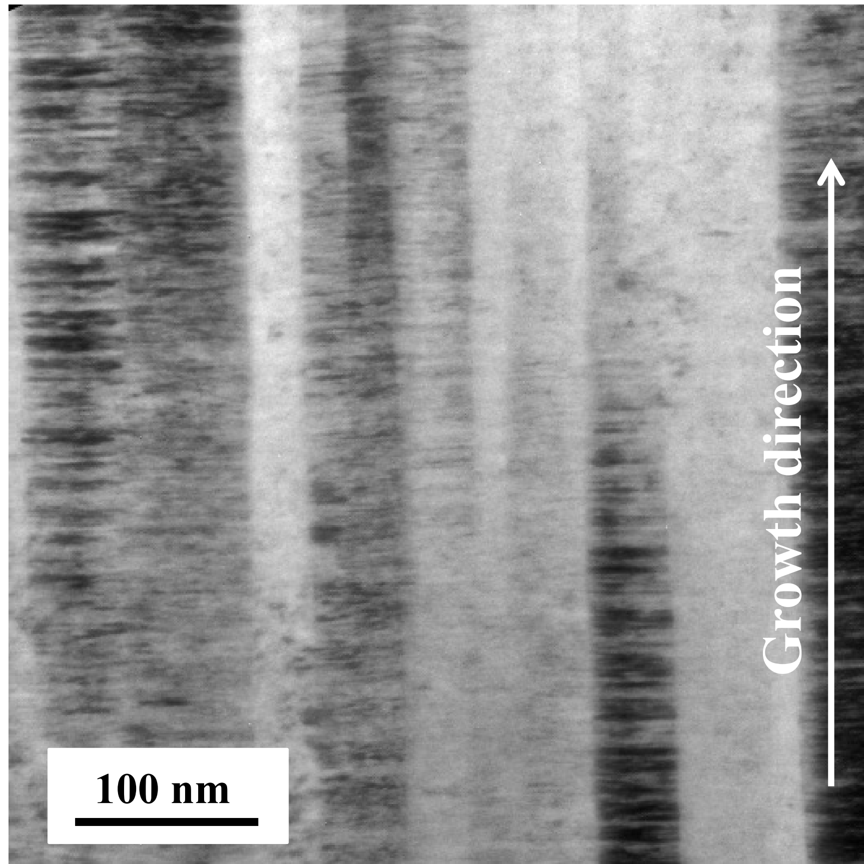

Figure 5.12: Representative low-magnification bright field micrograph from the films deposited at 0.5 nm/s, indicating a high density of nanotwins spanning across several grains.

The mechanistic reason behind this broad stability range for nanotwin formation is not clear, but a re-evaluation of the growth twin formation will help speculate. Shang et al. performed first-principles calculations of 26 different alloying elements with Ni and found that Mo and W were two of the most effective elements in reducing the SFE of pure Ni, which is reported as 130 mJ/m^2 [22]. For a composition of binary alloy $Ni_{71}X_{29}$, the DFT simulations suggest that alloying with Mo and W reduced the SFE to 102 mJ/m^2 and 104 mJ/m^2, respectively [22]. It is predicted that the twin boundary energy (γ_t) is half of the SFE [23], which would equate to approximately 50 mJ/m^2 for binary $Ni_{71}Mo_{29}$ and $Ni_{71}W_{29}$ alloys. In comparison, low SFE materials such as silver and copper have SFE of 22 mJ/m^2 and 78 mJ/m^2, respectively [24, 25]. Zhang et al. used an analytical model to understand growth twin formation by calculating the critical radius of perfect nucleus and twinned nucleus as a function of deposition rate and SFE [9]. Coupling this model with experiments for 330 austenitic stainless steel, Zhang et al. found that twin densities and strength decreased when deposition rates were 0.2 nm/s and below [26]. The yield strength and nanotwin formation of the Ni-Mo-W films explored were invariant to the sputter deposition rate in the range of 0.5-2.3 nm/s. These deposition rates are within the region of stability that Zhang et al. reported, suggesting that Ni-Mo-W may have a similar SFE as the 330 austenitic stainless steel, $\gamma_t = 20$ mJ/m^2 [26]. Although there is evidence that binary Ni-Mo and Ni-W alloys have lower SFE than Ni, it has not been quantified for the atomic chemistry of ternary $Ni_{84}Mo_{11}W_5$.

5.6 Chapter summary

In summary, $Ni_{84}Mo_{11}W_5$ films were deposited at a range of deposition rates, 0.5-2.3 nm/s, and characterized to determine the effect of nanotwin formation on the compressive

yield strength. Films were highly {111} textured in the growth direction with similar in-plane grain sizes. Very fine nanotwins were observed in all films with no apparent change in twin density. High compressive yield strengths of 3.1-3.4 GPa were uniform in the range of explored deposition rates, purportedly governed by the dislocation interactions with the 3.2-3.7 nm spaced twins. The results suggest that the deposition rate is less significant in the formation of nanotwins and enhanced strength for the Ni-Mo-W alloys than the alloy chemistry. Alloying with Mo and W appears to reduce the SFE as compared to pure Ni, which enables ubiquitous nanotwin formation. The prolific formation of the nanotwins precludes use of deposition rate as a means for tailoring twin spacing or density and attendant mechanical properties, but it does provide a wide processing window for making nanotwinned Ni-Mo-W films for MEMS devices.

5.7 References for Chapter 5

1. Anderoglu, O., A. Misra, H. Wang, and X. Zhang, *Thermal stability of sputtered Cu films with nanoscale growth twins.* Journal of Applied Physics, 2008. **103**(9): p. 094322.
2. Dao, M., L. Lu, Y. Shen, and S. Suresh, *Strength, strain-rate sensitivity and ductility of copper with nanoscale twins.* Acta Materialia, 2006. **54**(20): p. 5421-5432.
3. Hodge, A., T. Furnish, C. Shute, Y. Liao, X. Huang, C. Hong, Y. Zhu, T. Barbee Jr, and J. Weertman, *Twin stability in highly nanotwinned Cu under compression, torsion and tension.* Scripta Materialia, 2012. **66**(11): p. 872-877.
4. Jang, D., X. Li, H. Gao, and J.R. Greer, *Deformation mechanisms in nanotwinned metal nanopillars.* Nature nanotechnology, 2012. **7**(9): p. 594-601.
5. Lu, K., L. Lu, and S. Suresh, *Strengthening materials by engineering coherent internal boundaries at the nanoscale.* Science, 2009. **324**(5925): p. 349-352.
6. Lu, L., Y. Shen, X. Chen, L. Qian, and K. Lu, *Ultrahigh strength and high electrical conductivity in copper.* Science, 2004. **304**(5669): p. 422-426.
7. Lu, N., K. Du, L. Lu, and H. Ye, *Motion of 1/3 ⟨ 111 ⟩ dislocations on Σ3 {112} twin boundaries in nanotwinned copper.* Journal of Applied Physics, 2014. **115**(2): p. 024310.
8. You, Z., X. Li, L. Gui, Q. Lu, T. Zhu, H. Gao, and L. Lu, *Plastic anisotropy and associated deformation mechanisms in nanotwinned metals.* Acta Materialia, 2013. **61**(1): p. 217-227.
9. Zhang, X., A. Misra, H. Wang, T. Shen, M. Nastasi, T. Mitchell, J. Hirth, R. Hoagland, and J. Embury, *Enhanced hardening in Cu/330 stainless steel multilayers by nanoscale twinning.* Acta Materialia, 2004. **52**(4): p. 995-1002.
10. Dahlgren, S., W. Nicholson, M. Merz, W. Bollmann, J. Devlin, and R. Wang, *Microstructural analysis and tensile properties of thick copper and nickel sputter deposits.* Thin Solid Films, 1977. **40**: p. 345-353.
11. Oliver, W.C. and G.M. Pharr, *An improved technique for determining hardness and elastic modulus using load and displacement sensing indentation experiments.* Journal of materials research, 1992. **7**(6): p. 1564-1583.
12. Thornton, J.A., *Influence of substrate temperature and deposition rate on structure of thick sputtered Cu coatings.* Journal of Vacuum Science and Technology, 1975. **12**(4): p. 830-835.
13. Thornton, J.A., *High rate thick film growth.* Annual review of materials science, 1977. **7**(1): p. 239-260.
14. Schuh, C.A., *Nanoindentation studies of materials.* Materials today, 2006. **9**(5): p. 32-40.

15. Trelewicz, J.R. and C.A. Schuh, *The Hall–Petch breakdown in nanocrystalline metals: a crossover to glass-like deformation.* Acta Materialia, 2007. **55**(17): p. 5948-5958.

16. Sim, G.-D., J.A. Krogstad, K.M. Reddy, K.Y. Xie, G.M. Valentino, T.P. Weihs, and K.J. Hemker, *Nanotwinned metal MEMS films with unprecedented strength and stability.* Science Advances, 2017. **3**(6): p. e1700685.

17. Sim, G.-D., J.A. Krogstad, K.Y. Xie, S. Dasgupta, G.M. Valentino, T.P. Weihs, and K.J. Hemker, *Tailoring the mechanical properties of sputter deposited nanotwinned nickel-molybdenum-tungsten films.* Acta Materialia, 2018. **144**: p. 216-225.

18. Burns, D.E., Y. Zhang, T.P. Weihs, and K.J. Hemker, *Properties of sputter deposited Ni-base superalloys for microelectromechanical systems.* Thin Solid Films, 2014. **558**: p. 20-23.

19. Schwaiger, R., B. Moser, M. Dao, N. Chollacoop, and S. Suresh, *Some critical experiments on the strain-rate sensitivity of nanocrystalline nickel.* Acta materialia, 2003. **51**(17): p. 5159-5172.

20. Lu, L., R. Schwaiger, Z. Shan, M. Dao, K. Lu, and S. Suresh, *Nano-sized twins induce high rate sensitivity of flow stress in pure copper.* Acta materialia, 2005. **53**(7): p. 2169-2179.

21. Ott, R., J. Geng, M. Besser, M. Kramer, Y. Wang, E. Park, R. LeSar, and A. King, *Optimization of strength and ductility in nanotwinned ultra-fine grained Ag: Twin density and grain orientations.* Acta Materialia, 2015. **96**: p. 378-389.

22. Shang, S., C. Zacherl, H. Fang, Y. Wang, Y. Du, and Z. Liu, *Effects of alloying element and temperature on the stacking fault energies of dilute Ni-base superalloys.* Journal of Physics: Condensed Matter, 2012. **24**(50): p. 505403.

23. Murr, L., *Temperature coefficient of twin-boundary energy: The determination of stacking-fault energy from the coherent twin-boundary energy in pure FCC metals.* Scripta Metallurgica, 1972. **6**(3): p. 203-208.

24. Bernstein, N. and E. Tadmor, *Tight-binding calculations of stacking energies and twinnability in fcc metals.* Physical Review B, 2004. **69**(9): p. 094116.

25. Murr, L.E., *Interfacial phenomena in metals and alloys.* 1975.

26. Zhang, X., O. Anderoglu, A. Misra, and H. Wang, *Influence of deposition rate on the formation of growth twins in sputter-deposited 330 austenitic stainless steel films.* Applied physics letters, 2007. **90**(15): p. 153101.

CHAPTER 6: FABRICATION AND CHARACTERIZATION OF Ni-Mo-W MICROCANTILEVER BEAMS

6.1 Introduction

The majority of this thesis work was spent on characterizing and understanding the outstanding balance of physical and mechanical properties of nanotwinned Ni-Mo-W alloys. However, the motivation for synthesizing Ni-Mo-W alloys is grounded in the ability to integrate them into high temperature microelectromechanical systems (MEMS) applications. This chapter focuses on moving beyond the exceptional suite of properties to demonstrate the feasibility of fabricating prototype MEMS device structures. Cantilever beams are the most ubiquitous structures in MEMS, with applications in sensors, actuators, switches and resonators [1, 2]. Because of their widespread use, the attention will be focused on fabricating Ni-Mo-W cantilever structures.

Silicon-based MEMS cantilevers currently dominate the industry and are commonly fabricated in cleanrooms to control the level of contaminants introduced during the fabrication process. Any organic matter introduced to MEMS devices can impact the reliability and function due to the size of the contaminants relative to the micrometer sized features. In addition, these particles can act as insulators and cause an electrical short circuit during use, diminishing the quality and function of the device. Cleanrooms are subjected to different classifications, quantified by the number of particles per cubic meter. If we consider particle sizes greater than 500 nm, the everyday air we breathe contains more than 30 million particles per cubic meter. In comparison, typical MEMS fabrication is performed in class 100 cleanrooms, where the maximum particle content is only 3.5 thousand per cubic meter [3]. Depending on the device sensitivity to contaminants, industries sometimes require use of

class 10 cleanrooms that have only 350 particles per cubic meter [3], but these concentrations are extremely expensive to maintain. All Ni-Mo-W fabrication techniques outlined in this chapter were carried out in a class 100 cleanroom to demonstrate the applicability of conventional MEMS fabrication methods. This work was carried out at the Singh Center for Nanotechnology at the University of Pennsylvania.

Exceptional dimensional stability and control is required for MEMS sensors and actuators [4, 5] but can be difficult to achieve. Previous studies on metallic Ni components have demonstrated the micromachining capabilities needed to fabricate microcantilever beams [6-10], but their relatively low temperature microstructural instabilities limited widespread use [11, 12]. The primary goal and achievement of this chapter is to demonstrate that the robust mechanical and thermal properties of nanotwinned Ni-Mo-W thin films can translate into high temperature MEMS structures. This chapter describes the detailed fabrication process and requisite characterization to ensure flat and stable microcantilever beams with required dimensional control.

6.2 Fabricating Ni-Mo-W microcantilevers

6.2.1 Blanket thin films

Direct current (dc) magnetron sputtering chambers were used to deposit Ni-Mo-W thin films, and various powers and argon (Ar) pressures were used to control the residual stresses. All thin film fabrication was performed in one of two commercial sputtering chambers: an AJA International Inc. ATC 1800 UHV, located at the University of Illinois Urbana Champaign (UIUC) in Professor Jessica Krogstad's laboratory (Figure 6.1a) and a Kurt J. Lesker Pro Line PVD 75, located at The University of Pennsylvania's (UPenn) Singh Caner for Nanotechnology (Figure 6.1b). The two chambers were equipped with a centralized gun

at the bottom of the chamber to hold a 3-inch single alloy target of $Ni_{84}Mo_{11}W_5$ (at. %) from ACI Alloys, Inc. A custom order was placed from WRS Materials for (100) Si wafers with 100 mm diameter and 300±25 μm thickness were double-side polished and 300±15 nm of super low stress silicon nitride (Si_3N_4) was deposited on both sides via low pressure chemical vapor depositions (LPCVD). The Ni-Mo-W thin films were deposited at room temperature with a base pressure of 10^{-7}-10^{-8} Torr and a substrate rotation of 40 rpm. These deposition conditions were held constant throughout the different deposition runs. A wide range of dc powers (200-600 W) and Ar pressures (1-4 mTorr) were explored to produce nominally 2.5 μm thick films.

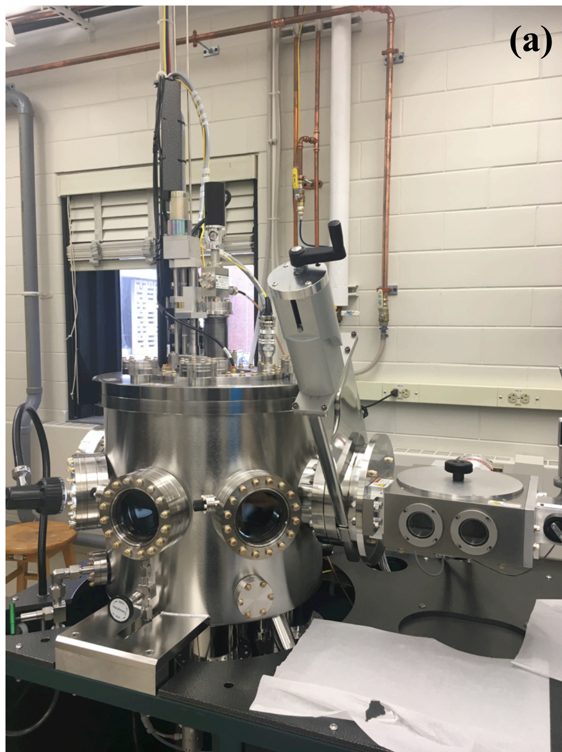

Figure 6.1: (a) AJA International Inc. ATC 1800 UHV located at UIUC in Jessica Krogstad's laboratory and (b) Kurt J. Lesker Pro Line PVD 75 located inside the cleanroom at UPenn Singh Center for Nanotechnology.

Ni-Mo-W films for previous studies had been sputtered at high power (2500 W) in a custom chamber with a low Ar pressure of 1 mTorr and contained a strong {111} out-of-plane texture with a very fine nanotwinned microstructure, as detailed in Chapters 2-4. The current study was undertaken to survey lower and more conventional powers to determine if the desirable texture and nanotwins were still present. Initial characterization of the sputter-deposited thin films was performed prior to any microfabrication. Focused ion beam (FIB) lift-out techniques were employed to make electron transparent foils for transmission electron microscopy (TEM). Bright field micrographs and selected area electron diffraction (SAED) patterns provided a direct indication of the underlying as-sputtered microstructure. Representative cross-sectional TEM images taken from a film deposited at 400 W with 1 mTorr Ar pressure are shown in Figure 6.2. The entire film thickness is captured in Figure 6.2a and long columnar grains parallel to the growth direction are clearly visible. These columnar grains start at the substrate with no evidence of a nanocrystalline seed layer at the substrate-film interface. Higher magnification images of the columnar grains provide clear evidence of nanotwins (Figures 6.2b and 6.2c), which was confirmed by SAED pattern analysis, as shown in Figure 6.2d. Similar microstructures and planar defects were observed for all films sputtered in the specified power and pressure range (200-600 W and 1-4 mTorr) for this study. More detailed microstructural analysis was provided previously in Chapter 5. The broad processing window for sputtering nanotwinned Ni-Mo-W ensures robust control of the material composition, microstructure and properties for commercial deposition protocols.

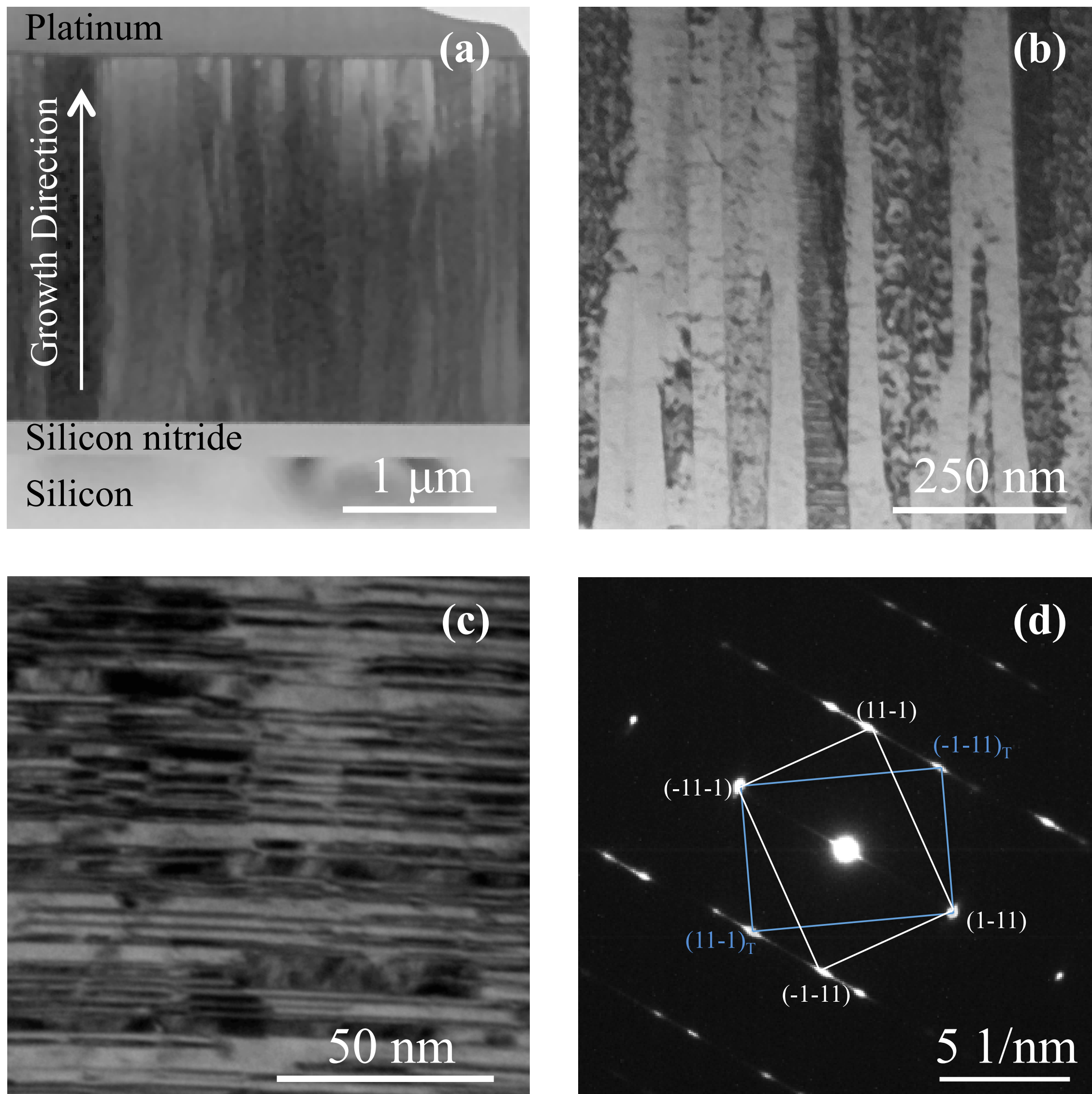

Figure 6.2: TEM micrograph of (a) entire film thickness on 300 nm of silicon nitride and silicon, (b) magnified bright field image of columnar grain with (c) magnified view of nanotwins and (d) the associated selected area electron diffraction pattern indexed for the matrix and twins.

The effect of Ar sputtering gas pressure is important in the development of the overall film microstructure and physical properties [13-15]. An overview of the stresses in sputtered deposited films is necessary to understand the choice of 1-4 mTorr Ar pressures. Ohring provides a detailed analysis on the development of internal stresses in sputtered films and the correlation with the deposition parameters [13]. A brief review of important sources of stress and their effect of the Ni-Mo-W films are outlined below:

i. **CTE mismatch between substrate and film**: For a film deposited at elevated temperature with a different CTE than the substrate, a misfit strain develops when the system is cooled back to room temperature due to the CTE mismatch. For the Ni-Mo-W films sputtered at room temperature, minor substrate heating of less than 15°C was observed. As a result, stresses due to CTE mismatch are expected to be a small contribution in this study.

ii. **Grain growth**: Room temperature deposition of materials with high melting temperatures results in low adatom mobility during the sputtering process and tensile stresses develop. Use of a high Ar pressure further decreases the adatom mobility, creating more tensile stresses. However, decreasing the Ar pressure has an associated increase in the mean free path for the sputtered atoms. This allows for less atomic collisions so that atoms are more energetic when arriving at the substrate, with increased adatom mobility and compressive stresses. The development of growth stress in the Ni-Mo-W is expected to be the most important contribution during deposition.

Figure 6.3a shows the relative contributions of the intrinsic stress compared to the stresses due to CTE mismatch, as a function of deposition temperature. The growth stress is expected to have the largest impact on the Ni-Mo-W films with small contributions from the CTE mismatch. The goal of tuning the Ar pressure variable during deposition was to transition the internal stresses from highly tensile to moderately compressive. Ohring describes this compressive transition to have films with near-bulk values of electrical resistivity, deposited with parameters of low Ar pressure, high-mass sputtering target (Ni-Mo-W) and low deposition rates [13]. From Figure 6.3b the transition Ar pressure is predicted to be 3 mTorr for Ni. Hence, the small window of Ar pressures investigated was restricted to 1-4 mTorr in this study. Wafer curvature was used to quantify the average residual stress of the as-deposited films. Curvature profiles were obtained using a KLA Tencor P7 2 Profilometer (Figure 6.4). Measurements were taken on the Si/Si_3N_4 substrate both before and after Ni-Mo-W deposition to isolate the film stresses, Figure 6.5. The Stoney equation [16, 17] was used to calculate the film stresses reported in Table 6.1. Deposition rates varied from 0.4-1 nm/s and the sputter duration was adjusted to achieve ~2.5 μm thick films. In these specified power and pressure ranges, all films had a compressive stress state with representative wafer curvature profile shown in Figure 6.5 concave down.

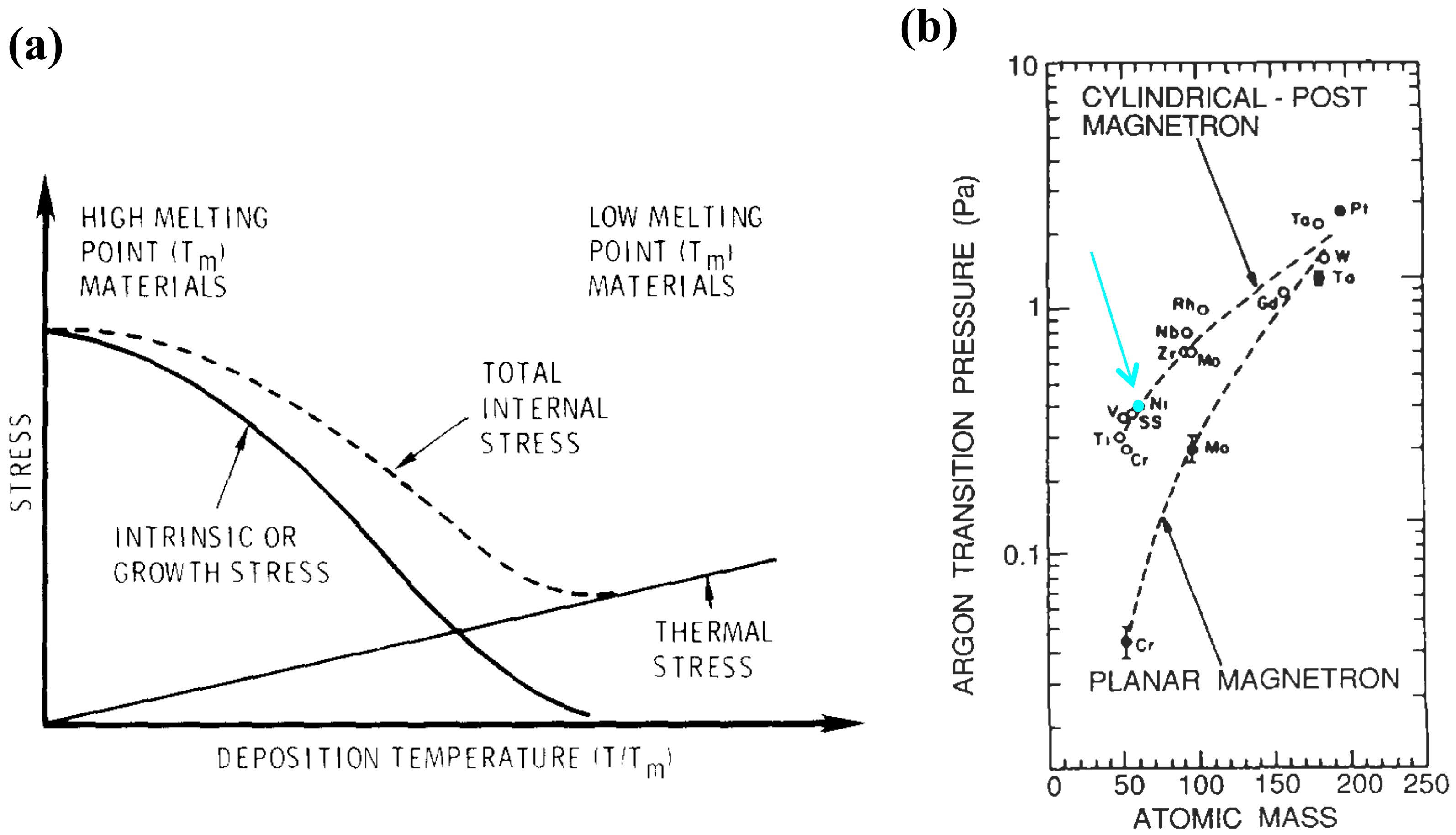

Figure 6.3: (a) The relative contributions from the intrinsic growth stress compared to the CTE thermally induced stress [15]. (b) The tensile to compressive transition Ar pressure for different sputter deposited metals, adapted from [13], highlighted for Ni.

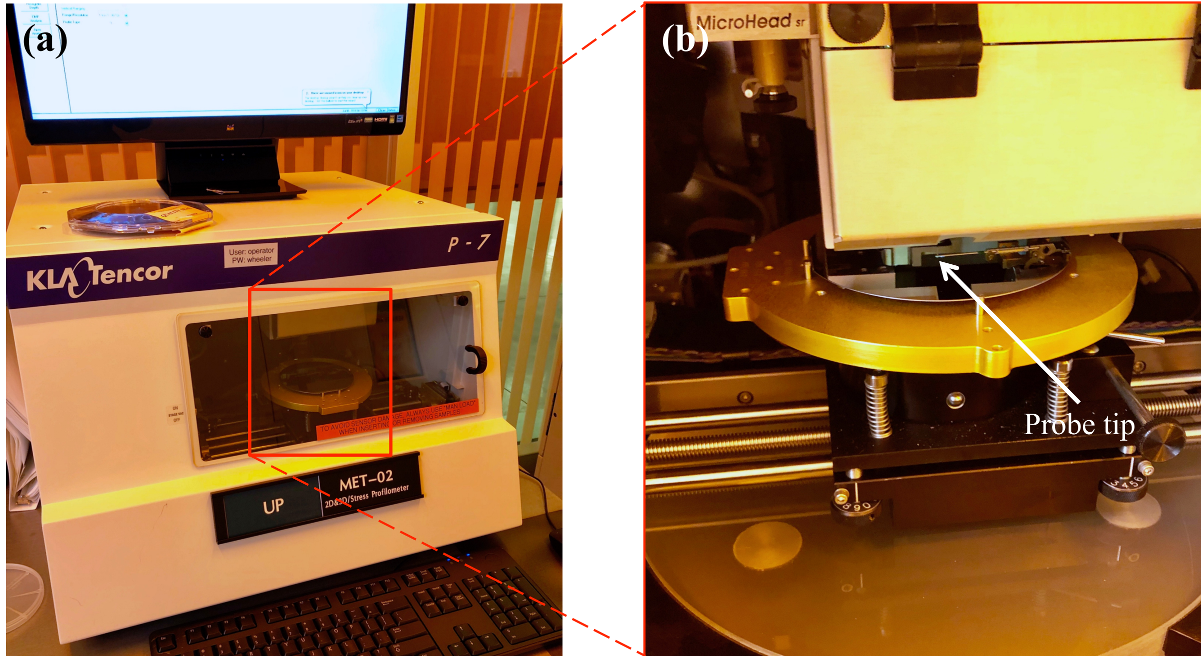

Figure 6.4: (a) KLA Tencor P7 2 Profilometer located inside the cleanroom at UPenn Singh Center for Nanotechnology and (b) magnified image of the probe tip scanning a silicon wafer to measure its curvature.

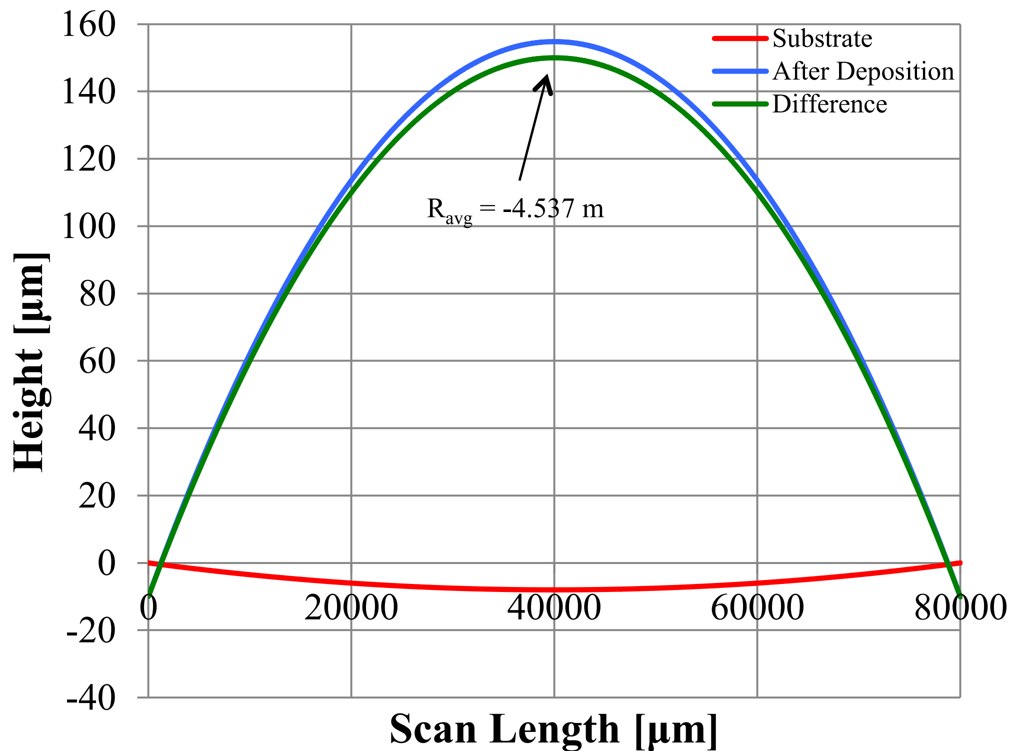

Figure 6.5: Wafer curvature measurement for the blank Si/Si_3N_4 substrate, the curvature after Ni-Mo-W film deposition and the difference between the two. The Ni-Mo-W has an average radius of curvature -4.537 m, used to calculate the residual stress.

Table 6.1: Average film stress from wafer curvature measurements for various Ni-Mo-W films as-deposited. Deposition rates calculated from ~2.5 μm thick films with dc powers 200-600 W and Ar gas pressures 1-4 mTorr.

Power [W]	Ar pressure [mTorr]	Deposition rate [nm/s]	Average film stress [MPa]
200	3	0.46	-249
200	3.5	0.55	-221
200	4	0.57	-181
400	1	0.91	-405
400	2	0.88	-386
400	3.5	0.83	-267
600	1	1.10	-467

6.2.2 Micromachining

Blanket $Ni_{84}Mo_{11}W_5$ films were patterned, etched and shaped in a class 100 cleanroom using conventional semiconductor device fabrication techniques. Figure 6.6 outlines the general microfabrication process, but the full procedure can be found in Appendix 3. Blank Si wafers were coated with Si_3N_4 to provide a potassium hydroxide (KOH) etch stop (Step 1), followed by $Ni_{84}Mo_{11}W_5$ sputter deposition (Step 2). Photolithography was used to pattern the front side of the wafer with the sputtered film using a chromium mask (Figures 6.7a and b), consisting of arrays of cantilever beams with different aspect ratios, to determine the effect of geometry on the dimensional stability. The lithographic mask was donated by General Electric Global Research (GEGR) for use at Johns Hopkins University.

(1) ***Nitride (300 nm) coated Si wafer***

(2) ***Sputter Ni-Mo-W***

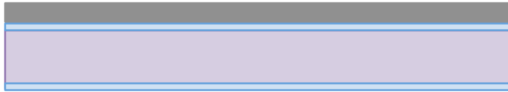

(3) ***Front & back lithography***

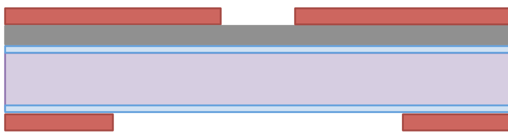

(4) ***Wet etch Ni-Mo-W, back side RIE***

(5) ***KOH etch from back***

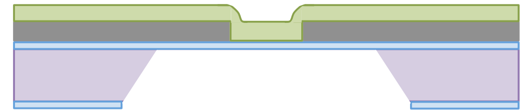

(6) ***RIE from back***

Si Si_3N_4 Ni-Mo-W S1818 ProTEK B3

Figure 6.6: Process for fabricating micro-cantilever beams though lithography and etching blanket Ni-Mo-W thin films.

The design of the chromium mask combines cantilevers of varying lengths (0.01-1 mm) and widths (10-100 μm) with a constant spacing of 100 μm between adjacent beams. Positive photoresist S1818 (Microposit) was spin-coated onto the front of the Ni-Mo-W film and exposed to UV light using the lithographic mask to pattern the shape the film (Step 3). Ni-Mo-W films were selectively wet etched using Nichrome etchant TFN (Transene Inc.) at 40°C to achieve an etch rate of 104±21 nm/min. For this etch rate, 25 minutes was sufficient to etch through the entire 2.5 μm thick Ni-Mo-W film. The Nichrome etchant only etched the Ni-Mo-W films, producing perpendicular sidewalls with no visible undercut, as shown in Figure 6.8. Once the fully etched structures were formed, the photoresist was removed and profilometer scans were used to determine the thickness of the cantilever beams.

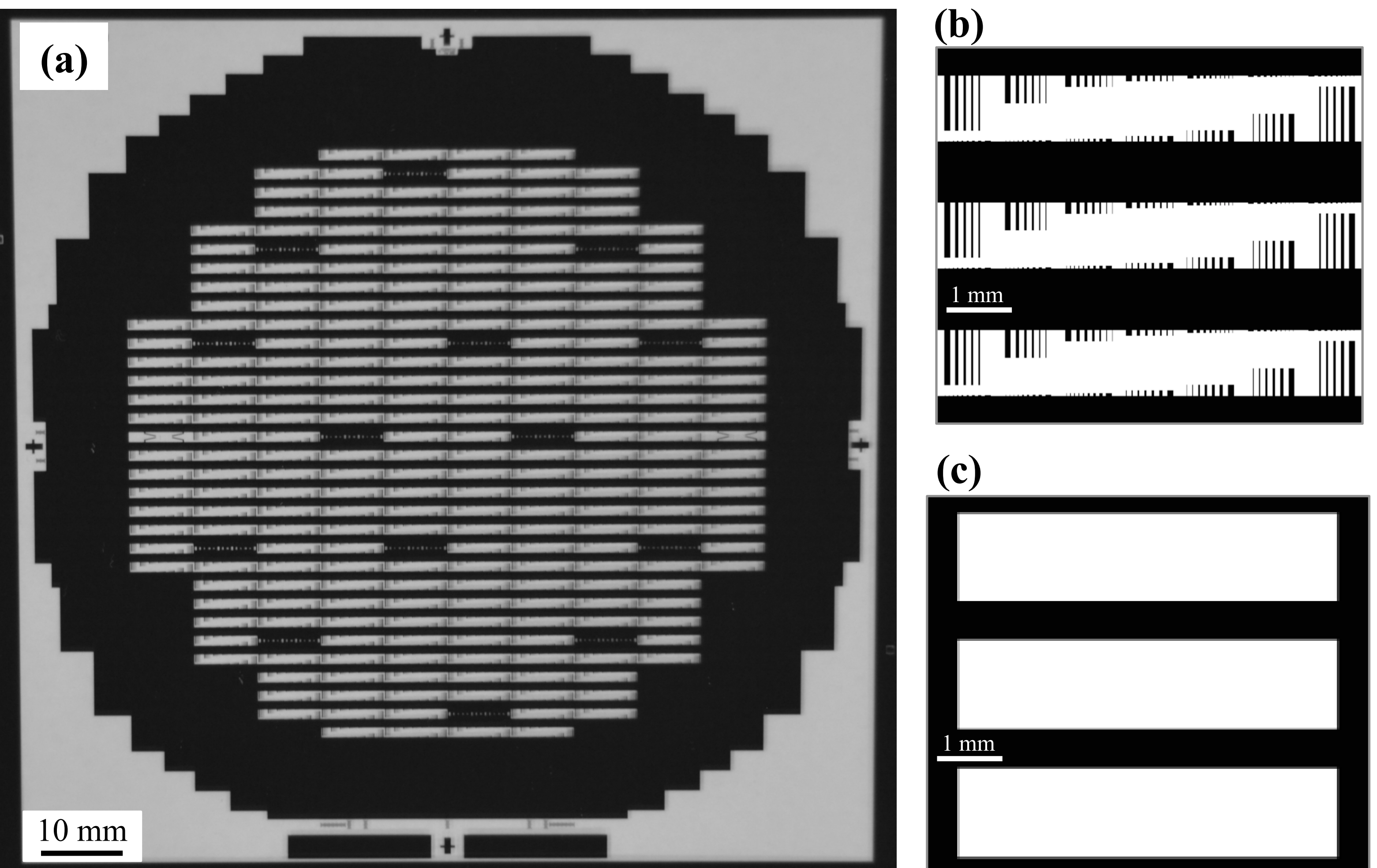

Figure 6.7: (a) Front chromium lithographic mask consisting of hundreds of arrays of microcantilevers, donated from GEGR. (b) Repeated arrays of micro-cantilever beams from the front chromium lithographic mask. (c) Empty windows representing the back lithographic mask.

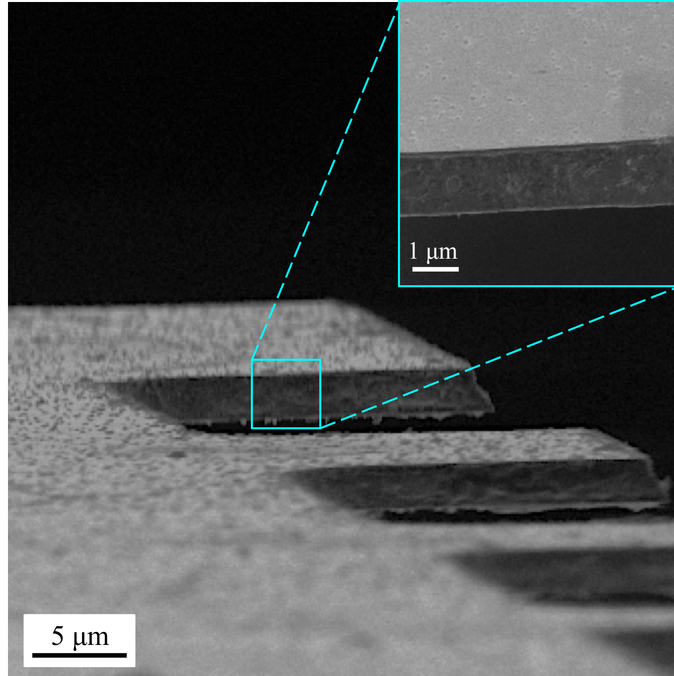

Figure 6.8: Cross-sectional view of 20 μm long cantilevers, demonstrating the perpendicular sidewalls achieved using the Nichrome wet etchant. No visible undercut was observed.

At this point, the wafer was flipped to the backside and photolithography was repeated using the back mask (Figure 6.7c). The backside Si_3N_4 was selectively etched using reactive ion etching (RIE) to expose the underlying Si substrate. The RIE process used trifluoromethane and oxygen (CHF_3/O_2), with an etch rate of 21±0.7 nm/min, followed by tetrafluoromethane (CF_4) for cleaning at an etch rate of 43±2 nm/min. Removal of the backside 300 nm Si_3N_4 layer was achieved after 10 minutes of CHF_3/O_2 and two minutes of CF_4 cleaning (Step 4). The photoresist was removed and protective alkaline coating ProTEK B3 (Brewer Science) with its primer was spin-coated onto the front of the wafer prior to the KOH wet etch. This alkaline coating prevented the KOH from etching the metallic Ni-Mo-W cantilevers. The 30% concentration KOH was heated to 90°C, producing a Si etch rate of 2.3 μm/min. A full through wafer etch was achieved after 135 minutes (Step 5). The remaining

Si_3N_4 layer was removed via RIE to release the microcantilevers from the backside. Finally, the wafer was diced using a class 1 IPG Photonics IX200F laser system inside of the cleanroom at UPenn. The green laser (532 nm) was used with a power of 150 kW and 100 passes to cut out individual dies, through the entire 300 μm Si wafer. After each die was sectioned, the ProTEK was removed using ProTEK B3 Remover 100 (Brewer Science), exposing freestanding microcantilever beams (Step 6).

6.3 Characterizing dimensional stability

6.3.1 Interferometry

A Michelson interferometer was used to measure the out-of-plane deflection of the beams using a custom-built setup at GEGR. Interferometry is a measurement technique that uses electromagnetic light waves to measure changes in displacement or surface topology. Figure 6.9 illustrates the Michelson interferometer setup, where a coherent light source is split into two different beam paths. One beam travels towards the reference mirror, while the other beam travels towards the movable mirror. The individual beams are reflected back towards the beamsplitter and are recombined prior to arriving at the detector. The optical path difference between the two beams creates a phase difference and produces an interference fringe pattern. The motion of interferometric fringes was used to monitor changes in beam path length and with it, deflection of the cantilever at various positions along its length.

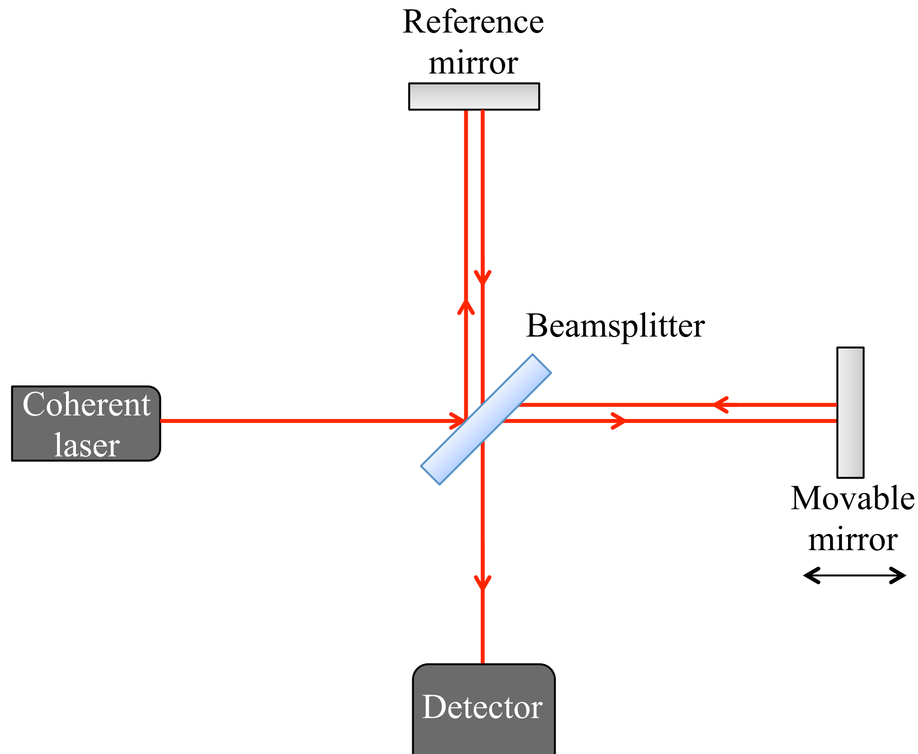

Figure 6.9: Principle of a Michelson interferometer, consisting of a beamsplitter and two mirrors (or reflectors).

The out-of-plane cantilever deflection profiles were fit to a second-order polynomial equation using traditional small deformation beam bending theory. With the coordinate system shown in Figure 6.10, u_y is the out-of-plane deflection, x the position along the beam, R the radius of curvature, θ_T the takeoff angle at the point of attachment and C is an arbitrary fitting constant.

$$u_y = \frac{1}{2R}x^2 + \theta_T x + C \quad \textbf{(6.1)}$$

The maximum deflection values at the end of the cantilever beam ($x = L$) are directly measured. First order differentiation of the deflection provides the takeoff angle, measured at

the fixed end ($x = 0$), whereas second order differentiation is related to the microcantilever beam curvature, $\kappa = 1/R$. Hundreds of microcantilevers were characterized with a variety of length and width ratios. Considering the practicality and feasibility of MEMS devices, only beam lengths of 20 to 100 μm with associated widths of 10 to 100 μm were investigated with the interferometer. Six individual dies consisting of 30 microcantilever beams were characterized in the as-fabricated state. Dies were also heat treated at 200°C and 400°C for 1 hour in 10^{-6} Torr vacuum. After cooling, interferometer measurements of beam deflections of these heat treated microcantilevers were used to demonstrate thermal stability.

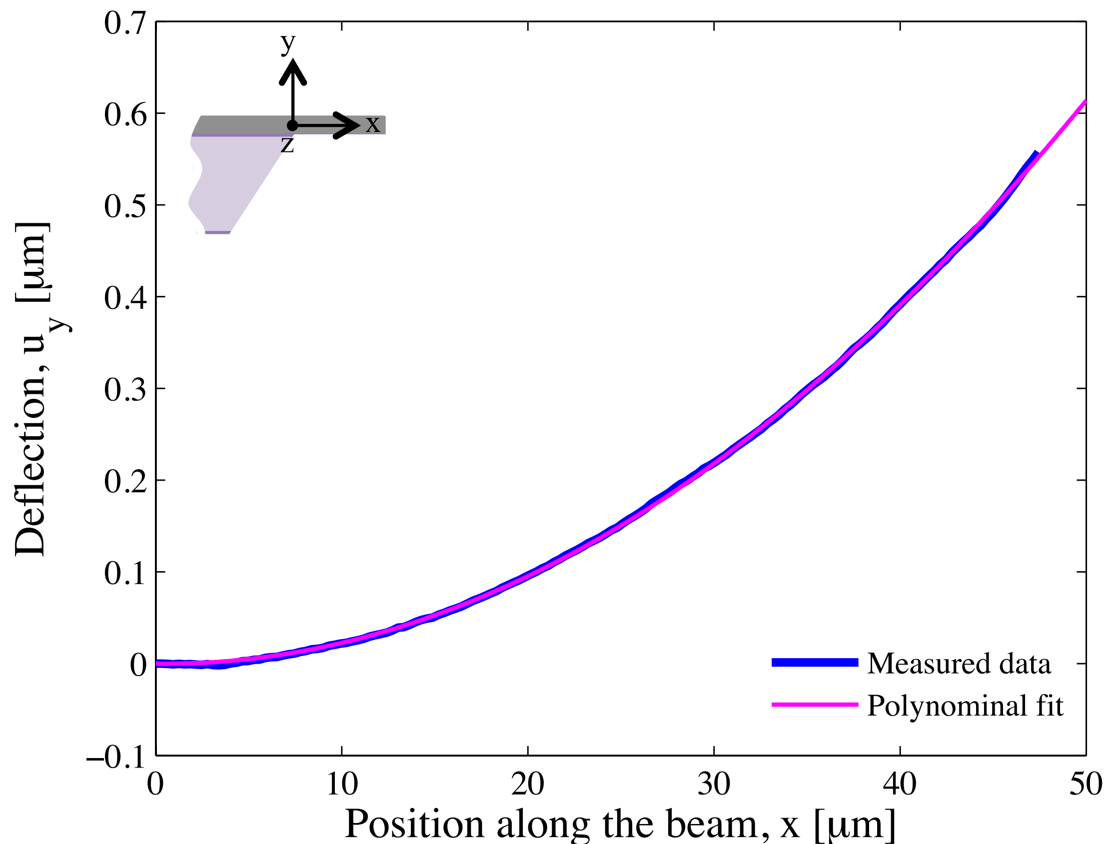

Figure 6.10: Interferometry measurement of the out-of-plane deflection profile measured along the length of a 50 μm cantilever beam compared with a polynomial fit.

6.3.2 Released beam deflections

A candidate set of films deposited using conditions of 200 W power and 3.5 mTorr Ar pressure for 80 minutes, achieving a thickness of 2.7±0.05 μm, were characterized. Wafer curvature measurements were used to determine the average residual stress in the as-deposited blanket films, as noted in Table 6.1. Freestanding arrays of microcantilever beams were fabricated using the process detailed in Figure 6.6, and a representative set of cantilevers with different aspect ratios is shown in Figure 6.11a. The deflection was measured and recorded along the length of each beam and used to determine the maximum deflection at the free end, the takeoff angle at the fixed end and the uniform curvature. An example set of interferometry fringes (Figure 6.11b) and associated deflection profiles (Figure 6.12) are displayed for 100 μm beams. Deflection profiles for beam lengths of 50 μm and 20 μm are shown in Figure 6.13 and Figure 6.14, respectively. It is clear from Figure 6.12-6.14 that for a given beam length, the deflection profiles are invariant with respect to the beam widths. As a result, all cantilever beam deflections were averaged across the associated widths and reported as the averaged deflection for each beam length. For example, Figure 6.15 shows the averaged deflection profiles for cantilever beam lengths of 20, 50 and 100 μm. The different length beams have the same curvature of 420 m^{-1}, but the magnitude of the maximum deflection scales with the beam lengths. The raw deflection profiles from 20 μm beam lengths show considerably more scatter and noise than beams of length 100 and 50 μm, but the averaged values align well with those in Figure 6.15. The spatial resolution of the interferometer setup is ~10 nm, which gives rise to the small perturbations observed for smaller 20 μm beams.

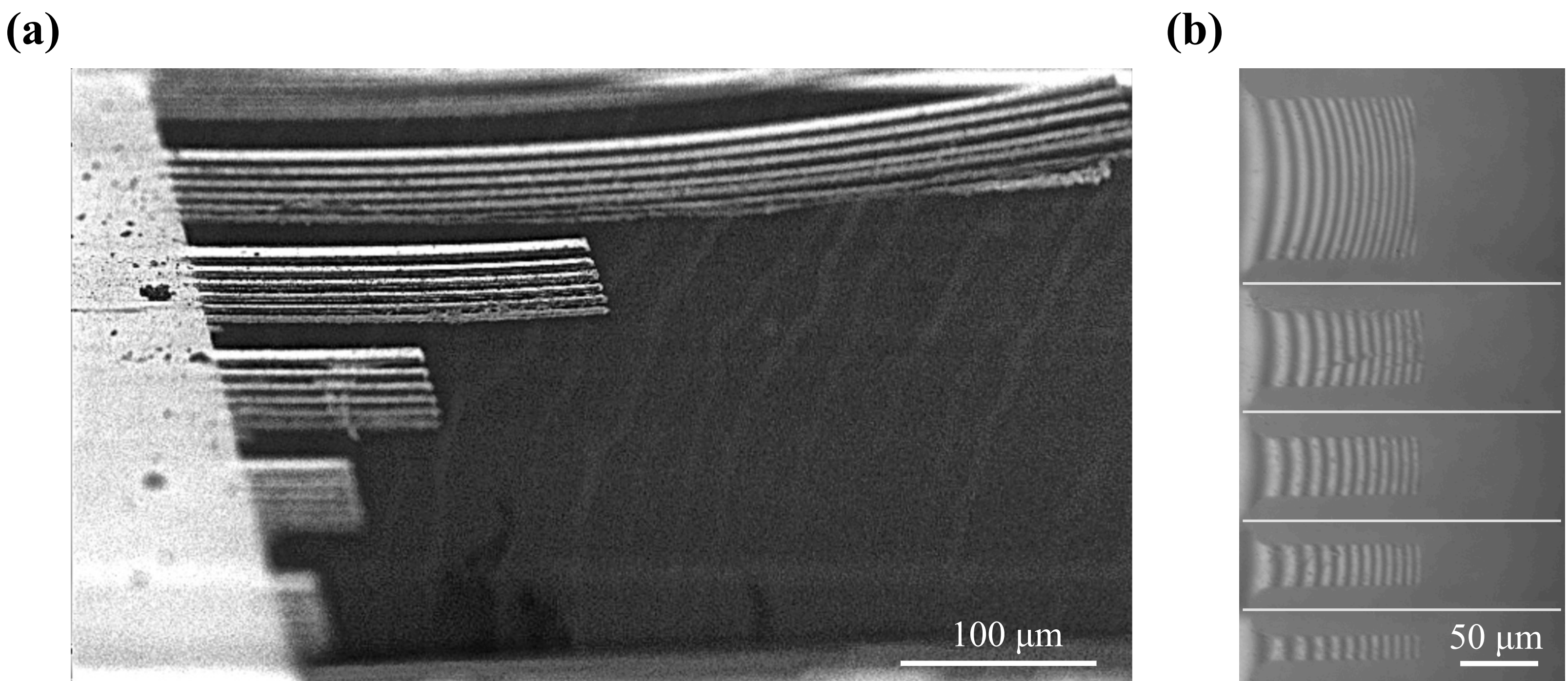

Figure 6.11: (a) SEM image of array of freestanding microcantilever beams group by length (500, 200, 100, 50 and 20 μm) with a range of widths (100, 50, 40, 30, 20, 10 μm) for each length. (b) Interferometry fringes for 100 μm long cantilevers with widths of 100, 50, 40, 30 and 20 μm. Spacing between cantilevers is 100 μm, not shown to scale here.

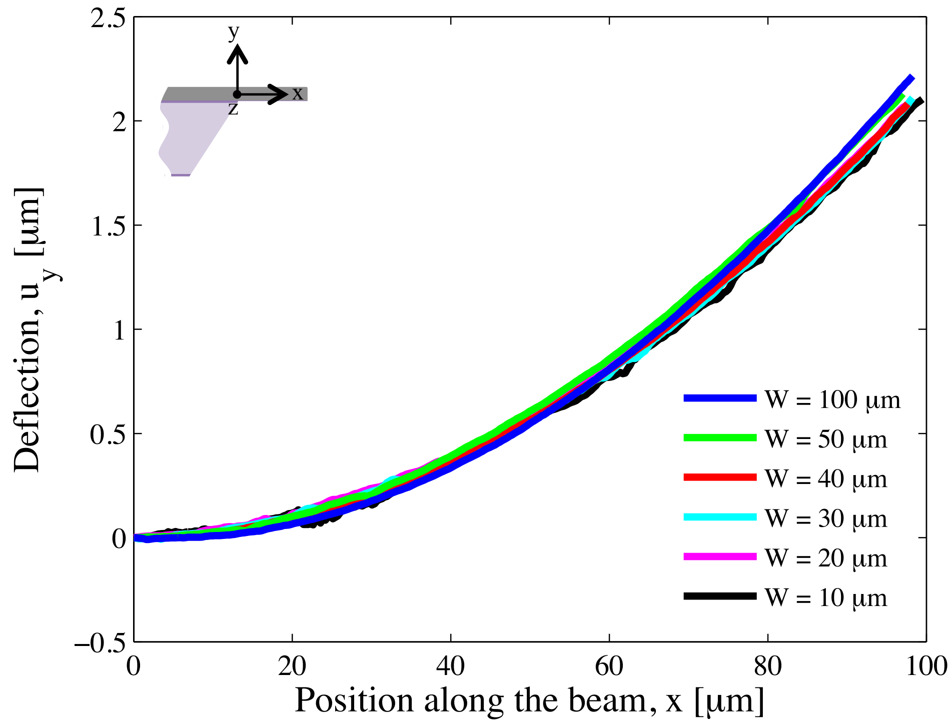

Figure 6.12: As-fabricated micro-cantilever beam deflection profiles for 100 μm long beams with different widths ranging from 10-100 μm.

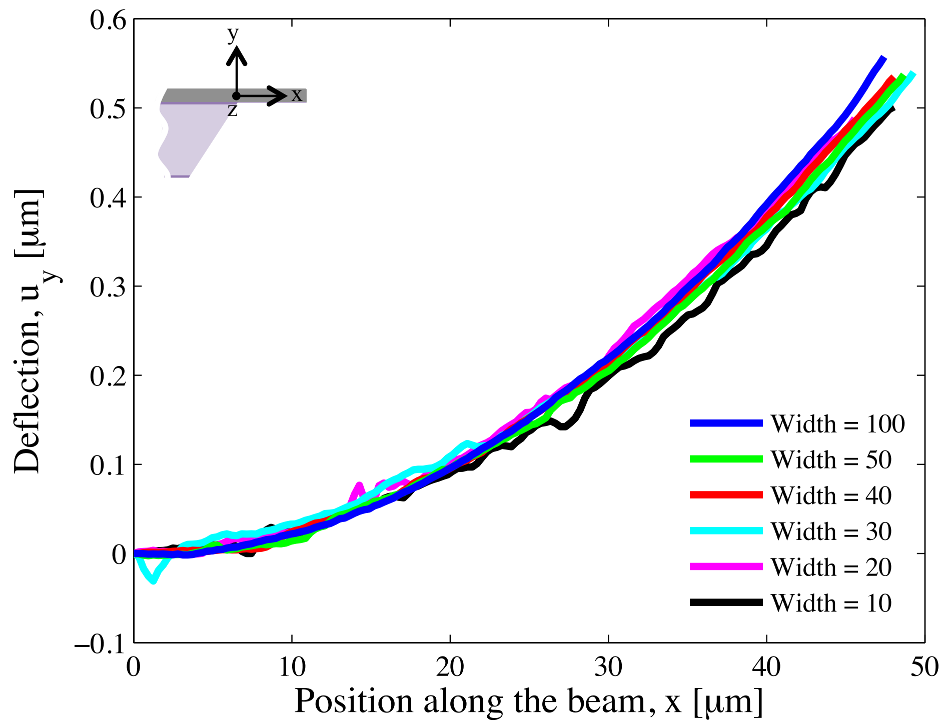

Figure 6.13: As-fabricated micro-cantilever beam deflection profiles for 50 μm long beams with different widths ranging from 10-100 μm.

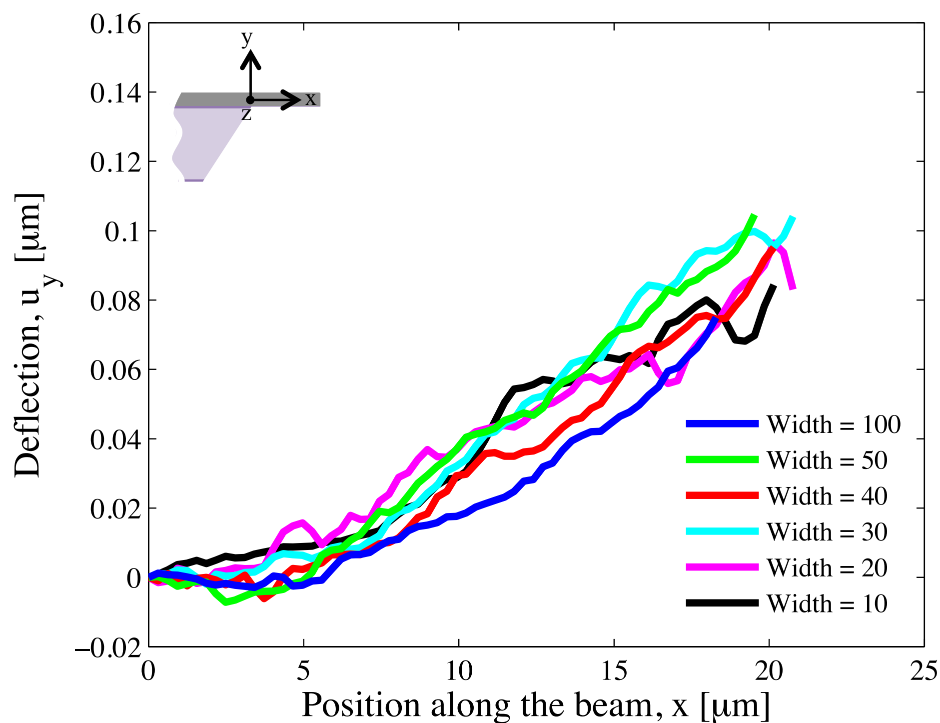

Figure 6.14: As-fabricated micro-cantilever beam deflection profiles for 20 μm long beams with different widths ranging from 10-100 μm.

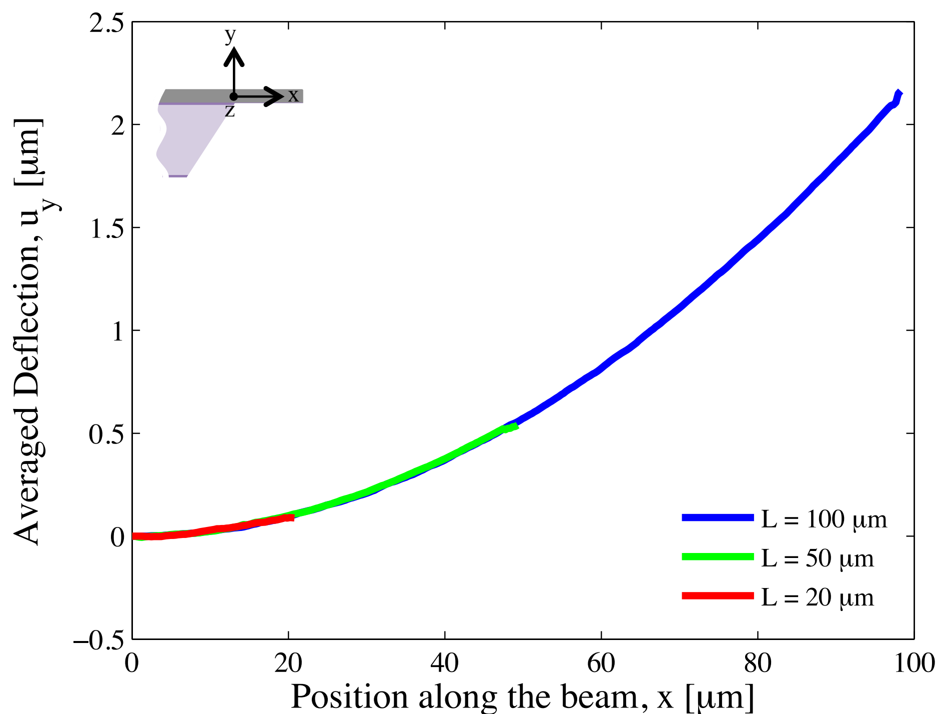

Figure 6.15: The average across different beam widths (10-100 μm) for three different beam lengths (20, 50 and 100 μm).

Table 6.2 summarizes the maximum deflections for more than 100 different as-fabricated microcantilevers across the wafer. The associated takeoff angle and curvature values were calculated using Equation 6.1 and presented in Table 6.3.

Table 6.2: Summary of micro-cantilever beam deflections for beams of length 100, 50 and 20 µm averaged over the respective widths for the as-fabricated and heat treated beams at 200°C and 400°C for 1 hour.

	Maximum Deflection at the End of the Cantilever [µm]		
Beam length [µm]	As-fabricated	200°C	400°C
100	2.17 ± 0.23	2.45 ± 0.06	1.79 ± 0.14
50	0.597 ± 0.12	0.685 ± 0.06	0.432 ± 0.04
20	0.107 ± 0.04	0.157 ± 0.01	0.050 ± 0.01

Table 6.3: Summary of micro-cantilever beam takeoff angles, curvatures and maximum stress gradients averaged over all beam lengths for the as-fabricated and heat treated beams at 200°C and 400°C for 1 hour.

Heat treatment	**Takeoff angle [rad × 10^{-3}]**	**Curvature [1/m]**	**Maximum σ_1 [MPa]**
As-fabricated	3.0 ± 2.6	419.7 ± 64.5	166.9 ± 25.7
200°C	2.6 ± 0.9	486.3 ± 57.0	193.4 ± 22.6
400°C	3.1 ± 2.2	358.8 ± 92.1	142.7 ± 36.6

6.3.3 Deflections associated with thermal exposure

Deflection profiles were measured after 1-hour heat treatments at 200°C and 400°C for 30 different microcantilever beams at each temperature to determine any dimensional changes. The maximum beam deflections, the associated takeoff angles and the curvatures are recorded in Tables 6.2 and 6.3, respectively. A small but measurable increase in the deflections was observed after the 200°C heat treatment compared to the as-fabricated microcantilever beams. The increase in deflections is associated with the increase in beam curvature after thermal exposure to 200°C. The takeoff angle at the fixed end of the microcantilever remained essentially the same. A different behavior was revealed for cantilevers heat treated at 400°C. The beam deflections and curvatures both decreased as a result of the 400°C heat treatment, while the takeoff angles remained the same. Understanding the relaxation of the microcantilever beam deflections at 400°C but not 200°C requires a closer investigation of the underlying mechanisms. The dimensional changes in deflection and its evolution with heat treatment temperature will be discussed below.

6.4 Mechanistic interpretation of dimensional changes

6.4.1 Quantifying intrinsic stresses

Geometric changes in the microcantilevers are intimately affected by changes in the residual stress, and thus, an understanding of the factors that underpin residual stress is imperative for dimensional and thermal control. The measured deflection profiles can be used to quantify the residual stresses in the microcantilevers and track its progression with thermal exposure. Small deformation beam bending assumptions were used with Hooke's law to express the microcantilever axial stress and relate it to the residual stress in the film. For a thin film in plane stress ($\sigma_y = 0$) with an in-plane biaxial stress ($\sigma_x = \sigma_z$), Hooke's law

can be rewritten in terms of the axial strain $\varepsilon_x = \frac{y}{R}$ and the transversely isotropic properties $(E_x = E_z = E_p, \nu_{xz} = \upsilon_{zx} = \upsilon_p)$.

$$\sigma_x = \frac{E_p}{1-\upsilon_p}\frac{y}{R} \quad \textbf{(6.2)}$$

$$M_z = -\frac{E_p}{12(1-\nu_p)}\frac{wt^3}{R} \quad \textbf{(6.3)}$$

The moment (M_z) for pure bending of a rectangular beam is shown in Equation 6.3 where E_p, ν_p, t and w are the in-plane Young's modulus, Poisson's ratio, beam thickness and beam width, respectively. Prior to releasing the microcantilever beams, the total axial residual stress (σ_x^{Total}) for thin films is often simplified to a first order linear approximation (Equation 6.4), where σ_0 is the uniform film stress and σ_1 is the maximum magnitude of the residual stress gradient [18]. The constant tensile or compressive stress (σ_0) is typically due to lattice or CTE mismatch between the film and the substrate, whereas the linear stress gradient (σ_1) is a result of the growth process.

$$\sigma_x^{Total} = \sigma_0 + \sigma_1\frac{y}{t/2} \quad \textbf{(6.4)}$$

$$M_z = -\frac{wt^2}{6}\sigma_1 \quad \textbf{(6.5)}$$

$$\sigma_1 = \frac{E_p}{2(1-\nu_p)}\frac{t}{R} \quad \textbf{(6.6)}$$

Balancing the moment using the total axial residual stress provides an expression (Equation 6.5), which is equated with the bending moment from Equation 6.3 to provide an expression for the maximum magnitude of the stress gradient (Equation 6.6). Second order differentiation of the measured deflection profile allows for calculation of the curvature. Implementing this value with Equation 6.6, the maximum stress gradient was computed by assuming an in-plane Young's modulus of 232 GPa (calculated for {111} out-of-plane texture using the stiffness matrix for single-crystal Ni [19]) and a Poisson's ratio of 0.3. Table 6.3 details the magnitude of the stress gradient as a function of heat treatment temperature. The as-fabricated stress gradient can be used for comparison, revealing that after heating at 200°C there is an increase of ~30 MPa whereas at 400°C there is a ~25 MPa decrease from the as-fabricated magnitude.

In addition to the residual stress gradient, the uniform compressive stress affects the overall geometry of the microcantilever beam. Figure 6.16 shows a schematic of a series of thought experiments adapted from [18] to decouple these effects. Figure 6.16a represents an as-fabricated film on a substrate with a schematic of the axial stresses in the film. For simplicity, the substrate and thin film are drawn as being completely flat, but the wafer curvature measurements indicated that they are curved concave down. In the first thought experiment, removing a portion of the substrate to create a freestanding cantilever beam will result in a slight lengthening of the beam to relieve the uniform compressive stress (σ_0). However, the stress gradient is still maintained and the beam remains flat. For this hypothetical intermediate stage, the cantilever will kink (θ_0) as a result of the boundary conditions at the point where the film is fixed to the substrate, Figure 6.16b.

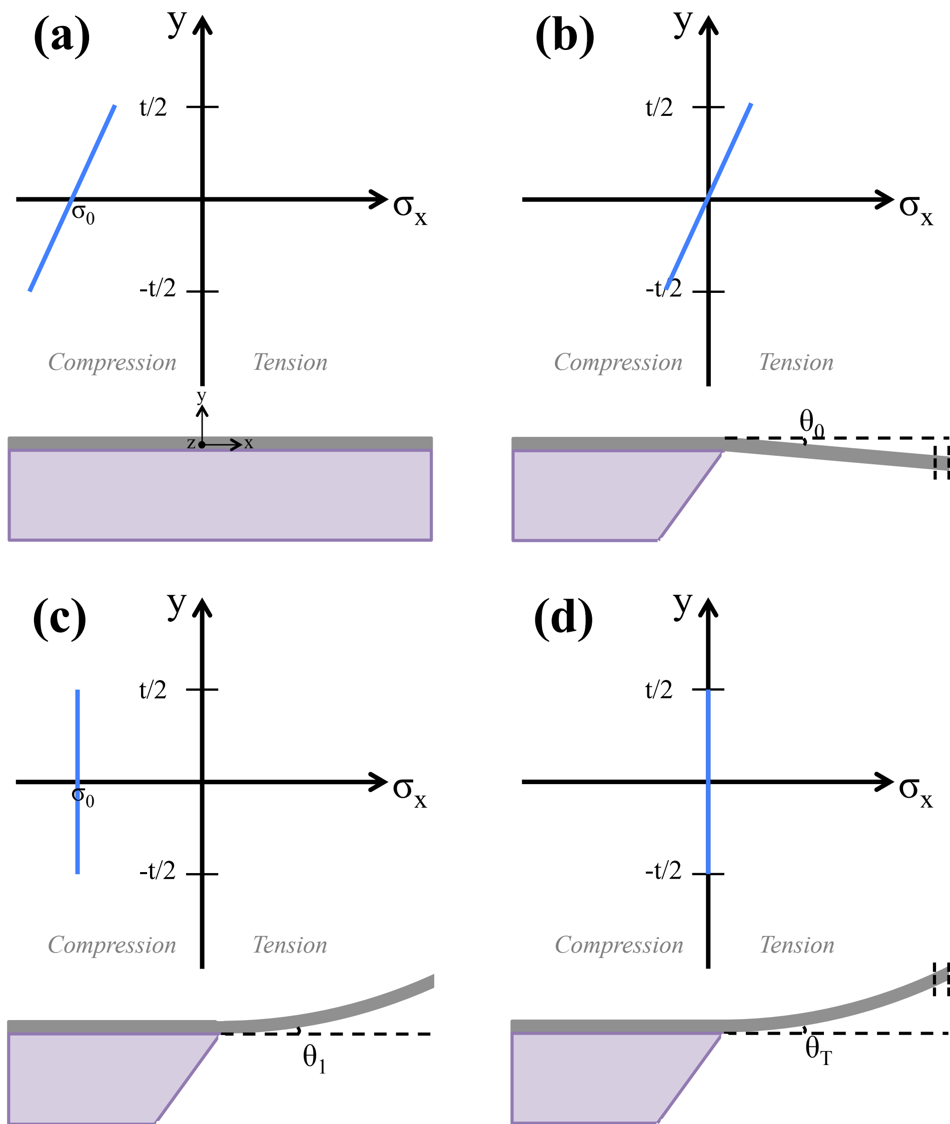

Figure 6.16: Schematic of a freestanding microcantilever and stress state prior to release, during hypothetical intermediate stages and after release, adapted from [18]. (a) As-fabricated stress gradient and uniform compressive stress in the thin film prior to release, (b) the effect of relieving the uniform compressive stress (σ_0) but maintaining the gradient (σ_1), (c) the effect relieving the stress gradient (σ_1) but maintaining the uniform compressive stress (σ_0) and (d) the geometric shape of the fully stress-relieved cantilever with zero stresses throughout the beam.

In the second thought experiment, removal of the substrate below the cantilever and relaxing only the stress gradient (σ_1) causes beam bending with constant radius of curvature, shown in Figure 6.16c. This hypothetical intermediate stage retains the uniform compressive stress (σ_0) and original beam length while the bending relieved the initial stress gradient. Assuming that the intrinsic stress gradient has a larger contribution than the uniform compressive stress ($\sigma_1 > \sigma_0$) prior to release, the overall shape of the freestanding cantilever resembles Figure 6.16d. The combined effects of the two hypothetical scenarios detailed in Figures 6.16b and 6.16c create the bending and lengthening observed in Figure 6.16d, providing there is zero stress everywhere in the beam. It is worth noting that the total takeoff angle in the fully released cantilever beam (θ_T) has a combination of the takeoff angle from the uniform stress (θ_0) relaxation and the stress gradient (θ_1) relaxation, such that $\theta_T = \theta_0 + \theta_1$. The angles measured in Table 6.3 display the total takeoff angles as being close to zero and nominally unchanged with thermal exposure. The modest positive angle suggests that the contribution from the stress gradient was large enough to offset the contribution from the constant compressive stress, $\theta_1 > \theta_0$. Thus, the dimensional changes observed in microcantilever deflections are driven by the ability to control the stress gradient and its development with temperature.

6.4.2 Effect of temperature

The residual stress evolution that occurs during thermal exposure, e.g. that associated with packaging, bonding and elevated temperature service, is needed for future MEMS integration. Freestanding microcantilevers require dimensional stability in the as-fabricated state in addition to the temperatures compatible with bonding techniques. Typical bonding temperature are in the range of 180-300°C for solder reflow [20], 300-400°C for

thermocompression [21, 22] and 400-450°C for glass frit bonding [23]. Heat treatments of 200°C and 400°C were examined to mimic these bonding temperatures and the results exhibited relatively flat microcantilever beams with subtle geometric changes. The evolution of microcantilever deflections is grounded in the as-sputtered residual stress gradient. Various papers in the literature examine the different stages of growth for physical vapor deposition [24, 25] and attribute the initial region to island growth on the substrate, followed by grain boundary formation or coalescence and film thickening. The final growth region is highly dependent on the deposition parameters and the material being deposited [15]. The measured values of maximum residual stress gradient in the $Ni_{84}Mo_{11}W_5$ films are consistent with metallic thin films of similar deposition rates [25].

The structure zone model proposed by Thornton [14] describes the microstructure of sputter deposited thin films as a function of Ar pressure and deposition temperature, shown in Figure 6.17. According to the structure zone model, the $Ni_{84}Mo_{11}W_5$ films sputtered at room temperature and 3.5 mTorr Ar pressure borders on the edge of two zones: zone T (transition) formed with a low Ar pressure at a low homologous temperature (T/T_m), creating dense columnar grains with a smooth surface, whereas zone 1 formed with higher Ar pressure at low T/T_m, results in rougher surfaces with columnar grains separated by open void containing boundaries [15]. During heat treatments, quenched vacancies from sputtering can annihilate at the surface or the grain boundaries and the free surfaces of the cantilever beam provide a high density of fast diffusion pathways. The increase in deflection observed after the 200°C heat treatment indicates that at this temperature there is sufficient thermal activation for local atomic rearrangement but not for extensive vacancy diffusion across the cantilever beam.

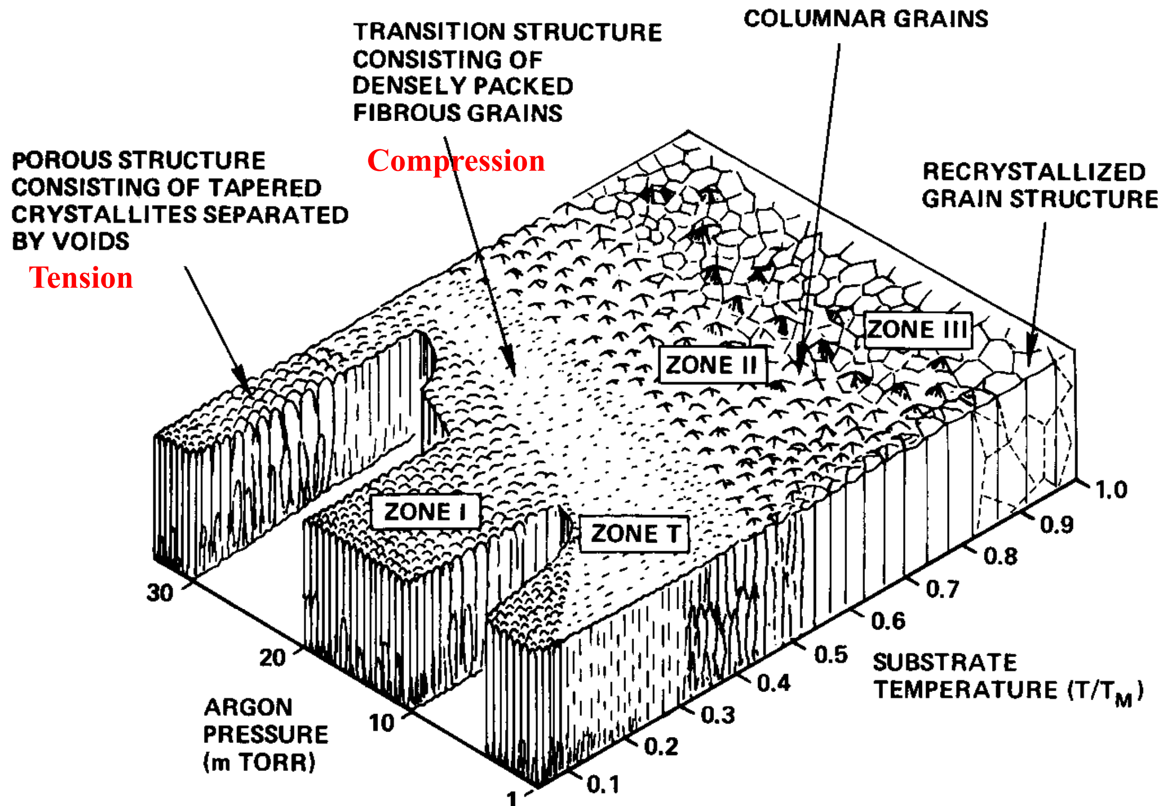

Figure 6.17: The structure zone model for sputter deposited films, adapted from [14].

However, at 400°C there is more thermal energy for overall vacancy annihilation throughout the microcantilever beam, promoting stress relaxation and an associated decrease in the deflection. The nanometer scale deflections of the microcantilevers demonstrate the potential for moving beyond blanket film deposition to the fabrication of geometrically stable, freestanding microcantilever beams. Careful control of the residual stresses was found to be critical for device uniformity and repeatability.

6.5 Chapter summary

The current study goes beyond the demonstration of enhanced material properties to demonstrate and elucidate of a path for micromachining dimensionally stable microcantilevers of nanotwinned Ni-Mo-W. The fact that Ni-Mo-W microcantilever can be reliably etched and shaped with wafer uniformity using conventional semiconductor processes greatly facilitates integration into existing manufacturing foundries and processes. Deflections of the as-fabricated cantilevers were measured to be on the order of hundreds of nanometers for smaller length beams (20-50 μm), whereas the longest cantilevers (100 μm) deflected a few micrometers. The nanotwinned Ni-Mo-W microcantilevers are shown to be dimensionally stable when exposed to processing and packing thermal cycles. It is noted that relaxation during thermal exposure to 400°C actually flattened the microcantilevers and resulted in increased dimensional stability, with beam deflection profiles of tens of nanometers. It is anticipated that the successful fabrication of nanotwinned Ni-Mo-W microcantilever arrays and demonstration of good dimensional control and stability will lay the groundwork for next generation metal MEMS design and fabrication.

6.6 References for Chapter 6

1. Brand, O., I. Dufour, S. Heinrich, S.M. Heinrich, F. Josse, G.K. Fedder, J.G. Korvink, C. Hierold, and O. Tabata, *Resonant MEMS: fundamentals, implementation, and application*. 2015: John Wiley & Sons.
2. Shaw, G.A., B.C. Prorok, and L.A. Starman, *MEMS and Nanotechnology, Volume 6: Proceedings of the 2012 Annual Conference on Experimental and Applied Mechanics*. Vol. 42. 2012: Springer Science & Business Media.
3. ISO, *Cleanrooms and associated controlled environments—Part 1: classification of air cleanliness*. 1999, International Organization for Standardization Geneva.
4. Wilson, S.A., R.P. Jourdain, Q. Zhang, R.A. Dorey, C.R. Bowen, M. Willander, Q.U. Wahab, S.M. Al-hilli, O. Nur, and E. Quandt, *New materials for micro-scale sensors and actuators: An engineering review.* Materials Science and Engineering: R: Reports, 2007. **56**(1): p. 1-129.
5. Esashi, M., *Revolution of sensors in micro-electromechanical systems.* Japanese Journal of Applied Physics, 2012. **51**(8R): p. 080001.
6. Kilinc, Y., U. Unal, and B.E. Alaca, *Residual stress gradients in electroplated nickel thin films.* Microelectronic Engineering, 2015. **134**: p. 60-67.
7. Luo, J., M. Pritschow, A. Flewitt, S. Spearing, N. Fleck, and W. Milne, *Effects of process conditions on properties of electroplated Ni thin films for microsystem applications.* Journal of the Electrochemical Society, 2006. **153**(10): p. D155-D161.
8. Majjad, H., S. Basrour, P. Delobelle, and M. Schmidt, *Dynamic determination of Young's modulus of electroplated nickel used in LIGA technique.* Sensors and Actuators A: Physical, 1999. **74**(1-3): p. 148-151.
9. Saile, V., U. Wallrabe, O. Tabata, J.G. Korvink, O. Brand, G.K. Fedder, and C. Hierold, *LIGA and its Applications*. Vol. 7. 2009: John Wiley & Sons.
10. Zhang, J., *Determination of Young's modulus of electroplated nickel–iron (Ni/Fe) and micro-machined Si thin films by the balance method.* Journal of materials processing technology, 2002. **123**(3): p. 329-335.
11. Cho, H., K. Hemker, K. Lian, J. Goettert, and G. Dirras, *Measured mechanical properties of LIGA Ni structures.* Sensors and Actuators A: Physical, 2003. **103**(1): p. 59-63.
12. Hemker, K.J. and H. Last, *Microsample tensile testing of LIGA nickel for MEMS applications.* Materials Science and Engineering: A, 2001. **319–321**: p. 882-886.
13. Ohring, M., *Materials science of thin films*. 2001, Elsevier.
14. Thornton, J.A., *Influence of apparatus geometry and deposition conditions on the structure and topography of thick sputtered coatings.* Journal of Vacuum Science and Technology, 1974. **11**(4): p. 666-670.

15. Thornton, J.A. and D. Hoffman, *Stress-related effects in thin films.* Thin solid films, 1989. **171**(1): p. 5-31.

16. Flinn, P.A., D.S. Gardner, and W.D. Nix, *Measurement and interpretation of stress in aluminum-based metallization as a function of thermal history.* IEEE Transactions on electron devices, 1987. **34**(3): p. 689-699.

17. Stoney, G.G., *Hie Tension of Metallic Films deposited by Electrolysis.* Nature, 1908: p. 366.

18. Senturia, S.D., *Microsystem design*. 2007: Springer Science & Business Media.

19. Ledbetter, H.M. and R.P. Reed, *Elastic Properties of Metals and Alloys, I. Iron, Nickel, and Iron-Nickel Alloys.* Journal of Physical and Chemical Reference Data, 1973. **2**(3): p. 531-618.

20. Sparks, D., G. Queen, R. Weston, G. Woodward, M. Putty, L. Jordan, S. Zarabadi, and K. Jayakar, *Wafer-to-wafer bonding of nonplanarized MEMS surfaces using solder.* Journal of Micromechanics and Microengineering, 2001. **11**(6): p. 630.

21. Cohn, M.B. and J.T. Kung, *Microelectromechanical systems using thermocompression bonding*. 2005, Google Patents.

22. Tsau, C.H., S.M. Spearing, and M.A. Schmidt, *Fabrication of wafer-level thermocompression bonds.* Journal of Microelectromechanical systems, 2002. **11**(6): p. 641-647.

23. Knechtel, R., *Glass frit bonding: an universal technology for wafer level encapsulation and packaging.* Microsystem technologies, 2005. **12**(1-2): p. 63-68.

24. Abermann, R. and R. Koch, *The internal stress in thin silver, copper and gold films.* Thin Solid Films, 1985. **129**(1-2): p. 71-78.

25. Floro, J.A., E. Chason, R.C. Cammarata, and D.J. Srolovitz, *Physical origins of intrinsic stresses in Volmer–Weber thin films.* MRS bulletin, 2002. **27**(1): p. 19-25.

CHAPTER 7: SUMMARY AND FINDINGS

This thesis work was undertaken to expand the current set of materials available for elevated temperature (300-500°C) microelectromechanical systems (MEMS). The enhanced microstructural and thermal stability of sputter deposited Ni-W [1, 2] was combined with Mo to reduce the coefficient of thermal expansion (CTE) [3], producing ternary Ni-Mo-W alloys. Initial characterization of candidate alloy $Ni_{83.6}Mo_{14}W_{2.4}$ revealed ultrahigh strengths, electrical conductivity and tailorable mechanical behavior derived from the formation of growth nanotwins [4, 5]. The goal of the research presented in this dissertation was to investigate a broader set of Ni-Mo-W alloys with the requisite nanotwinned microstructure and determine their applicability for the structural material in MEMS.

7.1 Review of key findings

A compositional spread of nanotwinned Ni-Mo-W alloys was sputter deposited from a combinatorial target of $Ni_{85}Mo_{15}$ and $Ni_{85}W_{15}$ (at.%). Thin films were sectioned into different regions with chemical compositions ranging from $Ni_{85}Mo_xW_{15-x}$, where x is 2-13 at.%W, to measure their physical properties, such as electrical resistivity and coefficient of thermal expansion (CTE). The measured electrical resistivity ranged from 104-116 μΩ-cm, which are comparable to the values reported for bulk Ni alloys, suggesting that the underlying microstructure does not impede electron motion. A non-contact method using digital image correlation (DIC) was developed for measuring the CTE of thin films and used to determine the effectiveness of alloying with Mo to reduce the overall CTE of Ni-Mo-W. The results can be summarized as follows:

- The experimental measure of all $Ni_{85}Mo_xW_{15-x}$ films resulted in a CTE that ranged from $8.9\text{-}13.0\times10^{-6}$ /°C between room temperature and 600°C. This is

dramatically reduced compared to the reported CTE of pure Ni, 13.0-16.4×10^{-6} /°C, in this same temperature range [3, 6, 7].

- The effect on CTE was observed to differ with alloying content. Room temperature CTE was found to be lowest for the W-rich alloys 8.2-8.9×10^{-6} /°C, while the Mo-rich alloys were found to have a temperature independent CTE. The ability to tailor the temperature dependence of CTE provides additional design flexibility for engineering dimensional stability into MEMS.
- The reduced CTE of $Ni_{85}Mo_xW_{15-x}$ films was found to match the CTE of commercial glass substrates commonly used in MEMS-based switches and micro-actuators, providing a pathway to mitigate the thermal distortions that would otherwise develop from CTE mismatch.

In addition to the physical properties, the mechanical properties of sputter deposited $Ni_{85}Mo_xW_{15-x}$ alloys were investigated as a function of their chemistry and underlying microstructure. Uniaxial tension specimens were evaluated for a representative set of $Ni_{85}Mo_xW_{15-x}$ films in the as-deposited state and after heat treatments for 1 hour at 400°C. The microstructural characterization and the mechanical results can be summarized as follows:

- Cross-sectional transmission electron microscopy (TEM) demonstrated the columnar grains oriented in the growth direction filled with perpendicular nanotwins. X-ray diffraction (XRD) was used to measure the crystallographic peaks of the films, revealing a strong {111} texture out-of-plane associated with face centered cubic (fcc) single-phase Ni. The columnar grains were found to have a tilted <111> direction that developed as an artifact of the sputtering

process. These microstructural variations did not appear to have any fundamental correlation with alloy composition and instead were a result of the custom combinatorial alloy target geometry and its generated plasma during sputtering.

- Fluctuations in the measured fracture strengths (2-3 GPa) and the associated elastic moduli (180-220 GPa) were found to vary as a function of the microstructure morphology rather than alloy chemistry. Had the artifacts in sputtering not been present, the microstructural variations causing changes in fracture strengths and elastic moduli would likely not be present.

- The stress-strain tensile response displayed a linear-elastic behavior, which is attractive for MEMS because it is extremely reproducible and easy to model. High tensile strengths of 2-3 GPa were measured and facilitated by a high density of nanotwins. The careful control and design of the underlying microstructure facilitated the strengthening behavior observed in $Ni_{85}Mo_xW_{15-x}$ alloys with mechanical integrity at temperatures up to 400°C.

Changing the loading orientation with respect to the twin boundaries led to an in situ study on micropillar compression, where the loading axis is perpendicular to the film surface and the associated twin boundaries. Post-mortem characterization with TEM techniques was used to investigate microstructural changes after deformation and the results can be summarized as follows:

- In situ compression displayed anisotropic plasticity that was highly localized to the top portion of the micropillar, with no visible deformation in the remainder of the pillar. Ultrahigh compressive strengths were measured greater than 4.5 GPa and are attributed to dislocation pile-up and slip transfer across twin boundaries.

- When the underlying twin boundaries were oriented perpendicular to the loading direction, the extruded localized plasticity was symmetric in nature, whereas twin boundaries with a slight inclination showed highly directional deformation. Extensive shear banding was found to facilitate the localized softening mechanisms and lateral shear parallel to the twin planes. All deformation was localized inside the shear band, which displayed recrystallized grains with a 4:1 aspect ratio, elongated in the direction of shear. However, no direct evidence of detwinning was observed. The nanotwinned microstructure facilitated the interaction between hard and soft deformation modes, providing a tailorable mechanical response for nanotwinned materials.

The effect of deposition rate on the formation of the highly beneficial nanotwins in Ni-Mo-W was investigated. Constant alloy composition $Ni_{84}Mo_{11}W_5$ was sputter deposited at rates of 0.5, 0.7 0.9 and 2.3 nm/s and the associated grain diameter, twin thickness and hardness were measured and the results can be summarized as follows:

- Highly textured <111> oriented columnar grains were observed for all deposition conditions with in-plane columnar grain diameters ranging from 58-89 nm. Grain diameter was shown to increase with deposition rate, as a result of more substrate heating at higher rates.

- Bright field TEM images were used to quantify the average nanotwin thickness, ranging from 3.2-3.7 nm across all deposition conditions with a maximum standard deviation of 2 nm. The dislocation interactions with the fine nanotwin spacing facilitated high hardness values and estimated compressive yield strengths 3.1-3.4 GPa across all films.

- The results suggest that the deposition rate is less significant in the formation of nanotwins and instead, the atomic chemistry from alloying with Mo and W is hypothesized to considerably reduce the stacking fault energy (SFE) compared to pure Ni, as predicted by Shang et al. [8].

Translation of the exceptional suite of properties was undertaken to move beyond thin films characterization and to fabricate prototype MEMS device structures. Microcantilever beams were fabricated and characterized to determine their geometrical changes with thermal exposure temperatures that mimic wafer bonding. The results are summarized as follows:

- Ni-Mo-W microcantilevers were reliably etched and shaped using conventional semiconductor processes (e.g. lithography, wet etchants, dry etchants) with wafer uniformity. The microfabrication process was carried out in a class 100 cleanroom such that the entire workflow can be integrated into existing manufacturing processes.

- Laser interferometry measurements were used to quantify the microcantilever out-of-plane deflection and showed deflection measurements on the order of hundreds of nanometers for the smaller length beams (20-50 μm) and a few micrometers for the longest length beams (100 μm).

- The curvature of the deflection profiles was used to quantify the magnitude of the stress gradient, which showed relaxation after thermal exposure to 400°C, flattening the microcantilevers and resulting in increased dimensional stability.

Taken as a whole, the experiments performed in this study highlight the importance of alloy chemistry and nanotwin formation on the balance of physical and mechanical properties

in Ni-Mo-W alloys. The wide range of $Ni_{85}Mo_xW_{15-x}$ alloys characterized with outstanding properties and manufacturability lays the groundwork for next generation metal MEMS design and fabrication.

7.2 Future directions

The results and conclusions presented in this dissertation help advance the available materials for high temperature MEMS applications and provide an understanding of the mechanical behavior and stability of nanotwinned Ni-Mo-W alloys. The findings also motivate future investigations that could be undertaken to promote a more fundamental understanding of the nanotwinned microstructure and its behavior at high temperatures. Key areas of focus are discussed as follows:

- All mechanical testing presented in this dissertation was conducted at room temperature, however the application of high temperature MEMS would require the device to be in service at the prescribed elevated temperature. Using the detailed study presented in this work for high temperature digital image correlation (DIC) aberration corrections provides an easy path to integrating DIC into an existing high temperature load frames to provide accurate strain measurements. A more expansive set of tensile testing at elevated temperature (300-500°C) would further reinforce nanotwinned Ni-Mo-W alloys for high temperature MEMS use. More specifically, performing these experiments in vacuum would provide the most realistic environmental conditions, where oxidation is hindered. MEMS devices are typically hermetically sealed during the packaging process to eliminate humidity and organic matter that can act as

insulators and cause electrical short circuits. These contaminants can diminish the quality and function of the device, which is mitigated through the hermetic seal.

- An important quantification in MEMS devices is the reliability and longevity of their mechanical parts, which points to an experimental study of the creep behavior. High temperature creep and fatigue studies on LIGA Ni [9] provide an experimental precursor to this investigation, but the role of the thermally and mechanically stable nanotwins in Ni-Mo-W has not been demonstrated. A recent review article on the fracture, fatigue and creep of nanotwinned metals notes that very few investigations have been performed to investigate the creep behavior of nanotwinned metals [10], and those that have all focused on low SFE materials such as Cu and Ag. For example, Bezares et al. used nanoindentation to measure the creep behavior of nanotwined Cu and Ag [11]. Their results compared nanotwinned Cu films electrodeposited and sputtered, finding that the sputtered films showed enhanced stability due to the finer twin lamellae achievable with sputtering. Additionally, Jiao and Kulkarni performed MD simulations on nanotwinned Cu with fine twin spacing (less than 5 nm) and found a new mechanism at high stresses, governed by twin boundary migration from partial dislocation nucleation from the twin boundary-grain boundary junction [12]. Because Ni has a higher SFE than Cu, the mechanisms governing the high temperature creep behavior of Ni-Mo-W may be completely different than those proposed for nanotwinned Cu and may even offer superior stability.
- In this work, micropillar compression was used to elucidate the anisotropic deformation mechanisms when changing the loading direction with respect to the

twin boundaries; however, only one tilt angle was investigated. A more extensive set of micropillars with different loading orientations with respect to the twin boundaries would provide a more comprehensive overview of the active mechanisms. Specifically, loading at 45° with respect to the twins, where the maximum resolved shear stress is on the twin plane, would provide the most intriguing results. You et al. demonstrated this loading orientation as a soft mode, where easy dislocation glide on the twin planes promotes detwinning [13]. Since Ni-Mo-W has displayed superior mechanical strength and stability than nanotwinned Cu, it remains to be demonstrated whether the same mechanisms would be active.

- The deformed micropillar compression presented in this dissertation showed shear banding as a dominant mechanism through post-mortem TEM characterization. The results suggested that the shear band started parallel to the modest twin boundary inclination and developed a band of recrystallized grains. There was no evidence of detwinning observed post-mortem, but it is unclear whether the shear band initiated from the twin boundary, as reported by Hatherly and Malin [14], or from some other interaction. In situ TEM pillar compression would be needed to confirm this behavior and would be an exciting area for future research to determine the role of twin boundary orientation and motion with the observed deformation.

- Most of the beneficial properties presented in this dissertation were attributed to the finely spaced nanotwins in the $Ni_{85}Mo_xW_{15-x}$ alloys. In this thesis work, it was suggested that the small additions of Mo and W were sufficient enough to lower

the SFE of pure Ni, enabling the twin formation. An interesting question arises from these results; what alloying content of Mo and W is needed to promote the reduction of the SFE in Ni and to produce nantwins? Increasing the alloying content beyond 15 at.% would likely result in amorphous alloys or promote segregation and complex intermetallic phases [15, 16]. However, decreasing the alloying content could provide a critical solute concentration to facilitate nanotwin formation in Ni alloys. The effect of alloy chemistry in Ni-Mo-W may also provide a pathway to tailor the nanotwin thickness.

7.3 References for Chapter 7

1. Borgia, C., T. Scharowsky, A. Furrer, C. Solenthaler, and R. Spolenak, *A combinatorial study on the influence of elemental composition and heat treatment on the phase composition, microstructure and mechanical properties of Ni–W alloy thin films.* Acta materialia, 2011. **59**(1): p. 386-399.
2. Rupert, T.J., J.C. Trenkle, and C.A. Schuh, *Enhanced solid solution effects on the strength of nanocrystalline alloys.* Acta Materialia, 2011. **59**(4): p. 1619-1631.
3. Pavlovic, A., V.S. Babu, and M.S. Seehra, *High-temperature thermal expansion of binary alloys of Ni with Cr, Mo and Re: a comparison with molecular dynamics simulations.* Journal of Physics: Condensed Matter, 1996. **8**(18): p. 3139.
4. Sim, G.-D., J.A. Krogstad, K.M. Reddy, K.Y. Xie, G.M. Valentino, T.P. Weihs, and K.J. Hemker, *Nanotwinned metal MEMS films with unprecedented strength and stability.* Science Advances, 2017. **3**(6): p. e1700685.
5. Sim, G.-D., J.A. Krogstad, K.Y. Xie, S. Dasgupta, G.M. Valentino, T.P. Weihs, and K.J. Hemker, *Tailoring the mechanical properties of sputter deposited nanotwinned nickel-molybdenum-tungsten films.* Acta Materialia, 2018. **144**: p. 216-225.
6. Suh, I.-K., H. Ohta, and Y. Waseda, *High-temperature thermal expansion of six metallic elements measured by dilatation method and X-ray diffraction.* Journal of Materials Science, 1988. **23**(2): p. 757-760.
7. Sung, P. and D.R. Poirier, *Estimation of densities and coefficients of thermal expansion of solid Ni-base superalloys.* Materials Science and Engineering: A, 1998. **245**(1): p. 135-141.
8. Shang, S., C. Zacherl, H. Fang, Y. Wang, Y. Du, and Z. Liu, *Effects of alloying element and temperature on the stacking fault energies of dilute Ni-base superalloys.* Journal of Physics: Condensed Matter, 2012. **24**(50): p. 505403.
9. Cho, H., K. Hemker, K. Lian, J. Goettert, and G. Dirras, *Measured mechanical properties of LIGA Ni structures.* Sensors and Actuators A: Physical, 2003. **103**(1): p. 59-63.
10. Li, X., M. Dao, C. Eberl, A.M. Hodge, and H. Gao, *Fracture, fatigue, and creep of nanotwinned metals.* MRS Bulletin, 2016. **41**(4): p. 298-304.
11. Bezares, J., S. Jiao, Y. Liu, D. Bufford, L. Lu, X. Zhang, Y. Kulkarni, and R.J. Asaro, *Indentation of nanotwinned fcc metals: Implications for nanotwin stability.* Acta Materialia, 2012. **60**(11): p. 4623-4635.
12. Jiao, S. and Y. Kulkarni, *Molecular dynamics study of creep mechanisms in nanotwinned metals.* Computational Materials Science, 2015. **110**: p. 254-260.
13. You, Z., X. Li, L. Gui, Q. Lu, T. Zhu, H. Gao, and L. Lu, *Plastic anisotropy and associated deformation mechanisms in nanotwinned metals.* Acta Materialia, 2013. **61**(1): p. 217-227.
14. Hatherly, M. and A. Malin, *Shear bands in deformed metals.* Scripta metallurgica, 1984. **18**(5): p. 449-454.

15. Kurz, S., C. Ensslen, U. Welzel, A. Leineweber, and E. Mittemeijer, *The thermal stability of Ni–Mo and Ni–W thin films: Solute segregation and planar faults.* Scripta Materialia, 2013. **69**(1): p. 65-68.

16. Trelewicz, J.R. and C.A. Schuh, *The Hall–Petch breakdown in nanocrystalline metals: a crossover to glass-like deformation.* Acta Materialia, 2007. **55**(17): p. 5948-5958.

APPENDIX 1: X-RAY PENETRATION DEPTH

The penetration depth in XRD is not precisely known, especially for metallic materials that strongly absorb X-rays. The intensity of the incident X-rays exponentially decreases with specimen thickness. However, an approximation can be made of the specimen depth from which the diffraction peaks were obtained, assuming an infinitesimally thin layer below the surface. Equation A1.1 defines the integrated intensity diffracted by the thin layer at depth x below the surface for the powder diffraction configuration. I_0 is the incident beam intensity, I_D the diffracted beam intensity, μ the linear absorption coefficient of the material, a the volume fraction of the specimen with planes oriented for reflection of the incident beams, b the fraction of the incident energy that is diffracted by unit volume and θ the scattering angle [1].

$$dI_D = \frac{I_0 ab}{\sin\theta} e^{-\frac{2\mu x}{\sin\theta}} dx \qquad \textbf{(A1.1)}$$

By defining a ratio, G_x, of the intensity diffracted by a specified layer x to the total intensity diffracted over the entire specimen, constants I_0, a and b will cancel (Equation A1.2) [1]. This can be rewritten to a form to facilitate calculations, where $K_x = \ln\left(\frac{1}{1-G_x}\right)$, as in Equation A1.3.

$$G_x = \frac{\int_{x=0}^{x=x} dI_D}{\int_{x=0}^{x=\infty} dI_D} = 1 - e^{-\frac{2\mu x}{\sin\theta}} \qquad \textbf{(A1.2)}$$

$$x = \frac{K_x \sin\theta}{2\mu} \qquad \textbf{(A1.3)}$$

The linear absorption coefficient was calculated from mass absorption coefficients and densities obtained from literature [2, 3]. Assuming that 95% of the intensity diffracted was due to the information from depth x, then it can easily be calculated for the various crystallographic peaks. Using the powder diffraction file values of pure Ni, the depth was calculated for each crystallographic peak. For example, $2\theta_{\{111\}} = 44.497°$ corresponds to 95% of the diffracted intensity from depth 12.94 μm, but 50% of that information comes from the first 2.98 μm). Using this calculation, we can conclude that 50% of the XRD information comes from the first 3-6 μm depth of the film and the rest of the information comes from 13-25 μm deep into the film. The large spread in penetration depth is due to the varying 2theta, from smallest to largest.

References for Appendix 1

1. Cullity, B.D., *Elements of X-ray diffraction*. 1956, Addison-Wesley Pub. Co.: Reading, Mass. p. 269-272.
2. Handbook, M., *American society for metals.* Cleveland, Ohio, 1948. **397**.
3. Peisien, H. and H. Rooksry, *X-Ray Diffraction By Polycrystalline Materials*. 1955: The Institute Of Physics; London.

APPENDIX 2: MICROPILLAR COMPRESSION

Additional micropillar experiments were carried out for a loading orientation that was at an 11° angle with respect to the columnar grains and their perpendicular twin boundaries. Figures A2.1-A2.8 detail the stress-strain response of the compressed micropillars.

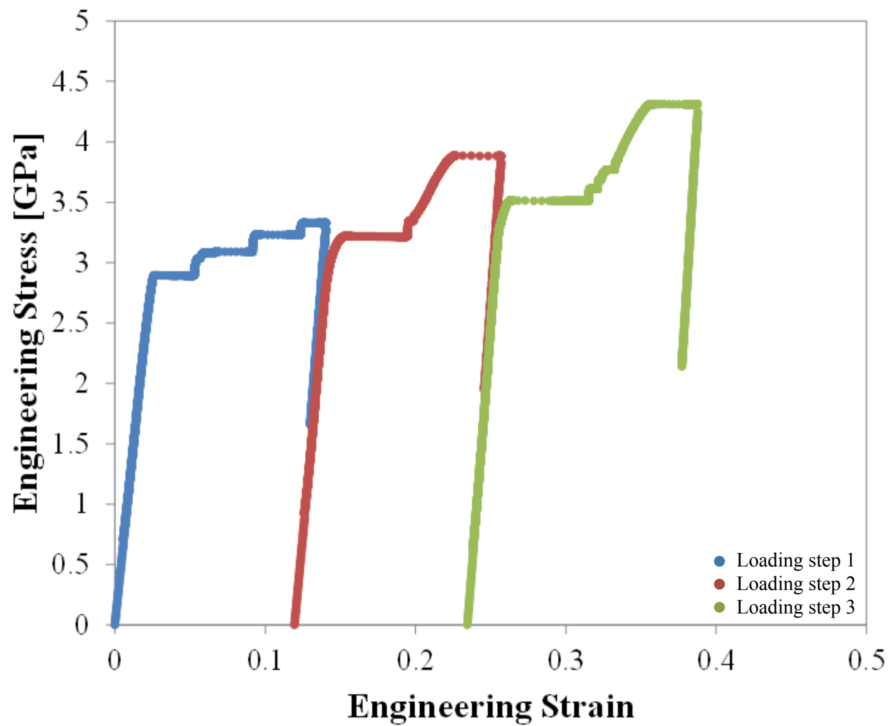

Figure A2.1: Stress-strain curve of a micropillar with an 11° columnar grain tilt that was loaded-unloaded-reloaded for 3 cycles in increments of 1 μm at a nominal strain rate of 10^{-3} s^{-1}.

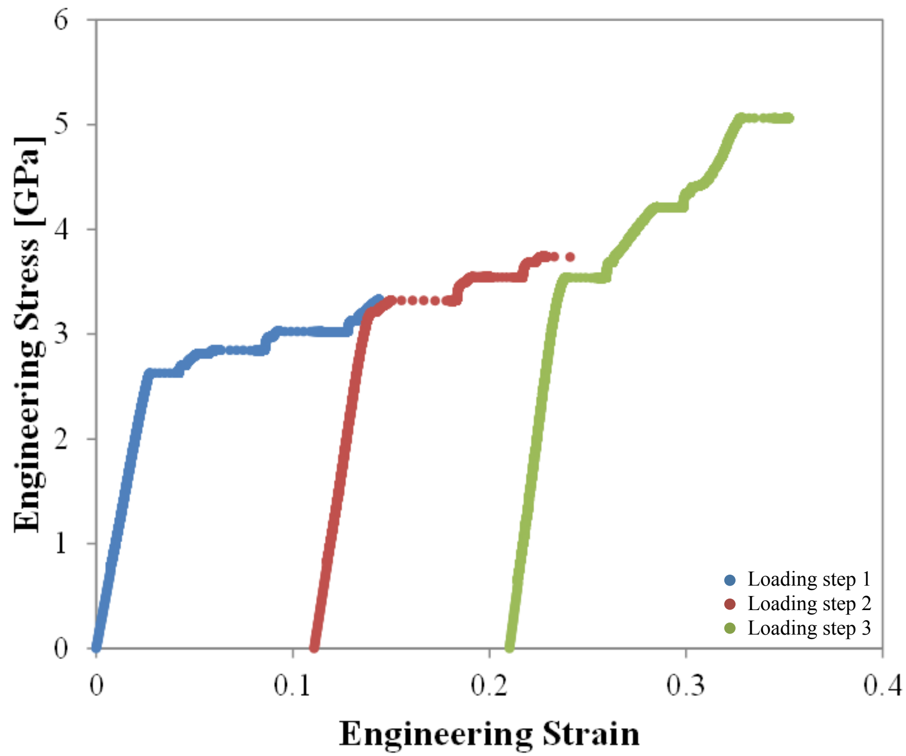

Figure A2.2: Stress-strain curve of a micropillar with an 11° columnar grain tilt that was loaded-unloaded-reloaded for 3 cycles in increments of 1 μm at a nominal strain rate of 10^{-3} s^{-1}.

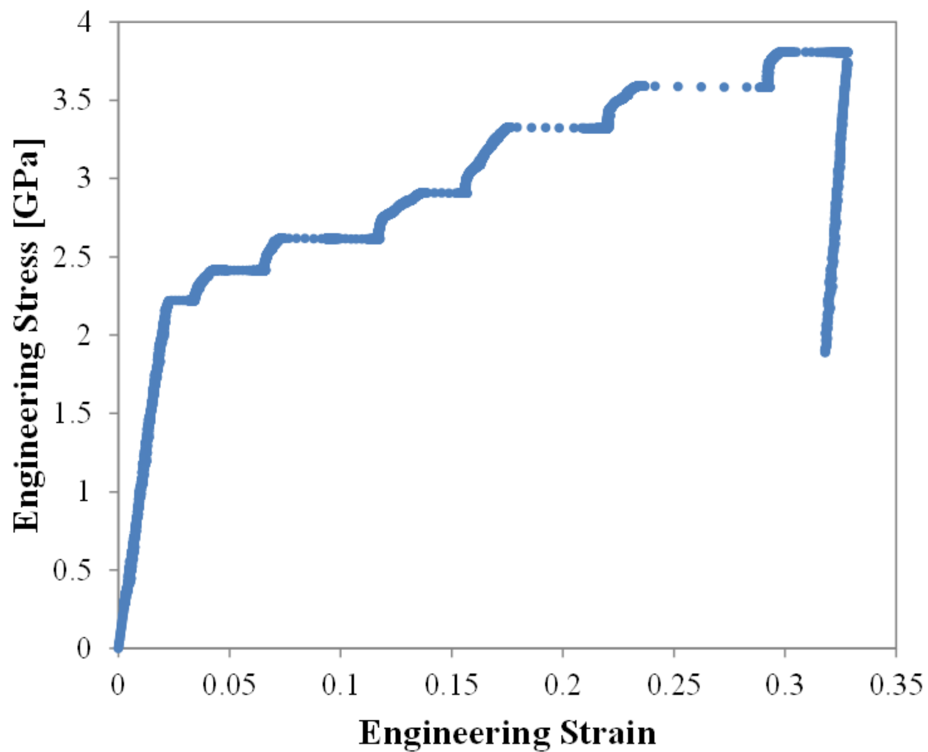

Figure A2.3: Stress-strain curve of a micropillar with an 11° columnar grain tilt that was loaded to a depth of 2 μm at a nominal strain rate of 10^{-3} s^{-1}.

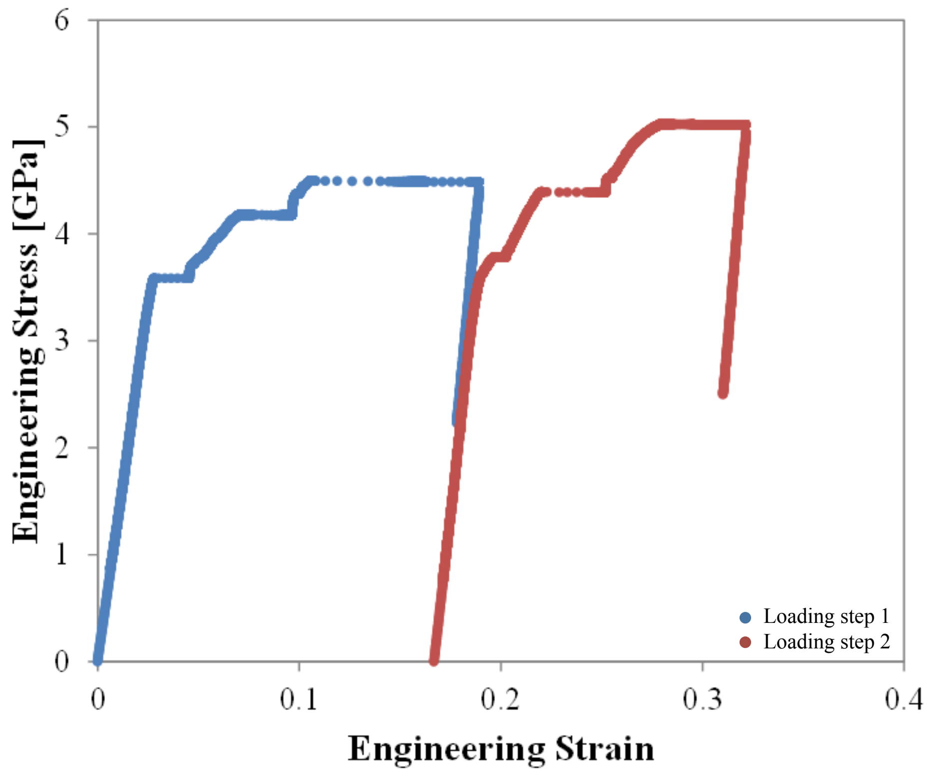

Figure A2.4: Stress-strain curve of a micropillar with an 11° columnar grain tilt that was loaded-unloaded-reloaded for 2 cycles in increments of 1 μm at a nominal strain rate of 10^{-3} s^{-1}.

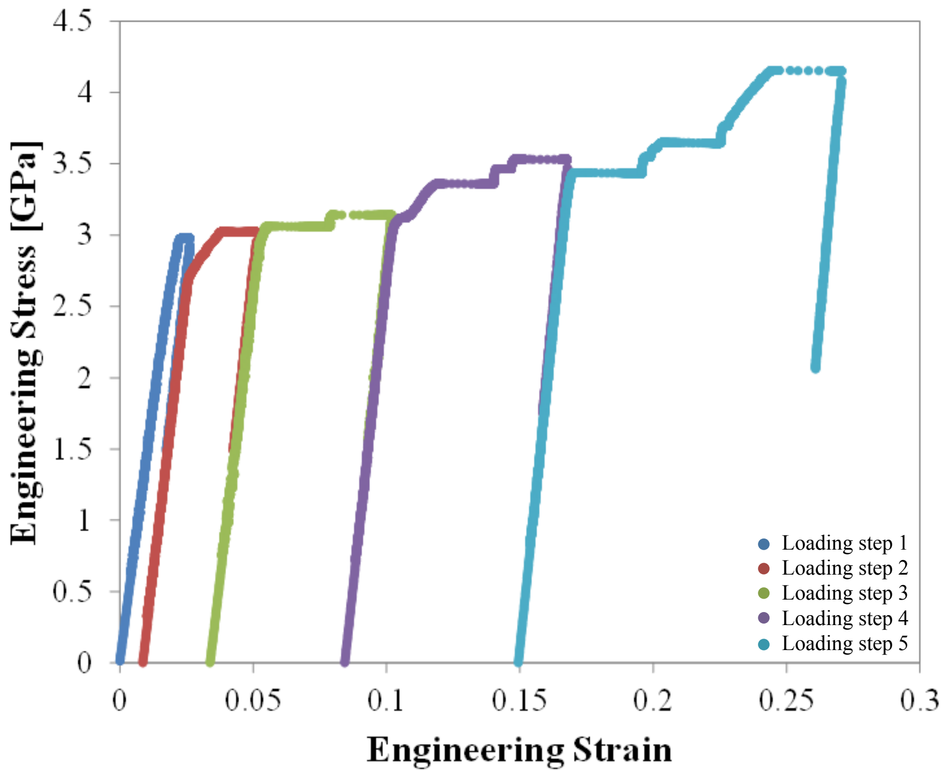

Figure A2.5: Stress-strain curve of a micropillar with an 11° columnar grain tilt that was loaded-unloaded-reloaded for 5 cycles in increments of 100 nm at a nominal strain rate of 10^{-3} s^{-1}.

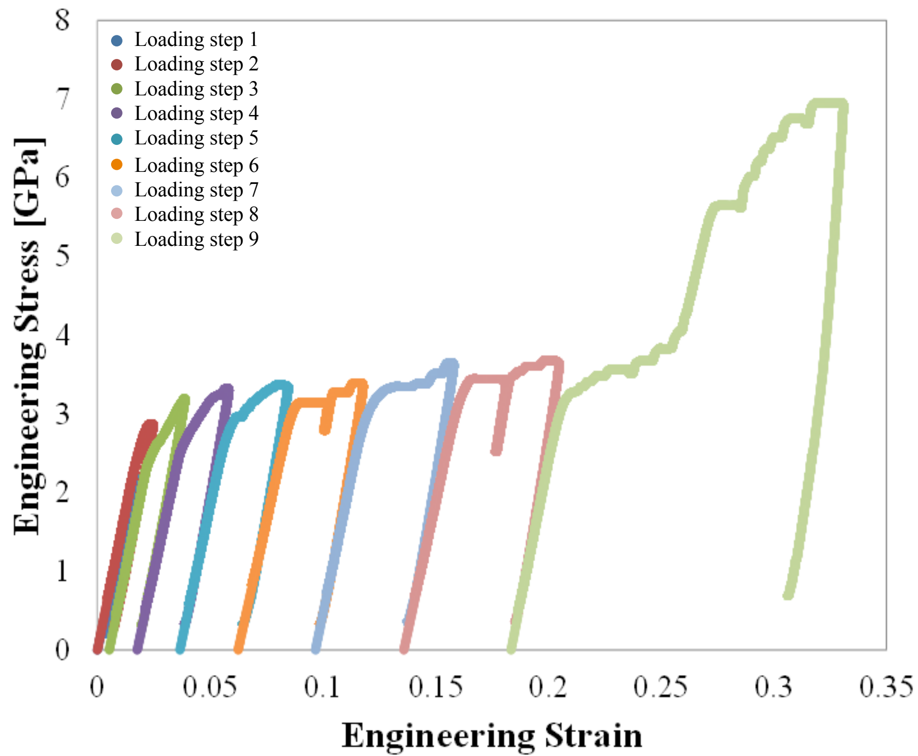

Figure A2.6: Stress-strain curve of a micropillar with an 11° columnar grain tilt that was loaded-unloaded-reloaded for 9 cycles in increments of 50 nm at a nominal strain rate of 10^{-4} s^{-1}, where loading step 1 started at 150 nm.

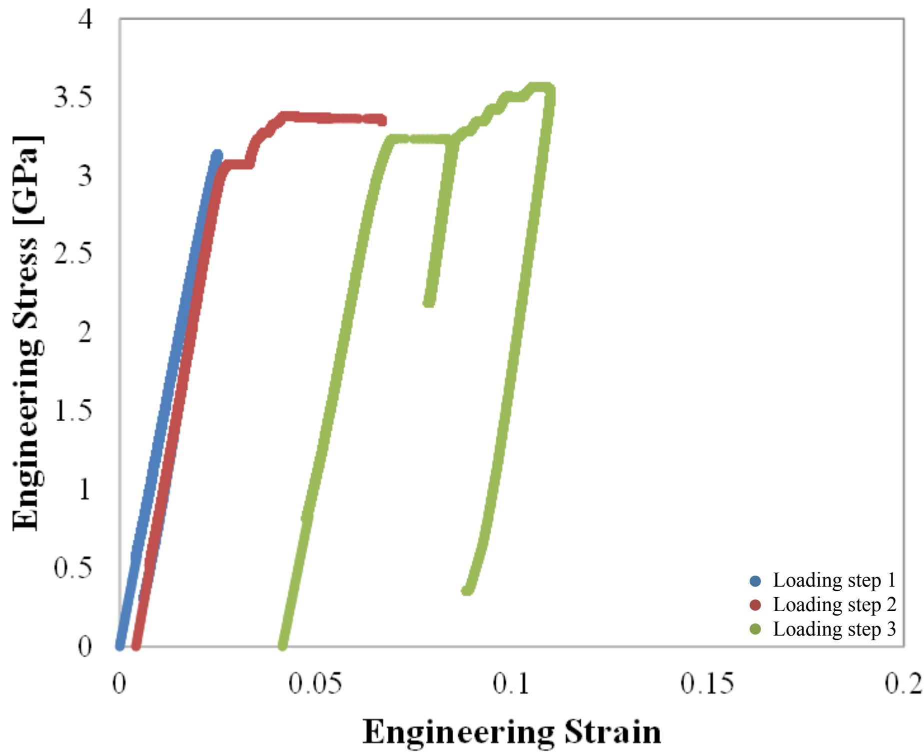

Figure A2.7: Stress-strain curve of a micropillar with an 11° columnar grain tilt that was loaded-unloaded-reloaded for 3 cycles in increments of 100 nm at a nominal strain rate of 10^{-4} s^{-1}, where loading step 1 started at 200 nm.

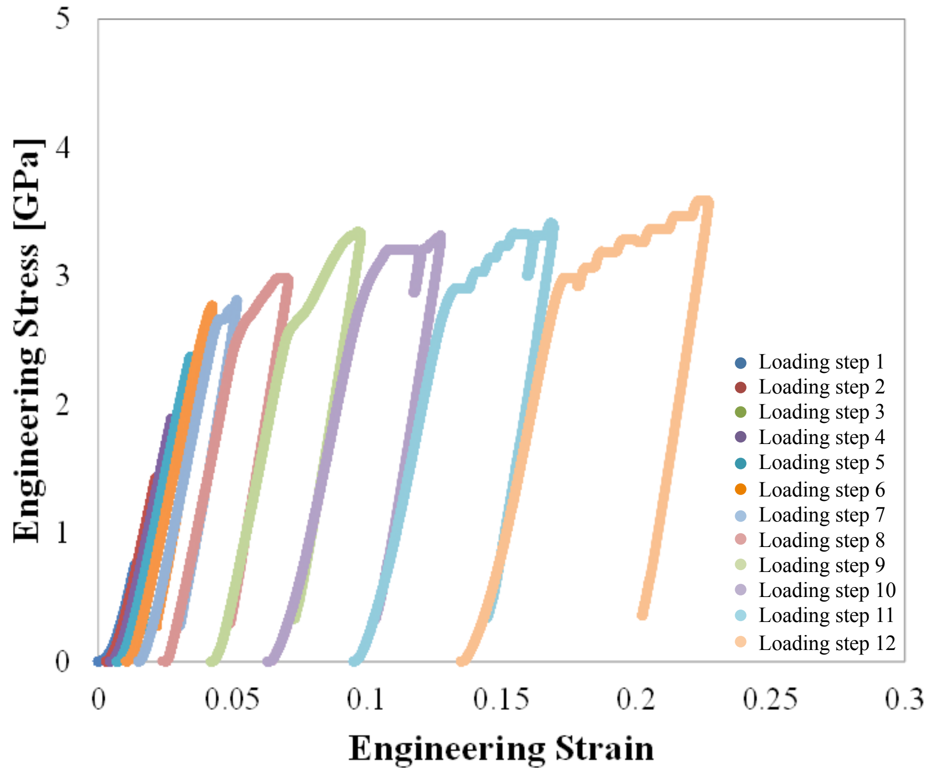

Figure A2.8: Stress-strain curve of a micropillar with an 11° columnar grain tilt that was loaded-unloaded-reloaded for 12 cycles in increments of 50-100 nm at a nominal strain rate of 10^{-4} s^{-1}, where loading step 1 started at 200 nm. Pillar diameter was 5 µm instead of 3 µm to examine size effects.

Similarly, additional micropillar experiments were carried out for well-aligned columnar grains and their perpendicular twin boundaries to the loading orientation. Figures A2.9 and A2.10 detail the stress-strain response of the compressed micropillars. All compression experiments show discrete strain bursts, high hardening and flow strengths exceeding 3.5 GPa.

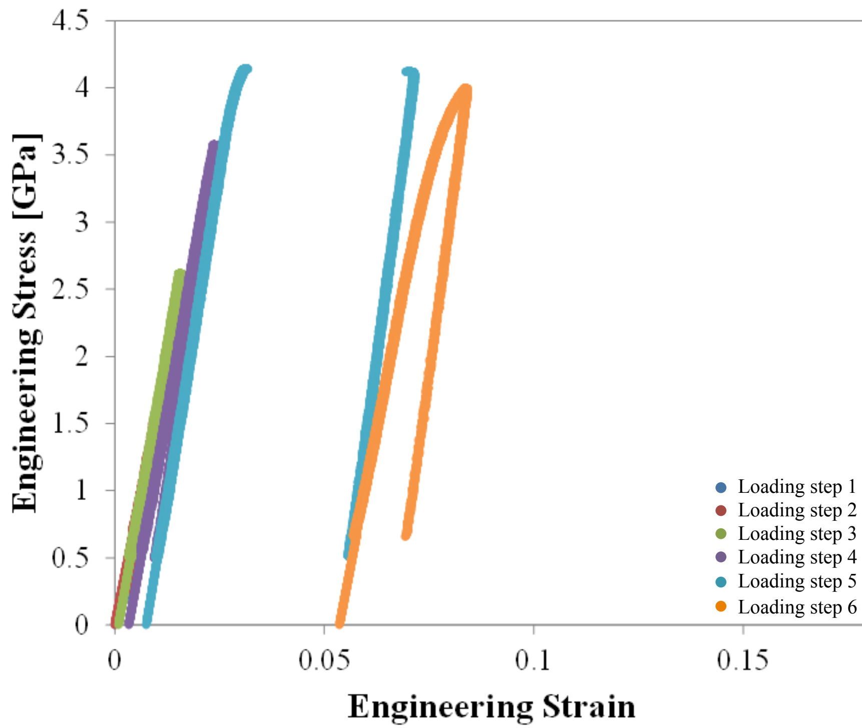

Figure A2.9: Stress-strain curve of a micropillar with well-aligned columnar grains and perpendicular nanotwins with the compression axis. Six different loaded-unloaded-reloaded cycles were performed in 50 nm increments at a nominal strain rate of 10^{-4} s^{-1}.

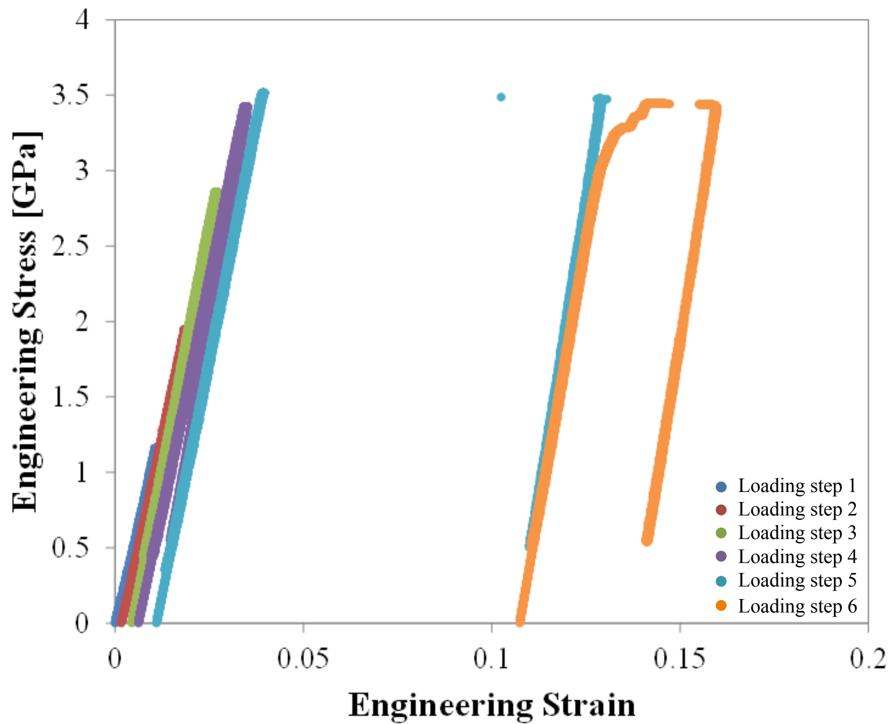

Figure A2.10: Stress-strain curve of a micropillar with well-aligned columnar grains and perpendicular nanotwins with the compression axis. Six different loaded-unloaded-reloaded cycles were performed in 50 nm increments at a nominal strain rate of 10^{-4} s^{-1}, where loading step 1 started at 100 nm.

APPENDIX 3: MICROCANTILEVER FABRICATION

The detailed step-by-step process flow for fabricating freestanding microcantilever beams is given below. Substrate preparations were performed inside the class 100 cleanroom at UPenn and wafers were either sputtered in the chamber inside the cleanroom or shipped to UIUC for sputter deposition. The chamber as UIUC was equipped with a higher dc power supply (maximum 600 W) compared to the chamber at UPenn (maximum 400 W), so often the UIUC chamber was chosen for deposition. All post-film-deposition processing was performed inside of the cleanroom at UPenn, where all necessary tools, chemicals and data sheets are available.

1. Take a clean Si wafer (100 mm diameter, 300±25 μm thickness, <100> orientation, double-side polished with 300±15 nm super low stress silicon nitride) and rinse in acetone, isopropyl alcohol (IPA) and deionized (DI) water. Blow dry via compressed air and dehydrate the wafer for 10 minutes at 200°C on a hot plate. Allow the wafer to cool to room temperature (RT).

2. Measure the bare wafer curvature using the KLA Tencor P7 2 Profilometer about the flat of the wafer. Rotate the wafer 90° to obtain wafer curvature measurements about the perpendicular direction. It is important to take note of which side of the wafer measurements were obtained for later thin film deposition.

3. Sputter deposit Ni-Mo-W films on the same side of the wafer that profilometer scans were measured. Using the desired power (200-600 W) and Ar pressure (1-4 mTorr) settings to obtain ~2.5 μm, depositions were performed at room temperature with a base pressure of 10^{-8} Torr and a substrate rotation of 40 rpm.

4. Using the KLA Tencor P7 2 Profilometer to measure the wafer curvature post-film-deposition, both in the direction of the wafer flat and the perpendicular direction, provides average film stress measurements.

5. Spin-coat positive photoresist S1818 (without primer) on the Ni-Mo-W side of the wafer (referred to as the frontside hereafter) in a two step process:

   i. 5 second at 500 rpm.

   ii. 45 second at 3000 rpm.

6. Perform a soft-bake at 115°C for 1 minute, then cool to RT.

7. Use the SUSS MicroTec MA-6 mask aligner to pattern arrays of microcantilever beam geometries into the resist with the following settings: top-side alignment process, vacuum contact and exposure at a constant dose 100 mJ/cm^2 for 5 seconds.

8. Develop the photoresist using Microposit MF-319 developer for 45 seconds with mild agitation. Remove the wafer from the developer and thoroughly rinse in DI water and blow dry via compressed air.

9. Perform a hard-bake for 1 minute at 115°C, then cool to RT.

10. Setup a bath of Nichrome etchant TFN (Transene Inc.) at 40°C and submerge the wafer with the frontside facing upward. Leave wafer in the etchant for 25 minutes (or until the Ni-Mo-W appears fully etched).

11. Remove wafer from the acid bath and thoroughly rinse with DI water. Check under the Zeiss Axio Imager M2m microscope to ensure all of the Ni-Mo-W metal is fully etched in the areas not protected by the photoresist. If needed, repeat step 10 until all of the Ni-Mo-W is etched, but do not over-etch the wafer.

12. Remove the photoresist from the frontside of the wafer by submerging in a bath of IPA for 1 minute with gentle agitations. Rinse with acetone, IPA and DI water. Blow dry with compressed air to reveal the patterned Ni-Mo-W microcantilevers.

13. Measure microcantilever beam thickness using the KLA Tencor P7 2 Profilometer. Take several measurements at different locations across the wafer to determine the uniformity and provide accurate film stress measurements.

14. Flip the wafer over to the backside of the wafer with blank silicon nitride. Spin-coat primer SurPass 4000 on the backside using the two step process below. During the last 15 seconds, rinse with IPA while its spinning.

15. Soft-bake the primer for 1 minute at 115°C, then cool to RT.

16. Spin coat positive photoresist S1818 on top of the primer using the two step process:

i. 5 second at 500 rpm.

ii. 45 second at 3000 rpm.

17. Soft-bake the photoresist for 1 minute at 115°C, then cool to RT.

18. Use the SUSS MicroTec MA-6 mask aligner to pattern windows for etching on the backside of the wafer with the following settings: back-side alignment process, vacuum contact and exposure at a constant dose 100 mJ/cm^2 for 5 seconds.

19. Develop the photoresist using Microposit MF-319 developer for 45 seconds with mild agitation. Remove the wafer from the developer and thoroughly rinse in DI water and blow dry via compressed air.

20. Use reactive-ion etching (RIE) to dry etch through the silicon nitride layer that is not protected by photoresist. The following process was used:

- Trifluoromethane and oxygen (CHF_3/O_2) with 100 standard cubic centimeters per minute (sccm) of CHF_3 and 4 sccm of O_2 at a pressure of 50 mTorr and radio frequency (RF) power 150 W. Capacitor starting points: capacitor #1: 60%, capacitor #2: 80%.
- Tetrafluoromethane (CF_4) with 20 sccm of CF_4 at a pressure of 65 mTorr and RF power of 150 W. Capacitor starting points: capacitor #1: 80%, capacitor #2: 60%.

  i. CHF_3/O_2 etch for 8 minutes.

  ii. Vent the chamber so it does not overheat and rotate the wafer 180°.

  iii. CHF_3/O_2 etch for another 2 minutes.

  iv. CF_4 etch for 2 minutes.

21. Check under the Zeiss Axio Imager M2m microscope to ensure all of the silicon nitride is fully etched in the areas not protected by the photoresist. If needed, repeat CHF_3/O_2 for 1 minute followed by CF_4 for 1 minute.

22. Remove the photoresist from the backside of the wafer by submerging in a bath of IPA for 1 minute with gentle agitations. Rinse with acetone, IPA and DI water. Blow dry with compressed air.

23. Flip the wafer back to the frontside, with Ni-Mo-W cantilevers, and spin-coat protective alkaline coating ProTEK primer (Brewer Science) onto the cantilevers with the following two step process:

  i. 5 second at 500 rpm.

  ii. 60 second at 1500 rpm.

24. Bake on the hot plate for 1 minute at 205°C and let cool to RT.

25. Spin-coat protective alkaline coating ProTEK B3 onto primer with the following two step process:

  i. 5 second at 500 rpm.
  ii. 60 second at 3000 rpm.

26. Bake on the hot plate for 2 minutes at 115°C and then an additional 1 minute at 205°C. Let the wafer cool to RT.

27. Prepare a 30% concentration potassium hydroxide (KOH) bath heated to 90°C. Submerge the wafer into the KOH bath with the ProTEK side facing upward. Keep submerged for 135 minutes (or until the full Si wafer is completely etched).

28. Remove the wafer from the KOH bath and rinse thoroughly using DI water.

29. Carefully rinse the only the backside with a cycle of acetone, IPA and DI water. Blow dry via compressed air. Note that the ProTEK is attacked when exposed to IPA and acetone, so care must be taken for this step.

30. Use reactive-ion etching (RIE) to dry etch through the silicon nitride layer from the backside. The following process was used:

- Trifluoromethane and oxygen (CHF_3/O_2) with 100 standard cubic centimeters per minute (sccm) of CHF_3 and 4 sccm of O_2 at a pressure of 50 mTorr and radio frequency (RF) power 150 W. Capacitor starting points: capacitor #1: 60%, capacitor #2: 80%.
- Tetrafluoromethane (CF_4) with 20 sccm of CF_4 at a pressure of 65 mTorr and RF power of 150 W. Capacitor starting points: capacitor #1: 80%, capacitor #2: 60%.

i. CHF_3/O_2 etch for 8 minutes.

ii. Vent the chamber so it does not overheat and rotate the wafer 180°.

iii. CHF_3/O_2 etch for another 2 minutes.

iv. CF_4 etch for 2 minutes.

31. Check under the Zeiss Axio Imager M2m microscope to ensure all of the silicon nitride is fully etched.

32. Dice individual dies using the class 1 IPG Photonics IX200F green laser (532 nm) system. Ablation power of 150 kW was used with 100 passes needed to cut through the entire Si wafer.

33. Remove the ProTEK using ProTEK B3 Remover 100 (Brewer Science) with the following multistep process:

i. Immerge individual dies in a bath of ProTEK B3 Remover 100 for 20 minutes at 23°C.

ii. Remove the dies and immerge them into a second bath of ProTEK B3 Remover 100 for 20 minutes at 23°C.

iii. Remove the dies and rinse with IPA for 5 minutes.

iv. Rinse the dies with DI water for 2 minutes and gentle dry with compressed air.

The above micromachining workflow can be summarized into the frontside lithography (Figure A3.1) and backside lithography (Figure A3.2).

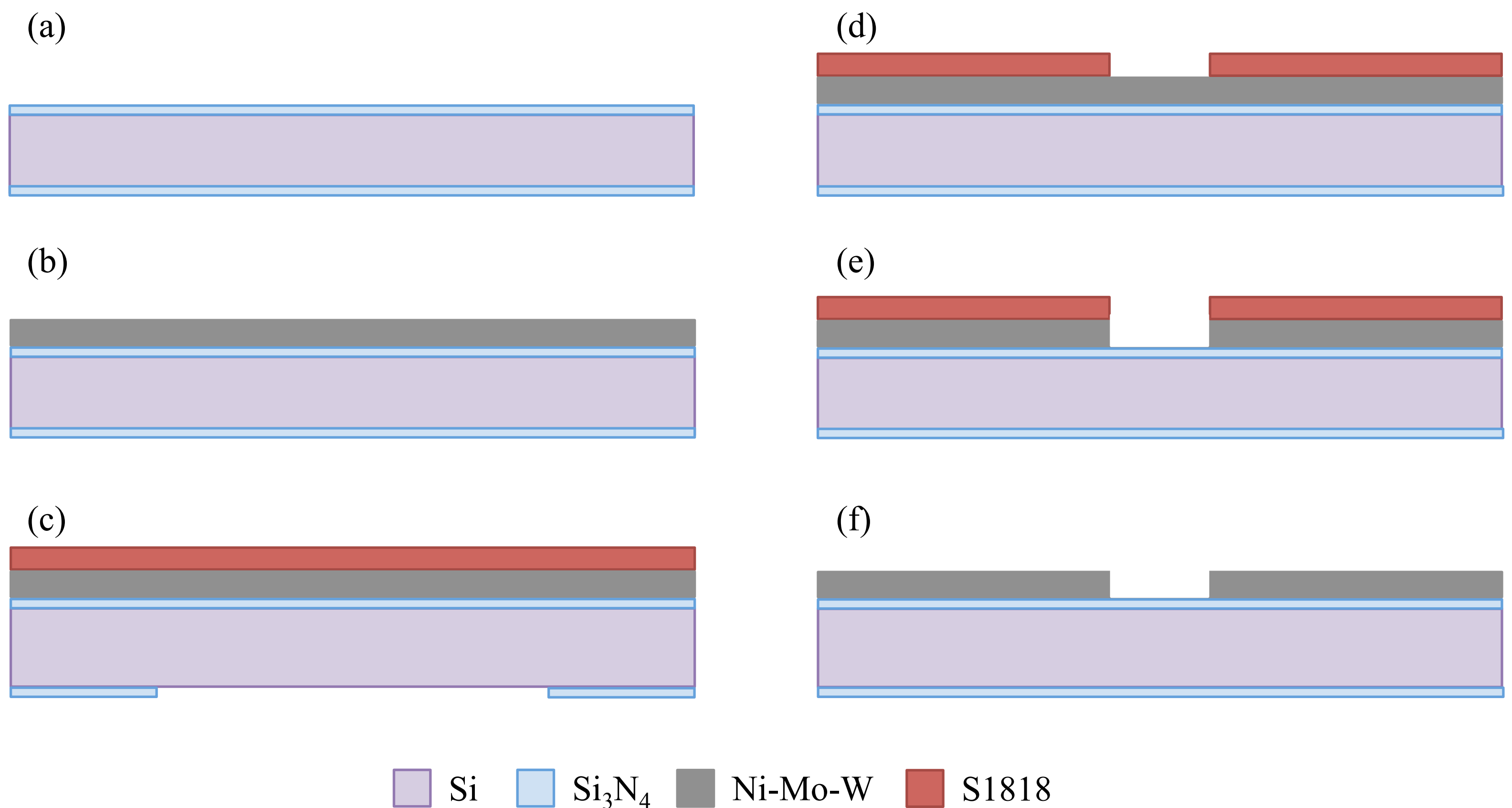

Figure A3.1: Frontside lithography processes with: (a) the blank wafer, (b) Ni-Mo-W thin film deposition, (c) spin-coated photoresist, (d) patterned photoresist, (e) wet etch to shape the Ni-Mo-W cantilevers and (f) removal of the photoresist.

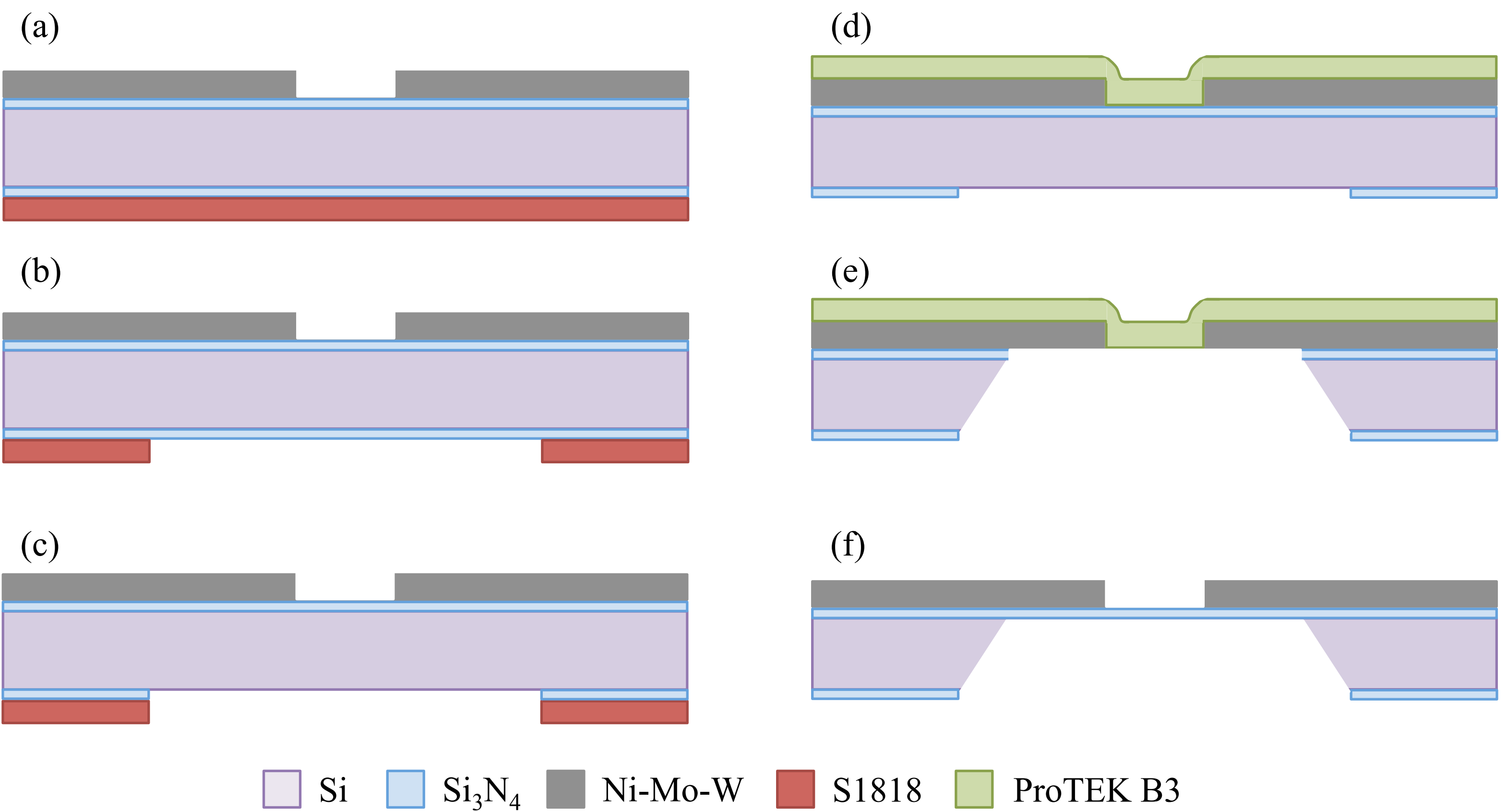

Figure A3.2: Backside lithography processes with: (a) spin-coated photoresist, (b) patterned photoresist, (c) backside RIE to remove silicon nitride, (d) spin-coated ProTEK B3, (e) KOH wet etch of Si and (f) removal of the ProTEK.

Vita

Gianna M. Valentino was born in Camden, New Jersey on October 22nd, 1991 to parents Cynthia and Carmine Valentino Jr. Gianna graduated from Cherry Hill High School East in 2010 and went on to study Physics at Saint Joseph's University in Philadelphia, PA. She completed an honor's research thesis titled, "Optofluidic Switching Devices using Ferrofluids" and in May 2014, she earned a Bachelors of Science degree in Physics with a minor in Mathematics. Thereafter, she joined the department of Mechanical Engineering at Johns Hopkins University in August 2014 for her doctoral studies under the advisement of Professor Kevin J. Hemker. In May 2016 she earned a Master of Science in Engineering degree in Mechanical Engineering and continued on fulfilling the requirements for a Doctor of Philosophy degree in Mechanical Engineering to completion in July 2019.